On the Development of Intercalation-Based Cathode Materials for All-Solid-State Fluoride Ion Batteries

TECHNISCHE
UNIVERSITÄT
DARMSTADT

Dem Fachbereich Material- und Geowissenschaften
der Technischen Universität Darmstadt

zur Erlangung des akademischen Titels
Doktor-Ingenieur (Dr.-Ing.)

vorgelegte Dissertation
von
M.Sc. Mohammad Ali Nowroozi
geboren in Shiraz
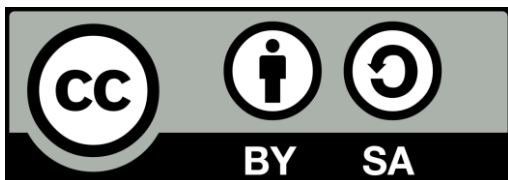
In memory of Salma Nowroozi
1978 – 2019

*"A little and a little, collected together, becomes a great deal;
the heap in the barn consists of single grains,
and drop and drop make the inundation".*

Saadi Shirazi
1210 – 1291

Erklärung zur Abschlussarbeit

Hiermit versichere ich, Mohammad Ali Nowroozi, die vorliegende Dissertation ohne Hilfe Dritter und nur mit den angegebenen Quellen und Hilfsmitteln angefertigt zu haben. Alle Stellen, die Quellen entnommen wurden, sind als solche kenntlich gemacht worden. Diese Arbeit hat in gleicher oder ähnlicher Form noch keiner Prüfungsbehörde vorgelegen.

Darmstadt, den   Mohammad Ali Nowroozi

Abstract

Recently reversible batteries based on fluoride ions as a charge carriers have attracted some attentions as an alternative electrochemical energy storage system to conventional lithium ion batteries (LIBs). Fluoride is the most stable anion with a high mobility and therefore, fluoride ion batteries (FIBs) can theoretically provide a wide electrochemical potential window. Moreover, FIBs are capable of being built in an all solid-state modification. Previously, electrochemical fluoride ion cells based on conversion-based electrode materials have been built. However, the state of the art of the FIBs suffer from poor cycling performance in lack of well-developed cell components including the electrode materials. In the current study, intercalation-based cathode materials have been investigated as an alternative approach to make electrode materials for FIBs. In this respect, various compounds with mainly Ruddlesden-Popper-type structure including $LaSrMO_4$ (M = Mn, Co, Fe) and La_2MO_{4+d} (M = Co, Ni) as well as Schafarzikite-type compounds of $Fe_{0.5}M_{0.5}Sb_2O_4$ (M = Mg, Co) have been subjected to electrochemical measurements including galvanostatic cycling, cyclic voltammetry and electrochemical impedance spectroscopy and the structural changes upon electrochemical fluorination/de-fluorination were analyzed by X-ray Diffraction (XRD). $LaSrMnO_4$ has been fluorinated/de-fluorinated via electrochemical method confirming successful intercalation/de-intercalation of the fluoride ions, but showed problems for long-term operation. In contrast, La_2NiO_{4+d} showed to be the most promising intercalation-based cathode material (for FIB) in terms of cycling stability (>220 cycles and 60 cycles for cutoff capacities of 30 and 50 mAh/g, respectivly) with a nearly 100% Coulombic efficiency (average Coulombic efficiency of 97.68% and 95.44% for cutoff capacities of 30 and 50 mAh/g, respectively). This is the highest cycle life that has been reported so far for a FIB. One of the major challenges of the proposed FIB systems was found in avoiding oxidation of the conductive carbon which has been mixed with the electrodes to improve the electronic conductivity. This decomposition of the carbon matrix results in a remarkable increase in the impedance of the cell and can significantly impair the cycle life and discharge capacity. However, the critical charging conditions which could be determined by cyclic voltammetry and electrochemical impedance spectroscopy have a major impact on preserving the conductivity of the cell. In addition, the effect of volume change in the conversion-based anode materials has been studied showing that the overpotentials arising from the volume change can significantly influence the cycling behavior of the battery system (due to absence of well-developed intercalation-based anode materials for FIBs, conversion-based counter electrodes have been used as anode materials).

Abstrakt

In den letzten Jahren haben reversible Batterien auf der Basis von Fluorid-Ionen als Ladungsträger als alternatives elektrochemisches Energiespeichersystem zu herkömmlichen Lithium-Ionen-Batterien (LIBs) hohe Aufmerksamkeit erlangt. Fluorid ist das stabilste Anion mit einer hohen Mobilität; daher kann in Fluoridionenbatterien (FIBen) theoretisch ein breites elektrochemisches Potenzialfenster erschlossen werden. Außerdem können FIBen als reine Feststoffbatterien assembliert werden. Bisher wurden elektrochemische Fluorid-Ionen-Zellen auf der Basis von Elektrodenmaterialien auf Konversionsbasis gebaut. Dieses Funktionsprinzip leidet jedoch unter einer geringen Zyklierbarkeit, wobei es zudem an gut entwickelten Zellkomponenten einschließlich der Elektrodenmaterialien mangelt. In dieser Arbeit wurden Kathodenmaterialien auf Interkalationsbasis als alternativer Ansatz zur Herstellung von Elektrodenmaterialien für FIBen untersucht. Hierbei wurden verschiedene Verbindungen im Ruddlesden-Popper Strukturtyp, einschließlich $LaSrMO_4$ (M = Mn, Co, Fe) und La_2MO_{4+d} (M = Co, Ni) sowie Verbindungen des Schafarzikit-Typs $Fe_{0.5}M_{0.5}Sb_2O_4$ (M = Mg, Co) elektrochemischen Messungen einschließlich galvanostatischem Zyklieren, Cyclovoltammetrie und elektrochemischer Impedanzspektroskopie unterzogen. Strukturänderungen im Rahmen der elektrochemischen Fluorierung/Defluorierung wurden mittels Röntgenbeugung (XRD) analysiert. $LaSrMnO_4$ wurde mit dieser elektrochemischen Methode reversibel fluoriert/defluoriert, was die strukturelle Stabilität der Verbindung aufzeigte, jedoch gleichzeitig Probleme für den Langzeitbetrieb aufwies. Im Vergleich dazu erwies sich La_2NiO_{4+d} als das vielversprechendste Kathodenmaterial auf Interkalationsbasis aufgrund seiner Zyklenstabilität (>220 Zyklen bzw. ~60 Zyklen für Cutoff-Kapazitäten von 30 bzw. 50 mAh/g), mit einer fast 100%igen Coulomb-Effizienz (durchschnittliche Coulomb-Effizienz von 97,7 % bzw. 95,4 % für Cutoff-Kapazitäten von 30 bzw. 50 mAh/g). Dies stellt die höchste Lebensdauer, die bisher für eine FIB berichtet wurde, dar. Eine der größten Herausforderungen der vorgeschlagenen FIB-Systeme besteht darin, die Oxidation des leitfähigen Kohlenstoff-Additivs zu vermeiden, das im Elektrodenkomposit zur elektrischen Kontaktierung des Aktivmaterials beigemengt ist. Es konnte gezeigt werden, dass diese Zersetzung der Kohlenstoffmatrix zu einer starken Erhöhung der Impedanz der Zelle führt und dadurch die Lebensdauer und erhaltbare Entladekapazität erheblich beeinträchtigen kann. Die kritischen Ladebedingungen, die durch Cyclovoltammetrie und elektrochemische Impedanzspektroskopie bestimmt werden konnten, zeigen einen großen Einfluss auf die Erhaltung der Leitfähigkeit der Zelle. Darüber hinaus wurde die Auswirkung der Volumenänderung der Anodenmaterialien auf Konversionsbasis untersucht, was zeigt, dass die aus der Volumenänderung resultierenden Überpotenziale das Zyklierungsverhalten des Batteriesystems erheblich beeinflussen können.

Table of Contents

1   Introduction

1.1   Fluoride Ion Batteries: An Alternative Energy Storage System

Undoubtedly our modern life is extremely dependent on the portable energy storage devices. From small gadgets such as smart phones, tablets and laptops to the brand new electric vehicles and airplanes, that seems to be the future of mobility, all benefit from the modern rechargeable energy storage technology that can be used almost everywhere. Moreover, energy storage technologies play an essential role when it comes to harvesting and converting solar and wind energy, mechanical vibration, waste heat, etc. to electricity, as a solution for producing green and sustainable energy. Therefore, there is a significant increasing demand for rechargeable power sources.

In the last two decades, Li-ion batteries (LIBs) turned out to be the first choice for portable electronics, power tools, and electric vehicles due to their unique electrochemical properties including high energy and power density, high potential and cyclic stability [1]. Such a well-developed electrochemical behavior and flexibility in adapting into a wide range of applications made lithium to be considered as "The New Gold" [2]. Significant amounts of lithium can be found in sea water and hard rocks, though, the extraction from these sources is extremely expensive and tricky. Therefore, most of the produced lithium ($\sim$ 83%) comes from brine lakes and salt pans [2, 3]. Nevertheless, there is a controversial debate about the availability of lithium reserves (in terms of production of Li_2CO_3) in long term run [1-5]. Furthermore, most of the world's economic lithium reserves are found in a small location on earth between the borders of Chile, Bolivia, and Argentina [4, 6]. This potentially can be a strategic problem for the rest of the world, especially for the industrialized countries.

On the other hand, current state of the art of the LIBs are based on organic liquid electrolytes, leading to some drawbacks including insufficient lifetime, high cost, low power density and most importantly safety issues [7, 8]. In this respect, all solid-state post-lithium ion batteries can be a solution to address both current LIB issues of the possible lithium shortage and the safety concerns.

Alternative rechargeable battery systems (which perform based on shuttling of ions other than Li) have been so far proposed and investigated including sodium ion batteries (NIBs) [9, 10], magnesium ion batteries [10, 11] and aluminum ion batteries [12] from the Li side of the standard reduction potential series and chloride ion batteries [13] and fluoride ion batteries (FIBs) [14] from the other side of electromotive force (EMF) series. Among them, batteries based on fluoride ions as the charge carriers (FIBs) can, at least theoretically, be a suitable candidate since fluorine is the most electronegative element in the periodic table and therefore, the fluoride ion is a very stable anion, facilitating access to a wide electrochemical potential window. Furthermore, fluoride containing materials are globally more abundant as compared to lithium reserves, for instance, in the form of CaF_2 [15].

1.2   Development of FIBs: A Review

In this section the development of FIBs and their components will be reviewed more or less in a chronological way. It should be taken into consideration that some of the investigations in this field have been accomplished during the current study.

FIBs have been firstly proposed in 1970s (mostly they were referred to as fluoride galvanic cells at the time). Baukal [16] claimed that CaF_2 could serve as a solid electrolyte in an all-solid-state FIB at a temperature range of 400 – 500 °C. However, no experimental results on operation of a full cell were reported. Kennedy and Miles [17] showed the first experimental observation of an electrochemical cell based on shuttling of fluoride ions, using KF-doped β-PbF_2 as a solid electrolyte in $CuF_2|\beta$-$PbF_2|Pb$ and $AgF|\beta$-$PbF_2|Pb$ electrochemical cells. Although the observed starting potentials (0.70 V and 1.3 V for CuF_2/Pb and AgF/Pb cells, respectively) were close to OCV ($Pb + CuF_2 \longrightarrow PbF_2 + Cu$; $\Delta E° = 0.72$ V; $Pb + 2\,AgF \longrightarrow PbF_2 + 2\,Ag$; $\Delta E° = 1.32$ V), poor capacities were observed due to strong polarizations which have been suggested to be a result of formation of α-PbO_2 phase in the anode material leading to a poor ionic conductivity of the cell. In another work of the same research group, they reported on discharging a thin-film cell made up of CuF_2, Pb, and PbF_2 cathode, anode, and electrolyte materials, respectively [18]. Results revealed that discharge capacities as large as ∼ 40 % of the theoretical capacity of CuF_2 (528 mAh/g) could be obtained; though, further charge of the cell could not be achieved.

In 1976 Schoonman [19] reported on building a $Pb|\beta$-PbF_2:$AgF|BiO_{0.09}F_{2.82}|Bi$ cell by spring-loading the disks of Pb and Bi which have been painted by the β-PbF_2:AgF and $BiO_{0.09}F_{2.82}$ powders dispersed in ethyl acetate. The observed discharge potential (0.330 – 0.335 V) was close to the OCV (0.37 V), showing that oxyfluorides can principally be candidates for the electrolyte materials in FIBs. However, no further information about the reversibility of the cell was reported. Following the Schoonman's work, in 1978 Danto et al. has reported on reversible cycling of thin film (mean thickness of 0.55 μm) solid-state galvanic cells made up of Pb as the anode, $BiF_3|Bi$ as the cathode, and PbF_2 (cubic β-PbF_2) as the electrolyte [20]. The measurements were performed in room temperature. They reported on a starting discharge potential as large as 353 mV followed by a flat discharge plateau at around 280 mV for a current density of 40 μA/cm^2.

Investigations on the electrolytes for fluoride ion galvanic cells were followed up by Schoonman, where in 1979 he reported [21] on new solid solution based on $M_{1-x-y}U_xCe_yF_{2+2x+y}$ (M = Ca, Sr, Ba) for thin film galvanic cells with BiF_3 and Ca as cathode and anode materials, respectively. In 1981 the term of solid-state fluoride ion battery has been used for the first time from Schoonman and Wolfert [22, 23]. In these publications, they reported on improvements in ionic conductivity of CaF_2 as the anode by doping La or Yb (for instance $Ca_{1-x}La_x$ to form the corresponding fluoride of $Ca_{1-x}La_xF_{2+x}$).

Since 1981 until 2011 not much has been done in the field of FIBs. However, in 2011 FIBs attracted some attentions again, where Reddy and Fichtner reported on reversible all-solid-state conversion based FIBs using metal/metal fluoride electrode materials and Ba doped in LaF_3 ($La_{1-x}Ba_xF_{3-x}$) as the electrolyte. The cathodic and anodic reactions during discharge of their cell can be written as follows (sketch of the battery is illustrated in Figure 1-1):

At cathode side: $xe^- + MF_x \longrightarrow M + xF^-$;

At anode side: $xF^- + M´ \longrightarrow M´F_x + xe^-$.
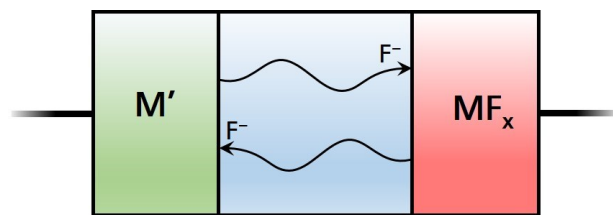
Figure 1-1. A schematic illustration of the metal/metal fluoride conversion base FIB proposed by Reddy and Fichtner [14].

In that study, it was shown that doping of Ba into tysonite-type structure LaF_3 results in a significant increase (roughly two orders of magnitude) in the ionic conductivity. Results suggest that $La_{0.9}Ba_{0.1}F_{2.9}$ which was produced by milling of BaF_2 and LaF_3 has the highest ionic conductivity among all other $La_{1-x}Ba_xF_{3-x}$ ($0 \leq x \leq 0.15$) compounds (about 2.8×10^{-4} S/cm at 160 °C [14]). Then various metal fluorides including CuF_2, BiF_3, SnF_2, and $KBiF_4$ as cathode materials were tested against Ce metal to make an all-solid-state FIB in charged state. Since most of the electrode materials (e.g. BiF_3 and CuF_2) suffered from low ionic and electronic conductivity, they were mixed with the solid electrolyte and carbon for a better electrochemical performance. The results revealed that for CuF_2 composite material the highest discharge capacity of 322 mAh/g (in the first cycle) with a flat discharge potential of around 2.7 V could be obtained, when the cell was discharged at 150 °C using a current density of 10 $\mu A/cm^2$. For the BiF_3 cathode composite, a flat plateau around 2.5 V with a discharge capacity of 126 mAh/g observed. However, the discharge capacity could be further increased up to 190 mAh/g by synthesizing a BiF_3 (tysonite-type) solid solution through mechanical milling with increased rotational speed up to 600 rpm. Further, the average discharge potential slightly reduced to ~ 2.15 V for the BiF_3 solid solution. The improvement of the discharge capacity has been attributed to a higher fluoride ion mobility within the BiF_3 solid solution as compared to BiF_3 composite.

Considering the cycling performance of the Bi/BiF_3 (solid solution) against Ce/CeF_3 reveals a poor cycling behavior of the cell: A large capacity loss (~ 35%) can be detected only after the first cycle followed by more capacity fading in the next cycles, leading to only ~ 26% capacity retention after 40 cycles (see **Figure 1-2**).
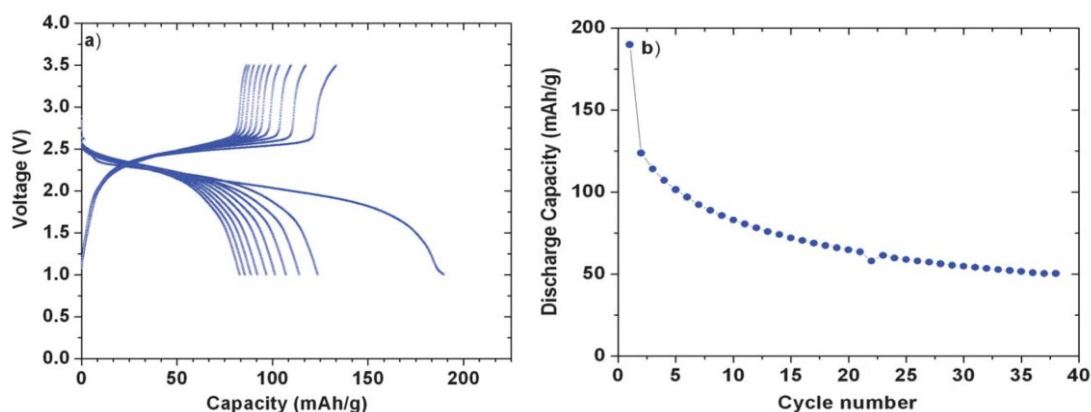
Figure 1-2. (a) Cycling performance of the BiF₃ (solid solution)/Ce cell for the first 10 cycles; (b) changes of discharge capacity with cycle numbers for the same electrochemical cell. The figures have been reprinted from [14] with permission[1].

Further investigations have been done on tysonite-type $La_{1-x}Ba_xF_{3-x}$ and fluorite-type $Ba_{1-x}La_xF_{2+x}$ electrolyte materials by the same research group in order to have a better understanding on the mechanism of conductivity and to improve the ionic conductivity of the solid fluoride ion conductors [24, 25]. Results [24] revealed that sintering of $La_{0.9}Ba_{0.1}F_{2.9}$ ion conductor at 800 °C for 2 h can significantly increase the ionic conductivity (up to 9.06×10^{-4} S/cm at 160 °C), though, increasing the sintering time does not remarkably change the conductivity. For $Ba_{0.6}La_{0.4}F_{2.4}$, however, the ionic conductivity reduces almost by one order of magnitude upon sintering the electrolyte material at the same sintering condition, highlighting different mechanism in ion conductivity in tysonite and fluorite-type solid ion conductors: Reduction in the ionic conductivity of fluorite-type $Ba_{0.6}La_{0.4}F_{2.4}$ over sintering originates from reduction in grain boundaries due to grain growth. Therefore, it is concluded that the ionic conductivity in the fluorite-type $Ba_{0.6}La_{0.4}F_{2.4}$ is controlled by the migration of vacancies along the grain boundary pathways [26]. However, in the tysonite-type $La_{1-x}Ba_xF_{3-x}$ fluoride ion conductors, grain boundaries result in a partial blocking of the migration pathways. Thus, sintering treatments increase ionic conductivity due to grain growth (reduction in grain boundaries) [27]. Further investigations showed that synthesis of tysonite-type $La_{0.95}Ba_{0.05}F_{2.95}$ electrolyte material by coprecipitation method followed by sintering the material at 800 °C for 2 h increases the ionic conductivity by two orders of magnitude as compared to ball milled $La_{0.9}Ba_{0.1}F_{2.9}$ [25]. Better performance of the coprecipitated electrolyte was then attributed to lower amounts of impurities during the synthesis process as compared to mechanical alloying. The improvement of the electrolyte material resulted in a significant increase in the discharge capacity of BiF_3/Ce electrochemical cell up to 250 mAh/g; though, the cell still suffered from a strong capacity fading over cycling of the cell (the discharge capacity reached to 90 mAh/g after only 8 cycles, when the cells were cycled at 150 °C).

In 2014 studies of new anode composite materials for FIBs have been conducted by Fichtner et al. [27]. In this study, all solid-state cells in discharged state have been subjected to galvanostatic cycling using Bi or Cu as the cathode material, CeF_3, CaF_2 and MgF_2 as the anode material, and $La_{0.9}Ba_{0.1}F_{2.9}$ as the electrolyte material. Due to poor ionic/electronic conductivity of the cathode materials, they have been mixed with the electrolyte (60 wt%) and C black (10 wt%). CeF_3 anode material was only mixed with C black (10 wt%), since it has a reasonable ionic conductivity, however, other anode materials have been mixed with both C and the electrolyte at different weight ratios. The results suggested that the electrochemical fluorination of Bi against CeF_3 (during charging) takes place in several steps: First, traces (remaining from the starting powder) of Bi_2O_3 were fluorinated and β-$BiF_{3-2x}O_x$ formed, which was accompanied by a charge plateau below 2.4 V. In the second step, BiF_3 forms from Bi (desired reaction) and a plateau between $2.5 - 2.7$ V could be observed. Last step was referred to formation of BiF_5 from previously formed BiF_3. Considering the theoretical capacity of Bi/BiF_3 (385 mAh/g), the first charge capacity seemed to be higher than that (404 mAh/g). The authors attributed such an extra charge capacity as conversion of BiF_3 to BiF_5 side reaction. Other possibilities such as carbon or electrolyte decomposition were not evaluated as the source of the side reaction in correlation with the observed excessive charge capacity. Cycling performance of the Bi cells against CeF_3, CaF_2 and MgF_2 showed large capacity fading in the first cycle: Although the Bi/CeF_3 cell was charged up to $\sim$ 400 mAh/g (cutoff voltage of 4 V), the first discharge capacity determined to be only 20 mAh/g. In the next cycle the discharge capacity reduced further only up to 10 mAh/g. The cycling behavior for CaF_2 or MgF_2 appeared to be even worse. The reason for such a poor cycling performance were attributed to high reactivity of Ca or Mg (e.g. towards O_2) in the anode after charging. To improve the cycling behavior of the cells, the authors have

implemented a strategy based on mixing charge and discharge products to make the anode material (mixing metal and the respective metal fluoride, e.g. $Mg+MgF_2$). This strategy led to a significant improvement in the cycling performance of the cells (both in CuF_2 and BiF_3), though, the capacity fading was still very large and the charge capacity reached from ~ 270 mAh/g in the first cycle to ~ 25 mAh/g in the 10th cycle for $BiF_3/Mg+MgF_2$ and from ~ 380 mAh/g to 50 mAh/g from cycle 1 to cycle 2 for $CuF_2/Mg+MgF_2$ cell (please see **Figure 1-3**).
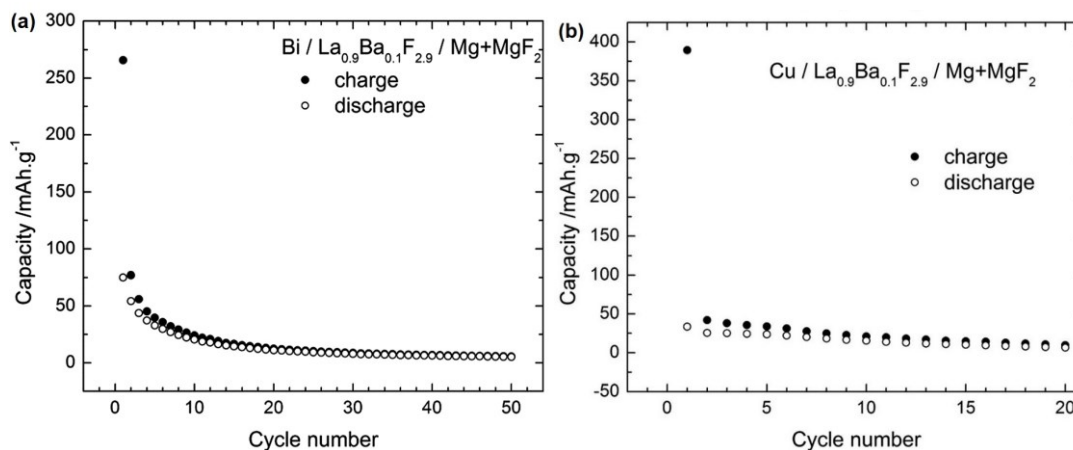
Figure 1-3. Cycling performance of (a) Bi/Mg+MgF₂ and (b) Cu/Mg+MgF₂ electrochemical cells. The figures have been reprinted from [27][2].

Conversion-based electrode materials were the main focus of the developers of FIBs so far. It is worth mentioning that, investigations on fluorine insertion in oxides via electrochemical fluorination have been performed even before recent development of FIBs. For instance, $Y_1Ba_2Cu_3O_{7-x}$ structure has been electrochemically fluorinated in an all-solid-state configuration in 1991 by MacManus et al. [28] using single crystal of Eu-doped in LaF_3 as the ion conductor and Cu/CuF_2 as the counter electrode (at T = 300 °C). Careful evaluation of the structural changes upon fluorine insertion, they reached to the conclusion that the fluorination process resulted in a shrinkage in c parameter of the cell which has been explained as the occupation of fluorine in oxygen sites in the basal plane of the lattice. The other example is electrochemical fluorination of La_2CuO_4 in a classic three electrode configuration using organic fluorinated electrolytes (in liquid state) and gold foil and Pt wire as counter and reference electrodes, respectively [29]. In this work, it was claimed that 0.18 fluoride ions have been electrochemically inserted in the vacant interlayers of La_2CuO_4, resulting in an increase in the parameter c of the cell from 13.141 Å before electrochemical fluorination to 13.205 Å after fluorine insertion. The results were in a good agreement with the other fluorination methods including using F_2 gas. It should be taken into consideration that in both mentioned cases, no electrochemical behavior has been reported since the investigations were solely devoted to the fluorine insertion (intercalation). However, efforts on developing of all-solid-state FIBs based on intercalation mechanism have been reported by Clemens et al. in 2014 [30]. In this study, perovskite type compound $BaFeO_{2.5}$ has been investigated as an intercalation based cathode material against Ce/CeF_3 or Mg/MgF_2 conversion based anode materials using $La_{0.9}Ba_{0.1}F_{2.9}$ electrolyte (at 150 °C). The cell has been charged up to 4.0 V (vs. CeF_3) corresponding to ~ 80 mAh/g which is slightly larger than the theoretical capacity of $BaFeO_{2.5}/BaFeO_{2.5}F_{0.5}$

---

[2] Open Access

(57.5 mAh/g). This was claimed to be arising from side reactions. Diffraction experiments revealed that upon the electrochemical fluorination (charging), a decrease in the lattice parameter of the $BaFeO_{2.5}$, down to the range where oxidatively fluorinated compounds is expected, could be observed together with a symmetry change from a vacancy ordered modification to a cubic (or nearly cubic) perovskite. Structural changes upon electrochemical fluorination were in agreement with fluorinating the perovskite $BaFeO_{2.5}$ compound via other routes such as chemical fluorination using F_2 gas. Although the chemical fluorination was successful, only negligible discharge capacities could be obtained upon discharging the cell against CeF_3. From Galvanostatic cycling of a $BaFeO_{2.5}/La_{0.9}Ba_{0.1}F_{2.9}/MgF_2$ cell, a discharge capacity of around 6 mAh/g (starting discharge potential was measured to be ~ 2.7 V followed by a sloping plateau) could be obtained at the first cycle (the cell was initially charged up to 4.0 V which corresponds to a charge capacity of ~ 45 mAh/g and the cell was discharged to 1.0 V). In the next cycles, a large charge overvoltage could be observed, leading the cell to meet the potential cutoff criteria (4.0) at a significantly shorter charge capacity of around 12 mAh/g followed by a small discharge capacity fading (5 mAh/g). In this paper, only the first three cycles of the mentioned cell have been reported; however, a large extra overvoltage and capacity fading could be detected. Nevertheless, it was shown that intercalation-based electrode materials can in principle serve as reversible electrode materials for FIBs. The highlight of this research lies within the fact that the cell is suitable to fluorinate perovskite-type compounds.

Efforts on developing the electrolyte materials for FIBs were not only allocated to solid-state fluoride ion conductors, but liquid or polymer electrolytes were also considered as an alternative ion conductor with improved conductivity at even room temperature. Gschwind and Fichtner have reported [31] in 2014 about developing a new electrolyte system based on ammonium bifluoride-doped polyethylene glycol (PEG) matrix mixed with a mixture of MeCN as the solvent. The electrolyte showed an ionic conductivity as large as 2.1 mS/cm for a concentration of 0.02 M at room temperature. The electrochemical cells based on the PEG liquid electrolyte, BiF_3 (mixed with C) cathode material and lithium foil as the anode material were subjected to galvanostatic discharging experiments at 25 °C using a discharge current of 10 μA. Results showed that discharge capacities of 136 mAh/g and 189 mAh/g could be achieved for the concentrations of 0.02 M and 0.05 M. Surprisingly, increasing the electrolyte concentration up to 0.08 M significantly deteriorated the discharge capacity to almost 110 mAh/g. This has been explained by precipitation of the electrolyte since the concentration of 0.08 M was too close to the saturation point of the solute [31]. No further cycling behavior has been reported in this study.

Further investigations towards solid-state room temperature electrolyte materials for FIBs have been carried out on tysonite-type structure $Sm_{1-x}Ca_xF_{3-x}$ ($0.05 \leq x \leq 0.17$) by Demourgues et al. in 2015 [32]. The electrolyte materials have been prepared through solid state synthesis followed by sintering at 1000 °C. Rietveld analysis of the XRD data showed a reduction in the unit cell volume over increasing the amount of Ca dopant. This unexpected volume cell reduction has been attributed to creation of anionic vacancies that decrease the cationic coordination. The best ionic conductivity as large as 1.0×10^{-4} S/cm has been obtained for $Sm_{0.95}Ca_{0.05}F_{2.95}$ at room temperature. Further increase in the x values resulted in reduction in conductivity. This has been explained by modification of the fluorine environments and a segregation of the vacancies around the calcium by increasing the x values. Later in 2017 the same research group reported on tysonite-type structure $Ce_{1-x}Sr_xF_{3-x}$ solid-state room temperature electrolyte [33]. The compound series have also been prepared by solid state

synthesis at 900 °C for 24 h. Unlike the previous electrolyte, by increasing the amount of Sr dopant, the cell volume increases linearly. The highest ionic conductivity has been determined to be 3×10^{-4} S/cm corresponding to a $Ce_{0.975}Sr_{0.025}F_{2.975}$ composition which is slightly higher than that for $Sm_{0.95}Ca_{0.05}F_{2.95}$. They further concluded that in a tysonite-type ion conductor with a general formula of $RE_{1-x}AE_xF_{3-x}$ (RE = rare-earth and AE = alkaline-earth) difference in the ionic sizes of the host element (RE) and the dopant (AE) plays a vital role in ionic conductivity: When the ionic sizes are comparable, conductivity reaches to maximum at a low substitution rate due to network relaxation of $[RE_{1-x}AE_xF]^{2-x}$ sabs in competition with the chemical pressure leading to a strong variation of $[RE_{1-x}AE_xF]^{2-x}$. On the contrary, the variations of the $[RE_{1-x}AE_xF]^{2-x}$ sheet thickness and the ionic conductivity are small, when the difference in the ionic sizes are large. They suggested that moderate ionic radii difference serves to optimize the ionic conductivity: Y-Ca, Eu-Ca and Gd-Ca could fulfill this requirement, though, no experimental results on the suggested systems have been reported so far. Moreover, no cycling performance of any electrochemical system have been shown using $Sm_{1-x}Ca_xF_{3-x}$ or $Ce_{1-x}Sr_xF_{3-x}$ as the room temperature solid-state electrolytes.

To have a better understanding on mechanisms of the ion transport in the Ba doped LaF_3 electrolyte material in order to optimize the conductivity of the electrolyte [34-38], further studies have been performed. It has been shown that $La_{0.9}Ba_{0.1}F_{2.9}$ thin film has a significant reduced resistivity as compared to bulk type electrolyte [34]. The $La_{0.9}Ba_{0.1}F_{2.9}$ thin film has been fabricated by spin coating. The highest conductivity obtained after a post sintering the thin film at 450 °C which was measured to be 1.6×10^{-4} S/cm at 170 °C. Further increasing the sintering temperature, however, resulted in formation of LaOF impurity. Later the $La_{0.9}Ba_{0.1}F_{2.9}$ thin film was used to build up a full cell using Bi/BiF_3 and MgF_2 or CaF_2 as the cathode and anode materials, respectively [37]. In this study, employing SnO_2 and indium tin oxide (ITO) – compared to carbon nanotubes – as the electronic conductor has been investigated, however, it is claimed that the best cycling behavior could be observed using carbon nanotubes as the electronic conductor and CaF_2 as the anode material (**Figure 1-4**). However, low Coulombic efficiency observed in the first cycle, as the cell has been initially charged up to ca. 320 mAh/g (slightly lower that the theoretical capacity of Bi/BiF_3 (385 mAh/g)) but only 120 mAh/g could be reversed during the discharge. In the next cycles the capacity fading was less severe compared to the first cycle. Nevertheless, the discharge capacity reached to ca. 66% of its initial value ($\sim$ 120 mAh/g) within only 10 cycles.

Deeper studies on the effect of nanocrystallization of the $La_{0.9}Ba_{0.1}F_{2.9}$ electrolyte material on ion conductivity has been conducted by Chable et al. in 2017 [35]. The optimum condition for nanocrystallization of $La_{0.9}Ba_{0.1}F_{2.9}$ by ball milling has determined to be milling time of 3 h (effective milling time, considering 15 min break after every 15 min of milling) at a rotational speed of 400 rpm. The authors then provide evidences on a significant improvement in the ionic conductivity up to 4×10^{-5} S/cm at room temperature (as compared to unheated sample with an ionic conductivity of 0.02×10^{-5} S/cm at room temperature) upon sintering of the electrolyte pellets (made from the nanocrystalline $La_{0.9}Ba_{0.1}F_{2.9}$) at an optimized temperature of 700 °C (higher sintering temperatures did not further improve the conductivity). Such an improved ionic conductivity has been attributed to the growth of the particle size above 500 °C [35].

Dambournet et al. carried out investigations on the electrochemical stability of LaF_3 doped with BaF_2 using Li and Pt electrodes [36]. Cyclic voltammetry measurements on $Li|La_{0.95}Ba_{0.05}F_{2.95}|Pt$ cell have been performed at 30 °C in a potential range up to 7 V and down

to -0.5 V. Results revealed that at around 0 V a redox peak can be observed which has been attributed to lithium plating/alloying and stripping (reduction and oxidation) both electrodes (described as a solid electrolyte interface (SEI)), while the electrolyte starts to decompose at potentials above 5 V. In the same study, the authors investigated on possible interactions of carbonaceous additives (as electronic conductor) with the fluoride conducting electrolyte. Over ball milling of the LBF electrolyte and carbon, no indication of formation of insulating graphite fluorite (CF_x) could be determined by NMR. However, according to impedance measurements, the conductivity of the mixed LBF-C composite (produced by ball milling) is lower by one order of magnitude (5×10^{-8} S/cm at 30 °C) as compared to milled $La_{0.95}Ba_{0.1}F_{2.95}$ (5.4×10^{-7} S/cm at 30 °C). The authors have further investigated on occurrence of reaction of carbon with LBF electrolyte to yield CF_x by conducting cyclic voltammetry experiments on Li|LBF|LBF-C cells which showed a rapid increase in the measured current at a potential range between 4.2 – 4.8 V. Then the standard potential of the electrochemical fluorination reaction of carbon (according to: $1/3\ LaF_3 + C \rightarrow CF + 1/3\ La$) has been calculated to be 4.19 V which is very close to the contribution to the current observed on the CV of the LBF-C cell, suggesting that carbon probably undergoes electrochemical fluorination to form CF_x.
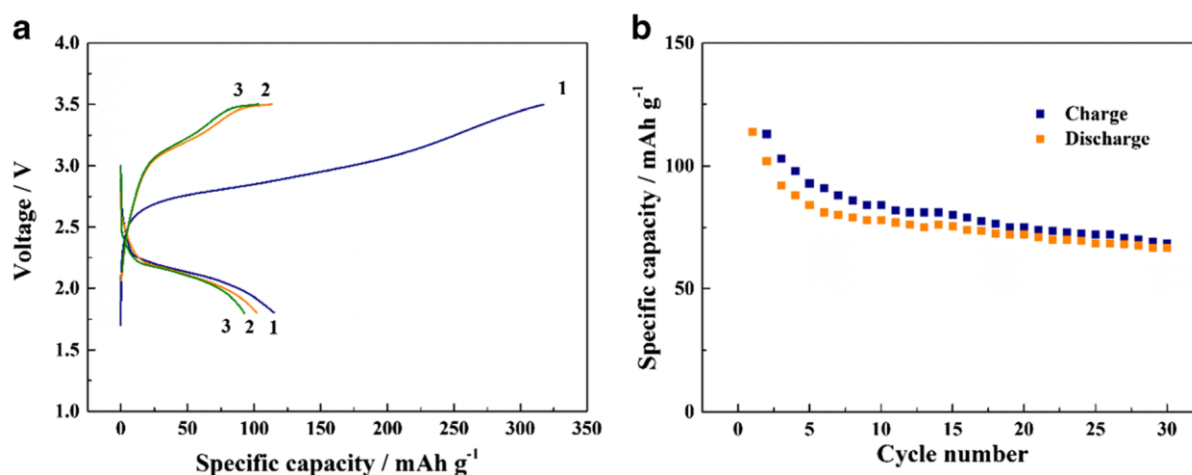
Figure 1-4. The first three charge/discharge curves (a) and cycling performance (b) of the cells with a Bi cathode vs. CaF₂/CNT anode in a voltage window of 1.8 – 3.5 V. The figures have been reprinted from [37] with permission[3].

Fluorite-type $Ba_{1-x}Sb_xF_{2+x}$ ($0.1 \leq x \leq 0.4$) has been investigated as a fluoride ion conductor by Reddy et al. in 2018 [39]. The highest obtained conductivity measured to be 4.4×10^{-4} S/cm at 160 °C which seems to be significantly larger than isostructural $Ba_{0.7}La_{0.3}F_{2.3}$, arising from the presence of an electron lone pair of Sb^{3+}.

Recently, attempts to develop room temperature FIBs have been made, using both liquid [40] and solid [41, 42] electrolytes. Room temperature FIB based on dry tetraalkylammonium fluoride salts in ether solvents (BTFE) as a liquid electrolyte and a copper-lanthanum trifluoride core-shell cathode has been built [40]. Impedance spectroscopy confirmed a conductivity of 0.24 S/cm at room temperature for a 0.75 M Np_1F/BTFE electrolyte solution. According to cyclic voltammetry measurements, a 0.75 M Np_1F/BTFE possesses a potential window between +0.7 V (cathodic voltage limit) and +4.8 V (anodic voltage limit) versus Li^+/Li. Cycling of Bi, Pb, and Cu electrodes using the liquid electrolyte resulted in dissolution of a considerable

---

[3] Copyright © 2017, Springer-Verlag GmbH Germany

amount of metal into the electrolyte. The performance could be improved by modification of the metal with a fluorinated solid electrolyte interphase (SEI) layer by pretreatment of Ca or Ce anodes with 1H,1H,2H,2H-perfluorooctyltriethoxysilance (FOTS) additive leading to formation of CF_n-containing SEI layer on the metal surface and improvement in the reversibility of Ce to CeF_3 conversion reaction in the anode material. For the cathode material, however, a core-shell nanostructure with an inert thin shell of LaF_3 ($Cu@LaF_3$) around the active material, like an artificial SEI, was designed to mitigate the challenges associated with the cathode metal dissolution. **Figure 1-5** shows the first 8 cycles of the half-cell using Core-shell Cu as the cathode material and the liquid electrolyte at room temperature. According to the figure, the half-cell has been charged up to at least 80 mAh/g, of which 50 mAh/g could be reversed during the first cycle. Taken into account the theoretical capacity of Cu/CuF_2 (843 mAh/) the obtained discharge capacity is far less than the theoretical capacity. The capacity fading seems to be stable after the early cycles, though, the Coulombic efficiency appeared to be very low (<50%). No further data has been reported about the performance of the cell over higher cycle numbers.
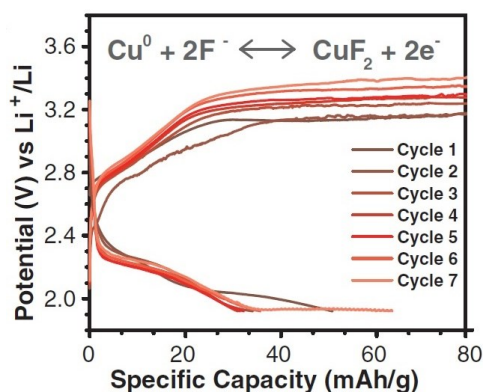
Figure 1-5. Electrochemical charge/discharge curves for a cell made up of Cu@LaF₃ cathode in 1 M Np₁F/BTFE at room temperature. The figure has been reprinted from [40] with permission[4].

The latest efforts toward developing room temperature (RT) solid-state electrolytes for FIBs have been made by Reddy et al. on $BaSnF_4$ [41, 42] that was synthesized by ball milling. According to the electrochemical impedance measurements, this ion conductor possesses an ionic conductivity as large as 3.5×10^{-4} at RT, making $BaSnF_4$ a suitable solid-state fluoride ion conductor at room temperature. $BaSnF_4$ could successfully serve as an electrolyte material in RT in cells made from BiF_3 cathode and Sn or Zn anode materials. The $BiF_3/BaSnF_4/Sn$ cell showed a strong capacity fading (discharge capacity of 120 mAh/g in the first cycle, whereas less than 10 mAh/g in the 10th cycle). For the $BiF_3/BaSnF_4/Zn$ cells, the discharge capacity appeared to be stable over the first 20 cycles (around 50 mAh/g throughout the whole cycling range), though, the discharge capacities were significantly larger at higher temperatures ($\sim$ 220 mAh/g in the first cycle at 150 °C, followed by further capacity fading at higher cycles). It should be taken into consideration that more electropositive anode metals could not be used due to low electrochemical stability window of the electrolyte. In order to address this issue, a thin layer of $La_{0.9}Ba_{0.1}F_{2.9}$ was pressed together with a thick layer of $BaSnF_4$ [42]. This strategy resulted in a reduction in ionic conductivity to 0.89×10^{-5} S/cm at RT, but still high enough to make a RT $BiF_3/La_{0.9}Ba_{0.1}F_{2.9} - BaSnF_4/Ce$ full cell. Discharge potential was significantly improved (from $\sim$ 0.6 V vs. Zn to 2.2 V vs. Ce at RT) at the expense of strong capacity fading (only 25 mAh/g at the first cycle which further reduced to 7 mAh/g at the second cycle, at RT).

Measuring the cell at higher temperatures (150 °C) significantly enhanced the discharge potential (up to 2.6 V) and capacity (up to 250 mAh/g in the first cycle). Nevertheless, the cell suffered from a large capacity fading (reached to $\sim$ 110 mAh/g within only 5 cycles). Apart from the weak cycling behavior that was observed at RT, the approach can pave the way to design and develop advanced electrolyte systems in FIBs.

1.3 Objectives of the Thesis

So far, most of the investigation in the field of FIBs were devoted to improve the electrolyte materials. However, less attention was paid to improve the electrode materials and simple conversion based systems were mainly used as the electrode materials. It should be taken into consideration that conversion-based electrode materials generally provide much higher theoretical capacities as compared to intercalation-based electrodes due to the ability to accommodate more electrons per formula unit and often a lower molar mass. However, conversion-based electrodes are often known for suffering from large volume changes during cycling, leading to destruction of the physical contact within the composite electrode [43]. This results in a poor cycling stability of the conversion-based electrode materials as compared to electrodes based on intercalation mechanism. Although some strategies have been proposed to mitigate the effects of conversion-based electrode materials in LIBs, the state of the art for LIBs still mainly lies on the intercalation-based electrode materials.

Considering the limitations of current FIBs including low cycling performances, development of the FIBs calls for new electrode materials. By analogy with the LIBs, intercalation-based electrode materials can be a mitigating strategy for the poor cycling stability of the FIBs. In this work, intercalation-based cathode materials for all-solid-state FIBs are investigated. Lacking a well-developed intercalation anode system for FIBs, conversion-based M/MF_x counter electrodes against the intercalation cathode materials are used. It is worth mentioning that in the course of this thesis, some efforts (i.e. $Sr_2TiO_3F_2$) have been made mainly by our research group in order to develop intercalation-based anode materials [44, 45]. The results show a principle reversibility (with respect to fluorination/de-fluorination) of the structures, though, development to make them work in an electrochemical setup are still on going.

To develop intercalation-based cathode materials for FIBs, investigations on perovskite-related Ruddlesden-Popper type structures with a general formula of $A_{n+1}B_nO_{3n+1}$ (or $(ABO_3)_nAO$) [46] were particularly interesting. As can be seen in **Figure 1-6** (left), K_2NiF_4 type structures (n = 1, A_2BO_4) consist of alternating layers of ABO_3 perovskite and AO units of rock salt along the *c*- axis, resulting in a tetragonal symmetry with the highest symmetry of $I4/mmm$ [47]. For n = 2, two perovskite ABO_3 units are located between every rock salt layer. According to the results obtained from chemical fluorination of K_2NiF_4 structures (i.e. $LaSrMnO_4$) up to 2 F$^-$ per formula unit can be inserted into the interstitial anion sites within the rock salt interlayers [48]. This renders the K_2NiF_4-type structure cathode materials to have theoretical capacities ($\sim$ 130 – 160 mAh/g) as high as the state of the art for LIBs (e.g. 140 mAh/g for insertion/removal of 0.5 Li$^+$ ion into/from $LiCoO_2$ [49]).

In the course of this dissertation first it will be shown that the electrochemical intercalation/de-intercalation method can be used to insert/remove fluorine into/from the host structures (K_2NiF_4 as well as Schafarzikite-type structures). Then the issue of carbon oxidation (leading to destruction of carbon conductive network) will be addressed as a limiting factor towards making all-solid-state FIBs. Based on the investigations about carbon side reaction, the

optimized cycling condition will be discussed for K_2NiF_4-type compound of La_2CoO_{4+d} and La_2NiO_{4+d} which seems to be the most promising cathode materials in terms of structural reversibility, discharge capacity and cycling stability. It will be shown that La_2NiO_{4+d} can serve as an active cathode material with high cycling stability (up to >220 cycles) and close to 100% Coulombic efficiency within an all-solid-state modification. Finally, the effect of volume change in the conversion-based anode materials that have been used in this study will be discussed.
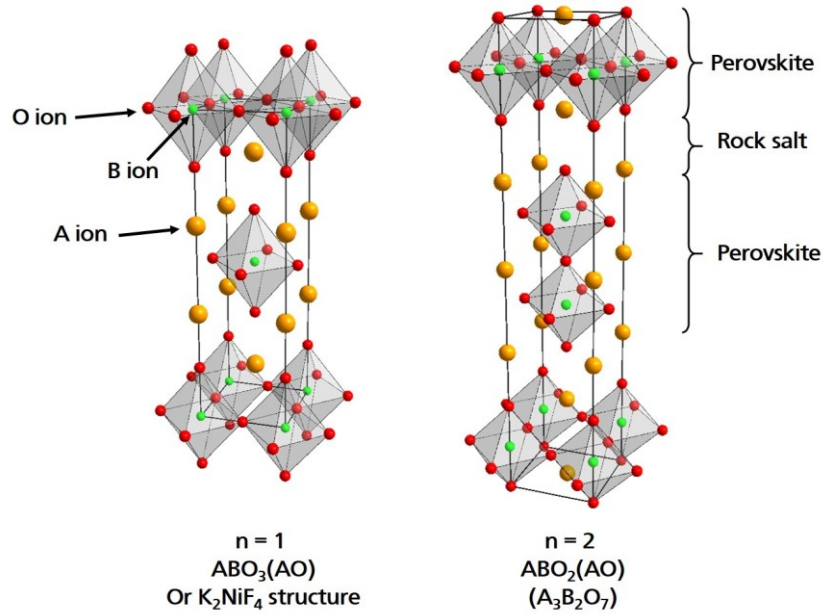
Figure 1-6. Schematic illustration of Ruddlesden-Popper type structures for n = 1, known as K₂NiF₄-type structures (left) and n = 2 (right).

2 Fundamentals of Electrochemistry of Batteries

2.1 Introduction

Batteries are electrochemical (energy storage) devices that can reversibly convert chemical energy into electrical energy through electrochemical oxidation/reduction (redox) reactions (the reactions occur at the electrodes). There is a difference between electrochemical "cell" and "battery", however, the term battery is often used as the basic electrochemical unit which is the definition of an electrochemical cell: An electrochemical cell provides electrical energy by converting the chemical energy into the electrical energy. A cell consists of anode, cathode, electrolyte and (in case of non-solid-state cells) separator while a battery is made up of an assembly of electrochemical cells which are connected in series or parallel arrangement.

Electrochemical batteries (cells) can generally be classified into two categories: 1- Primary batteries which are not capable of being recharged, and therefore, their life time is over once the battery is fully discharged. 2- Secondary (rechargeable) batteries which can be electrically recharged after discharge. Rechargeable batteries are also known as "storage batteries" or "accumulators". Secondary batteries can be used as an energy-storage device, which delivers the electrical energy from a prime energy source to the load on demand while they can be recharged (and reused) after discharge rather than being discarded. Note that the term of "battery" refers to electrochemical secondary cell throughout the whole dissertation.

2.2 Components of an Electrochemical Cell

An electrochemical cell mainly consists of three components:

1- The anode is the negative electrode and gives the electrons to the external circuit. The anode is oxidized during the electrochemical reaction.
2- The cathode which is the positive electrode and accepts electrons from the external circuit. The cathode is reduced during the electrochemical reaction.
3- The electrolyte which is the ionic conductor and offers the medium for charge transfer between the anode and cathode. The electrolyte only allows the passage of the ionic species; thus it should be an electronic insulator. The electrolyte can be a liquid, a solid or even a polymer. In the conventional batteries a liquid electrolyte is used. Although, liquid electrolytes provide a relatively low ionic resistivity, the major drawbacks of liquid electrolytes are safety issues, insufficient lifetime and high cost [8].

Note that anode and cathode materials are defined based on the role of the electrode during the discharge reaction. That means during the discharge reaction the oxidation reaction happens in anode material and reduction reaction occurs in cathode material. However, during a charge process, oxidation reaction takes place in the cathode material (which plays the role of anode) and reduction reaction in the anode material (which plays the role of cathode).

2.3 Electrochemical Reactions in the Electrodes for Storage of the Ions

Storage of the ions in electrodes takes place mainly through three types of reactions. Alloying is the first reaction type that can occur in an electrode during the electrochemical redox reaction. Alloying mechanism offers very high specific capacity (for example 4200 mAh/g for lithiation to $Li_{4.4}Si$ [50]). However, they are often accompanied by very large volume changes, typically more than 100%, and therefore, they show very poor cycling performance and capacity retention.

The second reaction is called conversion reaction. In a conversion reaction the electrode undergoes a solid-state redox reaction during charge/discharge. The conversion-based reactions are accompanied by a change in the crystalline structure together with breaking and recombining chemical bonds during the redox reactions. **Figure 2-1** schematically illustrates the structural changes during charge/discharge for Bi/BiF_3 as an conversion-based anode material for FIBs. Conversion-based reactions generally offer relatively high specific capacities (as compared to intercalation-based reactions) (see **Figure 2-2**) due to the ability of accommodating more electrons per formula unit and often lower molar mass of the active electrode material, though, this reaction type is also accompanied by large volume changes during redox reactions which leads to a poor cycle life.
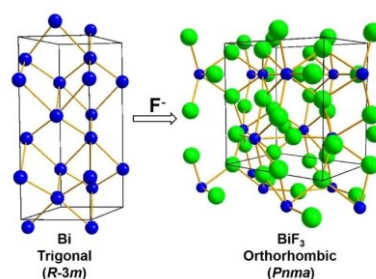
Figure 2-1. Schematic structural changes in a conversion-based FIB system of Bi (left) and BiF₃ (right).
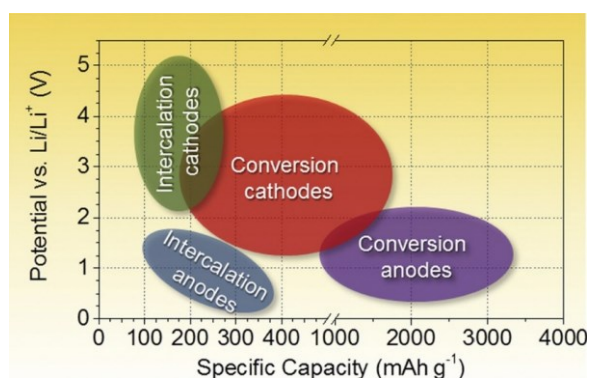
Figure 2-2. An overview of the average specific capacity and discharge potential for intercalation/conversion based electrode materials for LIBs. Alloying based electrode materials have specific capacities in the range of conversion-based electrode materials. This figure has been reprinted from [1] with permission from Elsevier[5].

The third reaction for storage of the ions is called intercalation mechanism (sometimes also called insertion or solid solution reactions). By definition, an intercalation electrode material is a solid host network, which can store guest ions within the vacant positions in the host lattice. In other words, the guest species are inserted into normally unoccupied interstitial sites in the crystal structure of a stable host material. The great advantage of the intercalation-based electrode materials lies within the fact that the ions can be inserted or removed into/from the host network reversibly with much lower volume changes during the redox reaction (e.g. in the order of 2% for $LiCoO_2$ [51]) while the identity, the basic crystal structure or amounts of the phase in the microstructure do not significantly change. Therefore, intercalation-based electrode materials generally provide a better cycling performance (as compared to conversion-

---

[5] Copyright © 2015, Elsevier

based electrode materials), however, they often have much lower specific capacity (as can be seen in **Figure 2-2**) as they are usually heavier in weight than the conversion-based electrode materials (e.g. theoretical capacity for $LiCoO_2$ (as a cathode material for LIB) is calculated to be 140 mAh/g, for lithiation/de-lithiation of 0.5 Li ions [52]).

The intercalation-based active electrode materials with layered, spinel, olivine and tavorite structures are widely used for LIBs. The most famous intercalation-based system is $LiMO_2$ (M is a transition metal such as Co, Mn, or Ni)/graphite cell in LIBs. **Figure 2-3** schematically illustrates a $LiMO_2$ (cathode material) vs. graphite (anode material) LIB. During the charge step Li-ions are produced in the cathode side and inserted in the free layers of the graphite anode. The reactions during the charge step can be written as follows:

Positive side: $$LiMO_2 \rightarrow Li_{1-x}MO_2 + xLi^+ + e^- \qquad (2.1)$$
Negative side: $$C + xLi^+ + xe^- \rightarrow Li_xC \qquad (2.2)$$
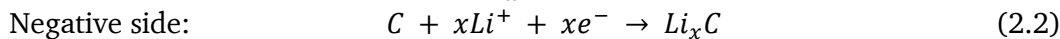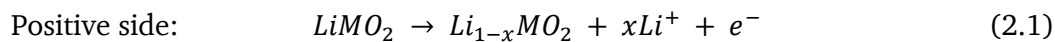
During the discharge, however, Li-ions intercalate into the free interlayers of $Li_{1-x}MO_2$ and form $LiMO_2$ and consequently C forms in the anode side.
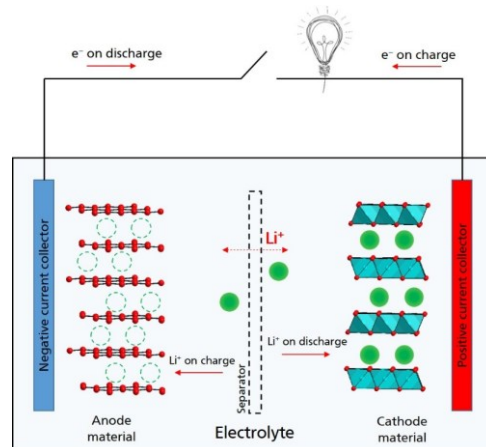
Figure 2-3. Schematic illustration of a cell based on the intercalation-mechanism electrode materials (e.g. LiCoO₂/graphite).

2.4 Parameters Affecting Battery Performance

2.4.1 Operating Voltage

The theoretical potential of a cell can be determined from thermodynamic data, however, the operating potential is always lower than the theoretical potential of a cell. The following definitions are also important when it comes to the potential of a battery system:

Theoretical voltage: It is defined as the theoretical potential of a cell which depends on the anode, cathode and the operating temperature (usually stated at 25 °C).

Open-circuit voltage: The potential of a cell under zero current (no external load) condition which is a close approximation of the theoretical potential.

Closed-circuit voltage: The potential of a cell under non-zero current (under external load) condition which is lower than the open-circuit.

Working (operating) voltage: Represents the actual operating voltage of a battery under actual load.

Average voltage: Is defined as the average discharge potential.

Cutoff (end) voltage: Is defined as the potential at the end of discharge (or charge).

2.4.2 Energy Density and Charge Capacity

The energy contained in an electrochemical system is determined as the integral of the potential multiplied by the charge capacity and can be written as follows:

$$Energy = \int V dq = \int V I dt \qquad (2.3)$$

where V is the operating potential, q is the amount of electronic charge that will pass through the external circuit and $I = dq/dt$. The term Idt is defined as the capacity of a battery and reflects the amount of charge than can be stored in a battery. Therefore, equation (2.3) shows that the energy of a battery is determined by the area under the charge/discharge curve in a voltage versus capacity (the unit of capacity is usually written as mAh or Ah in the battery community) plot. Instead of the absolute capacity, one often uses gravimetric (Coulombs per gram of electrode weight) or volumetric (Coulombs per milliliter of electrode) specific capacities [53].

2.4.3 Theoretical Specific Capacity

The theoretical capacity of an electrode material can be calculated based on the number of active electrons in the redox process and molar weight of the active electrode material according to the following equation [54]:

$$C_t = \frac{nF}{3.6 \times M} \qquad (2.4)$$

where F is the Faraday constant (9.64853399(24) $\times 10^4$ C/mol [55]), n is the number of active charges (electrons) per formula unit, and M stands for the molar weight of materials. According to the equation a higher theoretical capacity is expected by smaller molar weight of the active electrode material as well as accommodation of more electrons per formula unit.

2.4.4 Cycling Performance

This term is defined for the rechargeable (secondary) battery systems. During the cycling of a battery (cell) usually the capacity fading and potential drop is observed. Two determining factors in the cycling performance of batteries are Coulombic efficiency and cycle life. Coulombic efficiency is defined as "the fraction of the prior charge capacity that is available during the following discharge" [53]. Coulombic efficiency depends mainly on the nature of the electrode materials, the current density and the depth of discharge in each cycle. The cycle life of a battery, according to battery community, expressed as the number of cycles until the capacity fades to 80% of its initial reversible value [56].

2.5 Potential of an Electrochemical Cell

2.5.1 Electrode Potentials and Nernst Equation

The driving force between two electrodes is due to the difference in the electrochemical potentials of those electrodes. The electrochemical potential $\bar{\mu}$ (per mole) for a charged particle with charge n_iF is the sum of chemical and electrostatic components ($\bar{\mu_i} = \mu_i + n_iF\Psi$, where n_i is the number of transferred particles (in moles) and Ψ is referred to the electrostatic potential).

The difference in the electrochemical potential of two electrodes can be expressed as the change in the standard Gibbs free energy (per mole of reaction), $\Delta G°$. This thermodynamic term can be calculated based on the difference between the standard Gibbs free energies of formation of the products and the reactants. Then $-nFE°$ is the electrostatic energy (per mole) of an electrically charge species (ions or electrons), where n is the charge number of the mobile ionic species, E is the voltage between the electrodes (electromotive force) and F is the Faraday constant. The change in the standard free energy ($\Delta G°$) at standard condition (activity of unity, temperature of 25 °C and pressure of 1 atm) is expressed as:

$$\Delta G° = -nFE° \tag{2.5}$$

At non-standard conditions the potential E of a cell (with equation: $aA + bB \leftrightarrow cC + dD$) is determined by the Nernst equation:

$$E = E° - \frac{RT}{nF} \ln \frac{a_C^c a_D^d}{a_A^a a_B^b} \tag{2.6}$$

where a_i is the activity of relevant species, R is the gas constant (8.314 J mol^{-1} K^{-1} [57]) and T is the absolute temperature.

2.5.2 Open Circuit Voltage (OCV)

Open circuit voltage (OCV) can be simply defined as the potential difference in the terminal members (electrodes) of an electrochemical redox couple in a galvanic circuit under a no-load (no external current) condition. For a nonzero OCV of a galvanic cell, one of the electrodes has a more positive potential with respect to the other one. Naturally OCV will be zero in case of a symmetrical cell. For the galvanic cells with different end terminals OCV can be regarded as EMF when no external current is applied. The OCV of a cell can also be defined as the electrochemical potential difference between the anode and cathode and is determined as:

$$V_{OC} = \frac{(\bar{\mu}_A - \bar{\mu}_C)}{e} \tag{2.7}$$

where V_{OC} is the open circuit voltage, e is the magnitude of the electronic charge, and $\bar{\mu}_A$ and $\bar{\mu}_C$ are the electrochemical potential of the anode and cathode, respectively.

2.5.3 Cell Potential at Nonzero Current

For electrochemical systems under a nonzero current, anodic current flow (charge) is associated with a positive potential shift while a cathodic current flow (discharge) is accompanied by a negative potential shift ($\Delta E = E_i - E_0$, where E_i and E_0 are the potential of the cell at current density i and $i = 0$, respectively). ΔE is defined as the electrode polarization and it is positive for the charge and negative for discharge processes. In other words, the electrode polarization

decreases the discharge potential to occur below the OCV and it increases the charge potential higher than OCV (**Figure 2-4**). Furthermore, the internal resistance is also responsible for a potential drop (IR drop) between the end of the charge curve and the beginning of the discharge (see again **Figure 2-4**).
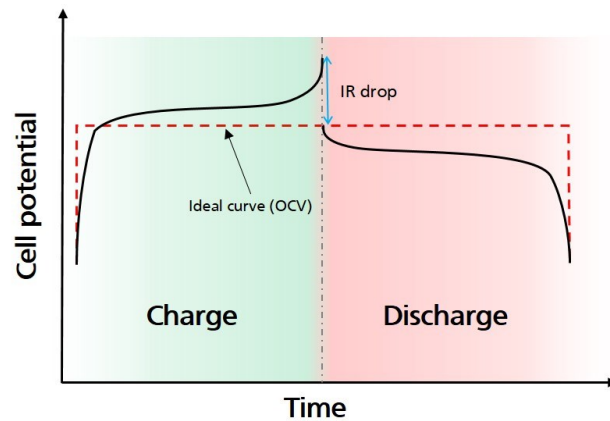
Figure 2-4. Schematic illustration of overpotential (potential drop) due to electrode polarization during charge/discharge.

2.5.4 Some Factors Influencing the Cell Potential

2.5.4.1 Discharge Current

Increasing the current drain of a battery results in an increase in the IR loss and polarization effects which leads to increase in the potential drop. **Figure 2-5** schematically depicts how increase in the current density increase the potential drop. Only at very low discharge current densities the operating voltage approaches the theoretical voltage of a battery system, though, at very long discharge periods chemical deterioration may result a in capacity loss [58]. With increasing the discharge current density, the discharge voltage decreases and the slope of the discharge curve becomes sharper.

C-rate is a parameter that is often used to express the rate at which a battery is discharged [53]. When R is the number of hours to completely discharge a battery, the C-rate is expressed as C/R. For instance, a 5 Ah battery which is discharged at a rate of $C/10$ (i.e. within 10 h), requires use of a current of 0.5 A to get fully discharged ($\frac{C}{R} = \frac{5\,Ah}{10\,h}$). Discharging a battery at a higher C rate is equivalent to discharge it with a higher current (density).
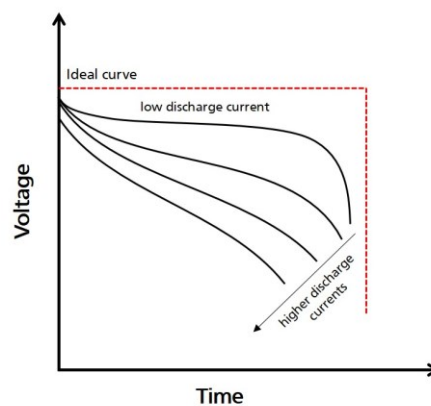
Figure 2-5. Schematic illustration of the effect of discharge current (density) on the potential drop.

2.5.4.2 Temperature

The chemical activity of the active electrode materials increases with increasing the operating temperature while the internal resistance reduces at higher temperatures. Generally, lowering the operating temperature of a battery not only results in a higher potential drop (and increase in the slope of the discharge curve) but also in a reduction of the discharge capacity. **Figure 2-6** schematically illustrates the effect of the decrease in the operating temperature on the potential drop (the lower the operating temperature, the higher the potential drop and capacity and energy loss).

The effect of operating temperature is more pronounced when it comes to solid-state batteries, since most of the known electrolytes have low ionic conductivities at low temperatures (as an example, $La_{0.9}Ba_{0.1}F_{2.9}$ as a fluoride ion conductor, has a conductivity in the order of 10^{-8} S/cm at room temperature [24]). On the other hand, at higher temperatures occurrence of thermally activated side reactions is more probable. Thus, it is important to note that the effect of temperature varies for each system and it should be considered within the battery system and its design.
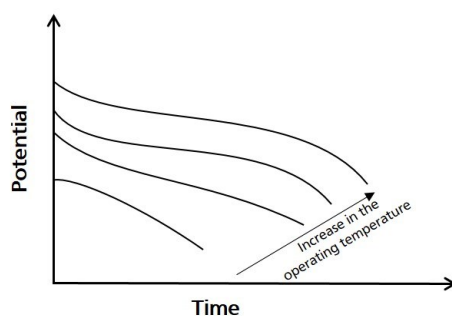
Figure 2-6. Schematic illustration of the effect of operating temperature on the discharge potential drop and capacity loss.

2.5.4.3 Effect of Microstructure

Previous studies [59] have suggested that nanomaterials can improve the electrochemical behavior of battery systems (especially in the field of LIBs). The enhancement in the electrochemical performance basically arises from the fact that the reduction in the particle size is accompanied by a significant increase in the rate of insertion and removal of the charged ions due to shortening of the ion transport distance [60]. Furthermore, the reduction in the particle size increases the active surface area which results in a better kinetic of the electrochemical reaction.

Although materials with nano-sized particles can pave the way for electrochemical improvements, the effects do not necessarily have always a positive impact on the electrochemical behavior. For instance, reducing the particle size of $LiCoO_2$ (as a widely used cathode material for intercalation-based LIB) leads to a significant potential drop accompanied by a severe capacity loss and a capacitor type behavior [61] (**Figure 2-7**). This has been explained by the increase in the site energy related to the insertion of Li-ion which results in a decrease in the energy difference before and after Li-ion insertion [49]. It should also be noted that reducing the particle size increase the surface area of reaction sites which may lead to more side reactions between the active electrode material and the electrolyte and ion/electron conductor particles [59].
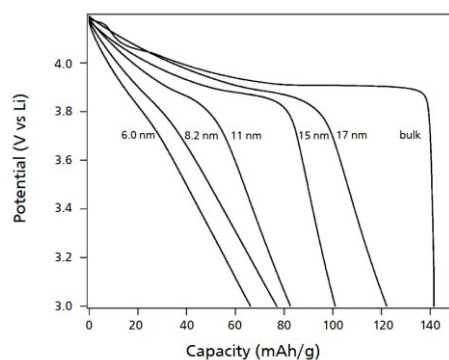
Figure 2-7. Effect of the microstructure (particle size) on the discharge profile of LiCoO₂. The figure has been reprinted from [61] with permission[6].

2.5.4.4   Effect of Crystal Structure

The electrochemical potential between a redox couple is determined by the change in the Gibbs free energy which directly depends on the energy that is required to add or remove the ions into or from the host crystal structure [49]. Occupation of the ions in different lattice sites or coordinations results in different changes in the Gibbs free energy and consequently different electrochemical potentials.

2.6   Electroanalytical Techniques

2.6.1   Galavnostatic Cycling

Galvanostatic cycling technique is a common method to study the performance of electrochemical cells. In this technique, a constant current, often at a specific *C*-rate, is applied to an electrode, and its potential response is recorded. By galvanostatic cycling, the kinetics and the electrode mechanisms can be studied. In this technique, voltage profiles which show the changes in the electrochemical performance during cycling can be obtained. This method is also used in order to follow the degradation processes occurring due to usage of the cell [62].

2.6.2   Cyclic Voltammetry

Cyclic voltammetry, also known as linear sweep voltammetry, is one of the important electroanalytical techniques that is widely used for battery development and characterization of the electrochemical performance of cells. This method is based on the imposition of a waveform with a triangular shape potential (as can be seen in **Figure 2-8**) on the working electrode [63]. During cyclic voltammetry a liner ramp voltage is applied to an electrode. For most of the commercial instruments, a voltage scan window of ±5 V is provided [58]. The scan rate (or sweep rate) in cyclic voltammetry is defined as the rate of change of the potential with time and often is shown as ν (V/s). The scan rate is the slope of the wave line in **Figure 2-8**. More detailed information about cyclic voltammetry can be found in Appendix (section 7.1).
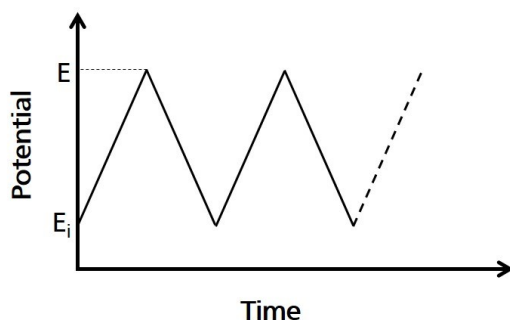
Figure 2-8. Schematic illustration of variations of potential against time at the working electrode during cyclic voltammetry.

2.6.3 Electrochemical Impedance Spectroscopy (EIS)

Electrochemical Impedance Spectroscopy (EIS) is an electroanalytical technique for investigating the electrode processes by measuring the change in the electrical impedance of an electrode. This method enables us to investigate the dynamics of bound or mobile charge in interfacial regions or bulk of solids or liquid materials. By EIS technique any intrinsic property that affects the conductivity of an electrode − materials system such as conductivity, and dielectric constant and capacitance of the interface region can be investigated.

In this method an alternating voltage (or current) is applied to across a sample and then the phase shift and amplitude (or real and imaginary parts) of the resulting current is measured [64]. In addition to the AC input, a DC voltage which is referred to as "offset voltage" or "offset electrochemical potential" can also be employed to the EIS in order to study electrochemical processes. For more information about how the current responds to a AC voltage signal from a mathematical point of view please see the Appendix (section 7.2.1).

2.6.3.1 Representation of Complex Impedance Data

a. Nyquist Plots

If the real part (Z_{re}) is plotted on the *x*-axis against the imaginary part (Z_{im}) on the *y*-axis, the obtained plot is so called "Nyquist plot" (or complex plane impedance diagram) which is a common way to present the results of the EIS. For a simple R-C circuit, the shape of the Nyquist plot is a semicircle (**Figure 2-9**). Each point at the Nyquist plot represents an impedance measurement in one frequency. For such a Nyquist plot, the impedance at low frequencies ($Z_{im} = 0$) becomes a complete resistance and is equal to R (equal to diameter of the Nyquist plot) while at very high frequencies the impedance is completely capacitive. The term critical frequency f_c corresponds to a midpoint where the phase angle is 45° $Z_{re} = Z_{im} = R/2$.

Nyquist plots are very useful in analyzing conduction mechanisms or kinetic governing phenomena. For instance, a perfect semicircle shows that the impedance response corresponds to a single activation energy controlled (or charge transfer) process. Multiple loops reveal the fact that more phenomena are responsible for the behavior of the material. Note that often only a portion of one or more semicircles can be observed within the frequency range of the experiment [65].
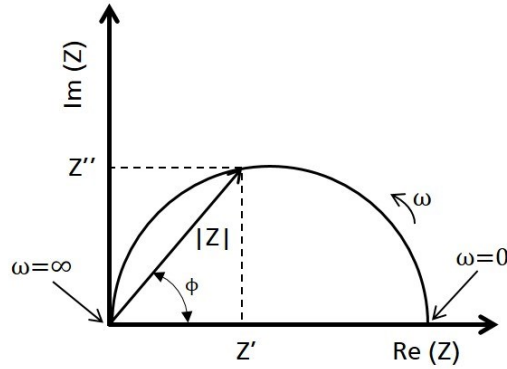
Figure 2-9. Schematic illustration of a complex impedance plot.

b. Bode Plots

Although Nyquist plots are very useful in analyzing the impedance behavior of the process, these plots do not give detailed information about the frequency at which the impedance has been measured. Another form of presenting the impedance data is called "Bode" plot, which shows the variation of phase angle (ϕ) and the logarithm of the impedance magnitude ($|Z|$) with respect to the logarithm of frequency. A schematic Bode plot of a simple R-C circuit can be seen in **Figure 2-10**.
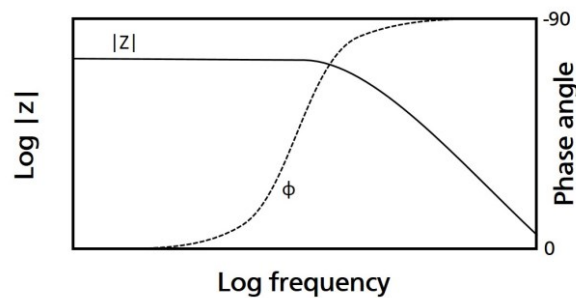
Figure 2-10. Schematic Bode plot for a simple R-C model that has been proposed in Figure 2-9.

2.6.3.2 Equivalent Circuits

The impedance behavior of all processes may not be described simply by an ideal resistor or capacitor. Therefore, to analyze the experimental impedance data, an equivalent circuit made up of ideal resistors, capacitors and other circuit elements is used in order to model the behavior of the impedance. The equivalent circuits should always be selected on the basis of understanding of the electrochemical system. That means, it is not enough to just find a model that mathematically fits the data, but the implemented model should be in line with the chemical and physical properties of the system [65].

a. Common Electrical Elements

Most common circuit elements are resistors, capacitors and inductors which represent a basic ideal component. The impedance and the relationship between current and voltage for the most common elements are described in **Table 2-1**. For a resistor, the impedance is independent of the frequency since it only has a real impedance component. Therefore, the current through a resistor is always in phase with the applied voltage. However, for a capacitor the impedance decreases by increasing the frequency of the AC voltage. Unlike a resistor, a capacitor only has an imaginary component and therefore, the current through a capacitor has always a phase

shift of -90° with the AC voltage. A combination of a resistor and a capacitor can physically be described by a parallel R|C circuit (**Figure 2-11**) which consist of an ideal resistor ($R = 10000$ ohm) in parallel with an ideal capacitor ($C = 1$ μF). More mathematical information about R|C circuits can be found in the Appendix (section 7.2.2).
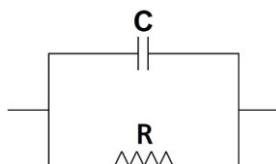
Figure 2-11. A simple R-C circuit.

Using equivalent circuits enables us to analyze the impedance data and understand the role of different contributing phenomena to the impedance behavior of the material. This can be done by determining the R and C values. Capacitance values are frequency dependent and at each frequency range there is a specific determining phenomenon. An overview of the obtained capacitance values and their possible responsible phenomenon is presented in **Table 2-2**.

Table 2-1. Most common circuit elements used in the models.

Physical Element	Current vs. Voltage	Impedance
Resistor	$V = IR$	R
Capacitor	$I = C\, dV/dt$	$1/j\omega C$
Inductor	$V = L\, di/dt$	$j\omega L$

Table 2-2. Capacitance values and their possible interpretation. This table has been reprinted from [66] with permission[7].

Capacitance (F)	Phenomenon Responsible
10^{-12}	Bulk
10^{-11}	Minor, second phase
$10^{-11} - 10^{-8}$	Grain boundary
$10^{-10} - 10^{-9}$	Bulk ferroelectric
$10^{-9} - 10^{-7}$	Surface layer
$10^{-7} - 10^{-5}$	Sample-electrode interface
10^{-4}	Electrochemical reactions

b. Constant Phase Element (CPE): Non-ideal Circuit Elements

The impedance behavior of systems often deviates from the ideal condition and reveals a frequency dispersion that cannot be easily described by simple elements such as resistances, capacitances or convective diffusion (e. g. Warburg-type behavior). The frequency dispersion is generally attributed to a "capacitance dispersion" expressed in terms of a constant phase element (CPE) [67], an element that is extensively used for impedance data modeling. For expressing the CPE one can find many different equations in the literature [64, 68], however, here the CPE is defined according to the definition that has been proposed by Zoltowski [69]:

---

[7] Copyright © 2004, John Wiley and Sons

$$Z_{CPE} = \frac{1}{Q(jw)^{\alpha}} = \frac{1}{Q\omega^{\alpha}}[cos(\alpha\pi/2) - jsin(\alpha\pi/2)] \qquad (2.8)$$

where Q is a constant with dimension of $(\Omega^{-1} s^{\alpha})$ and α is the CPE exponent (α does not have any unit). Although the CPE does not have a physical meaning, it has been considered to represent a circuit parameter with limiting behavior as a capacitor for $\alpha = 1$ ($Q = 1/R$), a resistor for $\alpha = 0$, a Warburg element for $\alpha = 0.5$, and an inductor for $\alpha = -1$ [65, 67]. A single CPE element creates a straight line that produces an angle of $-\alpha \times 90°$ with the x-axis, as shown in **Figure 2-12**. However, a CPE in parallel with a resistor makes depressed semicircles in the Nyquist plot with an angle of $(\alpha-1) \times 90°$. In fact, a CPE can be divided into a frequency dependent pure capacitor ($\alpha=1$) and a pure resistor ($\alpha=0$) that can be connected in parallel or series [65]. More information about CPE can be found in the Appendix (section 7.2.3).
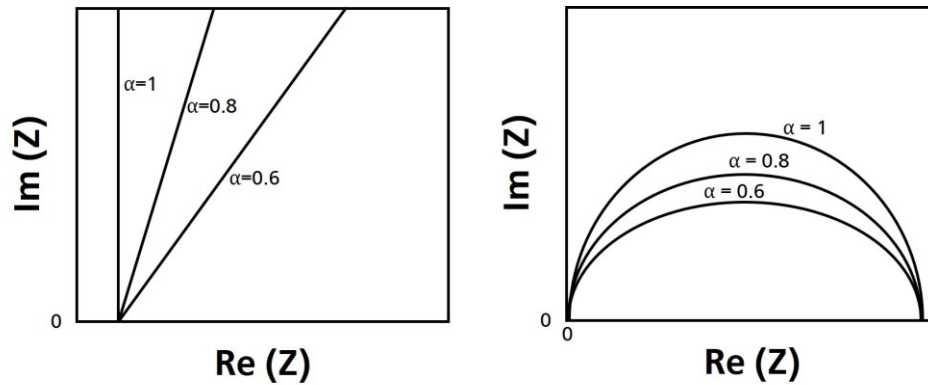
Figure 2-12. Schematic Nyquist plots of a single CPE (left) and a CPE in parallel with a resistor (right) for different α values [65].

c. Warburg Element

Warburg element is referred to as the impedance that is created by the diffusion resistance (Z_{Diff}) to current flow carried by charged species. The Warburg impedance is inversely proportional to the square root of frequency. Warburg element appears as a line with slope of 0.5 in the Nyquist plot (as can be seen in **Figure 2-13a**). In a Bode plot, Warburg impedance shows a constant phase shift of -45° at low frequencies (**Figure 2-13b**). More information about the mathematical relationships of Warburg impedance can be found in the Appendix (section 7.2.4).
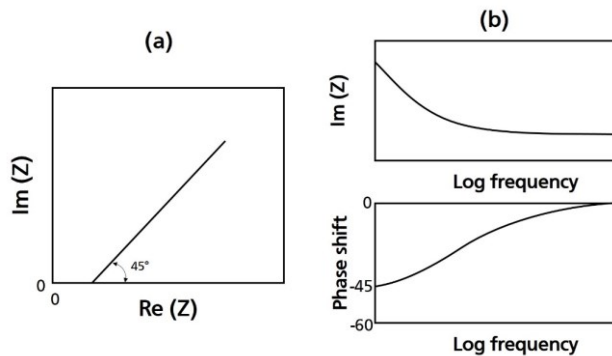
Figure 2-13. Schematic representation of a Warburg element: (a) Nyquist plot; (b) Bode plot [65].

3   Characterization Methods

3.1   X-Ray Diffraction

X-ray diffraction method is a very useful and powerful method to understand the fingerprint identification of solid crystalline materials and to determine their crystal structure (space group, lattice parameters, etc.).

3.1.1   Generation of X-Rays

X-rays can be produced by collision of accelerated (high energy) charged particles (electrons) to a target. The electron beam is accelerated through a high voltage electric field (e.g. 30 kV) followed by striking the beam to a metal target which is often Cu (other metals such as Cr, Fe, Mo, or Ag can also be used as a target). Then some of the Cu 1*s* (K shell) electrons can be ionized by the high energy incident electrons resulting in an immediate drop down of an electron in an outer orbital (2*p* or 3*p*) to occupy the vacant 1*s* level which leads to an energy release in form of X-ray radiation. Since these transition energies have fixed values, the emitted X-rays have characteristic wavelength. **Figure 3-1** represents a schematic illustration of a filament X-ray tube. The electron beam is provided by a heating tungsten filament and establishing a high potential between filament and the target. The chamber is evacuated in order to prevent oxidation of the W filament. The X-rays leave the tube through windows that has been made from Be while the tube is shielded by Pb since it is a very effective material for absorbing stray radiation.
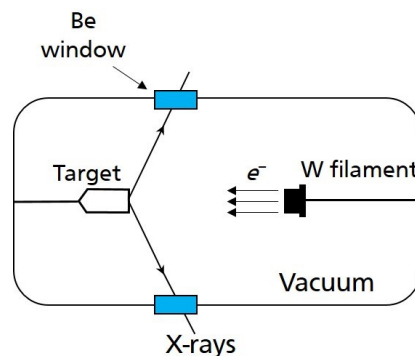
Figure 3-1. Schematic view of a filament X-ray tube. A high voltage electric field is established between the filament and the target.

3.1.2   Bragg's Law

When two X-ray beams of 1 and 2 that are reflected from two adjacent planes of A and B (**Figure 3-2**), beam 22′ needs to travel an extra distance of *xyz* as compared to 11′ beam. It is clear that from mathematical point of view:

$$xyz = 2d\,\sin\theta \qquad\qquad (3.1)$$

where *d* is the distance between two adjacent planes (often referred to as d-spacing) and θ is the angle of incidence or Bragg angle. However, for a fully constructive interference $xyz = n\lambda$. Therefore, the Bragg's law of diffraction can be written as:

$$2d\,\sin\theta = n\lambda \qquad\qquad (3.2)$$

Bragg's law states that, for an infinite set of lattice planes, the beams interfere constructively only at the Bragg angles. At angles of incident other than Bragg angle, reflected beams are out of phase and therefore, they cancel out each other and no reflection may occur.
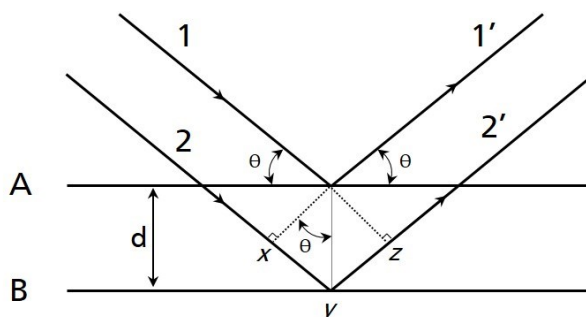
Figure 3-2. Schematic plot of diffraction of the X-rays from two atomic planes: derivation of Bragg's law.

3.1.3 Powder Diffractometery

In this technique a finely powdered sample (ideally the crystals randomly arranged in every possible orientation) are struck by a monochromatic X-ray beam. At least some crystals must be oriented at the Bragg angle for each set of lattice planes. A scintillation or Geiger counter or an image plate detector is used in order to scan a range of 2θ values at a constant angular velocity.

Powder diffractometery provides a series of peaks (reflections) on a strip of chart paper or computer screen. Each crystalline phase has a characteristic XRD pattern which can be used as a fingerprint for identification of the phase. The variables that can be obtained by powder diffraction method are peak positions (d-spacing which can be correlated to lattice parameters) and peak intensities. Typically, in a powder diffraction experiment, the intensity – diffracted by a polycrystalline sample – is measured as a function of 2θ Bragg angle. **Figure 3-3** shows an example of a XRD pattern for LaB_6. It is worth mentioning that the d-spacing can be very accurately measured by this method and this makes this technique unique and powerful.

To describe a typical powder diffraction pattern of a sample, three components including positions, intensities, and shapes are considered. For instance, peak positions mainly provide information about the unit cell parameters ($a, b, c, \alpha, \beta, \gamma,$) while peak intensity can determine the atomic parameters and peak shape shows the crystallinity of the sample. More information about peak positions, intensity and shape can be found in Appendix (section 7.3).

3.1.4 Rietveld Refinement

Rietveld refinement is a valuable method to confirm structural details of powdered samples. In this method the experimental XRD profile is compared with a calculated profile. Therefore, a starting model (from which a calculated powder XRD profile can be obtained) is required. In the Rietveld method the following groups of independent least squares parameters are often refined [70]: background, sample displacement, multiple peak shape function parameters (usually include full width at half maximum and asymmetry), unit cell dimensions, preferred orientation, scale factors, position parameters of all independent atoms (in the model of the crystal structure of each crystalline phase), population parameters (if certain site positions are occupied partially or by different atoms), and atomic displacement parameters. Note that one needs to be careful when many parameters are allowed to refine at the same time since in some

cases this can produce a false minimum with incorrect parameters. An example of using Rietveld method to refine the XRD pattern of LaB_6 can be seen in **Figure 3-3**.

The quality of the Rietveld refinement can be quantified by profile residual (R_p), weighted profile residual (R_{wp}), Bragg residual (R_B), expected residual (R_{exp}) and goodness of fit (χ^2). For more information about the mathematical equations of these terms see the Appendix (section 7.3.5). Note that for the evaluation of the quality of the refinement, the mentioned residuals are not a replacement for the plots of the observed and calculated diffraction patterns supplemented by the difference, plotted on the same scale [71].
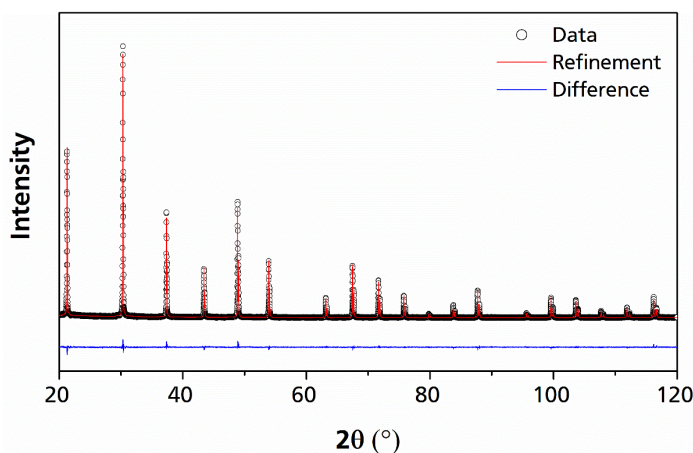
Figure 3-3. XRD pattern of LaB₆ together with the refinement using Rietveld method.

3.2   Electron Microscopy Techniques

The only radiation which is commonly used to obtain both diffraction patterns and microstructural images is electron. Electron Microscopy covers a wide range of materials investigation from complementary (to optical microscopy) studies on texture, topography and surface features of powders or solid pieces (by means of Scanning Electron Microscopy (SEM)) to structural and compositional information at the atomic scale (even less than 2 Å) using transmission electron microscopy (TEM), high-resolution electron microscopy (HREM) and scanning transmission electron microscopy (STEM). Electron microscopes operate in either transmission (sample should usually be thinner than ~ 2000 Å) or reflection (thickness of the sample is not important). Therefore, sample preparation can be a challenge in transmission mode.

Basic components of an electron microscope can schematically be seen in **Figure 3-4**. For using electrons in a microscope in order to form an image, the electron beam must be focused. This is done by either an electrostatic or a magnetic field. In this respect, several electromagnetic lenses are used in electron microscopes. The condenser lenses control the size and angular spread of the incident electron beam. Transmitted electrons pass through a series of lenses including objective and projector lenses to form a magnified image of the sample. The images can be recorded in either bright field or dark field. In the bright field image, the electrons transmitted by the sample form the image. Therefore, the image appears dark on a bright background. However, in the dark field imaging, only the beams diffracted from the particle of interest are allowed to form the image, resulting a bright image on a dark background.

There are many different techniques associated with electron microscopes. In the next sections, some of these techniques that have been used in this thesis will be briefly explained.
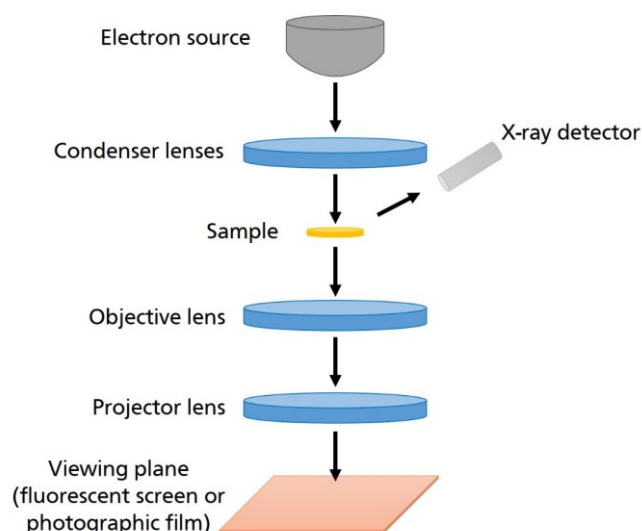
Figure 3-4. A schematic illustration of basic components of an electron microscope.

3.2.1 Transmission Electron Microscopy (TEM)

TEM related techniques are based on the transmitted electrons and radiation. TEM can provide both diffraction patterns and magnified images from the same sample area. From diffraction patterns (by TEM), unit cell and space group information can be obtained while TEM gives morphological information on the sample. The electron diffraction techniques can be divided into two groups: 1- Selected area diffraction (SAD), in which a parallel beam of electrons strikes the sample over a micrometer area. 2- Convergent beam diffraction (CBD), in which the focused beam on the sample has a spot size of ∼ 10 nm and gives a higher resolution than SAD.

3.2.2 Automated Diffraction Tomography (ADT)

ADT is a TEM-related technique to acquire electron diffraction data. The method is based on a collection of diffraction patterns at different tilt angles during sample tilt [72]. The tilting could be done in small steps without any prior information on the orientation of the crystal. However, it is essential to collect the data from the same crystal. Based on the information about the angular relationship between the diffraction patterns, the three-dimensional reciprocal volume can be reconstructed. A schematic plot of data acquisition in ADT is presented in **Figure 3-5**.

3.2.3 Energy-Dispersive X-ray Spectroscopy (EDS, EDX, or EDXS)

This technique operates usually in SEM mode and utilize the characteristic X-ray emission spectra generated when inner-shell electron atoms are ionized by high-energy bombardment [71]. EDX is a useful technique to obtain an overview about the elements present in a sample, though, it is less sensitive for light elements. Most of the SEM instruments are equipped with an EDX detector, which is very useful for routine elemental analysis and mapping of element distribution in a sample.

In EDX, the whole X-ray emission spectrum is detected simultaneously by a process in which X-rays are absorbed by a semiconducting material (e.g. Si or Ge). This leads to excitation of electrons and formation of electron-hole pairs. The electron-hole pairs are swept away by an applied voltage. This voltage is detected as a voltage pulse that is amplified and displayed on a screen. The voltage pulse is proportional to the energy of the incoming X-rays. This x-ray energy is characteristic of the elements responsible for the X-ray emission [71].
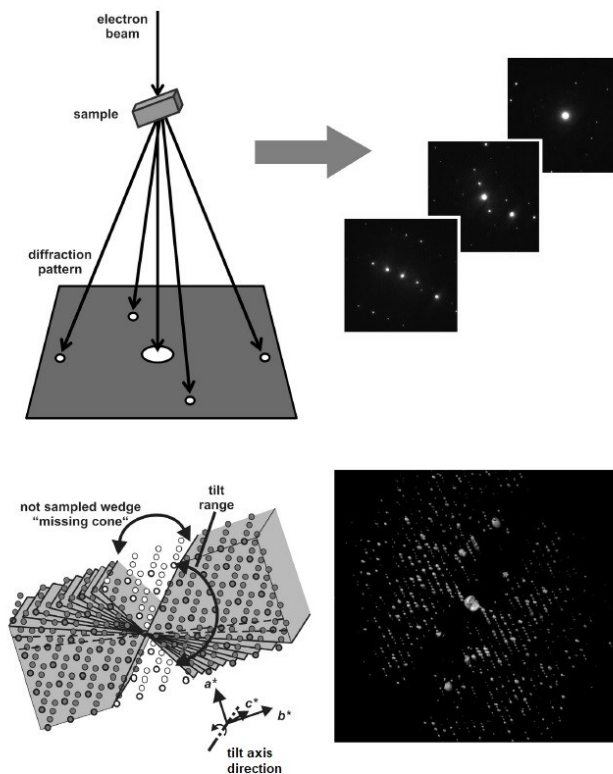
Figure 3-5. A schematic illustration of ADT data acquisition; the sequential collection of electron diffraction patterns and exemplary off-zone diffraction patterns (top); three-dimensional diffraction reconstruction and the missing cone volume (bottom left); exemplary reconstructed diffraction space (bottom right). The figure has been reprinted from [73] with permission[8].

3.3 X-ray Absorption Spectroscopy (XAS)

In this technique, characteristic X-ray absorption spectra of a sample is measured when the sample is hit by a (high energy) X-ray beam (in recent developments, X-ray radiation is produced by accelerating electrons in a synchrotron). When the energy of the incident photon is just sufficient to excite a core electron of the absorbing atom, an absorption edge occurs leading to a drastic increase in energy. The exact absorption peak position provides useful information about oxidation state, site symmetry, surrounding ligands and nature of the bonding.

3.4 X-ray Photoelectron Spectroscopy (XPS)

XPS is a surface analysis that monoenergetic soft X-rays are used to irradiate the sample. Then the energy of the detected electrons is analysed. In this method, usually X-rays such as Mg Kα (1253.6 eV), Al Kα (1486.6 eV) or monochromatic Al Kα (1486.7 eV) are used. The penetration power of these photons in a solid are limited to 1-10 micrometres. The surface atoms are interacted with the photons leading to emission of the electrons by the photoelectric effect. The kinetic energy of the electrons can be measured by the following equation:

$$KE = h\nu - BE - \phi_s \qquad (3.3)$$

where $h\nu$ is the energy of the photons, BE is the binding energy of the atomic orbital from which the electron originates and ϕ_s is the spectrometer work function.

---

[8] Copyright © 2013 Elsevier Inc.

The binding energy can be defined as the energy difference between initial and final states. The final state varies with different ions (from each type of atom). Therefore, there is a corresponding variety of kinetic energies of the emitted electrons. Each element has a unique set of binding energies. Therefore, XPS may be used to identify and determine the concentration of the elements in the surface.

4 Experimental

4.1 Synthesis of Precursors

LaSrMnO₄: Stoichiometric amounts of $SrCO_3$ (Sigma Aldrich, ≥ 98%), Mn_2O_3 (Sigma Aldrich, 99%), and La_2O_3 (Alfa Aesar, 99.9%) were ground with a mortar and pestle. La_2O_3 was dried at 1150 °C prior to use. The mixture was heated under a flow of pure argon (99.996%) with a flow rate of 0.5 standard liter per minute (SLM) at 1100 °C for 6 hours followed by heating at 1450 °C for 48 hours with one intermediate grinding.

La₂CoO₄₊d: Stoichiometric ratios of La_2O_3 (Alfa Aesar, 99.9%, pre-dried at 1200 °C before use) and Co_3O_4 (Alfa Aesar, 99.7%) were mixed using a ball mill made from ZrO_2 for 1 hour with a rotational speed of 600 RPM. For the milling process, a small fraction of isopropanol as the dispersing agent has been used. Then the mixture was heated at 1300 °C for 12 hours under Ar flowing (purity 99.999%, 0.4 SLM flow).

La₂NiO₄₊d: A variety of La₂NiO₄₊d compounds were synthesized by solid-state reactions according to previous reports [74, 75]: Stoichiometric ratios of La_2O_3 (Alfa Aesar, 99.9%, pre-dried at 1200 °C for 12 h before use) and NiO (Sigma Aldrich, +99.99%, pre-dried at 700 °C for 12 h before use) were mixed and heated under different atmospheres at 800 °C for 10 h. Then the mixture was hand-ground and re-heated under Air, oxygen or Ar at 1400 °C and kept for 4 h. The heating/cooling rates were 2 °C/min and 3 °C/ min, respectively. La₂NiO₄.₁₃ has been used to make the electrode composite, while the other La₂NiO₄₊d compounds have been used as references for XAS measurements. The treatment conditions and the respective lattice parameters for each La₂NiO₄₊d compound are summarized in **Table 4-1**. The XRD measurements of each phase can be found in **Figure 4-1**.

Table 4-1. Heating atmosphere under which the La₂NiO₄₊d compounds were made. The composition of the compounds were determined according to obtained lattice parameters in accordance with ref [76].

Compound	Heating atmosphere	Lattice parameters (*Fmmm*)				Ni oxidation state
		a (Å)	b (Å)	c (Å)	wt%	
La₂NiO₄.₀₃₀§	purified Ar (in presence of Mn as O₂ getter)*	5.483(1)	5.473(2)	12.599(1)	67	+2.06
		5.512(1)	5.466(1)	12.566(1)	33	
La₂NiO₄.₀₅₅	Ar	5.475(1)	5.469(1)	12.618(1)	100	+2.22
La₂NiO₄.₁₃	Air	5.466(1)	5.463(1)	12.676(1)	100	+2.26
La₂NiO₄.₁₇	O₂	5.466(1)	5.458(1)	12.697(1)	100	+2.34

* After heating at 800 °C for 12 h and 1400 °C for 4 h, the sample was heated once more at 900 °C for 4 h under presence of Mn.

§ An average oxygen content (d) was considered based on the obtained lattice parameters.
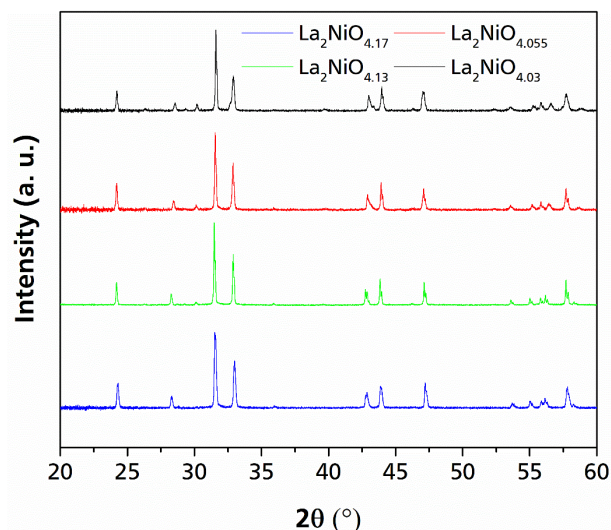
Figure 4-1. XRD patterns of La_2NiO_{4+d} (0.03 ≤ d ≤ 0.17) that were also used as standards for XAS measurements.

LaSrCoO₄: Stoichiometric amounts (according to literature [77]) of La_2O_3 (Alfa Aesar, 99.9%, pre-dried at 1200 °C for 12 h before use), Co_3O_4 (Alfa Aesar, 99.7%) and $SrCO_3$ (Sigma Aldrich ≥ 98%) are mixed and heated at 750 °C for 3 h under air (total weight of the batch = 0.5 g). The powders then hand ground and heated again at 1300 °C for 24 h under air.

LaSrFeO₄: To synthesize pure $LaSrFeO_4$, stoichiometric amounts of dry La_2O_3 (Alfa Aesar, 99.9%, pre-dried at 1200 °C for 12 h before use), $SrCO_3$ (Sigma Aldrich ≥ 98%) and Fe_2O_3 (Sigma Aldrich ≥ 99%) have been ball milled for 1 h at a rotational speed of 600 RPM, using isopropanol as a dispersing agent. The mixture then heated at 700 °C for 12 h and 1200 °C for 48 h with intermediate hand grinding. Heating/cooling rates were considered to be 2 °C/min.

SrFeO₂: To prepare $SrFeO_2$, first $SrFeO_3$ was made by ball milling of stoichiometric amounts of $SrCO_3$ (Sigma Aldrich ≥ 98%) and Fe_2O_3 for 5 min at 400 RPM using isopropanol as a dispersing agent. The powders then heated at 1100 °C for 10 h followed by the second heat treatment at 1100 °C for 8 h with intermediate hand grinding. The synthesized $SrFeO_3$ was further reduced using CaH_2 as the reducing agent (CaH_2 was used in excess). The mixture of oxide and reducing agent were loaded (inside an Ar-filled glovebox) in an air tight reactor and heated at 300 °C for 48 h (the sealed reactor was kept outside the glovebox during the heating operation, however, it was loaded/unloaded inside the glovebox). To remove the unreacted CaH_2, the obtained powders were washed (outside of the glovebox) with a mixture of methanol (400 ml, dried for 6 days with granular molecular sieve) and NH_4Cl. The powders were further re-washed with pure dried methanol and finally filtered.

(Co/Mg)₀.₅Fe₀.₅Sb₂O₄: Schafarzikite-type compounds with composition $Mg_{0.5}Fe_{0.5}Sb_2O_4$ and $Co_{0.5}Fe_{0.5}Sb_2O_4$ have been prepared in collaboration with School of Chemistry, University of Birmingham according to the preparation procedure described by de Laune *et al.* [78]: stoichiometric amounts of dried mixture of the metal oxides and antimony metal (CoO, 325 mesh Sigma-Aldrich; Fe_2O_3 ≥ 99.9% Sigma-Aldrich; Sb_2O_3, Reagent Plus, Sigma-Aldrich; Sb, BDH; MgO, ≥ 99% 325 mesh Sigma-Aldrich) were heated in evacuated sealed quartz tubes between 6 hours to 36 hours at 700 °C with intermittent grinding.

La₀.₉Ba₀.₁F₂.₉ Electrolyte material: Preparation of the $La_{0.9}Ba_{0.1}F_{2.9}$ was done according to literature [24]: Stoichiometric ratios of BaF_2 (STREM Chemicals, 99%) and LaF_3 (STREM Chemicals, 99.9%) were milled for 12 h at a rotational speed of 600 RPM using ZrO_2 vial and

balls (10 balls in total). The precursors were dried inside the glovebox at 190 °C for 4 h, prior to milling. All the milling operations within this thesis were performed by a RETSCH PM 100 or 100 CM planetary ball mill. The weight of each electrolyte batch was considered to be 10 g, resulting in a ball to powder ratio of 3.2:1.

4.2 Electrode Composites

Cathode composite materials: For preparation of the cathode composite materials, 30 wt% of the respective as-synthesized oxides were mixed with 60 wt% of the electrolyte (as milled $La_{0.9}Ba_{0.1}F_{2.9}$) and 10 wt% of black carbon or carbon nanotubes (dried at 190 °C under Ar) to improve the ionic and electronic conductivity of the cathode material. The mixture was then ball milled for 3 h at a rotational speed of 250 RPM. The milling intervals were considered to be 10 min followed by 20 min rest between each interval. Note that higher milling speed could result in amorphization of the oxide, by that destroying the layered structure which is a prerequisite for the structural reversibility of the intercalation of fluoride ions. Each milling batch contained a total 1 g of the cathode composite material (i.e. 0.3 g of active cathode material), resulting in a ball to powder ratio of 32:1.

In case of $LaSrMnO_4$, cathode materials based on silver and indium tin oxide (ITO) as the electronic conductor (instead of carbon) have been prepared. For making the cathode material using Ag as the electronic conductor, $LaSrMnO_4$ (30 wt%), $La_{0.9}Ba_{0.1}F_{2.9}$ (30 wt%) and silver particles (40 wt%) were milled for 3 h at a rotational speed of 250 RPM. In case of ITO, 10 wt% of ITO was milled together with $LaSrMnO_4$ (30 wt%), $La_{0.9}Ba_{0.1}F_{2.9}$ (60 wt%) at 250 RPM for 3 h again at the same milling conditions.

Anode composite materials: Different metal fluoride based anode composite materials have been prepared via mechanical milling. For each anode composite, the precursor weight ratios and the milling conditions are listed in **Table 4-2**. Each milling batch contained a total weight of 1 g (ball to powder ratio of 32:1). The milling operations were performed in ZrO_2 vial with 20 min rest after each 10 min interval.

Table 4-2. Composition of the anode materials. *The mixture of Mn+MnF$_2$+C (without the electrolyte) was milled for 16 h at 600 RPM prior to milling it with the La$_{0.9}$Ba$_{0.1}$F$_{2.9}$ electrolyte material.

Anode material	Composition	Rotational speed (RPM)	Active milling time (h)
PbF$_2$	90 wt% PbF$_2$ (Strem Chemicals, 99+) 10 wt% dried black carbon	600	12
Pb+PbF$_2$	45 wt% Pb (Sigma Aldrich, >99%) 45 wt% PbF$_2$ (Strem Chemicals, 99+) 10 wt% dried black carbon	600	12
Zn+ZnF$_2$	50 wt% La$_{0.9}$Ba$_{0.1}$F$_{2.9}$ (electrolyte material) 20 wt% Zn (ABCR, 98%) 20 wt% ZnF$_2$ (ABCR, 99%) 10 wt% dried black carbon	600	12
Mn+MnF$_2$*	50 wt% La$_{0.9}$Ba$_{0.1}$F$_{2.9}$ (electrolyte material) 20 wt% Mn (ABCR, 99.3%) 20 wt% MnF$_2$ (Strem Chemicals, 99%) 10 wt% (dried black carbon)	250	3

4.3 Electrochemical Cell Preparation

The whole process of pellet making was performed inside a high purity Ar-filled glovebox (99.999%). To make a full battery cell, first 200 mg of the electrolyte were poured into the cavity of a steel die and pre-pressed by hand. Then excess amount (typically 20x) of anode material (a weight between 12 – 20 mg, according to the type of the anode composite) has been added to one side of the electrolyte material inside the die. The powders were again pre-pressed by hand. Finally, ∼ 5 mg of the cathode composite material (containing 1.5 mg of active cathode material) was added to the other side of the electrolyte material and again pre-pressed. Note that higher active masses resulted in easy delamination of the cathode side, and were therefore not considered. Three layers of cathode/electrolyte/anode were pressed at a pressure of 2 tons for 90 seconds, using a desktop press (Specac). The dimensions of the pellet were measured to be 1.6 and 7.3 mm for the thickness and the diameter, respectively.

The prepared pellets were spring-loaded (as described in **Figure 4-2**) into modified air-tight (by Teflon tightening rings) Swagelok-type cells with current collectors made of stainless steel. All electrochemical cells were loaded, sealed and removed in a high purity Ar (99.999%) glovebox. However, for electrochemical testing, the sealed cells were operated outside the glovebox. To ensure sufficient mobility of the fluoride ions within the solid electrolyte, the electrochemical cells were heated between 150 – 200 °C (typically 170 °C). To minimize the thermal fluctuations (typically in the order of ± 1 °C) the electrochemical cells were covered with glass wool and the room was held at 21 °C by an air conditioner.
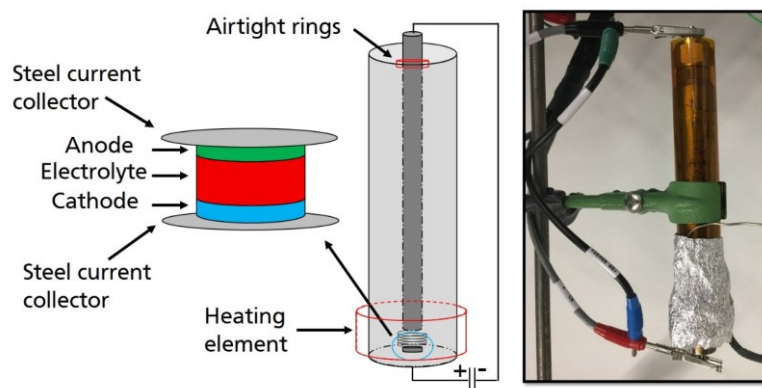
Figure 4-2. A schematic (left) and an operational (right) electrochemical cell used for the electrochemical measurements in this thesis.

4.4   Experimental Parameters for Electrochemical Measurements

Battery testing was performed using a potentiostat from BioLogic (SP-150 or VSP300) or Solartron device (1400 Cell Test System – 1470E). All voltages are given as potentials against the anode material. Anode composites were used in excess compared to the active cathode material; in this respect, all specific capacities are given with respect to the mass of the active cathode material. The charging/discharging/cycling experiments were performed galvanostatically, with charging and discharging currents of typically $+10\ \mu A$ ($\sim 24\ \mu A/cm^2$) and $-1.0\ \mu A$ ($\sim -2.4\ \mu A/cm^2$), respectively (unless stated otherwise).

Cycling voltammetry measurements were performed mainly for La_2NiO_{4+d} cathode material as the most promising cathode material against $Pb+PbF_2$ and $Zn+ZnF_2$ counter electrodes. The scan rate considered to be 0.1 mV/s (T = 170 °C).

The electrochemical impedance spectroscopy (EIS) of the cells was performed simultaneously during the galvanostatic charging at 170 °C within the frequency range between 500 kHz and 100 mHz with a current amplitude of $10\ \mu A$. All the measurements were performed by BIoLogic VSP300 device. The measurements were performed with 30 points per decade, averaging five measures per frequency.

4.5   Experimental Parameters for XRD Measurements

X-ray diffraction was used for analyzing the structure and composition of the electrode composites. The measurements were performed using a Bruker D8 Advance (**Figure 4-3**) in Bragg-Brentano geometry (for more information see section 7.3.1) with CuK_α radiation (VANTEC detector). For air sensitive samples, they were loaded into a low background specimen holder (Bruker A100B36/B37) and sealed inside an argon filled glovebox before every measurement to avoid potential side reactions with the atmosphere. Other non-air sensitive samples were measured by regular sample holders. Data were generally recorded in an angular range between 20° and 70° 2θ (unless otherwise is stated) for a total measurement time varying from 10 min to 4 h using a step size of ~0.007° and a fixed divergence slit of 0.3°. For high-resolution measurements, either the measurement time has been increased or the counting time was kept constant and the angular range was reduced (e.g. 27° - 36° 2θ).
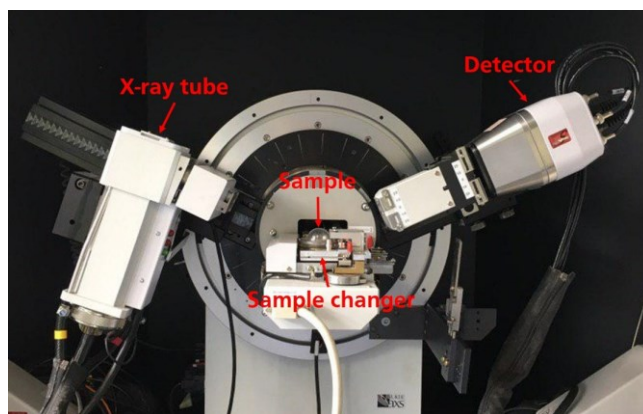
Figure 4-3 Representation of the Bruker D8 Advance X-ray powder diffractometer that has been used to measure all the samples in this thesis.

4.6 Electron Microscopy-Related Experimental Procedure

Electron microscopy related techniques have been used only to investigate the $La_2NiO_{4.13}$ cathode material in order to better understand the fluorinated phase. Such an approach (for evaluating the fluorinated phase) was used because of the fact that the chemical fluorination of $La_2NiO_{4.13}$ could not be achieved.

TEM samples were prepared by placing a drop of the powders dispersed in n-hexane on a carbon coated copper grid. A FEI Tecnai F30 S-TWIN transmission electron microscope equipped with a field emission gun and operated at 300 kV was used. 10-μm condenser aperture, spot size 6 and gun lens 8 were set to produce a quasi-parallel beam with a 200-nm size for the automated diffraction tomography (ADT) experiments. In case of the energy dispersive X-ray (EDX) spectroscopy measurements, a 50-μm condenser aperture, spot size 6 and gun lens 1 were used to increase the electron dose and have a reliable amount of counts on the EDX detector (EDAX EDAM III). STEM images were collected using a Fischione high-angle annular dark field (HAADF) detector. Electron diffraction patterns were acquired with an UltraScan4000 CCD camera provided by Gatan (16-bit, 4096 × 4096 pixels). Hardware binning 2 and exposure time of 2 seconds were used to acquire non-saturated diffraction reflections. ADT datasets were acquired with an automated acquisition module developed for FEI and JEOL microscopes, called hereby Fast-ADT, which allows the acquisition of electron diffraction tomographies in around 10 minutes for conventional CCD cameras and fixed tilt step of 1º [79]. Precession electron diffraction (PED) [80] was coupled to the Fast-ADT data collection to minimize the dynamical effects and improve the reflection intensity integration quality [81]. PED was generated by means of the DigiStar system developed by NanoMegas SPRL and it was kept to 1º.

Three-dimensional processing of the Fast-ADT data was done by the eADT software package [72]. Sir2014 [82] was used for ab initio structure solution and Jana2006 [83] was later used for crystal structure refinement. Intensity extraction for dynamical refinement was done by PETS [84]. EDX peak identification and quantification was carried out by the ES Vision software.

4.7   Experimental Parameters for X-ray Absorption Spectroscopy (XAS)

XAS measurements have been used to obtain information about the absorption energy of La_2NiO_{4+d} cathode composite (before and after charging) as compared to La_2NiO_{4+d} standards with different oxidation states of Ni. For the charged La_2NiO_{4+d} sample, 5 cells were charged to 120 mAh/g to obtain a sufficient amount of sample in a charged state. Then the cathode sides were carefully scratched off (inside the Ar-filled Glovebox) and merged. Preparation of the other La_2NiO_{4+d} ($0.030 \leq d \leq 0.17$) standards has been explained in section 4.1

X-ray absorption experiments were carried out at beamline P65 at Deutsches Elektronen-Synchrotron Desy in Hamburg (Germany). For the measurements at the Ni K-edge at 8333 eV, a Si(111) double-crystal monochromator was applied in continuous scan mode (180 s/spectrum). Due to the low Ni-concentration of the samples, spectra were recorded in fluorescence geometry using a passivated implanted planar silicon (PIPS) detector. The preparation of the samples was carried out under inert atmosphere in a glove box producing pellets diluted with boron nitride. Monochromator calibration was carried out using a Ni foil.

4.8   Experimental Parameters for X-ray Photoelectron Spectroscopy (XPS)

XPS measurement have been used only for the analysis of the La_2NiO_{4+d} cathode composite before and after charge. The XPS measurements were performed by a Physical Electronic VersaProbe XPS unit with the PHI 5000 spectrometer analyzer. As the X-ray source, Al K_α radiation (1486.6 eV) with a power of 50.6 W was used. The step size and pass energy for the detailed spectra were set to 0.1 eV and 23.5 eV and for the survey spectra to 0.8 eV and 187.85 eV, respectively. As reference materials gold and silver, with the respective gold 4f7/2 (Au4f7/2) emission line at 84.0 eV and the silver 3d5/2 (Ag3d5/2) emission line at 368.3 eV were measured, to correct the binding energy of the spectra by the characteristic shift of the instrument. In order to address sample related shifts in the spectra the valence band was also measured and the spectra corrected by the position of the valence band minimum. No sputtering was done previous and during the measurement, as well as no neutralization was necessary. For the background correction a Shirley-type correction was used. Note that prior to XPS measurement of the sample before charging, this sample has been heated at 170 °C for 6 h inside an Ar-filled glovebox to be more in line with the actual charging conditions.

5 Results and Discussions

Selected parts of this chapter have been published within the context of this thesis in [85-88] (All reprinted figures, tables and/or further excerpts are reprinted with permission).

5.1 Introduction

To investigate on suitable host structures serving as a reasonable intercalation-based cathode material for FIB, the three following compounds as potential cathode materials have been considered initially, each representing a structure-type group: $LaSrMnO_4$ (Ruddlesden-Popper), $(Mg/Co)_{0.5}F_{0.5}Sb_2O_4$ (Schafarzikite) and $SrFeO_2$ (perovskite). The reason for selecting these compounds was the availability of the information about the chemical fluorination of these materials. Therefore, it was possible to have an estimation about the degree of fluorination over an electrochemical fluorination, simply by comparing the changes in the structure of the material by chemical/electrochemical reactions. Preliminary results revealed that $SrFeO_2$ is not chemically stable in the electrochemical cell condition ($SrFeO_2$ reacted to the $La_{0.9}Ba_{0.9}F_{2.9}$ electrolyte material before any electrochemical reaction) and therefore, $SrFeO_2$ was not considered any further. In contrast, $LaSrMnO_4$ showed a very good structural stability within the experimental conditions. More importantly, compounds with Ruddlesden-Popper (K_2NiF_4)-type structures showed a very good structural reversibility over electrochemical fluorination/de-fluorination. Therefore, K_2NiF_4-type structures were the main focus of the investigations.

Figure 5-1 schematically illustrates a K_2NiF_4-type structure (Ruddlesden-Popper-type structure with a general formula of $(ABO_3)_nAO$ (n = 1 for K_2NiF_4)). Generally, in a K_2NiF_4 (A_2BO_4) structure BO_6 octahedra share corners with each other to form ABO_3 (two-dimensional) perovskite layer and the AO rock salt units exist between multiple layers of the perovskite along the c-axis, resulting in a tetragonal unit cell with the highest symmetry of $I4/mmm$ [46]. The vacant anion positions within the interlayers are suitable for accommodation of the fluoride ions (**Figure 5-1**): K_2NiF_4-type compounds are capable of accepting up to 2 fluoride ions per formula unit, resulting in theoretical capacities (see **Table 5-1**) comparable to the state of the art of LIBs (intercalation cathodes in LIBs typically have a practical specific capacity between 100 – 200 mAh/g [1]; e.g. $LiCoO_2$: 140 mAh/g, $LiMn_2O_4$: 120 mAh/g, and $LiFePO_4$: 165 mAh/g [89-91]). Considering the theoretical characteristics of K_2NiF_4-type structure compounds and the preliminary results showing a high degree of structural reversibility of $LaSrMnO_4$ on electrochemical cycling, systematic studies (in accordance with **Table 5-1**) have been performed on K_2NiF_4-type compounds including $LaSrMO_4$ (M = Mn, Co, Fe) and La_2MO_4 (M = Ni, Co). It should be taken into consideration that synthesis of La_2MO_4 (M = Fe or Mn) compounds which contain M^{2+} have not been reported yet and therefore, were not considered in this study.
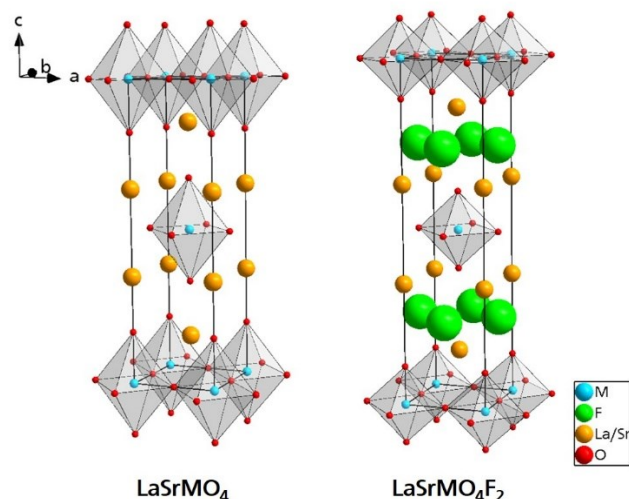
Figure 5-1. Schematic illustration of K$_2$NiF$_4$ structure of LaSrMO$_4$ (left) and fully fluorinated LaSrMO$_4$F$_2$ (right).

In the first approach, the main focus was on intercalation/de-intercalation of the fluoride ions (section 5.3). Therefore, LaSr(Mn/Co/Fe)O$_4$, La$_2$(Co/Ni)O$_{4+d}$ and (Mg/Co)$_{0.5}$F$_{0.5}$Sb$_2$O$_4$ compounds were subjected to galvanostatic charging/discharging experiments followed by structural analysis by XRD. In the course of the investigations, it was found that La$_2$MO$_{4+d}$ (M = Co, Ni) are the most promising candidates in respect of structural reversibility, discharge capacity, and energy density. Therefore, extended cycling experiments were only performed for La$_2$CoO$_{4+d}$ and La$_2$NiO$_{4+d}$ cathode composites. Furthermore, one of the major process limiting factors was found to be carbon oxidation during the charging process within the cathode composite, leading to a significant increase in the impedance of the electrochemical cell which results in a deterioration of the cycling performance. In this regard, the carbon side reaction has been investigated within the La$_2$MO$_{4+d}$ (M = Ni, Co) systems (section 5.4) and it was realized that the conductivity of the cell (highly affected by the carbon side reaction) can remarkably be preserved by regulating the cutoff conditions (voltage/capacity). Therefore, the cycling performance of La$_2$(Co/Ni)O$_{4+d}$ compounds highly depends on the cutoff conditions.

In the last section (section 5.5), potentially limiting factors arising from the conversion-based counter electrode materials (anode materials) have been studied. To do so La$_2$CoO$_{4+d}$ cathode material has been selected as an intercalation-based reference against M/MF$_2$ anode materials due to two reasons: 1- The desired electrochemical charge plateau can be separated from the side reaction plateau; 2- Since pure La$_2$CoO$_{4+d}$F$_x$ could be prepared via chemical reactions, internal overpotentials could be studied by making symmetrical cells of La$_2$CoO$_{4+d}$/La$_2$CoO$_{4+d}$F$_x$. The investigations revealed that a part of overpotentials arises from the used conversion-based anode materials (in lack of a well-developed intercalation-based anode material for FIBs) and that overpotentials are related to volume changes during electrochemical cycling within the conversion process.

Table 5-1. Theoretical capacities of some K_2NiF_4 type structure compounds that has been investigated in this study.

Compound	Theoretical capacity for insertion of 1 F– per formula unit (A_2MO_4F) (mAh/g)				Theoretical capacity for insertion of 2 F– per formula unit ($A_2MO_4F_2$) (mAh/g)			
	Mn	Fe	Co	Ni	Mn	Fe	Co	Ni
	($LaSrM^{4+}O_4F$)				($LaSrM^{5+}O_4F$)			
$LaSrM^{3+}O_4$	77.6	77.4	76.7	76.7*	155.2	154.7§	153.4§	153.5§
	($La_2M^{3+}O_4F$)				($La_2M^{4+}O_4F_2$)			
$La_2M^{2+}O_4$	67.5‡	67.4‡	66.9	66.9	135.1‡	134.8‡	133.8	133.8

‡ Starting oxides have not been reported yet. § The oxidation states were not reported for Fe, Co, and Ni within Ruddlesden-Popper-type oxyfluorides yet. * Could not be studied due to time limitations.

5.2 Screening of the Electrode Materials

In general, several selection criteria including economical and technical considerations play a vital role, when it comes to selection of the electrode materials. From the technical point of view, a suitable electrode material offers a large reversible storage capacity at the desired electrochemical potential with a suitable power density. As economic considerations one can name natural abundance, low production cost, eco-friendly nature and ease of recycling [56, 92]. In this study, however, the focus is more on the technical aspects since the economical perspectives becomes important when it comes to the state of the art and industrial mass production, a state which has not been obtained for FIBs yet.

One of the most important technical aspects of batteries lies on the capacity of the electrochemical cell. In many cases the practical capacity is much less than the theoretical capacity. As an example, $LiCoO_2$ possesses a theoretical capacity of 273 mAh/g (for insertion / removal of one Li ions per formula unit), however, only a capacity of 140 mAh/g can be obtained since only 0.5 Li ions can reversibly participate in the lithiation / de-lithiation (due to low structural stability of the de-lithiatet state) [93, 94]. The other essential criterion for a suitable electrode material is the voltage of the battery. To avoid decomposition of the electrolyte, the potential difference between the anode and cathode should lie within the potential window of the electrolyte material [49].

5.2.1 Selection of the Cathode Materials

Before considering the electrochemical fluorination, it is important to ensure that the possible structural changes during the electrochemical fluorination (charge) arises from the oxidative (electrochemical) intercalation of the F– ions and not from a chemical reaction between the electrode and the electrolyte materials. Due to limitations in ionic conductivity of the current FIB electrolyte materials, the electrochemical cells must be heated up (mainly around 170 °C). Thus, the chemical stability of the active cathode materials at the working temperature is an essential criterion. In this respect, full cells based on different active cathode materials were made and heated at the conditions identical to charging condition; i.e. the cells were heated up to 170 °C at typical experimental conditions without applying any current. Examples of the

structural changes in the active cathode materials over the heating process are presented in **Figure 5-2**.

As can be seen in **Figure 5-2a**, $SrFeO_2$ has low to no chemical stability on the heating: $SrFeO_2$ precursor has a tetragonal structure ($P4/mmm$, $a = 3.9933(1)$ Å, $b = 3.4837(2)$ Å). However, after heating the cell at 170 °C, $SrFeO_2$ active cathode material undergoes an oxidation reaction and a pseudocubic compound with high similarity to $SrFeO_2F$ ($Imma$, $a_{ps.cub.} = 3.9541(2)$ Å [95]) is obtained. The structural changes in terms of lattice parameter and space group of the oxyfluoride phase (over the chemical fluorination which is reported in literature [96]) is in a very well agreement with obtained structure after heating $SrFeO_2$ within the electrochemical cell configuration. It is worth noting that heating the $SrFeO_2$ cathode composite inside a glovebox (controlled atmosphere with an oxygen content <0.1 ppm) for 6 h already resulted in the formation of this phase (which would require oxidation). It is not clear how this oxidation takes place, since redox reaction with the electrolyte [36] and traces of oxygen can be considered of minor importance regarding that the compound even reacts in the glovebox under additional vacuum. Therefore, it seems that $SrFeO_2$ can be only stabilized at the highly reductive conditions in the presence of excess of CaH_2 used during its synthesis [97].
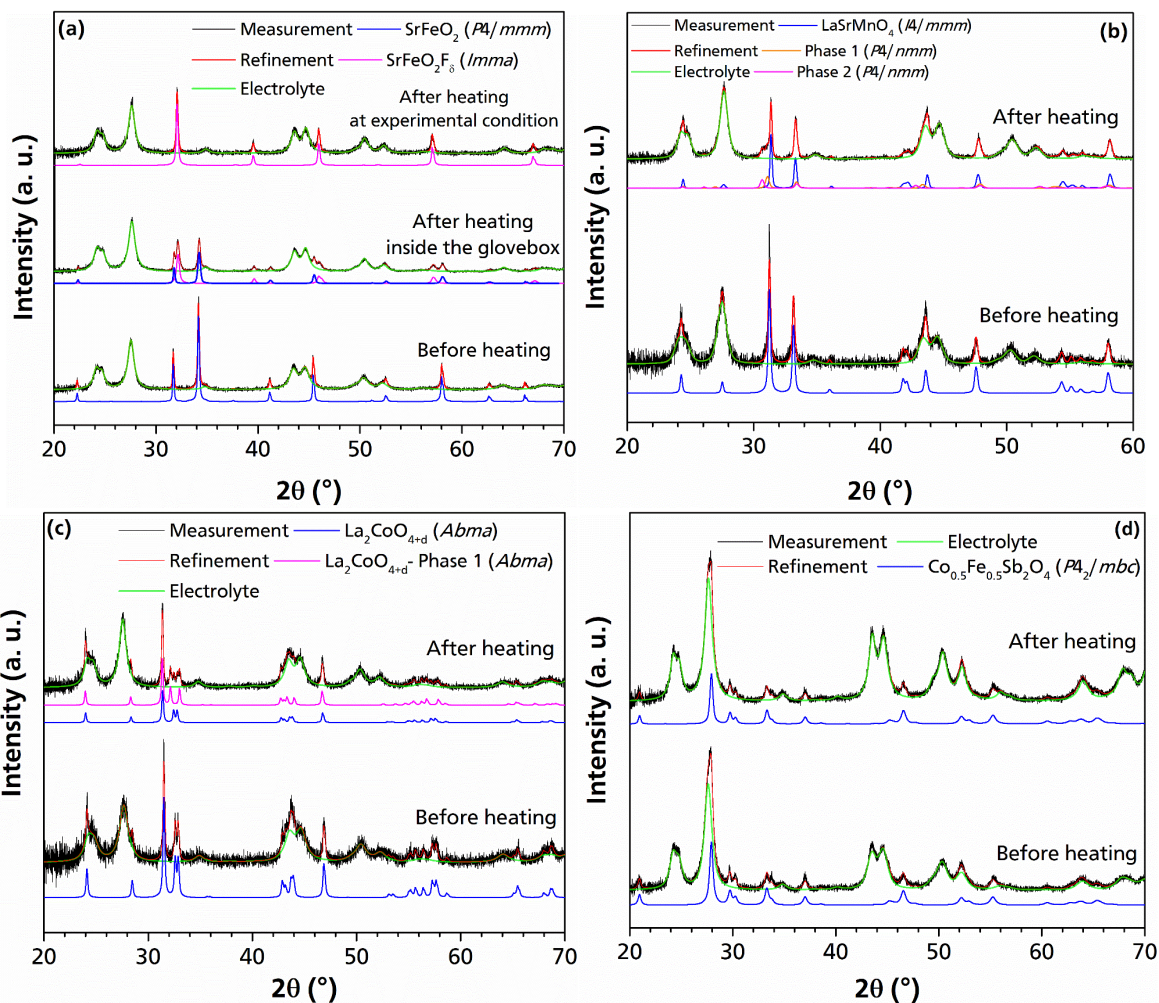
Figure 5-2. XRD patterns of different active cathode materials before and after heating the full cell (pellet) at 170 °C for a duration of 96 h without applying any current; (a) SrFeO₂; (b) LaSrMnO₄; (c) La₂CoO₄₊d; and (d) Co₀.₅Fe₀.₅Sb₂O₄.

LaSrMnO$_4$ shows a good chemical stability at the operational temperature (**Figure 5-2b**). Two additional tetragonal phases (Phase 1: *P4/nmm*, a = 3.8076(15) Å, c = 13.2941(92) Å, Phase 2: *P4/nmm*, a = 3.8059(19) Å, c = 13.7263 (97) Å) with relatively small weight fractions can be found after heating, though the majority of the initial LaSrMnO$_4$ phase (tetragonal *I4/mmm*, a = 3.8202(5) Å, c = 12.9582(21) Å) can still be found after the heating without significant structural changes (**Figure 5-2b**).

The XRD diffraction pattern of La$_2$CoO$_{4+d}$ before and after heating up the cell within the experimental conditions can be seen in **Figure 5-2c**. The obtained lattice parameters for the initial La$_2$CoO$_{4+d}$ phase (*Abma*, a = 5.5243(7) Å, b = 5.4762(7) Å, c = 12.6153(19) Å) reveals that the oxidation state of cobalt is $\sim$ +2.32 (corresponding to d = 0.16) [98]. After heating the cell, however, the initial phase can be determined together with a similar phase but with a higher degree of orthorhombic distortion (Phase 1: *Abma*, a = 5.5791(7) Å, b = 5.4347(7) Å, c = 12.6237(19) Å) which can be due to a slight increase in the oxidation state of Co [98]. Nevertheless, the structure is chemically stable enough to be considered for the electrochemical fluorination at the experimental temperature.

For Co$_{0.5}$Fe$_{0.5}$Sb$_2$O$_4$ with Schafarzikite-type structure, the heating process does not result in a significant change in the structure (**Figure 5-2d**) which again shows that Fe^{2+} seems to be stable here (same results are obtained for Mg$_{0.5}$Fe$_{0.5}$Sb$_2$O$_4$).

Since SrFeO$_2$ seems to have no chemical stability over the heating process (**Figure 5-2a**) further investigation on this compound was disregarded. However, other compounds with K$_2$NiF$_4$-type structures (LaSrMnO$_4$, La$_2$CoO$_{4+d}$, etc.) and Schafarzikite-type structures (MSb$_2$O$_4$) were considered further as potential candidates.

5.2.2   Selection of the Anode Materials

Unlike other Li/Na ion battery systems, no standard can be proposed as a counter electrode material for testing the FIB electrode materials since it is not possible to use fluorine gas as an electrode material while for the Li/Na ion batteries the respective metal element can be simply used as a reference. So far no other reference electrode material has been proposed for testing the new electrode materials for FIBs. Therefore, at the early stage of this study several active anode materials including CeF$_3$, MgF$_2$ and PbF$_2$ were used as a counter electrode. However, the best results obtained by using PbF$_2$ as the active anode material. In fact, using a less strong reducing agent (such as PbF$_2$) ensures less side reactions in the anode material during the redox reactions. Moreover, low melting point of Pb ($\sim$ 327 °C [57]) is in favor of a better reactivity within the solid-state reactions since the reactivity of a compound within a solid-state reaction is strongly enhanced the closer it is to the melting temperature of a compound [99]. Such a higher reactivity leads to a reduction in the overpotentials [87]. In the course of this thesis, it was realized that the anode composite materials, which consist of a mixture of metal fluoride plus the corresponding metal have a better electrochemical performance due to two reasons: 1- The metal particles ease the nucleation (as nucleation agents) of formation of metal particles during the electrochemical fluorination [87]; 2- During the cycling of the electrochemical cells some parts of the new formed metal (after reduction in the anode material during the electrochemical charging (fluorination)) may become inactive and does not take part in further redox reactions. Thus, additional metal particles may compensate for the inactivated particles. Such a strategy has also been proposed for FIBs by Fichtner et al. [27]. Furthermore, for improving the energy density of the electrochemical cells and improving the cycling

performance other metal plus metal fluoride anode composites such as $Zn+ZnF_2$ and $Mn+MnF_2$ have also been used.

5.3 Electrochemical Fluorination / De-Fluorination

In this chapter, first the electrochemical fluorination/de-fluorination of Ruddlesden-Popper (K_2NiF_4)-type structure $LaSrMnO_4$ will be investigated as a proof of concept since its fluorination chemistry has been well understood [48, 100]. Then other K_2NiF_4-type compounds such as $LaSr(Fe/Co)O_4$ and $La_2(Co/Ni)O_{4+d}$ will be discussed. Finally, electrochemical fluorination/de-fluorination of Schafarzikite-type structure MSb_2O_4 (M = $Co_{0.5}Fe_{0.5}$, $Mg_{0.5}Fe_{0.5}$) will be considered.

5.3.1 LaSrMO₄ (M = Mn, Fe, Co)

In this section, the electrochemical fluorination/de-fluorination of $LaSrMnO_4/PbF_2$ system (as a proof of concept) will be discussed. The observed structural changes on electrochemical fluorination will be compared with previous reports on chemical fluorination of $LaSrMnO_4$. The comparison shows that there is a principle agreement between the structural changes on electrochemical and chemical fluorination, confirming successful electrochemical intercalation of the F^- into the host structure of $LaSrMnO_4$. Later in this section electrochemical charging/discharging (fluorination/de-fluorination) of the $LaSr(Fe/Co)O_4/Pb+PbF_2$ systems will be further discussed.

5.3.1.1 LaSrMnO₄ / PbF₂ Cell: A Proof of Concept

The fluorination chemistry of $LaSrMnO_4$ has been well understood by means of neutron powder diffraction (NPD) and XRD analysis [48, 87, 100]. Aikens et al. report on chemical fluorine insertion in vacant interlayers of $LaSrMnO_4$ which shows a stage insertion of the fluoride ions in the alternate rocksalt bilayers rather than a random distribution of inserted anion species in all layers [48]. In fact, (chemical) intercalation of one F^- per formula unit in the structure of $LaSrMnO_4$ ($I4/mmm$, a = 3.7952(1) Å, c = 13.1410(9) Å) results in the occupation of one interlayer between two adjacent rocksalt layers. A close structural relationship between non-fluorinated $LaSrMnO_4$ and the fluorinated $LaSrMnO_4F$ has been observed, however, occupancy of one fluoride ion between a rocksalt interlayer results in a symmetry lowering and a large expansion of the unit cell ($\sim$ 7.3%) along the c-axis ($P4/nmm$, a = 3.7749(1) Å, c = 14.1049(3) Å) [48, 100]. Further fluorine insertion leads to occupation of the second vacant interlayer, which results in a further expansion of the lattice parameter c and recovery of the body centered symmetry ($LaSrMnO_4F_{2-\delta}$: $I4/mmm$, a = 3.77036(8) Å, c = 15.36195(2) Å) [87].

a. Electrochemical Fluorination

Figure 5-3a shows a typical charge curve of the $LaSrMnO_4/PbF_2$ cell in which two plateaus can be observed. The first one is a relatively short plateau and is observed at low potentials around 0.2 – 0.3 V. It is worth noting that this plateau is not predicted by the DFT (Density Functional Theory) calculations [87] (see **Figure 5-4**). The plateau can also be observed for some other active cathode materials with K_2NiF_4-type structure such as La_2CoO_{4+d}. Moreover, the first plateau seems to be irreversible since it can be only seen within the first cycle (see section (5.4.2)). Therefore, this plateau seems not to originate from an electrochemical reaction within $LaSrMnO_4$ and might most plausibly explained by a low potential side reaction which does not influence the ionic and electronic conductivity of the cell.

A very sharp increase in the potential can be seen at the end of the first plateau up to 1.2 V, after which the second plateau starts. According to **Figure 5-3a**, the second plateau occurs between $\sim 1.2 - 1.4$ V and seems to be a relatively flat plateau. The potential of this plateau (against PbF_2) is a bit higher than the DFT predictions for the formation of $LaSrMnO_4F$. This can be due to overpotentials; nevertheless, later it will be shown that by replacing Pb with a composite of $Pb+PbF_2$ as the active anode material, the second plateau occurs at lower potentials which is in a good agreement with the DFT calculations. After the second plateau the potential starts rising and the slope of the potential curve increases with increasing the charge capacity. Therefore, the DFT predicted plateau for formation of $LaSrMnO_4F_2$ (see **Figure 5-4**) cannot be observed like a flat plateau.

In order to study the structural changes of $LaSrMnO_4$ in a $LaSrMnO_4/PbF_2$ electrochemical cell during the charging step, identical pellets were charged at different cutoff potentials that are marked as red dots in the charge plot (**Figure 5-3a**) and the results are summarized in **Figure 5-3b** and **c**. The results reveal that charging of the cell up to 0.45 V (corresponds to a charge capacity of ~ 50 mAh/g) results in an expansion of $LaSrMnO_4$ cell along the c-axis ($c \sim 12.96$ Å before charge and $c \sim 14.00$ Å after charge) while almost 85% of the $LaSrMnO_4$ precursor converted to the phase with higher c parameter value (see **Table 5-2**). Further charging the cell up to 1.2 V leads to a further expansion of the cell along the [0 0 1] direction ($c \sim 14.21$ Å). At this cutoff voltage less than 3% of $LaSrMnO_4$ precursor still can be detected by XRD (see again **Table 5-2**). The obtained structure (at V = 1.2 V) have similarities to the structure of chemically fluorinated phase (to form $LaSrMnO_4F$ phase) [48, 100]. However, the c-parameter for the electrochemically fluorinated phase is larger than that for the chemically fluorinated phase (~ 14.2 Å for the electrochemical fluorination vs. ~ 14.1 Å [100] for the chemical fluorination). This may arise from a different degree of fluorination and/or oxygen ion exchange over the electrochemical reaction; i.e. the obtained phase does not have an exact composition of $LaSrMnO_4F$, rather it may have a slightly deviated composition of $LaSrMnO_{4\pm d}F_{1\pm\delta}$.

The cutoff voltage of 1.2 V corresponds to a charge capacity of 68 mAh/g (**Figure 5-3a**) which is smaller than the theoretical capacity for full occupation of one interlayer (formation of $LaSrMnO_4F$).Therefore, there is a possibility that the expansion of the lattice is due to partial occupation of the interlayer and not a full occupation of the vacant layer. This argument may also hold true for the cutoff potential of 0.45 V.
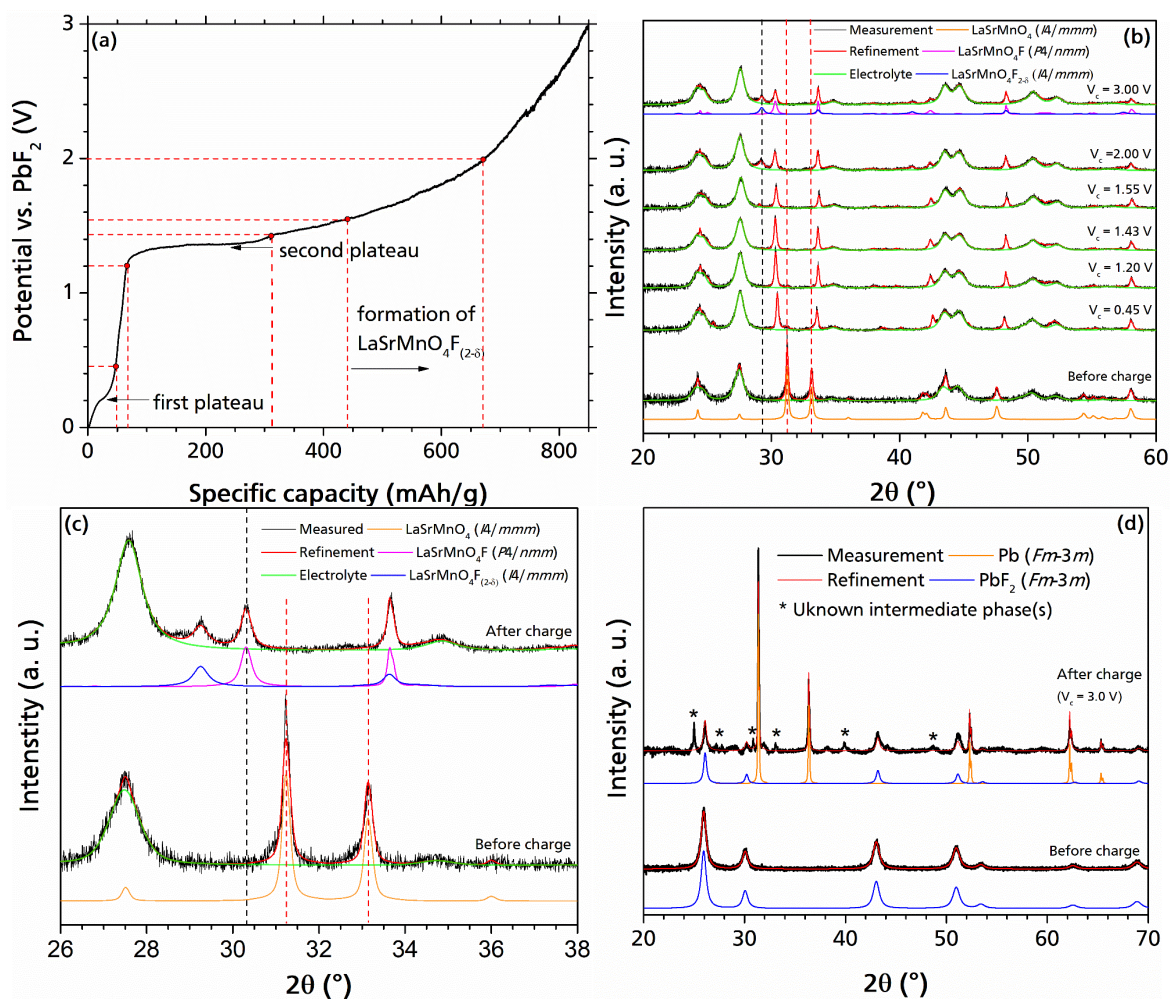
Figure 5-3. (a) Galvanostatic electrochemical charge curve of LaSrMnO₄/PbF₂ cell at an operational temperature and current density of 170 °C and 24 μA/cm², respectively; **(b)** corresponding XRD measurements of the LaSrMnO₄ cathode material at various cutoff potentials which are marked at the charge curve; **(c)** XRD measurements before and after charge for cathode material at cutoff voltage of 3 V; and **(d)** XRD measurements before and after charge for anode material also at 3 V.
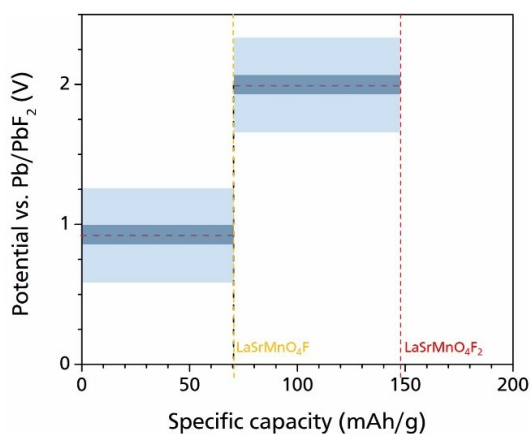
Figure 5-4. Schematic plot of the DFT predicted potential and capacity of charging LaSrMnO₄ vs. PbF₂. The figure is reprinted with some modifications from [87] with permission[9].

Table 5-2. Lattice parameters of the LaSrMnO₄ active cathode material after charge at different cutoff potentials at T = 170 °C and I = 24 µA/cm². Relative weight fraction (RWF) is calculated for LaSrMnO₄F based on the weight fraction of LaSrMnO₄F divided by the summation of LaSrMnO₄F and the initial LaSrMnO₄ phases and for LaSrMnO₄F₂₋δ based on the weight fraction of LaSrMnO₄F₂₋δ divided by the summation of LaSrMnO₄F and LaSrMnO₄F₂₋δ phases. The weight fractions are calculated according to the XRD data and the Rietveld method.

| V_c (V)	LaSrMnO₄ (*I4/mmm*)		LaSrMnO₄F (*P4/nmm*)		LaSrMnO₄F₂₋δ (*I4/mmm*)		LaSrMnO₄F (RWF%)	LaSrMnO₄F₂₋δ (RWF%)
	a (Å)	c (Å)	a (Å)	c (Å)	a (Å)	c (Å)		
Before charge	3.820(1)	12.957(2)	-	-	-	-		-
0.45	3.810(1)	13.100(11)	3.780(1)	14.000(1)	-	-	84.98(254)	-
1.20	3.816(2)	12.988(12)	3.770(1)	14.212(1)	-	-	97.44(191)	-
1.43	-	-	3.768(1)	14.218(1)	-	-	100	-
1.55	-	-	3.770(1)	14.231(2)	3.769(1)	15.991(5)	91.70(350)	8.30(276)
2.00	-	-	3.768(1)	14.246(3)	3.777(1)	15.627(7)	64.04(378)	35.96(720)
3.00	-	-	3.769(1)	14.224(3)	3.769(1)	15.649(6)	64.71(407)	35.28(671)

Between the cutoff voltages of 1.2 V and 1.43 V there is a relatively flat plateau in the charge plot (**Figure 5-3a**); however, the structural changes in this step is not as strong as previously: The lattice parameter c increases a bit (from ~ 14.22 Å to ~ 14.23 Å (**Table 5-2**)) and there is no sign of the initial LaSrMnO₄ precursor anymore. Therefore, there is a possibility that the partially occupied interlayers are getting further filled in this step (i.e. the oxidation state of +4 is approached further, and was generally lower than +4 at V = 0.85 – 1.2 V) without any noticeable change in the lattice parameters as the cell was already expanded due to partial occupation of the interlayer. Nevertheless, the practical charge capacity (~ 250 mAh/g at 1.43 V) is significantly higher than the theoretical capacity. Thus, there must be a side reaction which overlaps with the desired electrochemical reaction. There are some persuasive evidences showing that this side reaction is carbon oxidation (maybe fluorination) which results in a decomposition of the carbon network and consequently a destruction of the conductive matrix. It should be taken into consideration that based on the equation (2.4) the theoretical capacity of carbon for formation of CF (according to the following equation: "C + F⁻ → CF +e⁻") is calculated to be ~ 2230 mAh/g; therefore, observation of much higher charge capacities (higher than that for LaSrMnO₄) is reasonable in case of occurrence of such a side reaction. In section (5.4.1) the issue of carbon oxidation will be fully discussed.

The first indication for formation of highly fluorinated phase, LaSrMnO₄F₂₋δ, can be seen at the cutoff potential of 1.55 V which ~ 8.30% of the active cathode material is transformed to LaSrMnO₄F₂₋δ (c ~ 15.6 – 15.9 Å). Formation of the highly fluorinated phase of LaSrMnO₄F₂₋δ is accompanied by a further expansion in the lattice parameter c of the LaSrMnO₄F phase (c ~ 14.218 Å at 1.43 V; c ~ 14.231 Å at 1.55 V (**Table 5-2**)) which coexist with the LaSrMnO₄F₂₋δ phase. The amount of the high fluorine content phase of LaSrMnO₄F₂₋δ increases further up to ~ 36% at the cutoff capacity of 2 V. The charge capacities corresponding to the formation of LaSrMnO₄F₂₋δ is significantly higher than the theoretical capacity of LaSrMnO₄F₂

suggesting that the carbon side reaction is still ongoing with the desired electrochemical fluorination reaction.

At the cutoff potential of 3 V the XRD pattern of the cathode material shows a combination of LaSrMnO$_4$F and LaSrMnO$_4$F$_{2-\delta}$ phases (**Figure 5-3c**). At potentials above 2 V only a small increase in the lattice parameter c can be detected for the LaSrMnO$_4$F$_{2-\delta}$ phase (from $c \sim 15.63$ Å at 2 V to 15.65 Å at 3 V (**Table 5-2**)). Therefore, it is suggested that after 2 V the sloping charge plateau belongs mainly to side reactions. Also, the lattice parameters of the electrolyte fluctuates more severely at cutoff potential of 3 V as scompared to that within the uncharged state (from $a = 7.219(1)$ Å, $c = 7.388(2)$ Å before charge to $a = 7.204(1)$ Å, $c = 7.368(1)$ Å at cutoff capacity of 3 V (**Table 7-1**)). This can be an indication for partial decomposition of the electrolyte at high cutoff potentials.

Figure 5-3d shows the XRD pattern of the anode material after charging the cell up to 3 V that indicates formation of elemental Pb at the anode side coexisting with initial PbF$_2$ which confirms (partial) reduction of the PbF$_2$ in the anode side which is reasonable. Furthermore, some undetected phases can be seen in the XRD pattern of the anode side which is suggested to be formation of some intermediate phases.

b. Critical Parameters in the Electrochemical Fluorination (Charging)

Different charge current densities were tested within the LaSrMnO$_4$/PbF$_2$ cell (**Figure 5-5a**). The lowest overvoltage can be observed for the current density of 12 μA/cm^2 (I = 5 μA) while the first charge plateau which was suggested to be arising from the low potential side reactions seems to occur at much lower charge capacity ($\sim$ 10 mAh/g). It is also worth noting that increase in the current density results in further increase in the charge overpotentials (**Figure 5-5a**).

According to **Figure 5-5b** and **Table 5-3**, the relative weight fraction of the highly fluorinated (LaSrMnO$_4$F$_{2-\delta}$) phase reduces from $\sim$ 47% for the current density of 12 μA/cm^2 to 28% for 96 μA/cm^2 and no LaSrMnO$_4$F$_{2-\delta}$ phase can be detected by charging the cell with current density of 192 μA/cm^2. It is also worth noting that there is a significant difference between the lattice parameters of LaSrMnO$_4$F$_y$ phases that have been obtained at different charge current densities (**Table 5-3**). This may arise from different intercalation kinetics and different degree of fluorination (detailed chemical compositions F$_{1-x}$ or F$_{2-x}$) being obtained with respect to the current density. Further, increase in charge current density results in a higher overvoltage which can ease the occurrence of the side reactions.
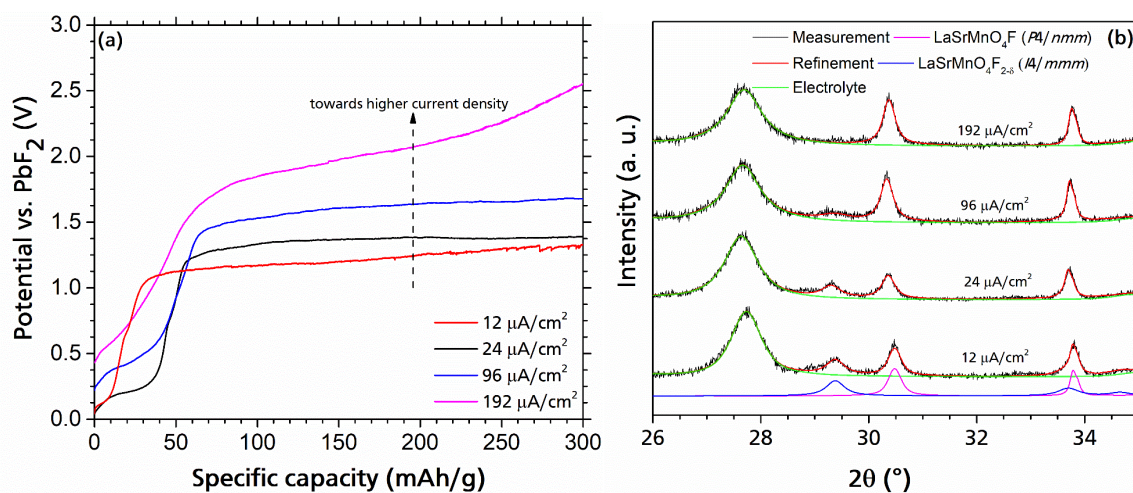
Figure 5-5. (a) Charging plots of LaSrMnO₄/PbF₂ cell which are charged up to 3 V at 170 °C and various current densities; **(b)** respective XRD measurements.

Table 5-3. Lattice parameters and relative weight fraction (RWF) of the products of the active cathode material after charging up to 3 V at different current densities at T = 170 °C.

Current density ($\mu A/cm^2$)	LaSrMnO₄F ($P4/nmm$)		LaSrMnO₄F$_{2-\delta}$ ($I4/mmm$)		LaSrMnO₄F (RWF%)	LaSrMnO₄F$_{2-\delta}$ (RWF%)
	a (Å)	c (Å)	a (Å)	c (Å)		
12	3.770(1)	14.221(3)	3.782(1)	15.616(7)	53.34(218)	46.66(302)
24	3.769(1)	14.224(3)	3.769(1)	15.649(6)	64.71(407)	35.28(671)
96	3.767(1)	14.300(3)	3.777(3)	15.540(23)	71.83(288)	28.17(266)
192	3.766(1)	14.289(2)	-	-	100	

The effect of the operational temperature on the overvoltage is provided in **Figure 5-6a** which shows an increase in the overvoltage during the charge step on reduction of operational temperature. At lower charge capacities the potential difference between the plateau of the cells which are operated at 150 °C and 200 °C is measured to be around 0.5 V. The charge plateau for the cell at 170 °C lies in between but closer to the plateau of the cell at 200 °C. By proceeding the process (after ∼ 150 mAh/g) the overvoltage of the cell at 150 °C increases significantly. Such a large overvoltage may result in occurrence of the side reaction instead of the desired electrochemical reaction particularly at higher charge capacities. Therefore, less highly fluorinated phase of LaSrMnO₄F$_{2-\delta}$ is formed at the operational temperature of 150 °C (in comparison with 170 °C and 200 °C, see **Figure 5-6b**). It is worth noting that operating the electrochemical cell at higher temperature of 200 °C results in an almost full transformation of lower fluorine content phase of LaSrMnO₄F to a higher fluorine content phase: According to **Figure 5-6b** the XRD pattern of the cathode material (after charge) shows that two highly fluorinated phases coexist. The first phase with a lattice parameter $c \sim 15.59$ Å which can also be found at the XRD pattern of the samples that are charged at 170 °C (that corresponds to occupation of the second interlayer of the host LaSrMnO₄ phase). Furthermore, a second phase can also be detected (**Figure 5-6b**) with a much higher increase in the lattice parameter c up to 16.82 Å (**Table 5-4**). This phase can only be seen at 200 °C. This phase has not been reported so far and more sensitive analyses (e. g. XANES, ADT, etc.) are needed to reveal the nature of this phase. However, from the c parameter of the cell (∼ 16.8 Å) this phase might be a LaSrMnO₄F$_y$ phase with a higher degree of fluorination which resulted in a further increase in the c parameter.
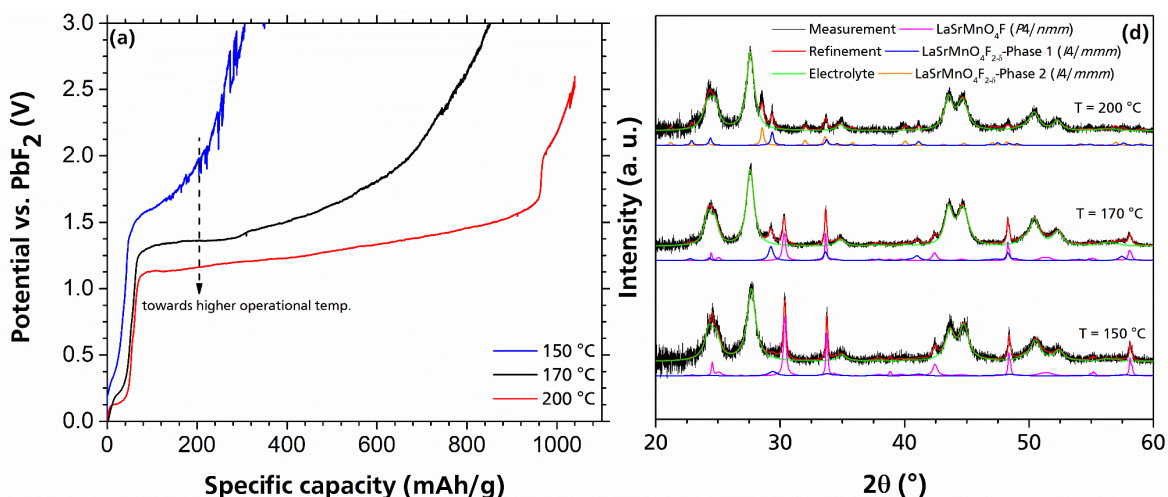
Figure 5-6. (a) Charging plots of $LaSrMnO_4/PbF_2$ cells which are galvanostatically charged up to ~3 V at various temperatures under a constant current density of I = 24 μA/cm²; **(b)** respective XRD patterns.

Table 5-4. Lattice parameters of the active cathode material after fluorination (charge) at various operational temperature up to 3 V at a current density of 24 μA/cm².

Operational temperature (°C)	$LaSrMnO_4F$ ($P4/nmm$)		$LaSrMnO_4F_{2-\delta}$ – Phase1 ($I4/mmm$)		$LaSrMnO_4F_{2-\delta}$ – Phase2 ($I4/mmm$)	
	a (Å)	c (Å)	a (Å)	c (Å)	a (Å)	c (Å)
150	3.768(1)	14.278(3)	3.765(5)	15.589(45)		
170	3.769(1)	14.224(3)	3.769(1)	15.649(6)		
200			3.766(1)	15.598(7)	3.780(1)	16.822` (7)

c. Electrochemical De-Fluorination

In the previous sections it was shown that the fluoride ions can be inserted into the vacant anion interlayers of $LaSrMnO_4$. In this section de-intercalation of the F⁻ ions (from the electrochemically fluorinated $LaSrMnO_4(F_y)$ host) will be investigated. As discussed, the carbon side reaction overlaps with the desired electrochemical reaction from the early stage of electrochemical fluorination. Therefore, destruction of the carbon conductive matrix results in an increase in the internal resistance which deteriorates the conductivity of the cell and consequently leads to relatively poor discharge behavior.

Figure 5-7a shows a typical discharge curve for the $LaSrMnO_4/PbF_2$ cell (charge cutoff potential 3 V). The discharge current density was reduced by a factor of 10 compared to the charge current density ($|I_{dis}|$ = 2.4 μA/cm²) since at a higher discharge (absolute) current density the drop in potential is so high that absolutely no discharge capacity can be obtained. This can be obviously seen in **Figure 5-7b** where the cell was discharged at a similar current density (24 μA/cm²) leading to a starting discharge potential which occurs at negative potentials ($\sim$ -1.3 V). Such a dependency between the kinetic of the electrochemical reaction and the current density is a very well-known phenomenon [63] which arises from the slower electron transfer kinetics and results in an increase in the polarization and internal impedance of the electrodes [101]. Nevertheless, later in section (5.3.2), it will be shown that higher current densities can be used for La_2NiO_{4+d} cathode composite, which might suggest that $LaSrMnO_4$ itself is very sensitive towards the discharge current density.

The discharge curve of the $LaSrMnO_4/PbF_2$ cell consists of a sloping plateau between $\sim$ 1.0 V (the start discharge potential) and 0.5 V followed by a sharper potential drop at $\sim$ 0.25 V. Then there is a relatively long plateau (roughly between 24 – 35 mAh/g) at a very low potential range (0.2 – 0 V). The XRD measurements detect a sharpening of $LaSrMnO_4F$ reflections and also a reduction in the lattice parameter c (for less fluorine content phase of $LaSrMnO_4F$ from $\sim$ 14.22 Å to $\sim$ 14.09 Å and for the higher fluorine content phase of $LaSrMnO_4F_{2-\delta}$ from $\sim$ 15.65 Å to $\sim$ 15.26 Å (please see **Table 5-4**)) after discharging, though, the initial un-fluorinated state of $LaSrMnO_4$ cannot be obtained.
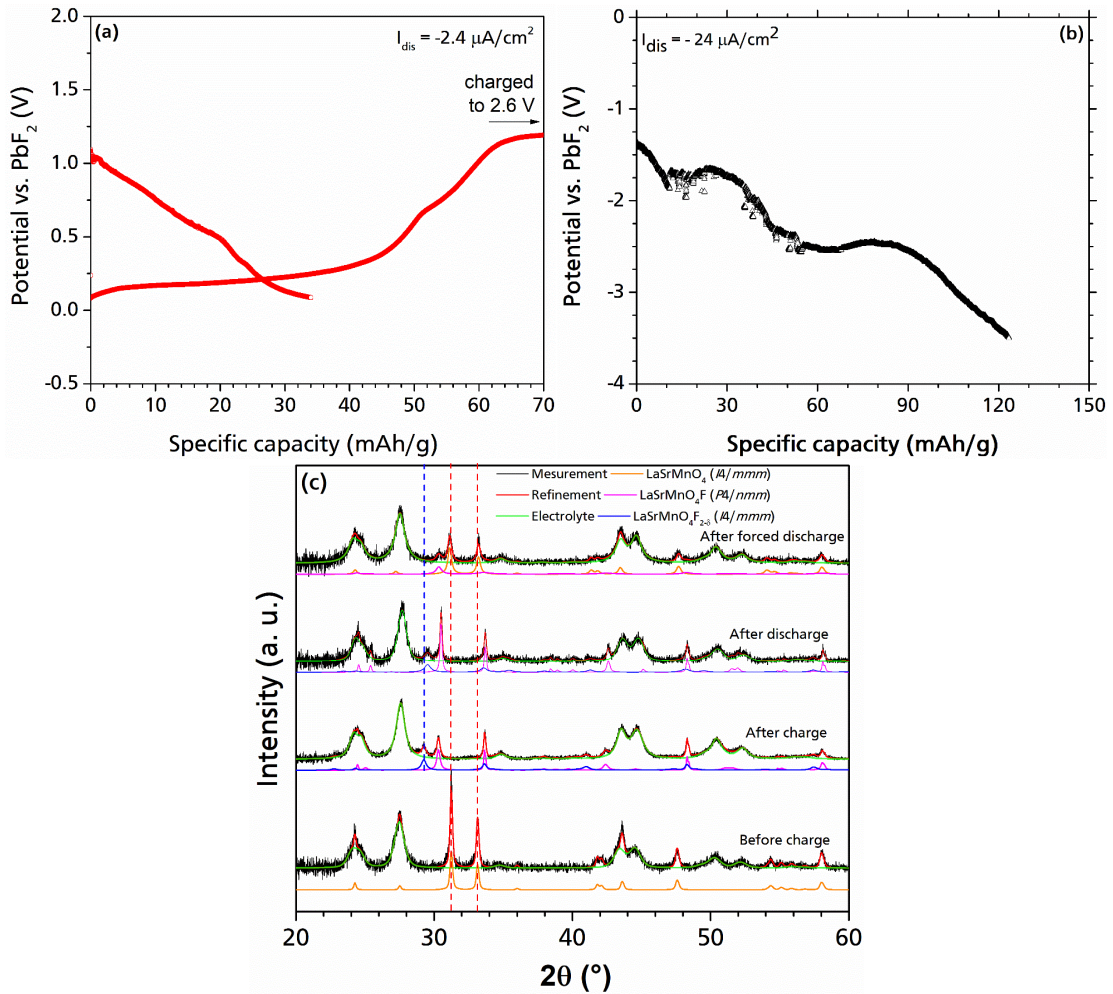
Figure 5-7. (a) Discharge curve of the $LaSrMnO_4$ against PbF_2 initially charged up to 2.6 V at an operational temperature of 170 °C and a charge/discharge current density of 24 µA/cm² and -2.4 µA/cm²; **(b)** discharge plot of the same cell towards negative potentials (up to -3 .5V) at T = 170 °C and $I_{ch/dis}$ = ±10 µA/cm²; **(c)** respective XRD patterns before charge, after charge, discharge and forced discharge.

Table 5-5. Lattice parameters of the active cathode material ($LaSrMnO_4$) before charge (pristine cathode material composite), after charge, after discharge, and after "forced discharge" at T = 170 °C, cutoff charge potential of 3 V, charge current density of 24 µA/cm², and discharge current density of -2.4 and -24 24 µA/cm² during discharge and "forced discharge" process, respectively.

	$LaSrMnO_4$ ($I4/mmm$)		$LaSrMnO_4F$ ($P4/nmm$)		$LaSrMnO_4F_{2-\delta}$ ($I4/mmm$)	
	a (Å)	c (Å)	a (Å)	c (Å)	a (Å)	c (Å)
Before charge	3.820(1)	12.957(2)				
After charge			3.769(1)	14.224(3)	3.769(1)	15.649(6)
After discharge			3.776(1)	14.099(3)	3.789(2)	15.264(16)
After forced discharge	3.812(1)	13.089(3)	3.770(5)	14.139(34)		

Further experiments revealed that upon discharging the $LaSrMnO_4/PbF_2$ cell (so called "forced discharge") to negative potentials against PbF_2 (up to – 3.5 V), as shown in **Figure 5-7b,** good recovery of the initial $LaSrMnO_4$ can be achieved (**Figure 5-7c** and **Table 5-4)**. This indicates that for the recovery of $LaSrMnO_4$ the overpotentials which are created during the charge step need to be compensated. The overpotentials are so high that the discharge plateau mainly lies at the negative potential axis. The obtained discharge capacity during a "forced discharge" process is very close to the theoretical capacity of $LaSrMnO_4$ (~ 130 mAh/g) which appears to be reasonable.

Summarizing the obtained discharge capacities and the structural changes over a discharge/forced discharge step, it can be concluded that the electrochemical fluorine removal from the host of $LaSrMnO_4(F_y)$ is possible. Therefore, the fluorination/de-fluorination is a reversible process, though, due to the overvoltages, a full structural reversibility can only occur on discharging the cell to negative potentials.

d. Modification of the PbF_2 Anode Material ($LaSrMnO_4/Pb+PbF_2$ Cell)

Mixing the discharge and charge products can result in preparation of electrode materials with more reactive interfaces [102]. A Similar strategy has been applied to prepare Pb/PbF_2 counter electrode material by making a composite of $Pb+PbF_2$ instead of using pure PbF_2.

A typical charge curve of $LaSrMnO_4$ against a $Pb+PbF_2$ anode composite material at operational temperatures of 170 °C and 200 °C can be found in **Figure 5-8a**. From the figure at least 5 distinct regions can be detected for both samples. It is worth noting that the overpotential for the sample with a higher operating temperature of 200 °C appears to be lower by roughly 0.15 V in the region (III) and ~ 0.4 V in the region IV-V. Such differences in the overpotentials are fully in accordance with the previous finding in the $LaSrMnO_4/PbF_2$ cell.

In **Figure 5-8a**, a short plateau can be observed in the first region (I) which corresponds to a capacity of only 20 mAh/g (between ~ 0.1 – 0.2 V) followed by a sharp rise in the potential up to 1.2 V (at 170 °C; ~ 1.0 V for the sample at the operational temperature of 200 °C). The XRD measurements reveal that at the cutoff potential of 0.5 V (within the potential jump shortly after the end of region (I)) two phases can be detected (**Figure 5-8b**): A phase with a relative phase fraction of ~ 65% which is very similar to the initial cathode material (tetragonal with space group $I4/mmm$) with a slight increase in the lattice parameter c (c ~ 12.967(2) Å for the

cutoff voltage of 0.5 V (**Table 5-6**) vs. 12.957(2) Å for the initial active cathode material) together with a phase that is similar to $LaSrMnO_4F$ (tetragonal, *P4/nmm*) but with a smaller *c* parameter (~ 13.710 Å) as compared to the similar ($LaSrMnO_4F$) phase that has been obtained after charging $LaSrMnO_4/PbF_2$ cell at V = 0.45 V (~ 14.00 Å).

A sharp increase in the charge potential from ~ 0.5 V – 1.2 V (corresponding to a capacity range between ~ 40 mAh/g – 75 mAhg/g) can be observed in the second charge region (II). Just before the end of region (II) (at cutoff voltage ~ 1.0 V) the XRD pattern of the active cathode material confirms a full transformation of the un-fluorinated $LaSrMnO_4$ to the fluorinated $LaSrMnO_4F_{1-\delta}$ phase with a lattice parameter *c* of ~ 14.182 Å (**Figure 5-8b** and **Table 5-6**).

At the region (III) a long potential plateau between $\sim 75 - 425$ mAh/g (correspond to the potential range of ca. 1.2 – 1.4 V) can be observed (**Figure 5-8a**). Such a large capacity range is obviously far higher than the theoretical capacity of $LaSrMnO_4$. Therefore, the plateau should be the result of an overlap between the desired electrochemical fluorination reaction with the side reactions. At the cutoff voltage of 1.3 V (corresponds to capacity of ~ 125 mAh/g) $LaSrMnO_4F_{2-\delta}$ with a lattice parameter *c* of ~ 15.5 Å can be observed in the XRD pattern of the cathode material (see **Figure 5-8b** and **Table 5-6**) coexists with the $LaSrMnO_4F$ phase with lattice parameter $c \sim 14.182$ Å (which is slightly higher than that at the cutoff capacity of 0.5 V (**Table 5-6**)). Note that in the $LaSrMnO_4/PbF_2$ cell, the highly fluorinated phase of $LaSrMnO_4F_{2-\delta}$ can only be detected at higher potentials (about 1.5 V) and charge capacities (almost 425 mAh/g) (see **Figure 5-8c**, also **Figure 5-3b** and **Table 5-2**). Thus, it can be suggested that using the $Pb+PbF_2$ anode material may ease the formation of $LaSrMnO_4F_{2-\delta}$ at a lower potential/capacity range.

Further charging the cell to higher cutoff potentials does not result in a significant change in the XRD pattern of the $LaSrMnO_4$ cathode material (**Figure 5-8b**); nevertheless, a slight increase in the lattice parameter of the formed $LaSrMnO_4F$ and $LaSrMnO_4F_{2-\delta}$ phases can be seen (see **Table 5-6**). Note that a full charge of the cell (up to 2.2 V) at an operational temperature of 200 °C results in a full conversion of $LaSrMnO_4/LaSrMnO_4F$ phases to highly fluorinated $LaSrMnO_4F_{2-\delta}$ phase ($a = 3.777(1)$ Å, $c = 15.420(7)$ Å) (as can be seen in **Figure 5-8d**). Such a temperature effect has been also shown for the $LaSrMnO_4/PbF_2$ cell (**Figure 5-6**).

Although using $Pb+PbF_2$ anode composite material (instead of PbF_2) significantly improves the kinetic of the formation of the highly fluorinated phase at much lower potential and capacity during charging, $Pb+PbF_2$ anode material does not remarkably change the discharge properties of the cell: As can be seen in **Figure 5-9a**, the discharge plots of $LaSrMnO_4$ against PbF_2 and $Pb+PbF_2$ are similar showing a discharge capacity of around 35 mAh/g. Moreover, the XRD measurements after the discharge (against PbF_2 and $Pb+PbF_2$) show no recovery of the initial $LaSrMnO_4$ phase (**Figure 5-9b**). It is worth noting that reducing the charge cutoff voltage to 1.3 V for the $LaSrMnO_4/Pb+PbF_2$ cell does not improve the discharge capacity (**Figure 5-9c**). Later in this chapter it will be shown that limiting the charge cutoff voltage/capacity may significantly influence the discharge behavior of the cells.
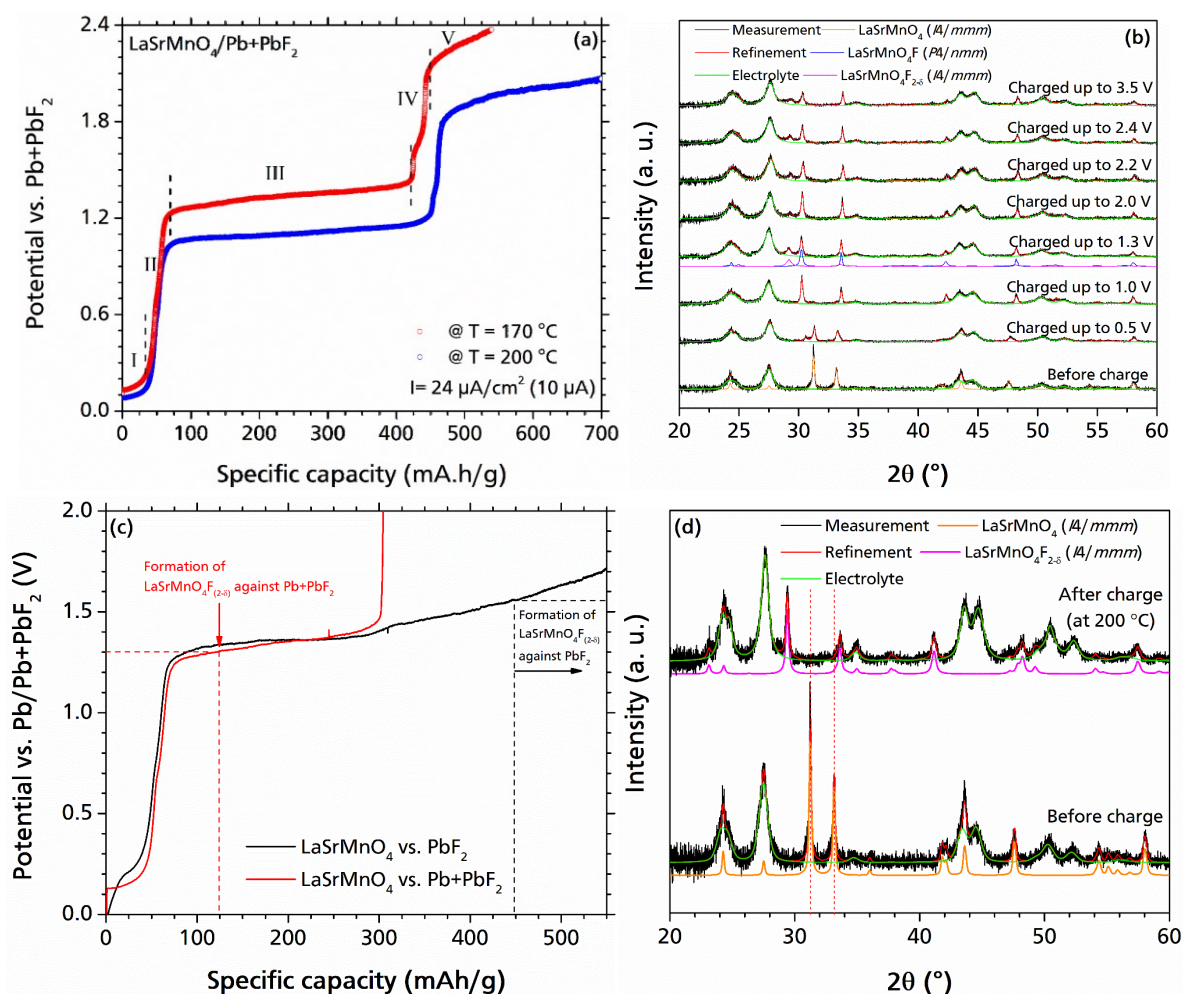
Figure 5-8. (a) Charge plot of LaSrMnO₄ vs. Pb+PbF₂ anode material at 170 °C and 200 °C (I = 24 µA/cm²); **(b)** XRD measurements before charge and after charge at different potentials for the LaSrMnO₄/Pb+PbF₂ cell at 170 °C and I = 24 µA/cm²; **(c)** a comparison between the charge curves of LaSrMnO₄ vs. PbF₂ and Pb+PbF₂; **(d)** XRD measurements before and after charge for the LaSrMnO₄/Pb+PbF₂ cell at 200 °C and I = 24 µA/cm².

Table 5-6. Respective lattice parameters of the LaSrMnO₄ active cathode material before and after charge against Pb+PbF₂ anode material at T = 170 °C and I = 24 µA/cm² (10 µA).

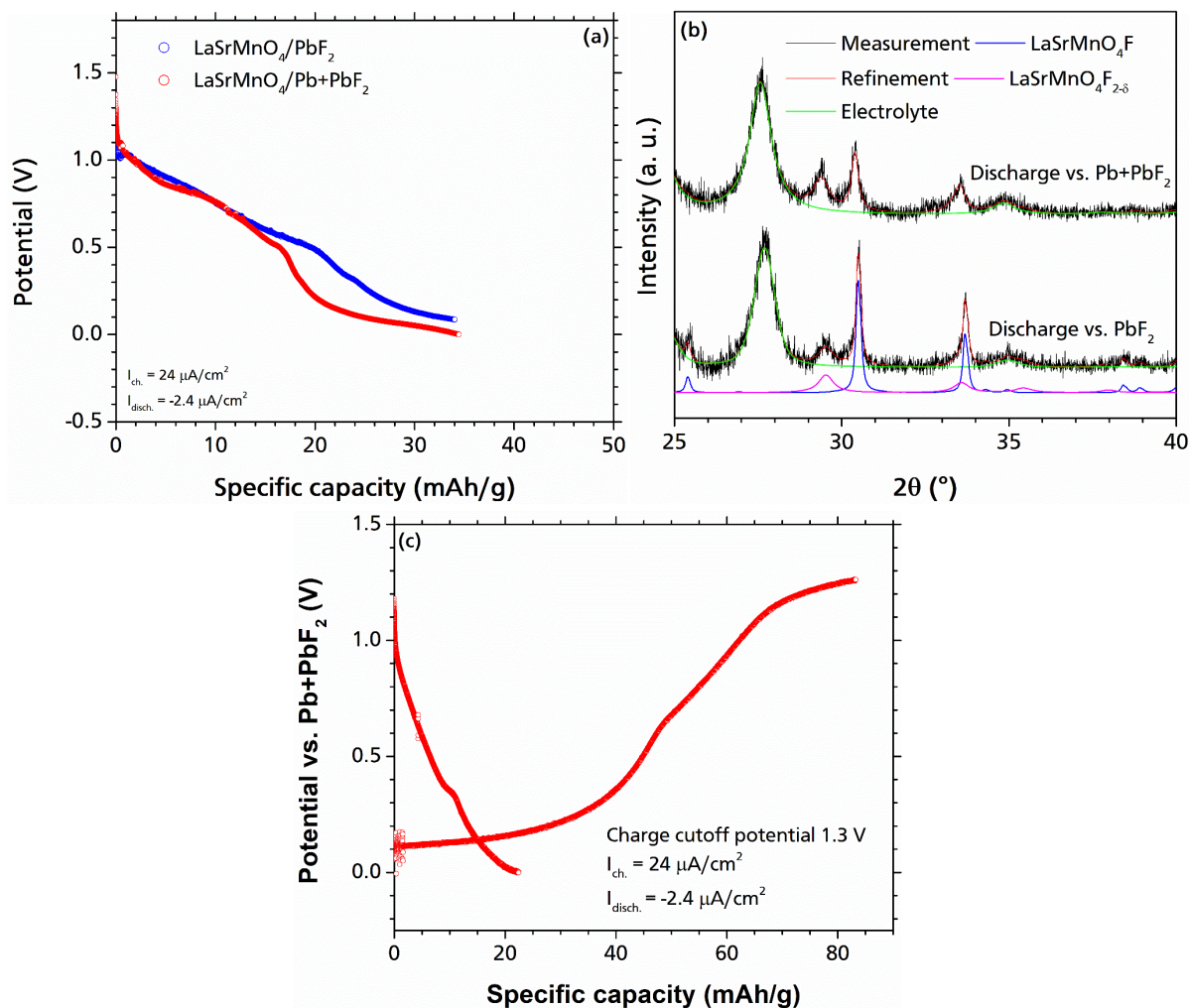| Cutoff Voltage (V)	LaSrMnO₄ ($I4/mmm$)		LaSrMnO₄F ($P4/nmm$)		LaSrMnO₄F$_{2-\delta}$ ($I4/mmm$)	
	a (Å)	c (Å)	a (Å)	c (Å)	a (Å)	c (Å)
Before charge	3.820(1)	12.957(2)				
0.5	3.818(1)	12.967(2)	3.799(1)	13.710(1)		
1			3.770(1)	14.182(2)		
1.3			3.769(1)	14.227(3)	3.779(1)	15.532(9)
2			3.768(1)	14.232(3)	3.774(2)	15.559(19)
2.2 (@ 170 °C)			3.771(1)	14.251(4)	3.777(1)	15.558(14)
2.2 (@ 200 °C)					3.777(1)	15.420(7)
2.4			3.770(1)	14.259(3)	3.776(1)	15.595(12)
3.5			3.769(1)	14.2674(4)	3.766(1)	15.586(14)

Figure 5-9. (a) A comparison between the discharge curves of the LaSrMnO₄ against PbF₂ and Pb+PbF₂ anode materials (I_{ch} = 24 μA/cm², I_{dis} = -2.4 μA/cm² and charge cutoff voltage ~ 2.6 V); (b) respective XRD diffraction pattern of the cathode material after charge against PbF₂ and Pb+PbF₂; (c) cycling curve of the LaSrMnO₄/Pb+PbF₂ cell at charge cutoff potential of 1.3 V. All the measurements are done at an operational temperature of 170 °C.
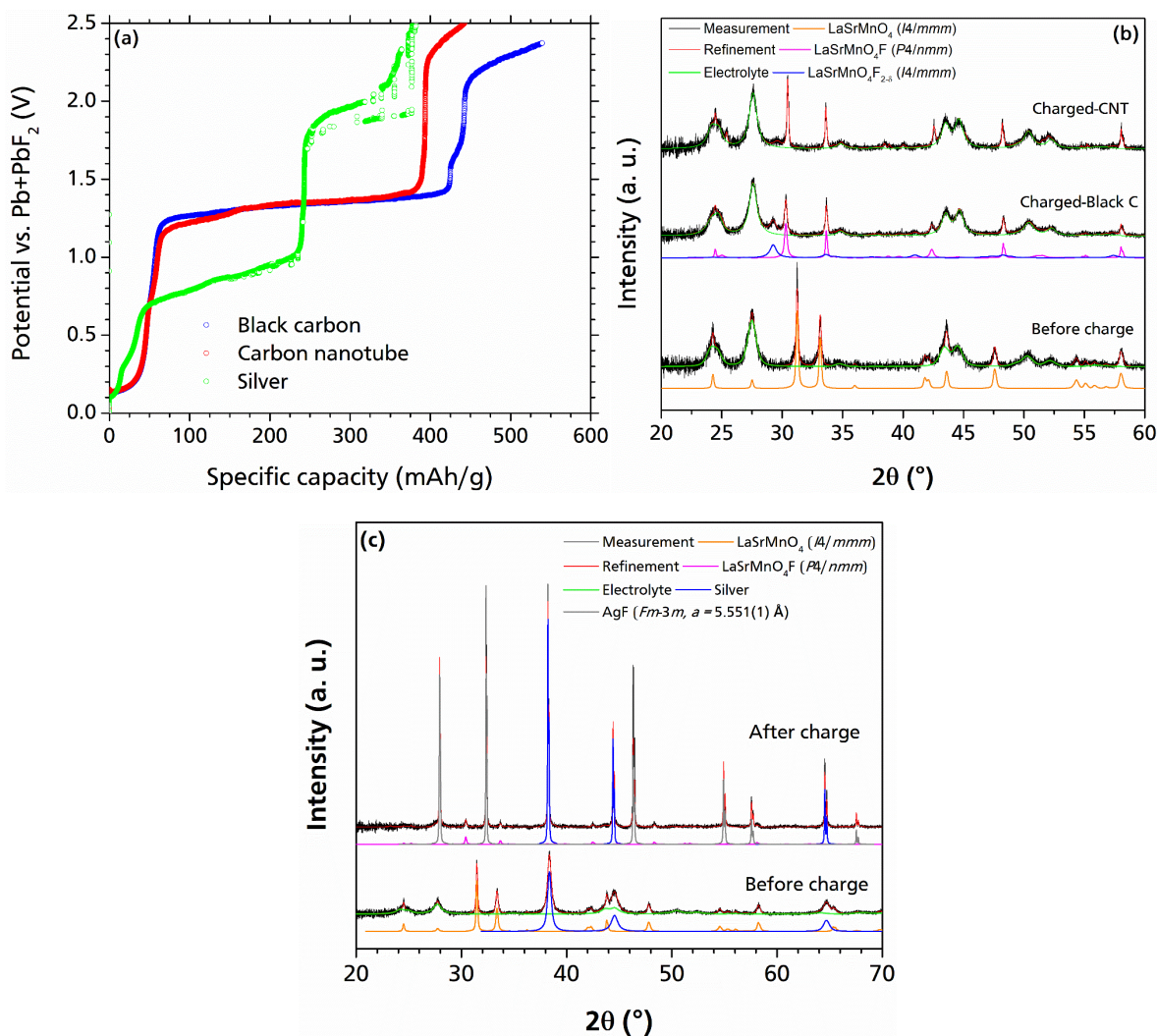
e. Effect of the Electronic Conductor Material

It seems that the reaction (oxidation) of carbon electronic conductor in the LaSrMnO₄ cathode material occurs during the charge step. Therefore, some alternative electronic conductors including carbon nanotubes, silver and indium tin oxide (ITO) have been considered to be used within the cathode composite material. Surprisingly using ITO as the electronic conductor resulted in a huge increase in the internal resistance and therefore, the voltage immediately exceeded to the upper safety limits without observation of any charge curve.

Figure 5-10a depicts the charge curves of LaSrMnO₄ cathode composites with different conductive additives versus Pb+PbF₂. The charge curves of the cathode materials with black carbon and carbon nanotube (CNT) seems very similar at capacities lower than 380 mAh/g. The length of the second charge plateau (which lies between ~ 1.2 – 1.4 V) is slightly higher (in the order of 25 – 30 mAh/g) for the sample with black carbon. For carbon nanotubes, the potential rises more rapid in high capacity region (>380 mAh/g), also the potential increases towards a higher potential range.

The respective XRD results of the cathode composites using different types of carbon as the electronic conductor (**Figure 5-10b**) show formation of LaSrMnO₄F + LaSrMnO₄F₂₋δ after

charging the cell; however, the relative weight fraction of the highly LaSrMnO$_4$F$_{2-\delta}$ fluorinated phase is lower for the cathode material with CNT (20% in comparison to 40% for the sample with carbon black as the electronic conductor) with a less degree of expansion along the c-axis (c = 15.130(40) Å for the cathode material with CNT as compared to 15.595(12) Å for the cathode material with black carbon). Taking into consideration that the charge curve for both cathode composites significantly exceeds the theoretical capacity of LaSrMnO$_4$, the issue of carbon reaction could not be resolved by using CNT instead of black carbon.

Figure 5-10. (a) Charge curves of LaSrMnO$_4$ vs. Pb+PbF$_2$ with different electronic conductor materials (in the cathode material) of black carbon, carbon nanotubes and silver (I_{ch} = 24 µA/cm^2, T = 170 °C, and cutoff voltage of about 2.4 V); (b) respective XRD patterns of the LaSrMnO$_4$ side (cathode side) before and after charge against Pb+PbF$_2$ at the mentioned experimental condition and black carbon/carbon nanotubes as the electronic conductor in the cathode material; (c) XRD pattern of LaSrMnO$_4$ after charge using Ag as the electronic conductor.

The other electronic conductor that has been used to make the cathode composite material was Ag. In **Figure 5-10a** galvanostatic charge curve of LaSrMnO$_4$ (with Ag as the electronic conductor) vs Pb+PbF$_2$ is shown: The charging potential increases right from the start of the charge step up to 0.7 V (roughly corresponds to 40 mAh/g). Then a sloping plateau can be seen up to 1 V ($\sim$ 240 mAh/g) followed by a sharp increase in potential up to 1.8 V. **Figure 5-10c** depicts the XRD pattern of LaSrMnO$_4$ (Ag as the electronic conductor) cathode material versus Pb+PbF$_2$ before and after charge. Before the charge step the electrolyte and the K$_2$NiF$_4$-type structure of LaSrMnO$_4$ together with elemental silver can be easily detected. However, due to

high intensity of Ag and AgF reflections LaSrMnO$_4$(F$_y$) can hardly be seen after charging the cell up to 2.5 V: Two reflections with a lattice parameter c of 14.187(8) Å (space group *I4/mmm*) can be detected. Furthermore, the discharging of the cell was not successful and no discharge curve could be obtained. Thus, one can conclude that silver does not improve the charge/discharge behavior. This originates from fluorination of silver during the charge step which can be considered as a side reaction.

5.3.1.2 LaSrMO$_4$ (M = Fe, Co)/Pb+PbF$_2$ Cells

Investigations on LaSrFeO$_4$ and LaSrCoO$_4$ have been highly influenced by poor electrochemical behavior of these compounds in terms of discharge capacity and energy density. Later in this section, it will be shown that regardless of cutoff conditions the discharge capacity of both of these compounds are very low (as compared to other K$_2$NiF$_4$-type structure compounds including LaSrMnO$_4$). Therefore, as less promising candidates, LaSrFeO$_4$ and LaSrCoO$_4$ were not studied as deep LaSrMnO$_4$ or La$_2$(Co/Ni)O$_{4+d}$.

a. Electrochemical Fluorination (Charging)

Charge curves of LaSrFeO$_4$ and LaSrCoO$_4$ as compared to LaSrMnO$_4$ have been depicted in **Figure 5-11a** which obviously shows a difference between the charging profile of LaSr(Fe/Co)O$_4$ and LaSrMnO$_4$. According to the figure, a relatively flat charge curve can be observed for LaSrFeO$_4$ at a charge potential of ~ 0.85 V within a capacity range of ~ 25 mAh/g. Then the potential increases rapidly with a sharp slope. The same trend can also be seen for LaSrCoO$_4$, however, the charge plateau lies around 1 V which is a bit higher than what was observed for LaSrFeO$_4$ (**Figure 5-11a**). Then the potential increases up to ~ 1.8 V (corresponding to 110 mAh/g), followed by a sharp increase in the potential afterwards (within LaSrCoO$_4$ cell). It is worth noting that Co^{5+} and Fe^{5+} are not common oxidation states of Co and Fe. Therefore, insertion of 2 fluoride ions is less expected within these systems.

A comparison between the charge curves of LaSr(Fe/Co)O$_4$ and LaSrMnO$_4$ (against Pb+PbF$_2$) (**Figure 5-11a**) reveals that the first charge plateau at ~ 0.1 V (up to ~ 50 mAh/g) for LaSrMnO$_4$ cannot be observed for LaSr(Fe/Co)O$_4$. The second charge plateau (starts around 1.2 V) for LaSrMnO$_4$ seems to be almost flat and stable over a long capacity range (**Figure 5-11**). But for LaSr(Fe/Co)O$_4$ such a long charge plateau cannot be seen as the potential rises rapidly after a short charge plateau. This can be a sign of decomposition of the carbon conductive matrix or maybe amorphization of the active cathode material (this seems to be reasonable according to XRD measurements showing the fact that the intensity of the main reflections of the initial active cathode material within the electrode composite have been significantly reduced and the absolute weight fraction of the K$_2$NiF$_4$ phase was reduced after charging (**Figure 5-11b** and **c**)).

Figure 5-11b and **c** show the changes in the XRD diffraction patterns of the cathode material in LaSr(Fe/Co)O$_4$/Pb+PbF$_2$ cells before and after charge up to 3 V (**Table 5-7** summarizes the changes in lattice parameters of the active cathode material and the electrolyte within the cathode composite). After a full charge of the LaSrFeO$_4$ cell (vs. Pb+PbF$_2$) the initial LaSrFeO$_4$ reflections can hardly be detected while a LaSrFeO$_4$(F$_y$) phase with a significant expansion along the c-axis (as compared to the initial LaSrFeO$_4$; from c = 12.713(1) Å before charge to c = 15.625(4) Å after charge) and a small increase along the a-axis (from a = 3.875(1) Å before charge to a = 3.897(1) Å after charge) was observed (**Figure 5-11b**) (*I4/mmm* space group has been used for fitting the XRD diffraction patterns before and after charge). Such a large

increase in the lattice parameter c can be seen for formation of $LaSrMnO_4F_{2-\delta}$ (occupation of both interlayers) only at very high charge capacities as a result of overlapping of the side reactions with the desired electrochemical reaction. Nevertheless, for $LaSrFeO_4$ such a large lattice parameter ($c \sim 15.6$ Å) is obtained at a fairly low charge capacity of 50 mAh/g which is almost 1/3 of the theoretical capacity of $LaSrFeO_4$ for taking two fluoride ions. Therefore, the expansion of the cell cannot be a result of the intercalation of 2 fluoride ions in the vacant interlayers and would imply that both half layers are partially filled with F^- ions only.

The same trend holds true for $LaSrCoO_4$: After a full charge (against $Pb+PbF_2$) the lattice parameter c increases from $c \sim 12.482(2)$ Å before charge to $c \sim 15.494(15)$ Å after charge which is also accompanied by a small increase in the lattice parameter a (from $a \sim 3.803(1)$ Å to $3.917(2)$ Å before and after charge, respectively, see **Table 5-7**). Also the initial $LaSrCoO_4$ cannot be detected. However, the relative phase fraction of the active cathode material phase is much less ($\sim 9.8\%$) than that in the un-charged initial cathode material ($\sim 30\%$). This is also evident from the low intensity reflections of the fluorinated phase (**Figure 5-11c**). Therefore, there is a possibility that the $LaSrCoO_4$ active cathode material at least partially was converted to an amorphous phase or decomposed.
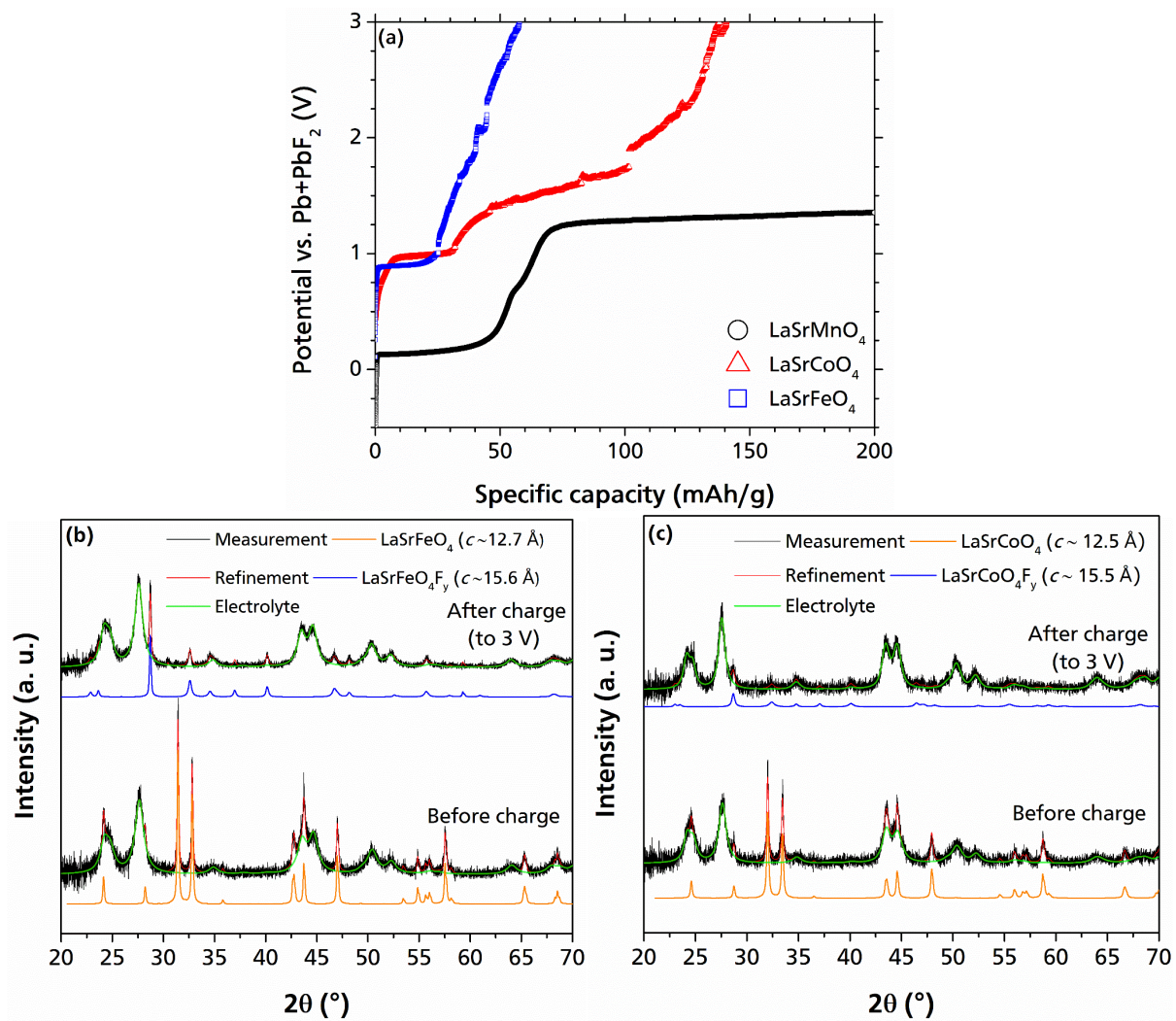
Figure 5-11. (a) Charge plots of LaSrMO₄ (M = Fe, Co) as compared to LaSrMnO₄ at T = 170 °C, I_ch. = 24 μA/cm² (10 μA) and cutoff voltage of ~ 3 V; **(b)** respective XRD measurements and refinements before and after charge of LaSrFeO₄; **(c)** respective XRD measurements and the refinements before and after charge of LaSrCoO₄.

Table 5-7. Respective changes in lattice parameters of LaSrMO₄ (M = Fe, Co) phase and the electrolyte before and after charge (charge conditions are stated in Figure 5-11).

		LaSrMO₄ (*I4/mmm*)		LaSrMO₄F_y (*I4/mmm*)		La₀.₉Ba₀.₁F₂.₉ (Electrolyte) (*P-3_c1*)	
		a (Å)	*c* (Å)	*a* (Å)	*c* (Å)	*a* (Å)	*c* (Å)
LaSrFeO₄	Before charge	3.876(1)	12.713(1)			7.222(1)	7.391(2)
	After charge			3.897(1)	15.625(4)	7.226(1)	7.393(1)
LaSrCoO₄	Before charge	3.803(1)	12.484(2)			7.224(1)	7.399(2)
	After charge			3.914(2)	15.500(14)	7.223(1)	7.393(2)

## b. Discharge Behavior of LaSr(Fe/Co)O₄ vs. Pb+PbF₂

For optimizing the discharge behavior of the LaSr(Fe/Co)O$_4$/Pb+PbF$_2$ electrochemical cells, a suitable charge cutoff potential/capacity needs to be determined. In this respect, the impedance behavior of the LaSr(Fe/Co)O$_4$ cathode materials during a charge step has been investigated by means of galvanostatic electrochemical impedance spectroscopy (EIS). The obtained Nyquist plots have been fitted by the model which is proposed in **Figure 5-12**. The changes of the real resistivity (R$_1$) and α exponent parameter with the charge capacity for both of the cathode materials can also be found in **Figure 5-12a** and **b**.

For LaSrFeO$_4$ (**Figure 5-12a**) the real resistivity seems to be more or less stable in the charge plateau region ($\sim$ 35 mAh/g) which corresponds to a charge potential of $\sim$ 0.9 V. When the cell is further charged, the real resistivity (R$_1$) increases significantly. A possible reason for such a rapid increase in the resistivity of the cell may arise from instability in the conductive carbon within the composite or even decomposition of the initial LaSrFeO$_4$ (at least partially) and formation of amorphous electric insulator phases. The same trend can also be observed for the LaSrCoO$_4$ cathode material (**Figure 5-12b**): Over the charge plateau region (corresponds to $\sim$ 1.0 V and $\sim$ 80 mAh/g) the real resistivity is stable and with further charging the cell the R$_1$ values start increasing, however, with a much lower slope as compared to LaSrFeO$_4$ (note the difference between the orders of magnitude in **Figure 5-12a** and **b**). Respective Nyquist plots for both LaSr(Fe/Co)O$_4$/Pb+PbF$_2$ cell can be found in **Figure 5-12c** and **d**.
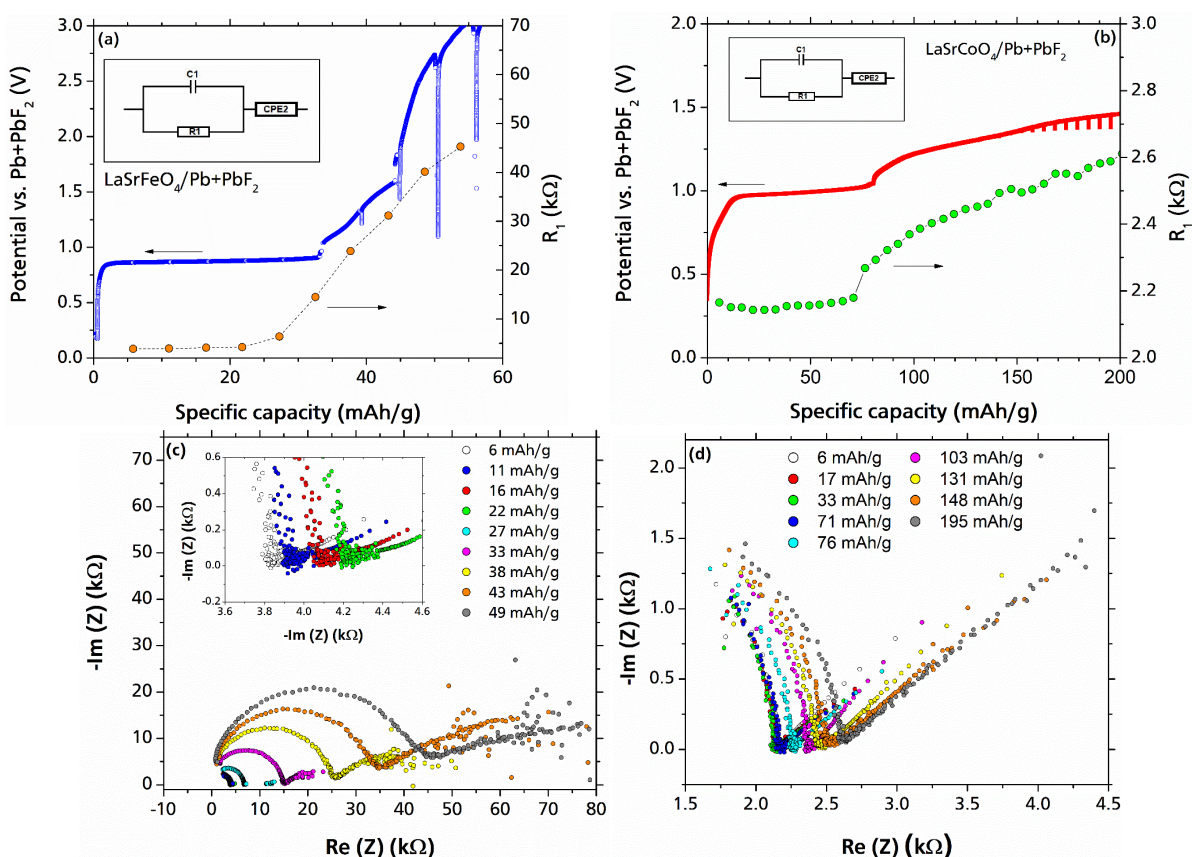
Figure 5-12. Results of the galvanostatic impedance spectroscopy and variations of R₁ values by charging of the electrochemical cells of (a) LaSrFeO₄/Pb+PbF₂ and (b) LaSrCoO₄/Pb+PbF₂. (c) Respective Nyquist plots of LaSrFeO₄/Pb+PbF₂ cell; (d) Respective Nyquist plots of LaSrCoO₄/Pb+PbF₂ cell. The measurements have been performed at 170 °C and a charge current density of 24 μA/cm² (10 μA).

The charge cutoff voltages have been determined according to the region at which the conductivity was stable, which were obtained by the impedance spectroscopy (0.9 V for $LaSrFeO_4/Pb+PbF_2$, and 1.0 V for $LaSrCoO_4/Pb+PbF_2$ cells). Discharge profiles of the $LaSr(Fe/Co)O_4/Pb+PbF_2$ cells can be found in **Figure 5-13**. For the $LaSrFeO_4/Pb+PbF_2$ cell (**Figure 5-13a**) a very sharp discharge plateau can be seen with a total discharge capacity of about 5 mAh/g which seems to be very low as compared to $LaSrMnO_4/Pb+PbF_2$ cell. For the $LaSrCoO_4/Pb+PbF_2$ cell, however, the discharge capacity measured to be higher (as compared to $LaSrFeO_4/Pb+PbF_2$) in the order of $\sim$ 15 mAh/g (**Figure 5-13b**) which is still significantly lower than that for $LaSrMnO_4/Pb+PbF_2$ cell (**Figure 5-9a**). Note that for the $LaSrCoO_4/Pb+PbF_2$ cell the charge cutoff voltage does not play a significant role on improving the discharge capacity as similar discharge capacities were obtained regardless of the cutoff potential (see **Figure 5-13b**) (unlike $La_2(Co/Ni)O_{4+d}$ cells, see section 5.3.2).
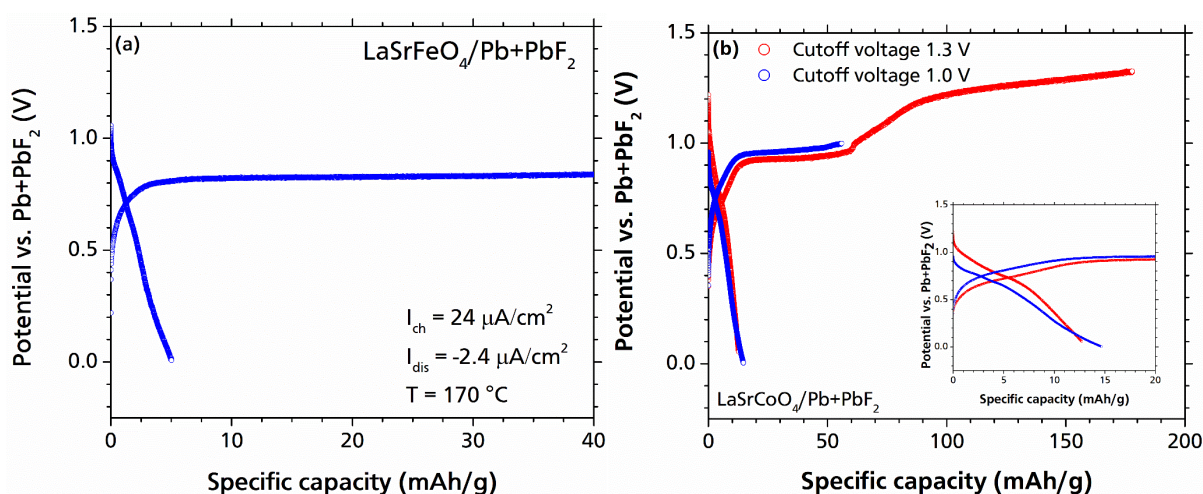
Figure 5-13. (a) Cycle curve of $LaSrFeO_4$ against $Pb+PbF_2$; (b) cycle curves of $LaSrCoO_4/Pb+PbF_2$ at cutoff charge capacities of 1.0 V and 1.3 V. For all the measurements, I_{ch} = 24 µA/cm^2, I_{dis} = -2.4 µA/cm^2, and T = 170 °C.

5.3.2 La₂(Co/Ni)O₄₊d Cathode Materials

La_2MO_4 (M = transition metals such as Cu, Ni, Co, Fe, etc.) show a variety of interesting superconductivity, magnetic and electrical properties [103]. These Ruddlesden-Popper-type compounds have mainly a distorted tetragonal K_2NiF_4 structure [104]. The structural distortions result in a symmetry lowering of the structures. For example La_2CoO_4 have an orthorhombic structure (*Abma* (No. 64 [105]) space group [98, 106]), and La_2NiO_4 structure can be fitted by tetragonal *Fmmm* space group [74, 107] which is a subgroup of *I4/mmm* super symmetry [105]. In fact, in all La_2MO_4 compounds the ideal M-O distances are too long to match perfectly the lattice parameters of the ideal rocksalt La-O layers. This interlayer lattice mismatch leads to a distortion of the ideal tetragonal structure [104]. Also, the small size of La is compensated by tilting of the octahedral, which lowers the coordination number of La. *Fmmm* is not allowing for such tilting, but stage ordering for La_2MO_{4+d} makes the symmetry appear to be higher.

In this section the possibility of the electrochemical fluorination/de-fluorination of La_2CoO_{4+d} and La_2NiO_{4+d} compounds will be discussed. To the best of our knowledge there is no report on chemical fluorination of $La_2CoO_{4.16}$ and $La_2NiO_{4.13}$ compounds. Therefore, the attempts on the chemical fluorination of these compounds will be discussed in order to have a reference to compare the electrochemical fluorination results.

5.3.2.1 La$_2$CoO$_{4+d}$ Cathode Composite Material

a. Chemical Fluorination of La$_2$CoO$_{4+d}$

Three strategies were used in order to chemically fluorinate La$_2$CoO$_{4+d}$. In this section the strategies and the respective results will be briefly described.

The first strategy relies on the usage of F$_2$ gas as a fluorinating agent which is a widely used method for fluorinating a variety of oxide compounds [48, 78, 100, 108]. The advantage of this method is the fact that pure fluorinated phase can be made, however, safety issues are the most important drawback for this chemical fluorination route. Fluorination of the La$_2$CoO$_{4+d}$ compound has been performed under fluorine gas (5% − 10% F$_2$ in argon) at a temperature range of 200 – 250 °C for different reaction time up to 48 h. Such a fluorination process resulted in either no change in the structure of La$_2$CoO$_{4+d}$ (at lower reaction temperatures for shorter time) or a full decomposition of the oxide and formation of an amorphous phase (at higher reaction temperature, higher concentration of fluorine gas or longer reaction time) [86].

The other fluorination method is based on using a fluorinating agent such as (less reactive) metal fluorides (including copper difluoride (CuF$_2$), silver difluoride (AgF$_2$)/silver fluoride (AgF) [87, 109]) or polyvinylidene fluoride (PVDF: C$_2$H$_2$F$_2$) [30, 110, 111]. In this respect, the fluorinating agents including CuF$_2$, AgF$_2$, AgF and PVDF were mixed with La$_2$CoO$_{4+d}$ precursor followed by heating at various temperatures (between 200 °C – 400 °C) under an inert Ar atmosphere; however, in most cases unreacted La$_2$CoO$_{4+d}$ and some intermediate fluorinated La$_2$CoO$_{4+d}$(F$_y$) phases were obtained.

The best results were obtained by using AgF as the fluorinating agent, for which no unreacted La$_2$CoO$_{4+d}$ was left (**Figure 5-14b**). Note that in order to obtain this highly fluorinated phase AgF was used in excess (almost twice higher than the stoichiometric ratio for formation of La$_2$CoO$_{4+d}$F$_2$ according to the following reaction: La$_2$CoO$_{4+d}$ + 2AgF → La$_2$CoO$_{4+d}$F$_2$ + 2Ag). Therefore, some silver rich phases (presumably an AgF-Ag$_2$O related phase) can still be found after the fluorination (**Figure 5-14b**).

Table 5-8 summarizes the lattice parameters (structural parameters can be found in **Table 5-9**) of the obtained phase (La$_2$CoO$_{4+d}$(F$_y$)) after chemical fluorination by AgF. The XRD pattern can be fitted by a monoclinic structure using a $C2/m$ space group, which can be transformed to non-standard setting $A12/m1$ for easier comparability with the initial structure. In addition to introduced monoclinic distortions, the La$_2$CoO$_{4+d}$ unit cell expands along the c-axis up to ~ 15.08 Å (**Table 5-8**) after the fluorination, which is in a well agreement with the observed structural changes after fluorination of the LaSrMnO$_4$.

Figure 5-15 schematically shows the structure of La$_2$CoO$_{4+d}$ before and after fluorine insertion into the vacant interlayers assuming that both of the interlayers are fully occupied only by F$^-$ ions which is not necessarily true since the exact taken fluoride ions cannot be detected by the XRD measurement. Also, it is not clear whether the oxygen ions partially occupy the anion site or not (i.e. one cannot claim that the product has a composition of La$_2$CoO$_4$F$_y$ or La$_2$CoO$_{4+d}$F$_y$). Iodometric titration also cannot be a suitable analysis to find out the oxidation state of Co in this case, due to coexistence of the fluorinated phase with silver rich fluoride/oxides phases. Electron diffraction analysis based on TEM (ADT) can be a suitable method to provide more information about the occupancy of the interlayers by fluoride ions.

Furthermore, since there is no indication of phases with intermediate lattice parameters ($\sim$ 14.0 Å, corresponding to occupation of one interlayer in staged fluorination of LaSrMnO$_4$), it is also not possible to claim that the fluorine insertion has been performed in a layer-wise ordering (the scenario that has been reported for LaSrMnO$_4$ [48]). This may arise from the fact that in La$_2$CoO$_{4.16}$ the anion sites are already partially filled by the oxygen ions.
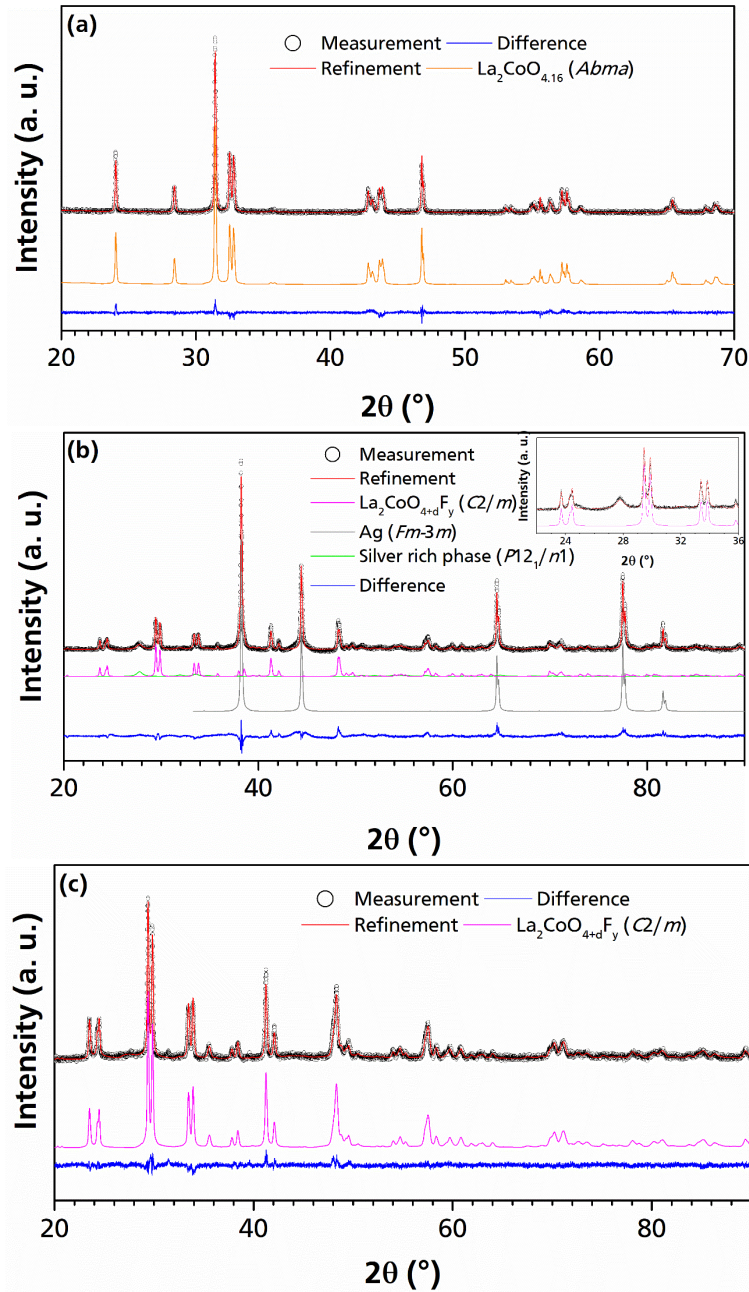
Figure 5-14. XRD patterns of **(a)** pure La$_2$CoO$_{4+d}$; **(b)** after chemical fluorination of La$_2$CoO$_{4+d}$ with AgF (excess of silver fluoride was used) at a temperature of 300 °C for a duration of 48 h under flow rate of Ar (0.3 SLM); **(c)** after chemical fluorination of La$_2$CoO$_{4+d}$ by CuF$_2$ (reactants were kept in two separate crucibles) at T = 270 °C for 72 h under flow of O$_2$ (0.1 SLM).
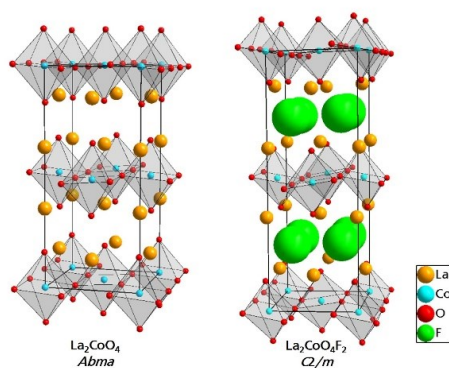
Figure 5-15. Schematic plot of orthorhombic La₂CoO₄₊d structure (left) and monoclinic (fluorinated) La₂CoO₄F₂ structure (right).

Table 5-8. Lattice parameters of precursor La₂CoO₄₊d (before chemical fluorination) and fluorinated La₂CoO₄₊dFy phase using AgF (mixed with the La₂CoO₄₊d) and CuF₂ (in separate crucibles - unmixed) as the fluorinating agents. The structure of La₂CoO₄₊dFy can be fitted by the standard setting of space group no. 12, *C*2/*m*, however, for easier comparability of axis lengths, transformed lattice parameters to a non-standard setting *A*12/*m*1 have been used.

	La₂CoO₄₊d (*Abma*)			La₂CoO₄₊dFy (*A*12/*m*1)			
	a (Å)	*b* (Å)	*c* (Å)	*a* (Å)	*b* (Å)	*c* (Å)	*β* (°)
Precursor	5.5245(1)	5.4763(1)	12.6131(3)				
Fluorination by AgF				5.3135(2)	5.3820(2)	15.0871(6)	91.184(3)
Fluorination by CuF₂ (at separate crucibles)				5.3014(2)	5.3697(2)	15.1930(6)	91.243(2)

Table 5-9. Structural parameters of chemically fluorinated La₂CoO₄₊dFy phase (lattice parameters can be found in Table 5-8) using AgF or CuF₂ (in a separate crucible) as the fluorinating agent. The occupancies of fluorine are approximated based on estimation of cobalt oxidation state by iodometric titration method on the pure La₂CoO₄₊dFy, assuming that the interlayers are only filled by fluorine (it will be discussed later in this section).

Phase	Atom	Wyckoff site	x	y	z	Occupancy
La₂CoO₄₊dFy (*C*2/*m*) Fluorination by AgF	La1	4i	0.6351(3)	0	0.982(2)	1
	La1	4i	0.8596(7)	0	0.507(2)	1
	Co1	2a	0	0	0	1
	Co2	2a	0	1/2	0	1
	O1	8j	0.499(7)	0.75(1)	0.25(1)	1
	O2a	4i	0.874(2)	0	0.99(1)	1
	O2b	4i	0.680(2)	0	0.48(1)	1
	F	8j	0.25(1)	0.24(1)	0.25(1)	0.25
La₂CoO₄₊dFy (*C*2/*m*) Fluorination by CuF₂ (at separate crucibles)	La1	4i	0.6313(3)	0	0.989(1)	1
	La1	4i	0.8572(3)	0	0.507(1)	1
	Co1	2a	0	0	0	1
	Co2	2a	0	1/2	1/2	1
	O1	8j	0.511(2)	0.763(8)	0.235(9)	1
	O2a	4i	0.880(3)	0	0.98(1)	1
	O2b	4i	0.633(3)	0	0.52(1)	1
	F	8j	0.249(5)	0.249(4)	0.25(3)	0.25

In the third fluorination method (according to literature [112]) the metal fluoride (in the current case CuF_2) is not directly mixed with the oxide, instead, La_2CoO_{4+d} and CuF_2 are heated in separate crucibles and the fluorination is carried out under a flow of oxygen (**Figure 5-16** shows the schematic plot of the fluorination process). The great advantage of this method lies within the fact that a pure desired fluorinated product can be obtained (without any traces of the − metal fluoride − fluorinating agent or the reduced respective metal).

Figure 5-17 depicts the XRD measurements after such a fluorination process (CuF_2 was used as the fluorinating agent) at different temperature. It was found that at lower temperature of 220 °C the pattern consists of some unreacted La_2CoO_{4+d} coexist with a relative small amount of fluorinated phase ($La_2CoO_{4+d}F_y$) and two other orthorhombic (intermediate fluorinated) phases with larger c parameters (first phase: $a = 5.611(1)$ Å, $b = 5.424(1)$ Å, $c = 12.641(2)$ Å and second phase: $a = 5.703(4)$ Å, $b = 5.402(3)$ Å, $c = 12.883(8)$ Å) as compared to initial La_2CoO_{4+d}. By increasing the temperature to 250 °C, the amount of $La_2CoO_{4+d}F_y$ increases, however, still some unreacted La_2CoO_{4+d} phase can be detected (**Figure 5-17**). The optimum fluorination temperature seemed to be 270 °C at which almost a pure fluorinated phase could be obtained. The XRD pattern and detailed refinement of the sample that was fluorinated at 270 °C (CuF_2 as the fluorinating agent and the process carried out at two separate crucibles) can be found in **Figure 5-14c.** The lattice parameter of the obtained phase is also provided in **Table 5-8**. It is worth noting that the lattice parameters of the $La_2CoO_{4+d}F_y$ phase obtained from this method has a higher degree of expansion along the c-axis ($c = 15.0871(6)$ Å by AgF compared to $c = 15.1980(6)$ Å by CuF_2 in separated crucibles, according to **Table 5-8**). Fluorination by CuF_2 is also accompanied by a higher degree of monoclinic distortion (slightly larger β value). Further increase in the fluorination temperature up to 300 °C resulted in a partial decomposition of the La_2CoO_{4+d} phase with formation of LaF_3 (marked with * in **Figure 5-17**).

The oxidation state of Co (after chemical fluorination) has been determined by ioiodometric titration method to be around + 2.5 which shows an uptake of ~ 0.5 fluoride ions, when assuming that only the fluoride ions occupied the interlayers (oxygen has not occupied the layers). For a more accurate estimation on the occupancy of the anion interlayers, more precise measurement techniques including TEM, ADT and XAS are required. In the next section it will be shown that during an electrochemical fluorination of La_2CoO_{4+d} the lattice parameters of the fluorinated phase, at the charge cutoff capacity corresponding to insertion of ~ 0.5 fluoride ions, are very similar to what is reported here for the chemical fluorination process that has been discussed. Taken into consideration that the fluorination with CuF_2 (as described above) resulted in a higher c parameter as compared to the fluorination by AgF, the occupancy of fluorine within the anion layers can be different in the obtained fluorinated phases (lower fluorine occupancy may result in smaller c parameter (fluorinated by AgF)). Later it will be seen that in an electrochemical fluorination the lattice parameter c of the fluorinated $La_2CoO_{4+d}F_y$ phase increases systematically by charge capacity which can be an indication for different occupancies of fluorine. That shows the flexibility of the electrochemical fluorination method and the possibility to obtain a variety of Co oxidation states in an electrochemical fluorination route.
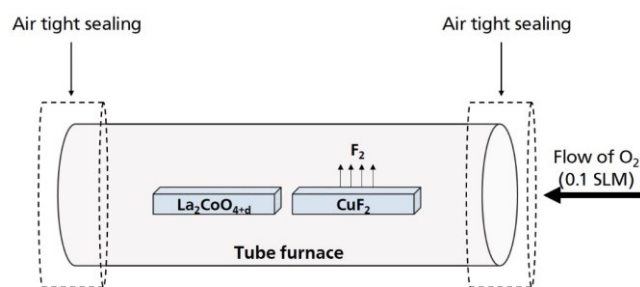
Figure 5-16. Schematic figure of the setup that has been used for fluorination of La₂CoO₄₊d with copper fluoride in two separate boat-shape crucibles.
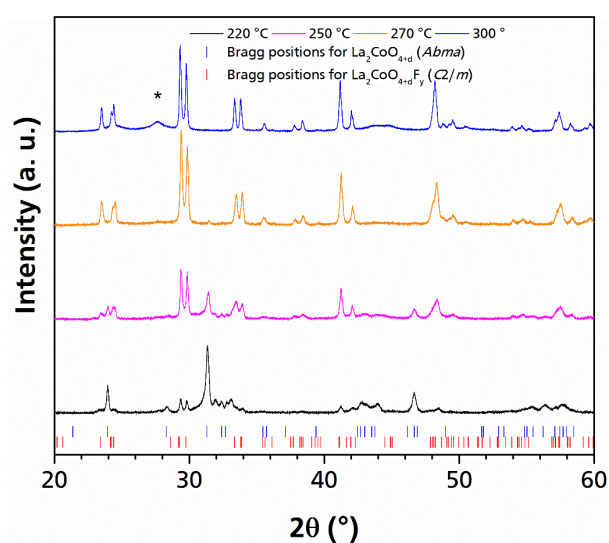

Figure 5-17. XRD patterns of the samples after chemical fluorination with CuF₂ (in a separate crucible according to Figure 5-16) as the fluorinating agent under flow of O₂ at different temperatures for a duration of 72 h.

b. Electrochemical Fluorination: Step by Step Charging

In this section, the structural changes of the La₂CoO₄₊d active cathode material during an electrochemical fluorination (charging) process will be discussed. Then the XRD results will be compared to the results that have been obtained by chemical fluorination. In this respect, La₂CoO₄₊d active cathode material has been charged against a Pb+PbF₂ anode composite material.

Figure 5-18 depicts a typical electrochemical charge plot of the La₂CoO₄₊d/Pb+PbF₂ cell. From the figure different charging regions can be observed which will be discussed later in this section with respect to the structural changes during charging.

The XRD pattern of the respective cathode material that has been charged up to 3.5 V (against Pb+PbF₂) can be observed in **Figure 5-19a** which shows no traces of the initial La₂CoO₄₊d active cathode material. The lattice parameters of the active cathode material before and after the electrochemical charging are listed in **Table 5-10**. The structural changes over the electrochemical fluorination route (**Figure 5-19b** and **Table 5-10**) are in the same direction as compared to the chemical method: The cell expands along the c-axis (from $c \sim 12.6$ Å to ~ 15.3 Å), together with a reduction in a and b parameters and a similar monoclinic distortion can be detected (the product phase after the electrochemical charge can be indexed by a monoclinic $C2/m$ space group (or $A12/m1$ non-standard setting)). However, the lattice

parameter c is larger for the electrochemically fluorinated sample which can be a sign of more intercalated F⁻ ions into the vacant interlayers (higher oxidation state of Co).
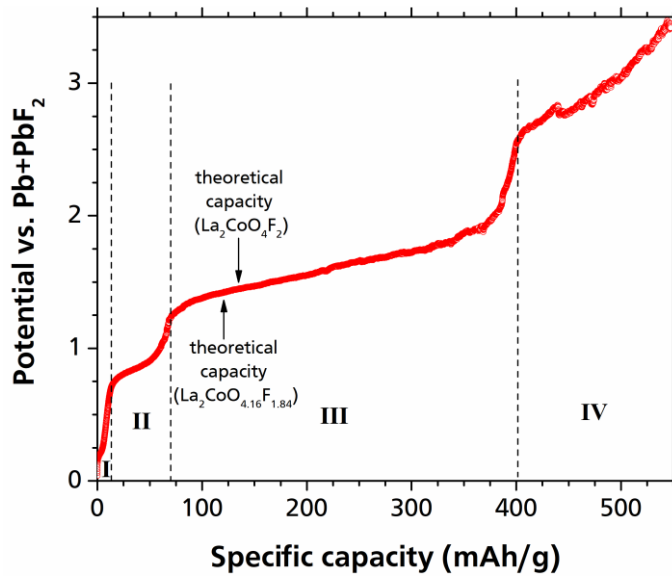
Figure 5-18. A typical charge curve for La₂Co₄₊d/Pb+PbF₂ electrochemical cell which was charged up to 3.5 V at T = 170 °C, and I = 24 µA/cm² (10 µA).
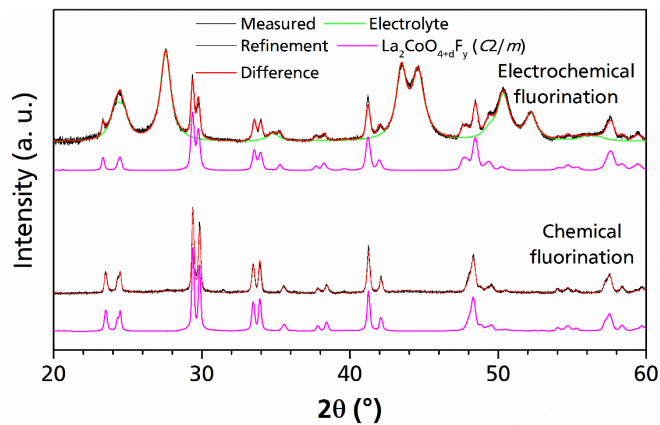

Figure 5-19. A comparison between the XRD patterns of La₂CoO₄₊d(Fy) obtained from the chemical fluorination (as described in Figure 5-16) and the electrochemical fluorination (charging). La₂CoO₄₊d/Pb+PbF₂ was charged to 3.5 V at 170 °C at a current density of 24 µA/cm².

Table 5-10. Lattice parameters of the active cathode material before/after electrochemical charge up to a cutoff voltage of 3.5 V at 170 °C and current density of 24 μA/cm² in comparison with the chemical fluorination of La₂CoO₄₊d with CuF₂ in two separate crucibles. Note that the lattice parameters of the active material after charge (the monoclinic phase) has been transformed (from standard *C*2/*m* space group) to non-standard setting of *A*12/*m*1 for easier comparability.

	La₂CoO₄₊d Orthorhombic (*Abma*)				La₂CoO₄₊dFy Monoclinic (*A*12/*m*1)				
	a (Å)	b (Å)	c (Å)	V (Å³)	a (Å)	b (Å)	c (Å)	β (Å)	V(Å³)
Before charge (cathode composite)	5.524(1)	5.476(1)	12.615(2)	381.64(9)					
After charge up to 3.5 V					5.289(1)	5.355(1)	15.295(2)	91.09(1)	433.19(4)
After chemical fluorination					5.301(1)	5.369(1)	15.193(1)	91.24(1)	432.40(3)

In order to understand the structural changes of the cathode material during the charging of the La₂CoO₄₊d/Pb+PbF₂ cell, several identical pellets were made and charged up to various cutoff capacities. The structural changes at different charge cutoff capacities as well as the respective electrochemical charge plots can be found in **Figure 5-20**. Based on the XRD measurements, the composition and the lattice parameters of the active cathode material for each cutoff capacity are also provided in **Figure 5-20**.

The charge plot of the La₂CoO₄₊d/Pb+PbF₂ electrochemical cell shows 4 distinct regions (**Figure 5-18**). At the first region (I), which lies within the low capacity (up to ~ 15 mAh/g) range, a very small plateau (around 0.2 V) can be seen followed by a sharp increase in potential up to ca. 0.7 V. This region seems to be arising from some unknown low potential side reaction(s) which fortunately does not impair the conductivity of the cell. The reason for such a conclusion about the region (I) is based on the fact that there is no significant structural change in the cathode material at the end of this region (according to **Figure 5-20a** and **b** there is no structural change up to ~ 0.7 V (corresponds to ~13 mAh/g)). Moreover, later in section (5.4.2) it will be shown that this region can only be observed at the first cycle and then disappears in further cycles.

The charge curve of the La₂CoO₄₊d/Pb+PbF₂ electrochemical cell at the second region (II) consists of a plateau located within a potential range approximately between 0.7 V – 1.0 V. This potential range corresponds to specific capacities between 15 mAh/g – 65 mAh/g. The potential then sharply rises up to ca. 1.25 V at ~ 75 mAh/g. The first traces of formation of fluorinated La₂CoO₄₊dFy phase can be observed within region (II) at around 30 mAh/g. During charging of the cell the lattice parameter c of both the La₂CoO₄₊d precursor (left overs) and the La₂CoO₄₊dFy product slightly increases according to **Table 5-11** (in the order of ~ 0.2 Å for both precursor/product phases), highlighting the fact that for both phases the occupancy of the interlayers may change by charging.
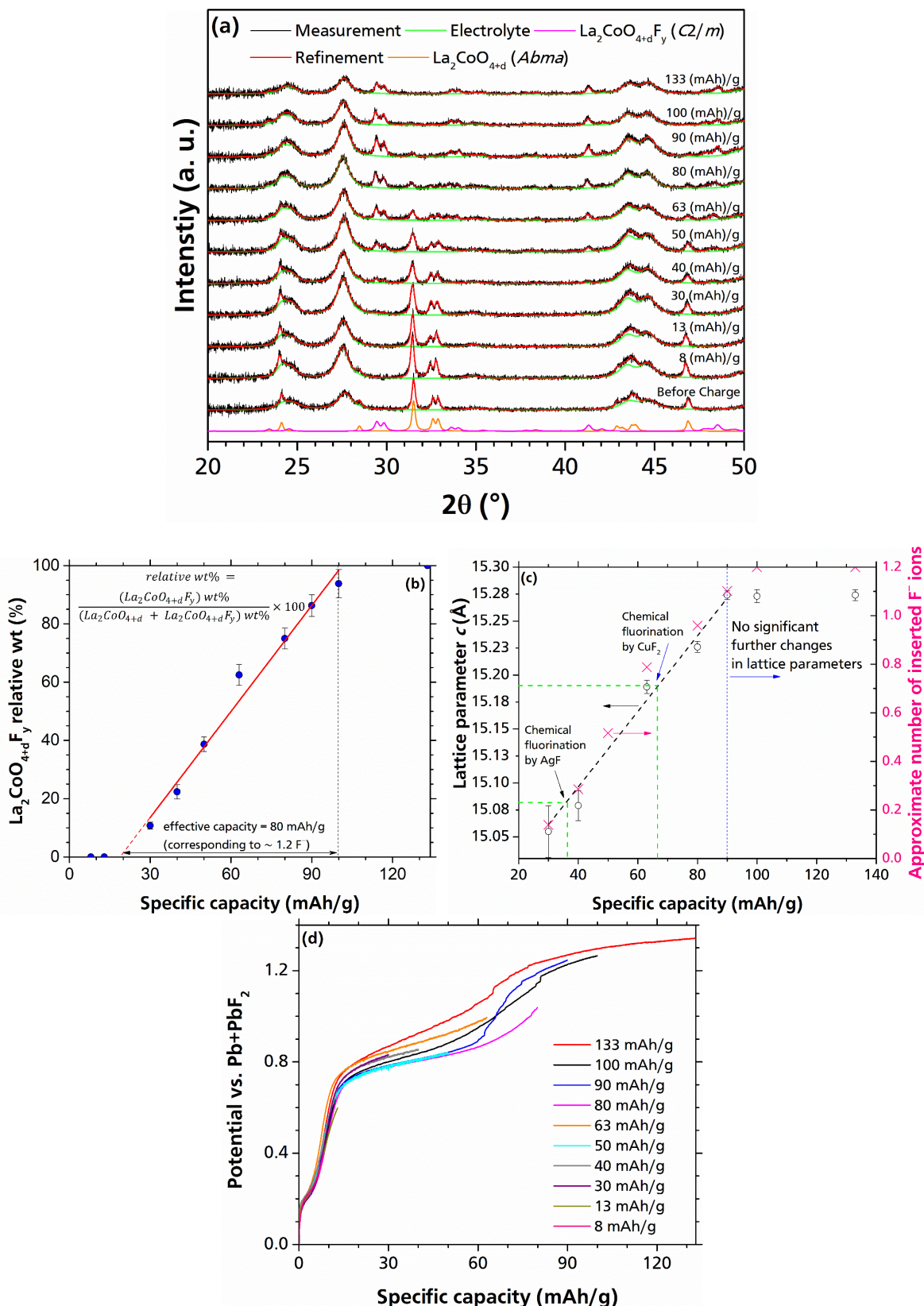
Figure 5-20. (a) XRD patterns of the cathode material after charge up to various cutoff capacities; **(b)** the relative weight fraction of the electrochemically fluorinated La₂CoO₄₊dF_y phase at different cutoff capacitates (according to the XRD measurements and the Rietveld method); **(c)** variations of *c* parameter and approximated intercalated fluoride ions with charge capacity (note that the dashed line shows linear fitting of the lattice parameters and for fitting the data series, 50 mAh/g has not been considered); **(d)** respective charge curves at different cutoff capacities. All the electrochemical charging processes were performed at T = 170 °C and I = 24 μA/cm² (10 μA).

Table 5-11. Lattice parameters and the relative phase fractions of the active cathode material (La$_2$CoO$_{4+d}$) after charging up to various cutoff capacities at T = 170 °C and I = 24 μA/cm^2 (= 10 μA). Note that the lattice parameters of La$_2$CoO$_{4+d}$F$_y$ (the monoclinic phase) has been transformed (from standard $C2/m$ space group) to non-standard setting of $A12/m1$ for the sake of easier comparability.

Cutoff Capacity (mAh/g)	La$_2$CoO$_{4+d}$ Orthorhombic ($Abma$)				La$_2$CoO$_{4+d}$F$_y$ Monoclinic ($A12/m1$)				
	a (Å)	b (Å)	c (Å)	Relative wt%	a (Å)	b (Å)	c (Å)	β (°)	Relative wt%
8	5.529(7)	5.474(1)	12.560(2)	100	-	-	-	-	0
13	5.532(1)	5.473(1)	12.563(3)	100	-	-	-	-	0
30	5.520(1)	5.462(1)	12.574(3)	89.24(362)	5.310(9)	5.418(8)	15.055(24)	91.15(12)	10.76(119)
40	5.524(2)	5.462(2)	12.598(5)	77.65(448)	5.321(1)	5.380(4)	15.079(14)	91.16(6)	22.35(245)
50	5.522(2)	5.456(2)	12.610(5)	61.33(324)	5.315(3)	5.386(2)	15.049(8)	91.21(3)	38.67(254)
63	5.524(2)	5.487(2)	12.623(7)	37.55(274)	5.306(2)	5.368(2)	15.189(6)	91.16(2)	62.45(363)
80	5.527(3)	5.4497(3)	12.649(8)	25.015(151)	5.292(2)	5.363(2)	15.226(5)	91.20(2)	74.98(358)
90	5.5328(4)	5.443(4)	12.694(12)	13.72(104)	5.288(2)	5.357(1)	15.274(4)	91.17(2)	86.28(372)
100	5.470(13)	5.488(13)	12.810(25)	6.17(98)	5.287(2)	5.350(2)	15.273(6)	91.19(2)	93.83(486)
133	-	-	-	0	5.291(2)	5.351(2)	15.274(5)	91.11(2)	100

Later in section (5.4.1) it will be shown (by means of impedance spectroscopy) that as long as the charge cutoff capacity is kept within region (II) –up to roughly 65 mAh/g– the impedance of the cell does not significantly increase. This may arise from the relative stability of carbon within this region. Therefore, it is assumed that the plateau in region (II) corresponds mainly to the desired electrochemical reaction. This can be a sign of preserving the conductive carbon as a result of controlling carbon oxidation side reaction that seems to be a problem for cycling of LaSrMnO$_4$. There is a sharp increase in the potential at the end of region (II) which most likely arises from the fact that the Co^{2+}/Co^{3+} redox couple is over and subsequently side reactions occur more intensely.

The electrochemical charge curve of the La$_2$CoO$_{4+d}$/Pb+PbF$_2$ cell shows a relatively long plateau between 1.25 V – 1.8 V at region (III) followed by a sharp increase in potential up to 2.5 V. The respective capacity range of the plateau in the region (III) (between 75 mAh/g to 380 mAh/g) is significantly higher than the theoretical capacity of La$_2$CoO$_{4+d}$. Moreover, the result of the step by step charging of the cell reveals that the active cathode material is almost fully transformed to La$_2$CoO$_{4+d}$F$_y$ at around 100 mAh/g without any further significant change in the structure (**Figure 5-20a** and **c**). Thus, the desired electrochemical reaction is ongoing only up to 100 mAh/g and the rest of the plateau after 100 mAh/g in region (III) is arising only from the side reactions which lead to significant increase in the impedance of the cell). Likewise, the side reactions are also going on at the region (IV), however, the potential rises sharper in this region (**Figure 5-18**).

Figure 5-20b and **Table 5-11** show that weight fraction of the fluorinated La$_2$CoO$_{4+d}$F$_y$ phase increases linearly with capacity. Then based on the intersection of the fitted line with the x-axis (see again **Figure 5-20b**) the effective charge capacity can be calculated to be ∼ 80 mAh/g. This capacity corresponds to an intake of almost 1.2 F$^-$ ions per formula unit. Nevertheless, it may be difficult to reversibly intercalate/de-intercalate all of 1.2 F$^-$ ions since the side

reaction(s) are overlapping with the electrochemical fluorination of La_2CoO_{4+d}, especially after $\sim$ 70mAh/g.

The changes of the lattice parameter c of the high fluorine content phase have been provided in **Figure 5-20**, showing a linear trend with charge cutoff capacity up to 90 mAh/g (in order to fit the data, the lattice parameter for the charge cutoff capacity of 50 mAh/g has not been considered since the data was not following the linear trend). However, at capacities higher than 90 mAh/g the c parameter does not significantly change. Moreover, as it is discussed in the previous section, over chemical fluorination of the La_2CoO_{4+d} (by CuF_2 in a separate crucible) roughly 0.5 fluoride ions (assuming that no oxygen has occupied the anion vacant layers) are intercalated in the interlayers (corresponding to Co oxidation state of +2.5) resulting in an increase in lattice parameter c up to 15.193(1) Å. According to the linear fit in **Figure 5-20c,** the obtained c parameter of $\sim$ 15.19 Å corresponds to intercalation of $\sim$ 0.7 fluoride ions which is close to what is calculated based on the estimated oxidation state of Co after fluorination obtained from titration method (0.5). This shows the flexibility of the electrochemical fluorination method and the possibility to obtain different oxidation states of Co by regulating the cutoff criteria.

c. Structural Reversibility: De-Fluorination (Discharging)

Figure 5-21a depicts typical cycling curves of the $La_2CoO_{4+d}/Pb+PbF_2$ cell at different cutoff capacities of 65 mAh/g, 75 mAh/g and 133 mAh/g, which highlights the vital role of the cutoff criteria (capacity/potential). It is also worth noting that the impedance of the cell is quite stable up to a capacity range of $\sim$ 65 mAh/g which lies before the sharp potential rise within region (II) (it will be further discussed in section (5.4.1)). Therefore, the highest discharge capacity ($\sim$ 32 mAh/g) is obtained at a charge cutoff capacity of 65 mAh/g. The respective discharge plateau is a sloping plateau corresponding to de-intercalation of ca. 0.48 ions. Note that when the cell is charged to 65 mAh/g, the active charge capacity can be estimated to be around 45 mAh/g (corresponds to intercalation of $\sim$ 0.67 fluoride ions) since the electrochemical fluorination of $La_2CoO_{4.16}$ does not start before $\sim$ 20 mAh/g (**Figure 5-20b**) due to unknown low potential side reactions. This low Coulombic efficiency within the first cycle, once more implies the occurrence of the side reactions which may at least be partially attributed to the carbon oxidation.

The structural changes of the active cathode material after the discharging is provided in **Figure 5-21c** (respective lattice parameters and relative phase fractions of the active cathode material can also be found in **Table 5-12**). The XRD measurements reveal that after discharging a cell that has been originally charged up to 65 mAh/g, there is no trace of highly fluorinated monoclinic $La_2CoO_{4+d}F_y$ phase (see **Figure 5-21c**). However, two phases can be detected which have been labeled as Phase 1 (with similar lattice parameters compared to La_2CoO_{4+d} in the initial cathode composite (see **Table 5-12**)) and Phase 2 with an orthorhombic structure with a larger lattice parameter c in the order of ~13.25 Å. Therefore, it can be concluded that the discharge step resulted in a good degree of structural reversibility of La_2CoO_{4+d}. Nevertheless, the proportion of the Phase 1 (which is closer to the precursor) can be even increased up to 70% upon discharging towards negative potentials (forced discharging (**Figure 5-21b**)) while the lattice parameter c of the phase 2 becomes even closer (up to $\sim$ 12.86 Å) to initial La_2CoO_{4+d}. From this a high degree of structural reversibility of La_2CoO_{4+d} can be concluded.

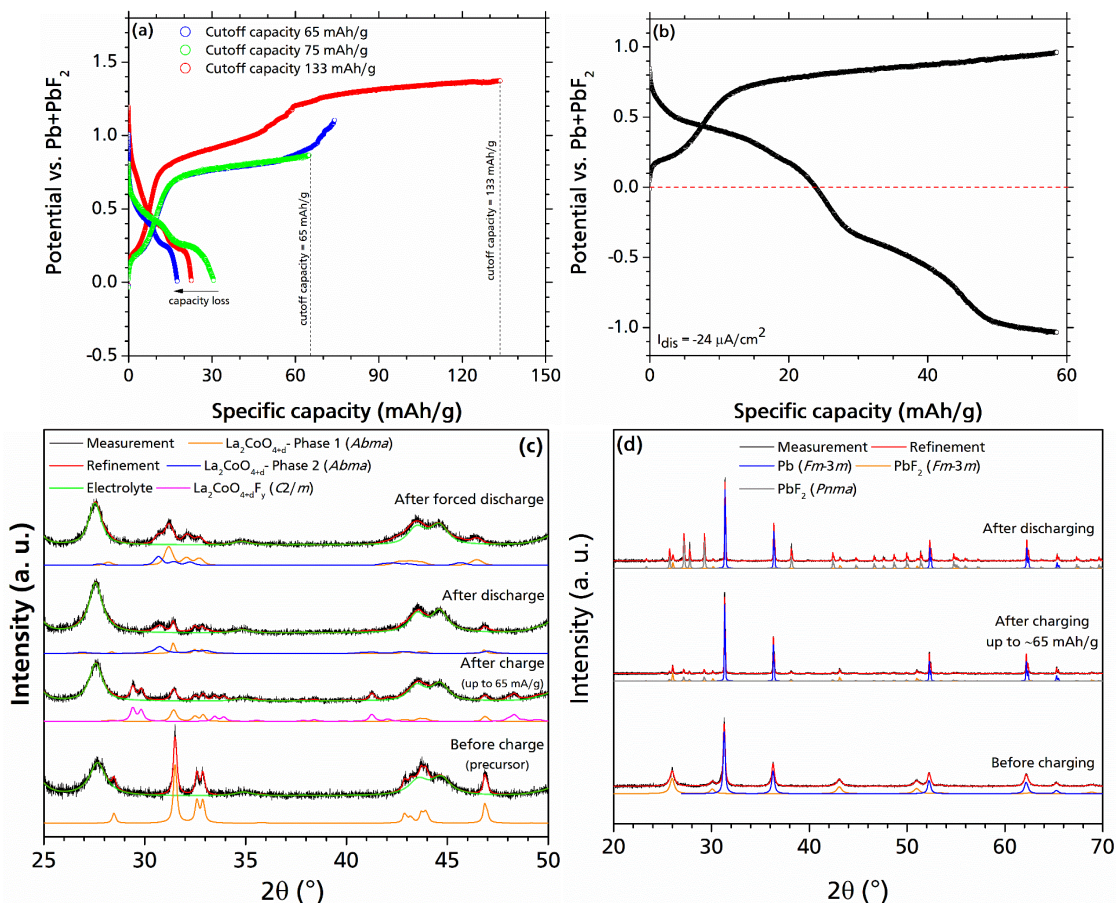**Figure 5-21. (a) Cycling curves of La₂CoO₄₊d/Pb+PbF₂ cell at different cutoff capacities of 65 mAh/g, 75 mAh/g and 133 mAh/g at T = 170 °C, I_ch = 24 µA/cm² and I_dis = -2.4 µA/cm²; (b) forced discharge curve of La₂CoO₄₊d/Pb+PbF₂ which was performed at a temperature of 170 °C and charge/discharge current density of ± 24 µA/cm²; (c) respective XRD patterns of the cathode side after discharge/forced discharge in addition to the precursor and a charged sample (up to 65 mAh/g); (d) respective XRD patterns of the anode side before/after charge and after discharge.**

Table 5-12. Lattice parameters and relative weight fractions (%) of the active cathode material after charge/forced discharge (at T = 170 °C, I_ch = 24 µA/cm² I_dis = -2.4 µA/cm² (-24 µA/cm² for the forced discharge) and cutoff capacity of 65 mAh/g) in comparison to the La₂CoO₄₊d cathode composite material. The relative wt% is calculated according to the partial weight percent of the phase divided by the total weight fraction of the active cathode material.

	La₂CoO₄₊d (Phase 1) (*Abma*)				La₂CoO₄₊d (Phase 2) (*Abma*)			
	a (Å)	*b* (Å)	*c* (Å)	Relative wt%	*a* (Å)	*b* (Å)	*c* (Å)	Relative wt%
After discharge	5.521(2)	5.464(2)	12.614(6)	22.69(26)	5.555(6)	5.422(5)	13.251(16)	77.31(93)
After forced discharge	5.584(2)	5.478(2)	12.667(6)	68.06(33)	5.692(5)	5.555(4)	12.862(12)	31.94(17)
Precursor (cathode composite)	5.524(1)	5.476(1)	12.615(2)	100				

A slight increase in the charge cutoff capacity up to 75 mAh/g results in a strong lowering of discharge capacity to 19 mAh/g (almost 40% capacity loss as compared to cutoff capacity of 65 mAh/g) (see **Figure 5-21a**). Proceeding the charging towards a higher charge cutoff capacity of 133 mAh/g leads to a slightly higher discharge capacity up to 22 mAh/g. This slight increase

in the discharge capacity may arise from a higher weight fraction of the fluorinated phase by further charging the cell (**Figure 5-21b**). As it is discussed previously, no significant structural changes could be detected by XRD after 100 mAh/g. Therefore, it is assumed that further increase in the charge cutoff capacity (more than 133 mAh/g) only results in occurrence of side reactions which can even deteriorate the conductivity of the cell leading to further capacity loss.

Figure 5-21d depicts the XRD measurements of the Pb+PbF$_2$ anode material before/after charging and after discharging. As can be seen in the figures, the broad peaks of the anode material before charge originate from the nanocrystalline nature of the anode material arising from the mechanical alloying/milling of the powders. The structures of Pb and PbF$_2$ before charging are determined to be cubic (*Fm-3m*). After charging of the La$_2$CoO$_{4+d}$/Pb+PbF$_2$ cell, XRD patterns show sharpening of the Pb reflections which is due to recrystallization of Pb arising from the operational temperature that is almost half of melting point of Pb ($T_m = 327.5\,°C$, operational T = 170 °C). On the other hand, a part of initial cubic (*Fm-3m*) structure of the β-PbF$_2$, transforms to orthorhombic (*Pnma*) α-PbF$_2$ after charging the cell. It has been reported that the β-phase is the thermodynamically most stable phase at ambient conditions, with the α-phase being a high pressure (>0.4 GPa) modification [113, 114]. Moreover, after the discharging of the cell the content of α-PbF$_2$ phase increases (**Figure 5-21d**). It is suggested that the electrochemical reactions seem to favor the formation of α-PbF$_2$ most likely due to kinetic reasons. Further, it can be concluded that metastable phases can be produced via electrochemical reactions.

Increase in the current density often leads to a reduction in the discharge capacity since it deteriorates the electron transport kinetics and increases the polarizations leading to a rise in the internal resistance of the cell [63]. It was shown (section 5.3.1.1) that for LaSrMnO$_4$ a discharge plateau can only be obtained at very low discharge current densities (e.g. -2.4 μA/cm^2). However, La$_2$CoO$_{4+d}$ seems to be less sensitive to increasing current densities and the discharge plateau can also be observed at higher discharge current density of -24 μA/cm^2 (10 times higher than the discharge current density that has been used for LaSrMnO$_4$). Nevertheless, as it is expected, increase in the discharge current density (absolute value) from 2.4 μA/cm^2 to 24 μA/cm^2 results in a reduction in the discharge capacity by 25% (from 32 mAh/g to 24 mAh/g) (see **Figure 5-22a**).

Operating temperature also plays an essential role on the overvoltages, discharge potential and capacity. **Figure 5-22b** summarizes the effect of operating temperature on the charge/discharge behavior in La$_2$CoO$_{4+d}$/Pb+PbF$_2$ cells. As can be seen in the figure, increase in the operating temperature results in a reduction in the charge overpotential (this effect also has been observed for LaSrMnO$_4$). Note that the cell that was operated at 155 °C has a higher charge potential in the order of 0.5 V as compared to the cell at 170 °C. However, further increase in the temperature from 170 °C to 200 °C has only limited impact on the charge potential (in the order of 0.1 V by increase the temperature from 170 °C to 200 °C) (see **Figure 5-22b**). This is due to the fact that the solid-state electrolyte possesses lower conductivity at around 150 °C which results in a higher internal resistance, but at around 170 °C its conductivity is high enough [24].

Although the lowest charge overpotential can be observed for the highest operating temperature of 200 °C, the largest discharge capacity loss is also detected for the cell which has been cycled at 200°C: Discharge at lower operational temperatures (<200 °C) results in a discharge capacity of around 20 mAh/g but further increase in the operating temperature up to 200 °C leads to a

reduction in the discharge capacity to 10 mAh/g (the discharge capacity almost halved). This must not be necessarily related to the active cathode material itself: Maybe the grain growth in Pb which becomes especially more severe at the temperatures higher than half of the melting point (T_m = 327 °C), results in a reduction in the Pb reaction surface leading to a deterioration of the transport kinetics of the fluoride ions during the oxidation of the Pb (formation of PbF_2) in the discharge reaction. Moreover, a higher discharge potential loss also can be observed for the cell that has been cycled at 200 °C (**Figure 5-22b**).
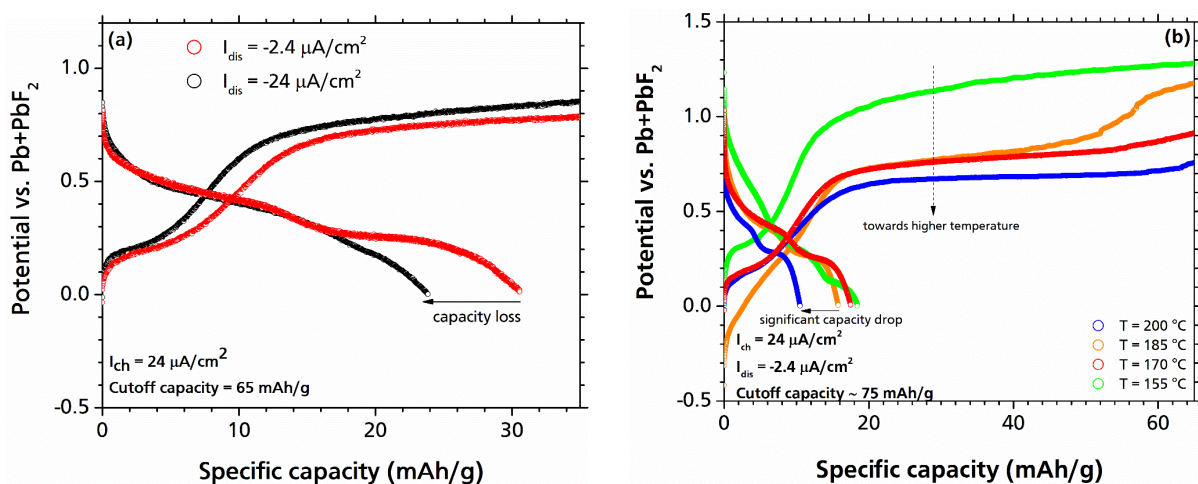
Figure 5-22. (a) Effect of discharge current density on the discharging behavior (T = 170 °C); (b) effect of operating temperature on the charge overpotential and discharge capacity (cutoff capacity = 75 mAh/g, I_{ch} = 24 µA/cm² and I_{dis} = -2.4 µA/cm²).

d. Modifying the Anode Material: La_2CoO_{4+d}/Zn+ZnF₂ Cell

Although galvanostatic cycling of the La_2CoO_{4+d}/Pb+PbF₂ cell confirms the very basic principle of the intercalation/de-intercalation of the F⁻ ions during the redox reactions, the potential of the La_2CoO_4+d/Pb+PbF₂ cell is relatively low (between 0.5 – 0.3 V) since Pb is not a strong reducing agent [57]. In order to increase the potential (and energy density) of the cell, it is necessary to widen the potential window between the cathode and the counter electrode. In this respect, other metal/metal fluoride anode composite materials have been used as counter electrode materials (anode material). In the course of the experiments it is realized that using Zn+ZnF₂ as the active anode material provides a higher discharge capacity, potential and energy density by factors of 1.3, 2 and 14, respectively. In this section the structural and electrochemical reversibility of the La_2CoO_{4+d}/Zn+ZnF₂ cell will be discussed.

Figure 5-23a depicts a charge/discharge curve for a La_2CoO_{4+d}/Zn+ZnF₂ cell using the optimized cutoff conditions as determined in section 5.3.2.1c. The charge plateau is observed around 1.3 – 1.6 V for the Zn+ZnF₂ anode composite material (vs. 0.6 – 0.8 V for Pb+PbF₂) which well matches with what would be expected from the EMF series (Δ = 0.64 V [57]). The discharge sloping plateau appears to be around 1.0 – 0.5 V for La_2CoO_{4+d}/Zn+ZnF₂ cell which is higher than that for Pb+PbF₂ by a factor of ~ 2. Moreover, a discharge capacity of about 40 mAh/g for the first cycle can be obtained for the La_2CoO_{4+d}/Zn+ZnF₂ cell (**Figure 5-23a**), which is ~ 25% higher than that for the cell with Pb+PbF₂ anode composite material. This also shows that intercalation systems (such as La_2CoO_{4+d}) can be further discharged upon using anode materials with stronger reducing power.

XRD measurements show (**Figure 5-23b** and **Table 5-13**) that after charging the $La_2CoO_{4+d}/Zn+ZnF_2$ cell, a fluorinated (monoclinic) phase, similar to what has been previously observed for $La_2CoO_{4+d}/Pb+PbF_2$ cell, was obtained ($A2/m$; a = 5.287 Å, b = 5.350 Å, c = 15.281 Å, β = 91.09°). In respect of the weight fraction of the fluorinated phase, it was observed that at a charge cutoff capacity of 100 mAh/g over 95% of La_2CoO_{4+d} is transformed to the fluorinated $La_2CoO_{4+d}F_y$ phase which is in agreement with the previous findings about the $La_2CoO_{4+d}/Pb+PbF_2$ cell.

Figure 5-23c and **d** compare the K_2NiF_4-type structure phases obtained after discharge of La_2CoO_{4+d} vs. $Pb+PbF_2$ and $Zn+ZnF_2$. In both cases, two fractions of the K_2NiF_4-type structure phase can be found (**Table 5-13**): 1- "Phase 1" with identical lattice parameters as compared to the initial La_2CoO_{4+d} phase ($c \sim 12.6$ Å). 2- "Phase 2" is an orthorhombic phase with a c parameter of ~ 13 Å which is larger than that for the initial La_2CoO_{4+d} phase, but significantly lower than high fluorine content phase of $La_2CoO_{4+d}F_y$. For discharge against $Zn+ZnF_2$ the La_2CoO_{4+d} phase is the main phase (~ 68 %), whereas it is found to be the minority phase for discharge against $Pb+PbF_2$ (~ 23 %) according to **Table 5-13**. This is in agreement with the fact that a higher discharge capacity can be obtained against $Zn+ZnF_2$ during the first cycles. Moreover, the phases obtained after discharge against $Zn+ZnF_2$ are similar to what was found for discharge the $La_2CoO_{4+d}/Pb+PbF_2$ cell to negative potentials (forced discharge). Therefore, it can be suggested that the $Zn+ZnF_2$ anode composite material provides a higher degree of structural reversibility (over cycling) in the active cathode material as compared to $Pb+PbF_2$.

The structural changes of the $Zn+ZnF_2$ anode composite during charge and discharge of a $La_2CoO_{4+d}/Zn+ZnF_2$ cell can be found in **Figure 5-23d**. ZnF_2 appears to suffer a nearly complete amorphization on milling and cannot be detected in the XRD pattern afterwards. The XRD measurements after charge/discharge of the cells do not show any significant change, indicating poor recrystallization behavior of ZnF_2. Clearly, this recrystallization behavior could therefore contribute to the overpotentials arising on extended charging for the $Zn+ZnF_2$ based cells.

The effect of operational temperature on the charge/discharge profiles and structural reversibility for the $La_2CoO_{4+d}/Zn+ZnF_2$ cells are depicted in **Figure 5-24**. As it is expected, increasing the operating temperature from 150 °C to 190 °C leads to a reduction in the charge overpotential by roughly 0.5 V, which is in a very well agreement with what has been observed for $La_2CoO_{4+d}/Pb+PbF_2$ cell. The charge potential for $La_2CoO_{4+d}/Zn+ZnF_2$ system at 170 °C seems to be located at the middle of the potentials for the same cells operating at 150 °C and 190 °C (**Figure 5-24a**). Note that for the $La_2CoO_{4+d}/Pb+PbF_2$ cell the potential at 170 °C is closer to the higher temperature of 200 °C (**Figure 5-6b**).

The discharge capacity of the cells at all three operating temperatures has been measured to be in a similar range of 35 − 40 mAh/g. However, a small potential drop (~ 0.2 V) can be observed for the cell at operational temperature of 190 °C (**Figure 5-24a**). Respective XRD patterns of cathode composites after discharge against $Zn+ZnF_2$ at different operational temperatures can be seen in **Figure 5-24b**. The XRD patterns for the samples at 150 °C and 170 °C have some similarities: Two La_2CoO_{4+d} phases with slightly different cell volume (a difference in lattice parameter c: phase 1 with $c \sim 12.6$ Å and phase 2 with $c \sim 13.0$ Å) can be identified. In addition, there is no indication of presence of a high fluorine content phase ($c \sim 15$ Å). However, for the sample at 190 °C (after discharge) phase 2 can hardly be detected (**Figure 5-24b**). Furthermore, a small amount of fluorinated phase still can be seen ($2\theta \sim 29.5$°).
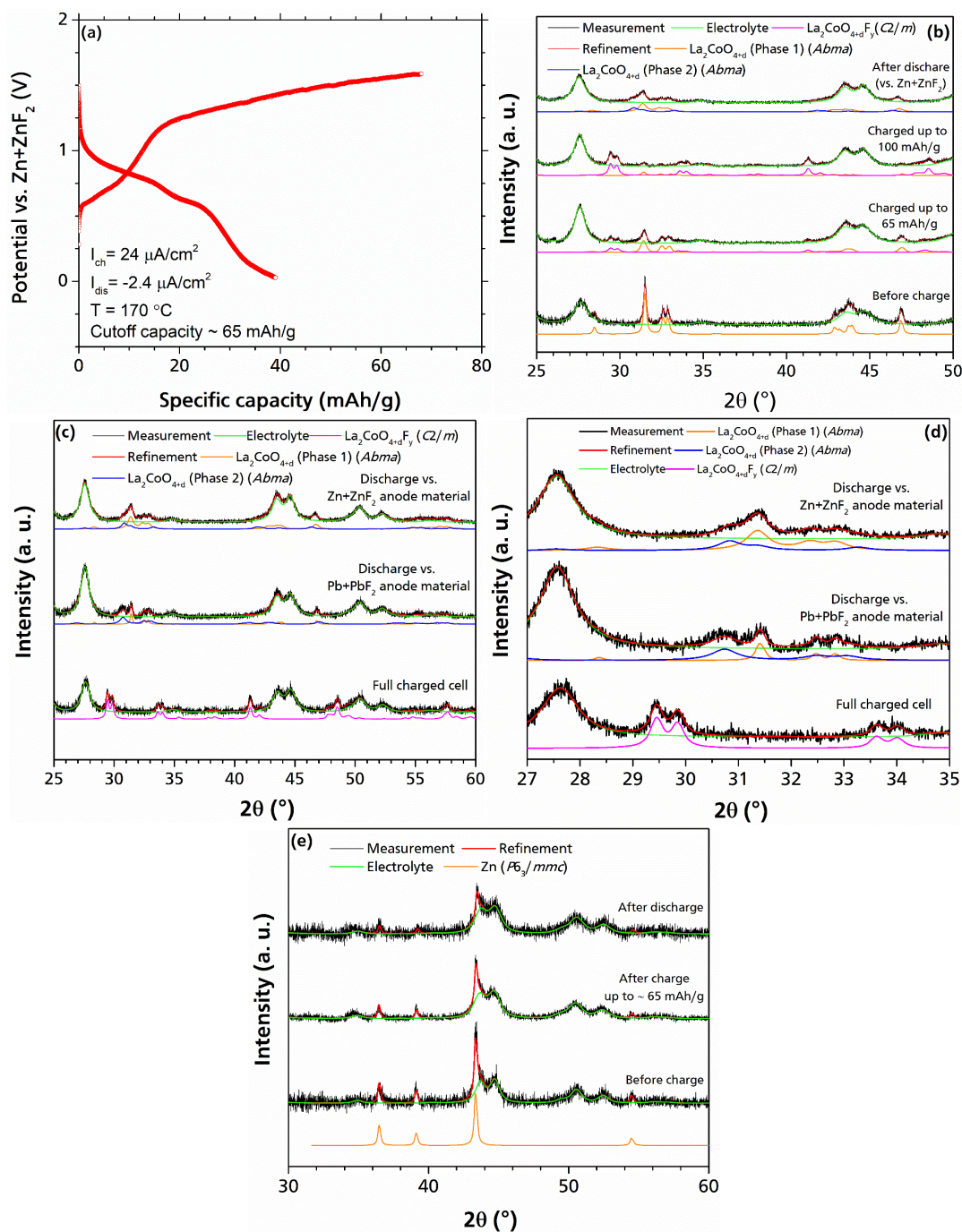
Figure 5-23. (a) Typical charge/discharge curves of La$_2$CoO$_{4+d}$/Zn+ZnF$_2$ cell T = 170 °C, I$_{ch}$ = 24 µA/cm^2, I$_{dis}$ = -2.4 µA/cm^2 and cutoff capacity of 65 mAh/g; (b) XRD patterns of the cathode material before charge, after charge and after discharge for a L$_2$CoO$_{4+d}$/Zn+ZnF$_2$ cell (at the same temperature and charge current density); (c, d) a comparison between the XRD patterns of the cathode material after discharge against Pb+PbF$_2$ and Zn+ZnF$_2$ as the active anode material (cells were initially charged up to 65 mAh/g; operational temperature T = 170 °C, I$_{ch}$ = 24 µA/cm^2 and I$_{dis}$ = -2.4 µA/cm^2); (e) respective XRD patterns of the Zn+ZnF$_2$ anode composite before and after charge in the same electrochemical cell.

Table 5-13. XRD structural data of the active cathode material after discharging against Zn+ZnF₂ and Pb+PbF₂ at T = 170 °C, I_ch = 24 μA/cm² and I_dis = -2.4 μA/cm²; cutoff capacity ∼ 70 mAh/g. The relative wt% is calculated according to the partial weight percent of the phase divided by the total weight fraction of the active cathode material.

	La₂CoO₄₊d (phase 1) (*Abma*)					La₂CoO₄₊d (phase 2) (*Abma*)				
	a (Å)	*b* (Å)	*c* (Å)	Cell volume (Å³)	Relative wt%	*a* (Å)	*b* (Å)	*c* (Å)	Cell volume (Å³)	Relative wt%
La₂CoO₄ (discharged vs. Zn+ZnF₂)	5.543(2)	5.460(2)	12.621(6)	381.97(45)	67.8 (39)	5.710(5)	5.393(4)	12.970(10)	399.39(95)	32.2 (20)
La₂CoO₄₊d (discharged vs. Pb+PbF₂	5.521(1)	5.464(2)	12.613(6)	380.49(39)	21.5 (20)	5.554(5)	5.423(5)	13.248(16)	399.02(242)	78.5(95)
La₂CoO₄₊d (precursor ACM)	5.525(1)	5.476(1)	12.615(2)	381.66(20)						
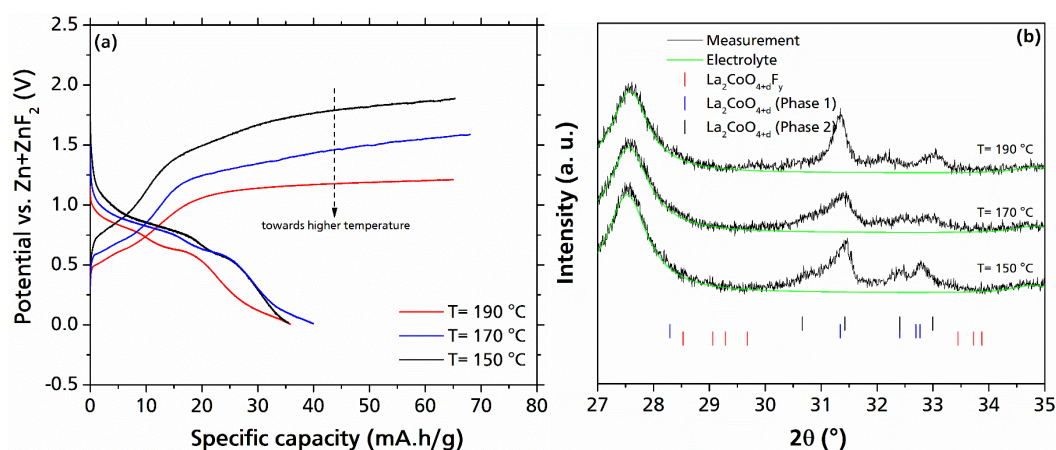
Figure 5-24. (a) Charge/discharge curves of La₂CoO₄₊d/Zn+ZnF₂ cell at different operational temperatures between 150 °C – 190 °C (I_ch = 24 μA/cm², I_dis = -2.4 μA/cm²); (b) respective XRD patterns after the discharge.

5.3.2.2 La₂NiO₄₊d Cathode Composite Material

La₂NiO₄₊d has been widely investigated because of its interesting magnetic and electric properties [115-117]. Furthermore, this compound has been considered as a potential cathode material for solid oxide fuel cells [118]. It has been reported [107] that the structure of La₂NiO₄₊d can be fitted by an orthorhombic structure with a *Fmmm* space group which is a translationengleiche subgroup of *I4/mmm* supersymmetry (highest symmetry of a K₂NiF₄ structure is *I4/mmm* [46]). Due to low orthorhombic distortions of the La₂NiO₄₊d unit cell, the structure can be also refined with a tetragonal model.

The oxygen content of La₂NiO₄₊d can be determined by the values of the lattice parameters, according to previous studies [76]. In this respect, the compound that has been used to make a cathode material composite here has approximately a composition of La₂NiO₄.₁₃ ($a = b = $5.4612(1) Å, $c = $ 12.6745(2) Å).

In this section, it will be shown that chemical fluorination route cannot be considered as viable tool to make a fully fluorinated La₂NiO₄₊dF_y phase, however, with an electrochemical fluorination process the fluorinated phase can be easily produced. Therefore, to have an

approximation on the numbers of intercalated fluoride ions per formula unit within an electrochemical process, another approach based on TEM (ADT) and XAS has been followed.

a. Chemical Fluorination

Several strategies have been used in order to perform the chemical fluorination including using F_2 gas and fluorinating agents such as CuF_2 and AgF_2 (**Figure 5-16**).

Fluorination under F_2 gas resulted in either no structural change at lower temperature range (lower than 250 °C, under a flow of 10% F_2) or complete decomposition of La_2NiO_{4+d} at higher reaction temperatures. Similar behavior has been observed for the fluorination of La_2CoO_{4+d} under flow of F_2.

The other method that has been used to fluorinate La_2NiO_{4+d} was fluorination under a flow of O_2 while the La_2NiO_{4+d} oxide and the CuF_2 fluorinating agent are kept in two separate crucibles (as described in **Figure 5-16**). This strategy has been used for La_2CoO_{4+d} and resulted in formation of a high purity fluorinated phase. However, after such a fluorination process on La_2NiO_{4+d} no phase with parameter c in the order of ~ 15.0 Å (which is indicative for occupation of both interlayers of the unit cell of a K_2NiF_4-type structure) could be detected (**Figure 5-25a**). Instead, an intermediate oxide phase with some degree of orthorhombic distortion was observed, which coexist with initial tetragonal La_2NiO_{4+d} phase. The obtained lattice parameters for both phases (tetragonal/orthorhombic) are provided in **Table 5-14**. Such an orthorhombic distortion has already been reported during topochemical fluorination of La_2NiO_{4+d} to form $La_2NiO_3F_2$ [45] and can be an indication for a (slight) change in the occupancy of the interlayer; however, the degree of distortion of the orthorhombic phase is much lower in the current fluorination reactions. Note that $La_2NiO_3F_2$ cannot be considered as a cathode material for FIB, since Ni^{2+} is a non-oxidizing species in this oxyfluoride compound.

To fluorinate La_2NiO_{4+d}, CuF_2 has been used (mixed with La_2NiO_{4+d} in one crucible) as the fluorinating agent under a flow of O_2 (at 300 °C for 60 h). After such a fluorination process three intermediate fluorinated (tetragonal) phases with different c parameters ranging from ~ 13.40 Å to ~ 14.48 Å form (**Figure 5-25b**) could be observed. Furthermore, a small amount (~ 8% of the total La_2NiO_{4+d}) of a (fluorinated) phase with a larger c parameter could be detected ($a = b = 5.386(2)$ Å, $c = 15.232 (11)$ Å). However, the majority phase was still the initial tetragonal La_2NiO_{4+d} phase but with a slightly expanded c parameter up to 12.708(1) Å. This may explain why CuF_2 stays mainly unreacted.

Figure 5-25c depicts the XRD pattern of $LaNiO_{4+d}$ after fluorination with AgF_2 as the fluorinating agent at 300 °C for 48 h under a flow of Ar (0.3 SLM) with a large excess of AgF_2. Two high fluorine content phases were formed after the fluorination process which can be seen in **Figure 5-25c**. The first one with an orthorhombic distortion and a larger expansion along the c-axis ($a = 5.477 (3)$ Å, $b = 5.453 (3)$ Å, $c = 15.026 (9)$ Å) with a relative weight fraction of 14% and the other one with lower expansion in the lattice parameter c ($a = 5.391 (4)$ Å, $b = 5.060 (4)$ Å, $c = 14.555 (9)$ Å).

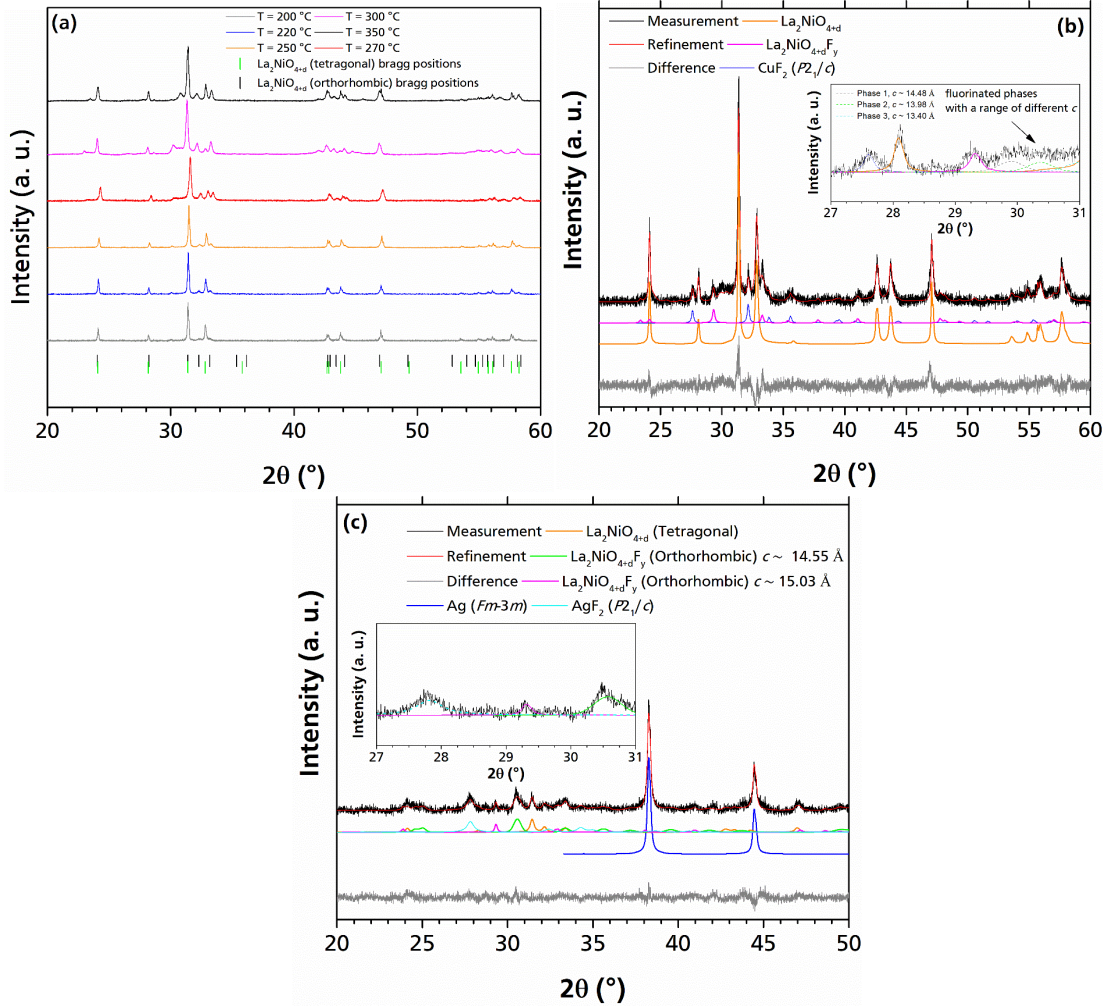**Figure 5-25. XRD patterns of the La₂NiO₄₊d after fluorination by (a) CuF₂ as the fluorinating agent (in two separate crucibles) at different temperatures under a flow of O₂ (0.1 SLM); (b) mixing the CuF₂ fluorinating agent and the oxide under a flow of O₂ (0.1 SLM) at 300 °C for 60 h; (c) mixing the AgF₂ fluorinating agent and the oxide under a flow of Ar (0.3 SLM) at 300 °C for 48 h.**

Table 5-14. Lattice parameters of La₂NiO₄₊d after chemical fluorination with CuF₂ under O₂ at separate crucibles at different temperatures.

	La₂NiO₄₊d/Tetragonal ($I4/mmm$)		La₂NiO₄₊d/Orthorhombic ($Fmmm$)		
T (°C)	a (Å)	c (Å)	a (Å)	b (Å)	c (Å)
200	5.463(1)	12.671(1)	5.406(1)	5.549(1)	12.669(3)
220	5.463(1)	12.674(1)	5.402(1)	5.556(1)	12.678(2)
250	5.463(1)	12.678(1)	5.403(1)	5.554(3)	12.679(1)
270	5.463(1)	12.678(1)	5.397(1)	5.561(1)	12.684(1)
300	5.464(1)	12.689(1)	5.386(1)	5.571(2)	12.695(1)
350	5.462(1)	12.678(1)	5.387(1)	5.581(1)	12.687(1)

The results of chemical fluorination of La₂NiO₄₊d reveal that making a pure La₂NiO₄₊dF_y phase seems to remain a challenge. This may be due to the fact that the chemical potential for the fluorination is not high enough. Only some traces of the fluorinated phase can be found after chemical fluorination with CuF₂ and AgF₂ as the fluorinating agents. Moreover, efforts have been done within our research group to fluorinate La₂NiO₄₊d under a flow of F₂ at mild

conditions (low reaction time (~ 15 min) and reaction temperature about 200 °C) which results in an increase in the weight fraction of the fluorinated phase as much as 20%.

b. Electrochemical Charging

During the course of the investigations, it was realized that Zn/ZnF_2 counter electrode material provides a higher energy density as compared to Pb/PbF_2 against the used K_2NiF_4-type structure compounds. Therefore, for evaluating the La_2NiO_{4+d} cathode composite, $Zn+ZnF_2$ has been used as an anode composite material.

The compound (La_2NiO_{4+d}) formed after solid-state synthesis has an approximate composition of $La_2NiO_{4.13}$ (d = 0.13) [76], based on the measured lattice parameters (more information about the correlation between the lattice parameters and the occupancy of oxygen in La_2NiO_{4+d} compounds can be found in **Table 4-1**). From this, a theoretical maximum capacity of 125 mAh/g for the formation of $La_2NiO_{4.13}F_{1.87}$ can be expected if one assumes a simple filling of all empty interstitial anion sites, according to the following reaction equation:

$La_2NiO_{4.13}$ + 1.87 F^- ⇋ $La_2NiO_{4.13}F_{1.87}$ + 1.87 e^-.
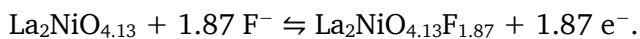
Schematic illustrations of an un-fluorinated $La_2NiO_{4.13}$ and fluorinated $La_2NiO_{4.13}F_{1.87}$ state have been plotted in **Figure 5-26**.
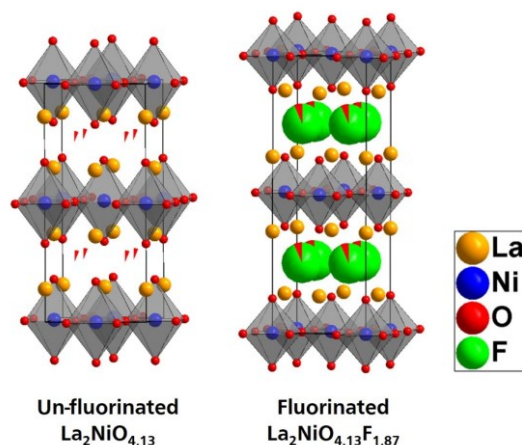
Figure 5-26. Schematic illustrations of the un-fluorinated La₂NiO₄.₁₃ (left) and the hypothetical fully fluorinated state (right) La₂NiO₄.₁₃F₁.₈₇. Fractional occupancies are depicted for the interstitial anion site.

In order to investigate the charging behavior and the capacity dependent structural changes during the electrochemical charging step, various $La_2NiO_{4+d}/Zn+ZnF_2$ cells were subjected to galvanostatic electrochemical charging at various cutoff capacities up to 155 mAh/g. **Figure 5-27a** depicts the charge curves showing a good reproducibility of the charge step. According to the figure, the charge curve can be divided into three separate regions. The starting potential of the $La_2NiO_{4+d}/Zn+ZnF_2$ cell is about 0.8 V (at the beginning of the region (I)) followed by a sharp increase in the voltage up to ~ 1.7 V.

In the second region (II) a charge plateau between 1.7 V and 2.0 V can be observed which seems to be due to the fluorination of La_2NiO_{4+d} (according to the XRD measurements that will be discussed later in this section) and some overlaps of a side reaction which does not significantly impair the conductivity of the cell. Ideally the charge plateau should be seen in a constant voltage (when a range of ion contents is not allowed, i.e. the fluorine rich phase has a specific composition and not a variation of different compositions), however, in practical point

of view sloping overvoltages are usually observed during charging mainly due to increase in internal resistance of the cell. This overvoltage may also come from the increase in the real current density: By proceeding the redox reaction in the electrodes some part of the electrode surface might become inactive which means the active reaction area reduces resulting in a local increase in the real current density [63]. Therefore, the increase in current density results in an increase in overpotential. This argument is also true for the discharge process.

In region (III) a sharp increase in voltage can be observed (**Figure 5-27a**). This increase in potential is accompanied by building up additional impedances mainly due to carbon decomposition which remarkably impairs the electric conductivity of the cell.

The respective XRD measurements of the cathode composite after charging the $La_2NiO_{4+d}/Zn+ZnF_2$ cells at various cutoff capacities up to 155 mAh/g are plotted in **Figure 5-27** and the respective lattice parameters (extracted from XRD) are listed in **Table 5-15**. The XRD pattern of the initial La_2NiO_{4+d} active cathode material before charge can be fitted by a tetragonal structure ($a = 5.4623(4)$ Å and $c = 12.6710(11)$ Å). After electrochemical charging of the cell up to 10 mAh/g two phases can be observed (**Figure 5-27c**): The first phase is the original La_2NiO_{4+d} with a tetragonal unit cell and the second phase is an orthorhombic (*Fmmm*) phase with an increase in the lattice parameter a and a decrease in the lattice parameter b (as shown in **Table 5-15**), compared to the original La_2NiO_{4+d}. In the previous section similar orthorhombic distortions by chemical fluorination method was observed. This phase is also present after charging up to 30 mAh/g with a larger a/b ratio (1.018 and 1.022 and for 10 mAh/g and 30 mAh/g, respectively, see **Table 5-15**). However, the orthorhombic La_2NiO_{4+d} phase cannot be anymore detected by proceeding the electrochemical charging towards higher cutoff capacities.

Further electrochemical charging of the cell results in formation of a $La_2NiO_{4+d}F_y$ phase, which can be very well fitted by an orthorhombic *Fmmm* model with a significantly larger lattice parameter c (~ 15.2 Å) as compared to the initial La_2NiO_{4+d} ($c \sim 12.7$ Å) (**Figure 5-27b** and **Table 5-15**). Later in this section, evidences will be provided showing that this phase is a rich fluorine content phase. The relative weight fraction of the high fluorine content phase of $La_2NiO_{4+d}F_y$ increases almost linearly with charge capacity and reaches to $\sim 60\%$ at 135 mAh/g as is shown in **Figure 5-27d**. Further charging of the cell leads to a more increase in the relative fraction of the fluorinated phase ($La_2NiO_{4+d}F_y$) up to $\sim 77\%$ at 155 mAh/g (**Figure 5-27d**).
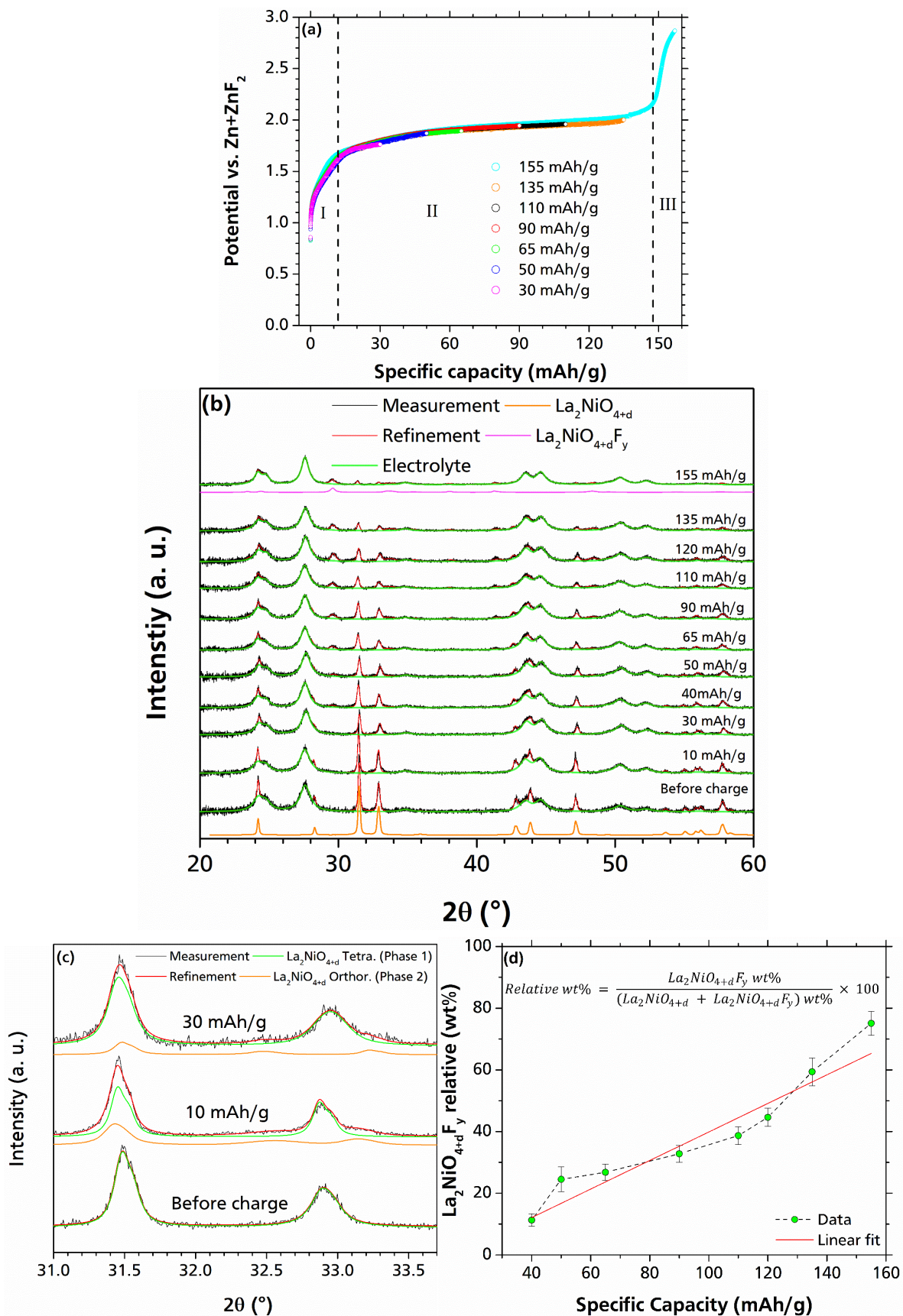
Figure 5-27. (a) Galvanostatic electrochemical charge curves of the La₂NiO₄₊d vs. Zn+ZnF₂ anode composite material at different cutoff capacities at the operational temperature and current density of 170 °C and 24 µA/cm², respectively; **(b), (c)** respective XRD patterns after charge; **(d)** relative phase fraction of the La₂NiO₄₊dFᵧ phase with respect to the charging cutoff capacity, according to the Rietveld analysis based on the obtained XRD data.

Table 5-15. Lattice parameters and volume (extracted from XRD data) of the La$_2$NiO$_{4+d}$ active cathode material before and after charge up to different cutoff capacities at T = 170 °C and current density of 24 µA/cm².

Cutoff capacity (mAh/g)	La$_2$NiO$_{4+d}$ (Phase 1) $I4/mmm$ or $Fmmm$				La$_2$NiO$_{4+d}$ (Phase 2) $Fmmm$				La$_2$NiO$_{4+d}$F$_y$ $Fmmm$			
	a (Å)	b (Å)	c (Å)	V (Å³)	a (Å)	b (Å)	c (Å)	V (Å³)	a (Å)	b (Å)	c (Å)	V (Å³)
Before charge	5.462(1)		12.671(11)	378.1(1)								
10	5.460(1)		12.680(1)	378.1(1)	5.516(2)	5.420(2)	12.686(3)	379.3(2)				
30	5.454(1)		12.715(2)	378.2(1)	5.526(2)	5.406(2)	12.665(5)	378.4(2)				
40	5.455(1)		12.727(2)	378.7(1)					5.370(9)	5.309(8)	15.199(31)	433.3(13)
50	5.443(1)	5.465(1)	12.733(2)	378.8(1)					5.360(8)	5.310(8)	15.255(30)	434.1(13)
65	5.444(1)	5.468(1)	12.748(2)	379.5(1)					5.374(5)	5.318(4)	15.205(16)	434.5(7)
90	5.447(1)	5.462(1)	12.742(2)	379.1(1)					5.363(3)	5.311(3)	15.199(12)	432.8(5)
110	5.438(1)	5.464(1)	12.743(30)	378.6(1)					5.358(3)	5.303(3)	15.227(11)	432.6(5)
120	5.440(1)	5.466(1)	12.757(3)	379.4(1)					5.363(2)	5.307(2)	15.229(9)	433.4(4)
135	5.444(1)	5.4661(1)	12.755(3)	379.6(1)					5.357(2)	5.308(3)	15.253(10)	433.7(4)
155	5.449(1)	5.466(1)	12.761(4)	380.1(2)					5.361(2)	5.303(3)	15.247(9)	433.5(4)

As discussed previously, the chemical fluorination of La$_2$NiO$_{4+d}$ did not serve as a method to provide detailed information about the fluorinated La$_2$NiO$_{4+d}$F$_y$ phase. Instead a new approach was used to analyze the fluorinated (charged) state of La$_2$NiO$_{4+d}$ with respect to fluorine content and Ni oxidation state, which combines electron diffraction tomography (ADT), EDX and XANES analysis.

Figure 5-28a and **b** show HAADF-STEM images of the cathode composite material after charging up to 120 mAh/g. In agreement with the XRD measurements, two different phases of the Ruddlesden-Popper-type compound could be identified. **Figure 5-28a** depicts a single crystal of a nearly un-fluorinated La$_2$NiO$_{4+d}$ (with $c \sim 12.67$ Å) after charge that is surrounded by carbon nanotubes and the La$_{0.9}$Ba$_{0.1}$F$_{2.9}$ electrolyte, whereas a well isolated particle of La$_2$NiO$_{4+d}$F$_y$ ($c \sim 15.2$ Å) could be observed, which is shown in **Figure 5-28b**. Both crystals were further analyzed by EDX and electron diffraction tomography using the ADT technique. The HAADF-STEM images of the un-charged samples are provided in Appendix (**Figure 7-8**).

The reconstruction of the observed diffraction space allowed the identification of the unit cell in the orthorhombic setting for both crystals: $a = 5.50$ Å, $b = 5.47$ Å, $c = 12.63$ Å for the un-fluorinated phase (La$_2$NiO$_{4+d}$), and $a = 5.37$ Å, $b = 5.31$ Å, $c = 14.45$ Å for the fluorinated phase (La$_2$NiO$_{4+d}$F$_y$). **Figure 7-9** shows the projections of the reconstruction of the observed diffraction space along the main axes of the fluorinated phase that allowed the determination of the cell. These results well confirm the expansion of the cell along the c-axis (contraction of the a and b axes) on fluorine insertion at the interstitial sites of the La$_2$NiO$_{4+d}$ host. This is in good agreement with the changes in the lattice parameters obtained by the XRD measurements (lattice parameters from electron diffraction are less accurate because of the camera length variation due to the electromagnetic lenses).
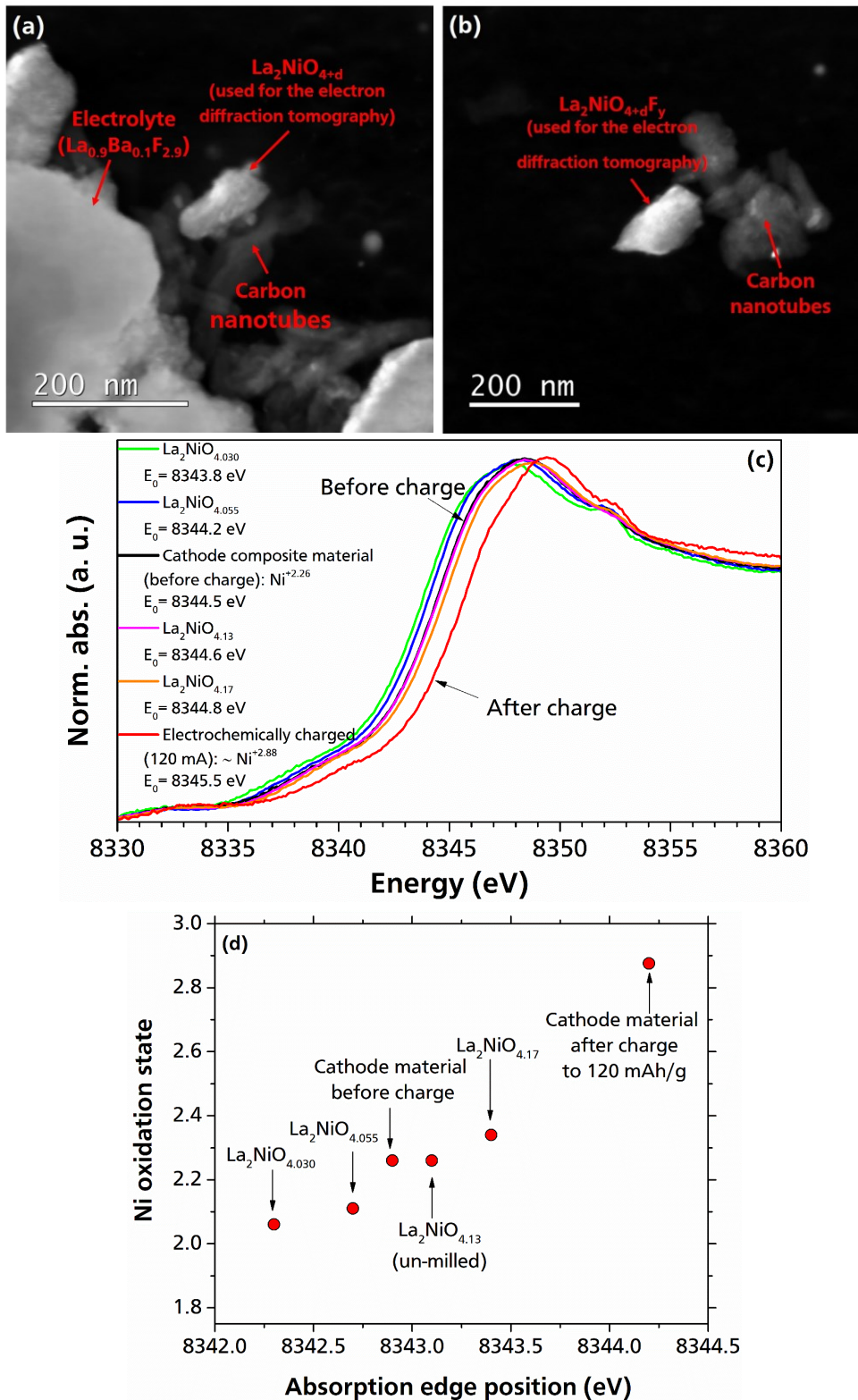
(a) Electrolyte (La$_{0.9}$Ba$_{0.1}$F$_{2.9}$)

La$_2$NiO$_{4+d}$ (used for the electron diffraction tomography)

Carbon nanotubes

200 nm

(b) La$_2$NiO$_{4+d}$F$_y$ (used for the electron diffraction tomography)

Carbon nanotubes

200 nm

(c)

La$_2$NiO$_{4.030}$ E$_0$= 8343.8 eV
La$_2$NiO$_{4.055}$ E$_0$= 8344.2 eV
Cathode composite material (before charge): Ni$^{+2.26}$ E$_0$= 8344.5 eV
La$_2$NiO$_{4.13}$ E$_0$= 8344.6 eV
La$_2$NiO$_{4.17}$ E$_0$= 8344.8 eV
Electrochemically charged (120 mA): ~ Ni$^{+2.88}$ E$_0$= 8345.5 eV

Before charge

After charge

Norm. abs. (a. u.)

Energy (eV)

(d)

Ni oxidation state

La$_2$NiO$_{4.030}$

La$_2$NiO$_{4.055}$

Cathode material before charge

La$_2$NiO$_{4.13}$ (un-milled)

La$_2$NiO$_{4.17}$

Cathode material after charge to 120 mAh/g

Absorption edge position (eV)

Figure 5-28. HAADF-STEM images of the cathode composite material after charge up to 120 mAh/g (at T = 170 °C and I$_{ch}$ = +24 µA/cm^2) showing the (a) un-fluorinated phase (La$_2$NiO$_{4+d}$) and (b) the fluorinated phase (La$_2$NiO$_{4+d}$F$_y$) which have been used for the Fast-ADT experiments. (c) The absorption edge energies of La$_2$NiO$_{4+d}$ (0.030 ≤ d ≤ 0.17) as compared to La$_2$NiO$_{4+d}$F$_y$ (after electrochemical fluorination up to 120 mAh/g with a current density of +24 µA/cm^2 at 170 °C) in agreement with the results of electron diffraction analysis and EDX (d) changes in the Ni oxidation state with respect to the absorption edge energies.

The degree of fluorination can be approximated from the refined interlayer occupancy (based on the ADT analysis) indicating a composition of $La_2NiO_4X_{1.72}$ for the fluorinated phase, which corresponds to a Ni oxidation state of $\sim +3.85$ for $d = 0.13$ ($La_2NiO_{4.13}F_{1.59}$) and $+3.72$ for $d = 0$ ($La_2NiO_4F_{1.72}$). Detail of the data refinement can be found in the appendix (section 7.5). In contrast, the interstitial site was found to be unoccupied for the un-fluorinated particle. This agrees well with the complementary elemental analyses via EDX, from which compositions of $La_2Ni_{1.04}O_{3.8}F_{1.8}$ (nearly fully filled interstitial sites) and La_2NiO_4 (nearly empty interstitial sites) can be approximated for fluorinated and un-fluorinated crystals, respectively (see **Figure 5-29** and **Table 5-17**).

XAS indicates a clear shift in the absorption spectrum to higher energies for the charged sample in comparison to the uncharged state ($La_2NiO_{4.13}$), as can be seen in **Figure 5-28c** and **d** (detailed X-ray absorption edges can be found in **Table 5-16**). Furthermore, reference samples of known compositions and oxidation states are also plotted for comparison (please see **Table 4-1** for the composition of the reference samples). This energy shift (~ 1.3 eV, see **Figure 5-28c** and **d**) matches well with what would be expected from the average oxidation state after charging (which can be determined from the refined phase fractions and the average oxidation states estimated from the crystallographic analysis of ADT). The absence of changes between the spectra in the prepeak area as well as in the whiteline also indicates a similar coordination geometry of Ni and therefore a pure electronic effect (change in oxidation state), which causes the energy shift of the spectra.

Table 5-16. X-ray absorption edges of the reference samples as compared to the cathode material before and after charging to 120 mAh/g.

Sample	Edge energy
$La_2NiO_{4.030}$	8343.8 eV
$La_2NiO_{4.055}$	8344.2 eV
Cathode composite material before charge: $Ni^{+2.26}$	8344.5 eV
$La_2NiO_{4.13}$	8344.6 eV
$La_2NiO_{4.17}$	8344.8 eV
Electrochemically charged (120 mAh/g): $\sim Ni^{+2.88}$	8345.5 eV
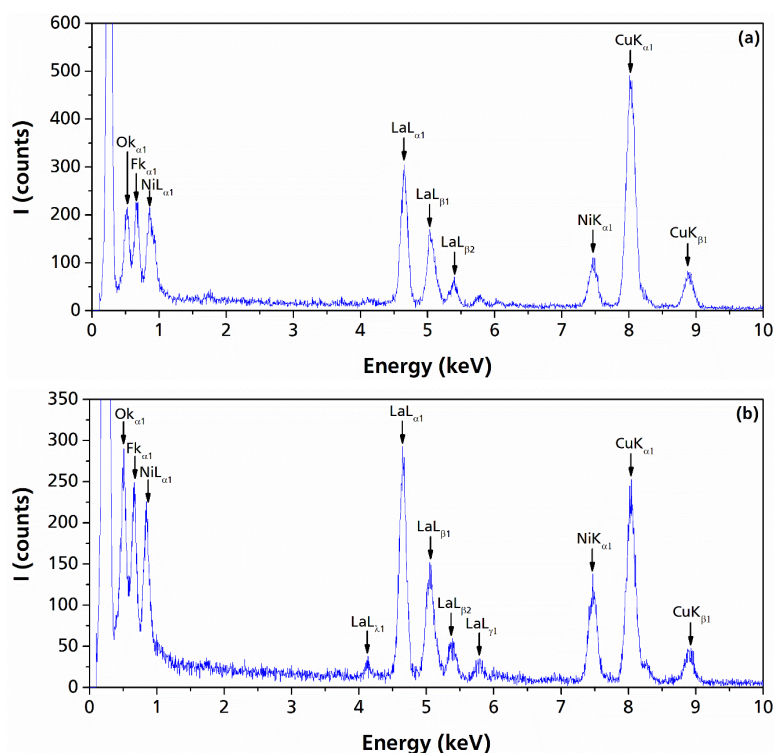
Figure 5-29. EDX spectra for the (a) un-fluorinated (La_2NiO_{4+d}) and (b) fluorinated ($La_2NiO_{4+d}F_y$) phases. Note that the un-fluorinated phase has been surrounded by the $La_{0.9}Ba_{0.1}F_{2.9}$ electrolyte material (see Figure 5-28a) and therefore fluorine also is detected in the spectrum. However, the fluorinated particle was isolated (see Figure 5-28b).

Table 5-17. EDX quantifications for the two particles measured with the Fast-ADT technique. *: the un-fluorinated particle contained some $La_{0.9}Ba_{0.1}F_{2.9}$ traces on the surface, which impact the composition determination via EDX (La:Ni ratio of 2.6 (un-fluorinated) instead of 1.93 (fluorinated)). The values obtained after correction are therefore given in the column marked as LBF-corrected.

Element (Line)	Weight %	Atomic %	Atomic % (corrected for secondary emissions of $La_{0.9}Ba_{0.1}F_{2.9}$ particles, not normalized)
*Un-fluorinated (La_2NiO_{4+d}) Particle**			
O (K)	12.4	41.0	41.0
F (K)	8.2	23.0	6.5 $=23.0 - 2.9 \times (25.9 - 2 \times 10.1)$
Ni (K)	11.2	10.1	10.1
La (L)	68.2	25.9	20.2 $=2 \times 10.1$
Fluorinated ($La_2NiO_{4+d}F_y$) Particle			
O (K)	13.9	43.5	
F (K)	8.1	21.4	
Ni (K)	14.0	12.0	
La (L)	64.0	23.1	

c. La₂NiO₄₊d/Zn+ZnF₂ cell: Electrochemical Discharging (De-Fluorination)

A typical charge/discharge curve of a La_2NiO_{4+d}/Zn+ZnF₂ electrochemical cell is depicted in **Figure 5-30a**. The discharge capacity was found to be around 70 mAh/g (from a cell that has been charged to 120 mAh/g). Therefore, a Coulombic efficiency of around 60% can be obtained (at higher cycles Coulombic efficiencies close to 100% can be seen (section 5.4.2.1)). The Coulombic efficiency of the La_2CoO_{4+d}/Zn+ZnF₂ cell is also in the same range within the first cycle. The obtained discharged capacity for the La_2NiO_{4+d}/Zn+ZnF₂ cell is the highest that could be obtained so far for a FIB with an intercalation based cathode material.
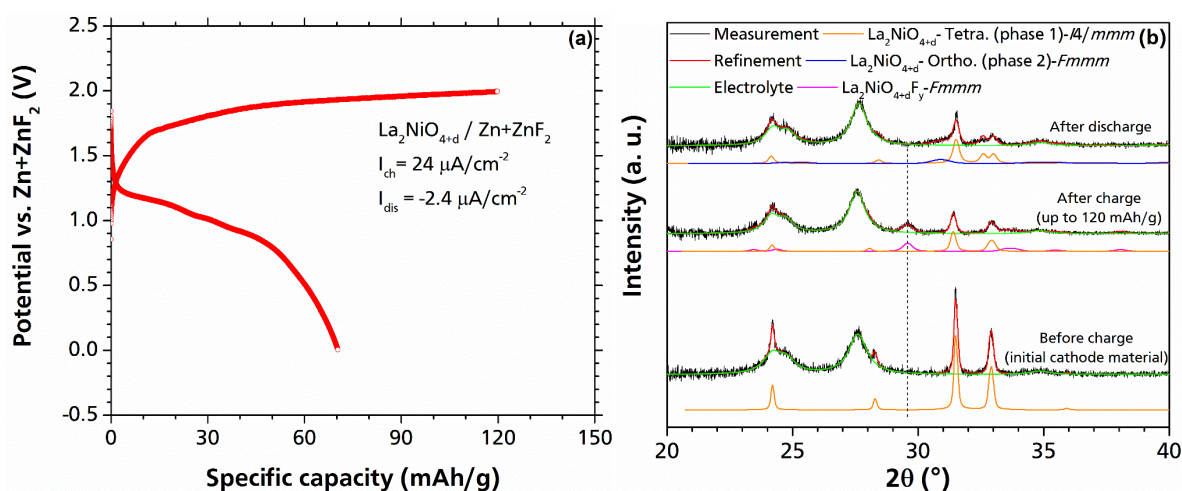
Figure 5-30. (a) A typical charge/discharge curve of the La₂NiO₄₊d/Zn+ZnF₂ cell: charge cutoff capacity of 120 mAh/g, operating temperature = 170 °C and charge and discharge current densities = +24 µA/cm² and -2.4 µA/cm², respectively; (b) respective XRD patterns of the cathode material (La₂NiO₄₊d) before and after charging at the same operating condition in comparison with the initial La₂NiO₄₊d cathode material.

According to **Figure 5-30a** there is a drop in discharge potential equal to ∼ 0.4 V between the end of the charge and the beginning of the discharge (IR drop). Also a potential drop of about 0.4 V (in addition to the initial IR drop right after the charge) can be observed in **Figure 5-30a** at the early stage of the discharge process followed by a sloping discharge plateau which lies between ∼ 1.2 and ∼ 0.8 V. There is a possibility that the sloping discharge plateau (instead of a flat plateau) arises from the difference of the anion site energy of the host lattice due to formation of phases with slightly different lattice parameters and volume (most likely coming from different concentration of fluoride ions in the La_2NiO_{4+d} lattice).

The discharge potential plateau for the La_2NiO_{4+d}/Zn+ZnF₂ cell seems to be higher than La_2CoO_4/Zn+ZnF₂ by approximately 0.4 V. This can be explained based on the difference in the electronegativity of the transition metals of Co and Ni. Co and Ni are both in the period 4 in the periodic table with $3d$ electron configuration in the outer shell. However, Co and Ni lie in the group 9 and 10 of the periodic table, respectively, i.e. Ni has a higher atomic number. The ionic radius of the transition metal cations in the same row would decrease with increasing atomic number, as the electrons in the outer shell are more strongly attracted by atomic nuclei, resulting in a higher energy consumption or release during electron transfer [49]. Therefore, charge and discharge plateaus for La_2NiO_{4+d} appears to occur at higher potential than the La_2CoO_{4+d} against the Zn+ZnF₂ anode material.

The XRD measurements show a good structural recovery of the initial compound after discharge of the La_2NiO_{4+d}/Zn+ZnF$_2$ cell (experimental conditions for discharging are provided in the **Figure 5-30**). Comparing the XRD patterns of the cathode composite after charging (up to 120 mAh/g) and discharging in **Figure 5-30b** reveals that after the discharge of the La_2NiO_{4+d}/Zn+ZnF$_2$ cell, the high fluorine content phase (with a lattice parameter c in the order of $\sim$ 15.2 Å) cannot be detected. Analysis of XRD data shows that two low fluorine content phases are formed after the discharge process (**Figure 5-30b**). The first phase (phase 1) is very similar to original La_2NiO_{4+d} before charging but with a larger cell volume (cell volume of the phase 1 (after discharge) = 379.80(15) Å^3 and the initial La_2NiO_{4+d} = 378.07(6) Å^3) and a relatively small orthorhombic distortion (a = 5.4598(10) Å, b = 5.5097(15) Å, c = 12.6256(28) Å). The second phase is a combination of four intermediate phases with c-lattice parameters ranging from $c \sim$ 12.8087 Å to $c \sim$ 13.5621 Å (for the sake of simplicity an average phase has been shown instead of all the mentioned phases and is named as "phase 2" in **Figure 5-30b**). The weight ratio of phase 1 to phase 2 is about 3:2. Comparing the discharge electrochemical and structural behavior of La_2NiO_{4+d} and La_2CoO_{4+d} (**Figure 5-23**) suggests a principal similarity between the behavior of the both systems: Discharging results in disappearance of the highly fluorinated phase (with the lattice parameter c in the order of $\sim$ 15.2 Å), instead a relatively broad reflection (shoulder) appears in the lower 2θ° side of the main reflection of La_2MO_{4+d} (M = Co, Ni) which indicates formation of low fluorine content phases with much smaller lattice parameter c values as compared to the high fluorine content phase.

In **Figure 5-31a** the effect of overcharging the cell on the discharge capacity can be observed. For La_2CoO_{4+d} it is observed that the overcharging the cell results in a discharge capacity loss. For the La_2NiO_{4+d} cell the same behavior can be observed: Overcharging the cell (towards region III) leads to a capacity drop by 15 mAh/g ($\sim$ 22%). The capacity fading can be even more severe at higher cycle numbers (will be discussed in section 5.4.2.1). Such a capacity fading may arise from carbon oxidation and consequently deterioration of the conductivity of the cell.

As discussed, increase in the discharge current density (absolute value) generally results in capacity loss. **Figure 5-31b** shows that increasing the absolute discharge current density to 12 μA/cm^2 (5 times higher) resulted in a potential drop and capacity loss by ca. 0.3 V and 20 mAh/g, respectively.

It is worth mentioning that a La_2NiO_{4+d} cell with Zn+ZnF$_2$ as the counter electrode has a higher discharge potential by approximately 0.5 V compared to that against Pb+PbF$_2$ anode material composite (**Figure 5-31c**). This is in well agreement with the difference in the standard reduction potentials of Zn^{2+} 2e$^-$ → Zn (-0.76 V [92]) and Pb^{2+} + 2e$^-$ → Pb (-0.12 V [92]). Furthermore, the obtained discharge capacity at the first cycle for La_2NiO_{4+d}/Pb+PbF$_2$ is significantly lower as compared to Zn+ZnF$_2$ by almost 30 mAh/g at the same experimental condition suggesting that using Zn/ZnF$_2$ counter electrode can significantly improve the energy density of the cell.
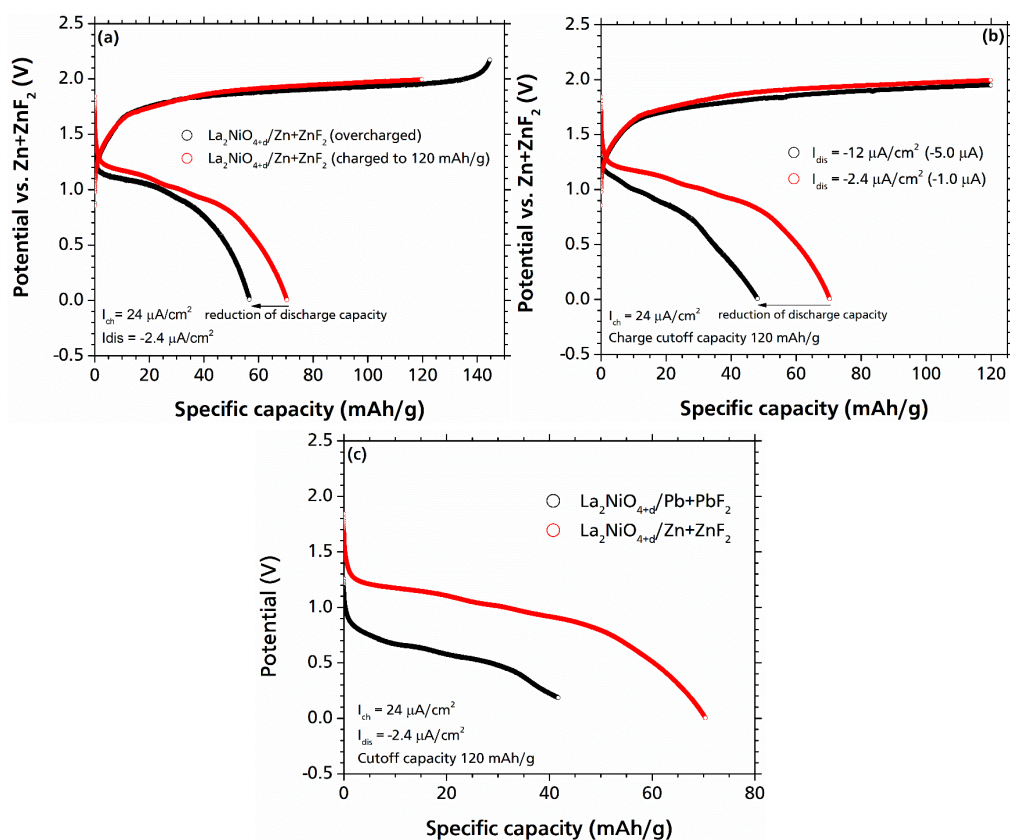
Figure 5-31. (a) Effect of overcharge on the discharge capacity (at an operational temperature of 170 °C and charge/discharge current density of 24/-2.4 µA/cm²); **(b)** effect of discharge current density on discharge capacity (T = 170 °C, I_{ch} = 24 µA/cm², cutoff capacity = 120 mAh/g); and **(c)** a comparison between the discharge behavior of La₂NiO₄₊d against Zn+ZnF₂ and Pb+PbF₂ anode composite materials (at T = 170°C, I_{ch} = 24 µA/cm², I_{dis} = -2.4µA/cm² and cutoff capacity of 120 mAh/g).

5.3.3   MSb₂O₄ (Schafarzikite-type Structure) Cathode Materials

Schafarzikite-type structure compounds (**Figure 5-32**) with a general composition of MSb₂O₄ [119] are known for their antiferromagnetic properties with various different magnetic structures [120, 121] and possess a tetragonal symmetry (space group $P4_2/mbc$). The structure can be understood as being built up of chains of edge-linked MO_6 octahedra running along the [0 0 1] direction; the chains are connected via trigonal pyramidal SbO_3 units. Recent studies have shown that it is possible to fluorinate variants of this material (**Figure 5-32**), which contain Fe^{2+} on the M site, via topochemical reactions [78, 119, 122]. The proposed mechanism for fluorination is based on two key principles [78]. Firstly, the phase must possess Fe^{2+} to act as the redox active center whilst the degree of oxidation is limited to the amount of Fe^{2+} to be oxidized to Fe^{3+}. Furthermore, it has been shown that there is a propensity for the Sb^{3+}, which line the walls of the channel, to also play a part in the oxidation process depending on the atmosphere and conditions that the material is heated in [123]. This material can be of interest for making electrode materials for FIBs because of the mechanism for the inclusion of excess fluoride ions within the channel of the structure (**Figure 5-32**). Therefore, it can be considered to be a 1D intercalation material, like olivine type materials for lithium ion batteries [124]. This is in contrast to the layered ordering of intercalated fluoride ions within Ruddlesden-Popper-type structure compounds that has been discussed in the previous sections, which are 2D intercalation materials (like layered materials, e.g., LiCoO₂ for lithium ion batteries [125]).

In this section the electrochemical fluorination/de-fluorination of the schafarzikite-type structure compounds $Mg_{0.5}Fe_{0.5}Sb_2O_4$ and $Co_{0.5}Fe_{0.5}Sb_2O_4$ will be discussed. The structural changes upon electrochemical fluorination will be compared to the previous data coming from chemical fluorination method, using of F_2 as the fluorinating agent, showing insertion of ca. 0.5 fluoride ions into the vacant channels of the structures [78]. This corresponds to a specific capacity of around 36 – 39 mAh/g. Although the obtained discharge capacity of these compounds is not promising compared to Ruddlesden-popper-type structure compounds, the electrochemical fluorination can still be considered as a safer alternative fluorination method (compared to F_2 gas as a fluorinating agent).
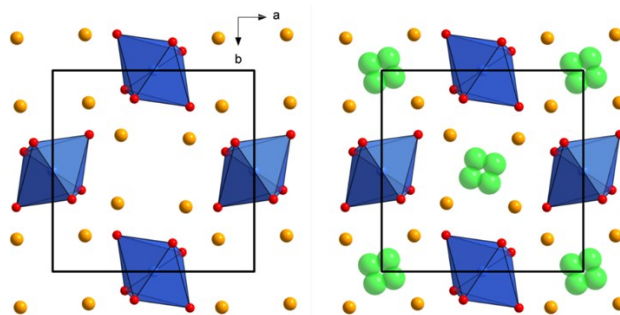
Figure 5-32. Schematic presentation of the non-fluorinated MSb_2O_4 (left) and fluorinated $MSb_2O_4F_y$ (right) Schafarzikite-type structure. Sb orange, M (Fe, Co) blue, O red, F (partially occupied to ~ 15 %) green. Structures are based on data provided in reference [78].

5.3.3.1 Electrochemical Fluorination

The electrochemical charge curves of $Mg_{0.5}Fe_{0.5}Sb_2O_4$ and $Co_{0.5}Fe_{0.5}Sb_2O_4$ vs. $Pb+PbF_2$ are shown in **Figure 5-33**. The charge curves show three distinct regions: First a sharp increase in the potential up to $\sim$ 1.5 V, followed by a plateau between roughly 1.6 – 1.7 V. In the third region a sharp voltage increase is observed, indicating the end of the electrochemical reaction. Within the first region, no reaction of the Schafarzikite-type structure compounds could be identified, and structural changes were mainly found to occur in region 2.

The lengths of the observed charging plateaus in region 2 obviously exceeded the maximum theoretical capacity (for insertion of 0.5 fluoride ions) significantly. This can be explained from an overlap of the charging plateau with the oxidation of the conductive additive of carbon [36] (the amount of carbon added can contribute to a charging capacity which is at least 10 times higher than the absolute capacity originating from the amount of the Schafarzikite-type structure compounds). As found previously, this can impede the discharging (de-fluorination) of the target compounds due to the destruction of the electronic conductive matrix under formation of C-F species [36]. For $Co_{0.5}Fe_{0.5}Sb_2O_4$ the plateau region is significantly longer, which might be explained by a higher catalytic activity for the fluorination of carbon.
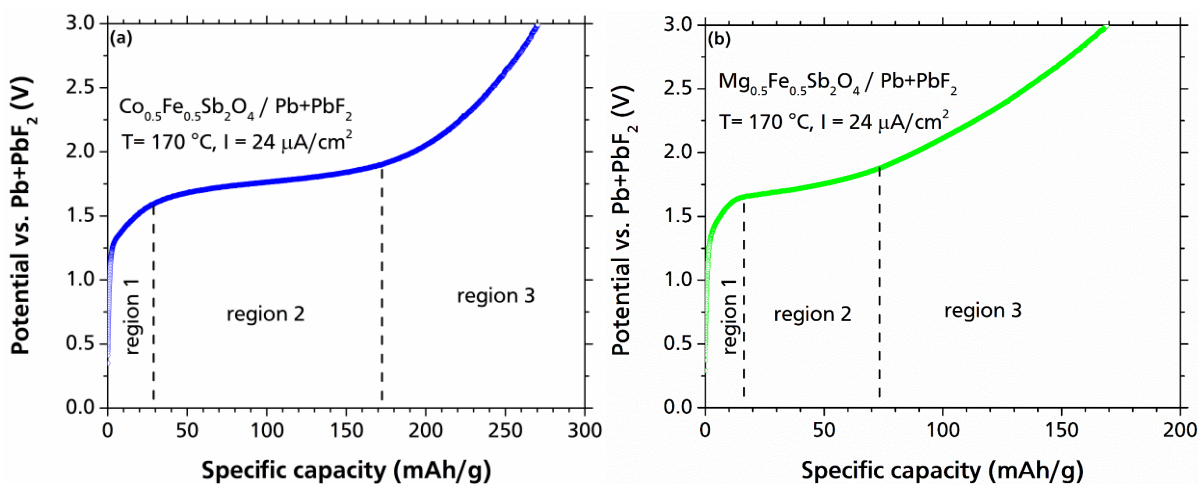
Figure 5-33. Electrochemical charging curves of (a) $Co_{0.5}Fe_{0.5}Sb_2O_4$; (b) $Mg_{0.5}Fe_{0.5}Sb_2O_4$ at T=170 °C, I = 24 µA/cm² (10 µA). The figures have been reproduced (with some modifications) from our open access publication in [21].

Furthermore, the potential for the fluorination of the compounds with Schafarzikite-type structure, which only involves the $Fe^{2+} \rightarrow Fe^{3+}$ redox couple [78], is higher than $Mn^{3+} \rightarrow Mn^{4+}$ and $Co^{2+} \rightarrow Co^{3+}$ in LaSrMnO₄ and La₂CoO₄₊d respectively ($\sim$ 1.2 V for LaSrMnO₄ and $\sim$ 0.9 V for La₂CoO₄₊d against a composite of Pb+PbF₂ at the same condition, and this would not be expected intuitively from the electrochemical series [92]. This could either result from an unusually high electrochemical potential of Fe^{2+} within this structure type, or from higher overpotentials for the Schafarzikite-type structure as compared to the Ruddlesden-Popper-type compounds. This might be related to a different dimensionality of the fluoride ion sublattices (channels (1D) of fluoride ions in MSb₂O₄ vs. planes (2D) of fluoride ions in A₂MO₄ (A = Sr, La)).

The change in lattice parameters after electrochemical fluorination can be followed visually from the changes of the reflection positions in **Figure 5-34**, where the refined values given in **Table 5-18** are consistent with the changes found by de Laune *et al* [78]. The small difference in the lattice parameters between the chemically fluorinated and electrochemical fluorination samples (**Table 5-18**) could arise from slightly different amounts of intercalated fluorine within each sample. In the previous sections, different cutoff capacities in combination with a quantitative phase analysis of the fluorinated and non-fluorinated phase were used in order to determine the detailed amount of intercalated fluoride ions for La₂MO₄₊d (M = Co, Ni) and LaSrMnO₄. However, such attempts did not prove to be successful in this study; here either the lattice parameters of the unreacted starting product were observed, or the lattice parameter had changed within errors to the ones obtained after charging to 3 V. No non-fluorinated parent phase was found in addition to the fluorinated phase.

It is also noted that the cell parameters after fluorination possess a pseudocubic metric $(a/(c \times \sqrt{2}) \sim 1$, see **Table 5-18**). This ratio is well reproduced regarding the chemical and electrochemical fluorination processes. The possibility that a higher cubic symmetry could exist for fluorinated compounds by testing possible supergroups of the tetragonal Schafarzikite-type structure was investigated. However, a re-arrangement of polyhedra within the Schafarzikite-type structure to result in 3-fold rotational axis (required for cubic symmetry) does not appear possible. Therefore, no simple group-subgroup relationships could be identified, which would explain a change to cubic symmetry, and this is in agreement with previous symmetry analyses [86].
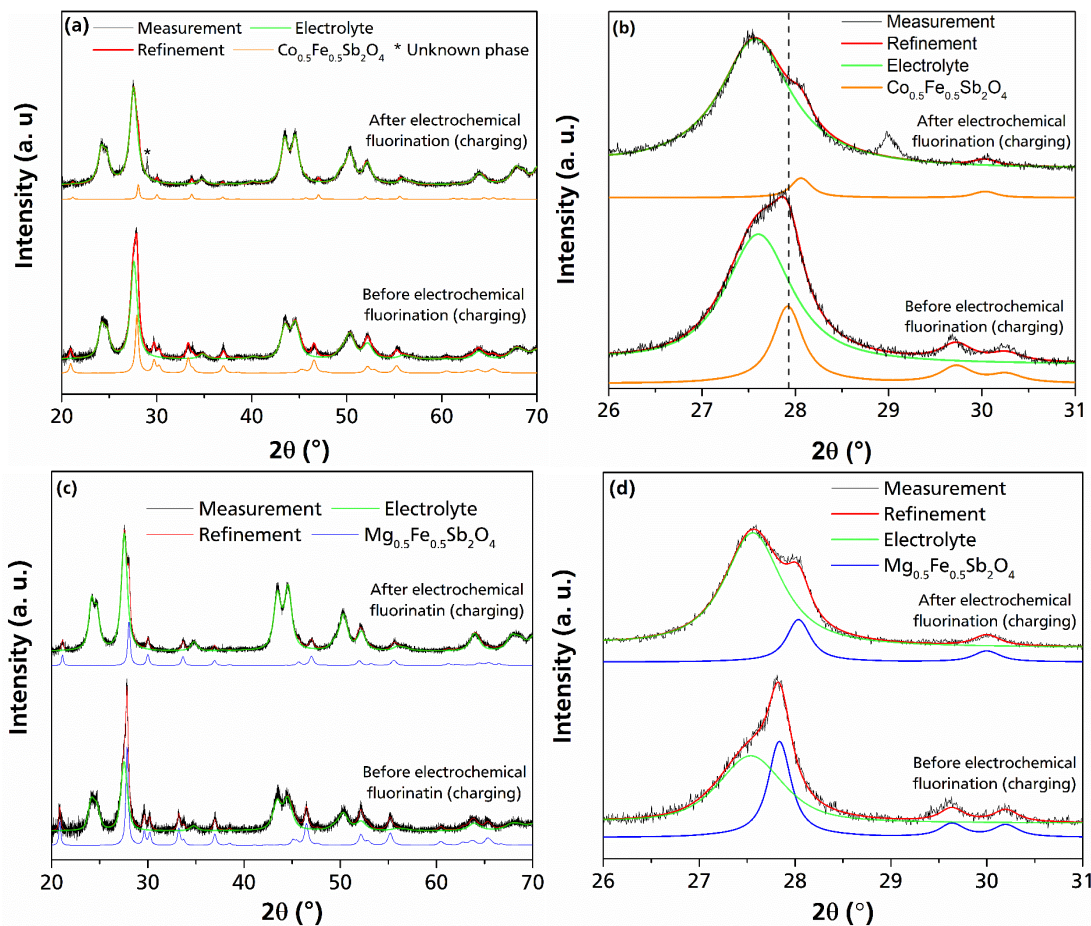
Figure 5-34. XRD patterns and refinements of (a, b) $Co_{0.5}Fe_{0.5}Sb_2O_4$ before charging and after charging up to 3 V at T = 170 °C and I = 24 µA/cm² (10 µA); (c, d) $Mg_{0.5}Fe_{0.5}Sb_2O_4$ before charging and after charging up to 3 V at T = 170 °C and I = 24 µA/cm² (10 µA).

Table 5-18. Lattice parameters of $Co_{0.5}Fe_{0.5}Sb_2O_4$ and $Mg_{0.5}Fe_{0.5}Sb_2O_4$ (space group P4$_2$/mbc) as observed before and after various electrochemical treatments or heating.

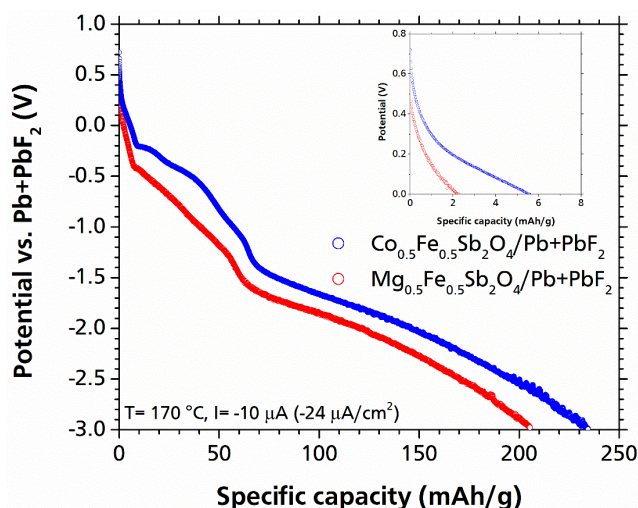|	$Co_{0.5}Fe_{0.5}Sb_2O_4$			$Mg_{0.5}Fe_{0.5}Sb_2O_4$		
	a (Å)	c (Å)	$a /(c \times \sqrt{2})$	a (Å)	c (Å)	$a /(c \times \sqrt{2})$
initial material (before milling)	8.5365(3)	5.9302(2)	1.018	8.5420(3)	5.9303(2)	1.018
within composite (mixture before heating)	8.5469(13)	5.9382(13)	1.018	8.5442(14)	5.9313(12)	1.019
after heating (at 170 °C for 24 h)	8.5449(12)	5.9383(13)	1.017	8.5520(14)	5.9290(12)	1.020
after electrochemical fluorination (charge)	8.4392(18)	5.9838(28)	0.997	8.4396(13)	5.9766(16)	0.999
after chemical fluorination [78]	8.4270(3)	5.9501(2)	1.001	8.4537(6)	5.9451(3)	1.005
after electrochemical de-fluorination ("forced discharge")"	8.5492(13)	5.9279(13)	1.019	8.5124(11)	5.9423(11)	1.013

5.3.3.2 Electrochemical de-Fluorination

Once fully charged, the discharge profiles of the both cathode materials were investigated as shown in **Figure 5-35**. The discharge capacities were found to be very low, in the order of ~ 6.0 mAh/g (corresponding to ~ 0.08 F⁻) and 3.0 mAh/g (corresponding to ~0.04 F⁻) for

$Co_{0.5}Fe_{0.5}Sb_2O_4$ and $Mg_{0.5}Fe_{0.5}Sb_2O_4$, respectively (according to **Figure 5-35**). It is worth noting that further reduction in the discharge current density does not significantly influence the discharge capacity and potential of the $(Co/Mg)_{0.5}Fe_{0.5}Sb_2O_4$ vs. $Pb+PbF_2$ cells. However, on discharging to negative potentials against Pb/PbF_2, lattice parameters were found to change back close to the values observed for the starting materials (see **Table 5-18** and **Figure 5-36a and b**). For $Mg_{0.5}Fe_{0.5}Sb_2O_4$, the difference in lattice parameters compared to the unreacted compound ($\Delta a = 0.0318$ Å and $\Delta c_{MFSO} = 0.0110$ Å) is larger (although overall small) as compared to $Co_{0.5}Fe_{0.5}Sb_2O_4$ ($\Delta a_{CFSO} = 0.0023$ Å and $\Delta c_{CFSO} = 0.0103$ Å), which might indicate the presence of residual fluoride ions within the compound (see **Table 5-18** and **Figure 5-36c and d**). From the shape of the (forced) discharge curve, one can also derive a principle fluorine content in the order of 40 – 50 mAh/g, which corresponds to 0.5 – 0.6 fluoride ions and is in well agreement with the fluorine contents found for the chemical fluorination reactions [78].

From the performed experiments, it can be concluded that the Schafarzikite-type structure allows for reversible intercalation/de-intercalation of fluoride ions by electrochemical fluorination. Therefore, the electrochemical fluorination method can be considered as a safer alternative method (instead of the routine chemical routes) for fluorination/de-fluorination of the Schafarzikite-type compounds. Also, the Schafarzikite-type structure compounds show a better structural reversibility (over intercalation/de-intercalation) as compared to complete disordered compounds without dimensionality such as $BaFeO_{2.5}$ [30], highlighting the issue of dimensionality of the lattice. Nevertheless, the discharge capacities of the compounds with Schafarzikite structure were found to be very low (as compared to Reuddlesden-Popper-type structures), rendering the proposed Schafarzikite-type structure compounds not to be considered as promising cathode materials for FIBs. Therefore, Schafarzikite-type structure compounds were not considered for extended battery cycling experiments.

Figure 5-35. Discharge (forced discharge) curves of $Co_{0.5}Fe_{0.5}Sb_2O_4$ and $Mg_{0.5}Fe_{0.5}Sb_2O_4$ against Pb+PbF₂ anode material at T=170 °C, I= ±24 µA/cm² (10 µA).

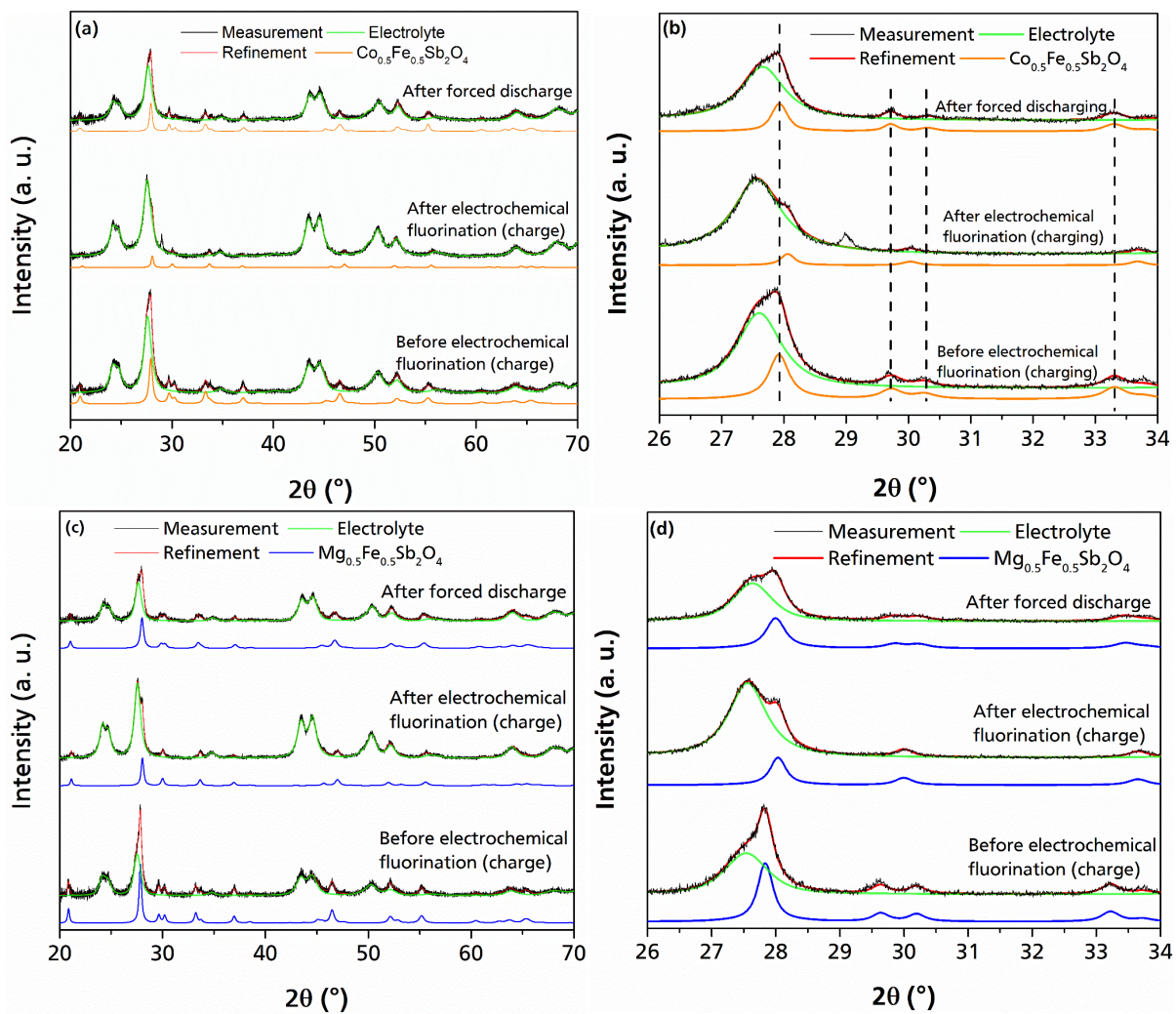**Figure 5-36.** Respective XRD measurement after discharge/forced discharge of (a, b) Co$_{0.5}$Fe$_{0.5}$Sb$_2$O$_4$ cell; (c, d) Mg$_{0.5}$Fe$_{0.5}$Sb$_2$O$_4$ vs. Pb+PbF$_2$ at T=170 °C, I= ±24 µA/cm^2 (10 µA).

5.3.4 Summary

In this chapter the electrochemical fluorination/de-fluorination and the structural reversibility of the Ruddlesden-Popper (K_2NiF_4) type compounds of $LaSrMO_4$ (M = Mn, Fe, and Co) and La_2MO_{4+d} (M = Co, Ni) as compared to $(Co/Mg)_{0.5}Fe_{0.5}Sb_2O_4$ with Schafarzikite-type structure were discussed. The results reveal that the electrochemical fluorination can be considered as a safer alternative fluorination method with a higher degree of flexibility as compared to the traditional chemical fluorination routes with fluorinating agents such as F_2, AgF_2, CuF_2, etc. If the fluorinated state can be prepared by chemical methods, the structural changes due to the electrochemical fluorination are in a good agreement with that after chemical fluorination. Furthermore, fluorine insertion seems to be more controllable within the electrochemical fluorination method as the number of inserted fluorides can be regulated by cutoff conditions (potential/capacity). This can be important when it comes to preparation of metastable compounds. More importantly, it is shown that the intercalation of fluoride ions is fully reversible.

The fluoride ions would layer-wise fill up (staged fluorination) the interlayers of $LaSrMnO_4$ (as it is observed for chemical fluorination of this compound). However, similar staged fluorination could not be observed for the $La_2(Co/Ni)O_{4+d}$ compounds: There, the electrochemical fluorination results in a direct expansion of the lattice parameter c to $\sim 15.2 - 15.5$ Å which indicates partial filling of both interlayers with absence of long-range ordering of vacancies and inserted ions. There is a possibility that such an occupancy of the interlayers in La_2MO_{4+d} compounds arises from the partial occupancy of the interlayers by oxygen ions leaving less space for fluoride ions in each interlayer. Nevertheless, intermediate phases (with smaller lattice parameter $c \sim 14.0$ Å, corresponding to occupation of only one interlayer) can be obtained by chemical methods and also after discharge for La_2MO_{4+d} compounds.

A major problem engaged with the electrochemical cells is overlapping side reactions (which mainly seem to be carbon fluorination (oxidation)) and the desired electrochemical reaction. This is evident in all of the mentioned redox systems. Efforts for replacing the carbon conductive particles with another electronic conductor (such as carbon nanotubes, silver or indium tin oxide) have been done, though other alternatives did not serve as an appropriate replacement for carbon conductive particles.

The charge cutoff conditions (potential/capacity) play a significant role in the electrochemical performance of the La_2MO_{4+d} cathode (composite) materials. This dependency is less prominent for the $LaSrMO_4$ compound as lower cutoff capacity/potential conditions resulted in even lower discharge capacities. Regardless of the cutoff conditions very low discharge capacities could be obtained for $LaSr(Fe/Co)O_4$ cathode materials.

Figure 5-37 provides an overview about the discharging behavior of the various materials after the first charging cycle. Results in **Figure 5-37** suggest that the discharge capacity that is obtained for La_2NiO_{4+d} is the highest among all the materials that have been tested: The highest discharge capacity that has been so far obtained for an intercalation-based cathode material for FIB measured to be about 70 mAh/g (accompanied by a high average discharge potential of ~ 1.2 V) for La_2NiO_{4+d} against a $Zn+ZnF_2$ anode composite material. The discharge capacity for $LaSrMnO_4$ cathode materials found to be around 30 mAh/g (**Figure 5-37**), however, only small structural reversibility can be observed after discharging. Nevertheless, excellent structural reversibility could be obtained upon further discharging towards negative potentials.

The lowest discharge capacity was obtained for the Schafarzikite-type structures ($Co_{0.5}Fe_{0.5}Sb_2O_4$) which was measured to be around 5 mAh/g (**Figure 5-37**). $LaSr(Co/Fe)O_4$ cathode composites materials show poor performance in respect of discharge capacity, though, still better than the Schafarzikite-type structure compounds. From this, a high potential of the K_2NiF_4-type compounds (especially La_2MO_{4+d}) for being considered as promising intercalation-based cathode materials for FIBs can be concluded.

In light of the fact that Ruddlesden-Popper-type structure compounds of La_2MO_{4+d} showed the best electrochemical performance in terms of discharge capacity and energy density, extended cycling behavior of La_2NiO_{4+d} and La_2CoO_{4+d} compounds have been further investigated. Further, carbon side reaction within $La_2(Co/Ni)O_{4+d}$ cathode materials and its effect on cycling performance have been studied. The results will be discussed in the next chapter.
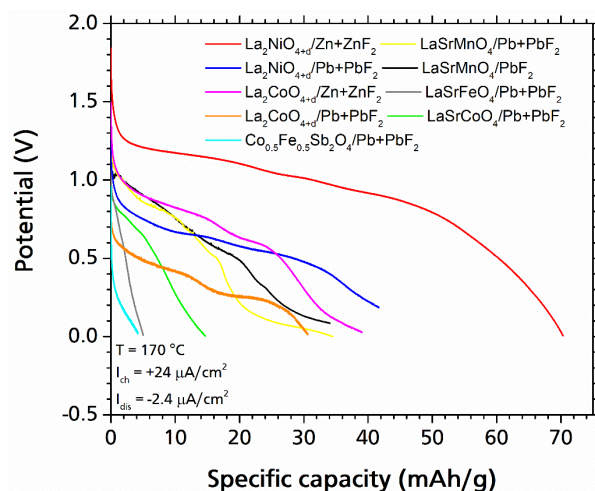

Figure 5-37. A comparison between the discharge curves of the cathode materials that has been introduced in this chapter. All the measurements have been done at 170 °C with charge / discharge current densities of +24 μA/cm² (10 μA) / -2.4 μA/cm² (-1.0 μA). The cutoff capacity/voltage has been setup in such a way that the highest discharge capacity is obtained.

5.4 Controlling the Carbon Side Reaction and Optimization of Cycling Performance

As shown in chapter 5.3, low Coulombic efficiencies were observed in the first cycle of almost all the cells (e.g. $\sim 60\%$ for La_2NiO_{4+d} and La_2CoO_{4+d} against Zn/ZnF_2). This indicates the presence of side reaction(s), which overlaps with the desired electrochemical reaction. There are some persuasive evidences suggesting that carbon oxidation (fluorination) is the main side reaction which results in destruction of the conductive matrix leading to a significant deterioration of the conductivity within the electrode composite. This impairs the cycling performance of the cell. A strategy to improve the cycling performance, is to somehow control the side reaction(s) by regulating the charge cutoff conditions. In this chapter evidences that confirm occurrence of the carbon side reaction in $La_2(Co/Ni)O_{4+d}$ systems (as the most promising candidates) will be discussed.

5.4.1 Carbon Side Reaction

Figure 5-38a shows a charging curve of a carbon cathode composite material (consist of 10% of C mixed with 90% of $La_{0.9}Ba_{0.1}F_{2.9}$ electrolyte material) against $Pb+PbF_2$ counter electrode material. The starting charge potential was measured to be around 1.2 V and the charge plateau seems to be sloping with an overall charge specific capacity of almost 450 mAh/g (charge cutoff potential considered to be 3.5 V and the specific capacity is calculated with respect to the active C mass). The observed charge plateau (**Figure 5-38a)** coincides with the potential range in which side reaction severely occurs within the cathode composites.

The results of cyclic voltammetry measurements of a $C/Pb+PbF_2$ cell (**Figure 5-38b**) show a very broad peak at the first cycle at around 2.1 V with a shoulder (at the left side) which starts at ~ 1.2 V in the forward direction. Note that this peak cannot be seen with such a large intensity after the first cycle. Also no cathodic peak can be detected in the backward direction, highlighting the fact that the peak in the forward direction (at ~ 2.1 V) can be attributed to an irreversible anodic reaction (carbon fluorination is not a reversible process within this system). The starting potential for the anodic peak (**Figure 5-38b**) is in the same range as the charge plateau of carbon fluorination (see **Figure 5-38a**). Considering the potential stability window of the $La_{0.9}Ba_{0.1}F_{2.9}$ electrolyte (0.5 – 6 V against Li [36]), together with the stability of the electrolyte that has been shown by XRD (only very small fluctuations can be detected for lattice parameters of the electrolyte within $La_2(Co/Ni)O_{4+d}$ (**Table 7-1**, **Table 7-2**) and $LaSr(Co/Fe)O_4$ (**Table 5-7**) systems during charging, but larger changes can be found for $LaSrMnO_4$, especially after 2 V, please see **Table 7-3**), occurrence of the irreversible anodic peak (in the cyclic voltammograms of carbon) due to electrolyte decomposition is implausible. Therefore, it can be concluded that the anodic reaction arises from the carbon oxidation reaction and most likely formation of fluorinated carbon (CF). This is studied in more detail (will be discussed later in this chapter) in the context of changes of the oxidation state of the carbon by charging a $La_2NiO_{4+d}/Zn+ZnF_2$ cell. Cyclic voltammograms of $La_2NiO_{4+d}/Pb+PbF_2$ cell shows (**Figure 5-38c**) the same anodic reaction in the forward direction, however, the anodic peak is shifted towards lower potential range (around 1.6 V). Thus, it is assumed that the active cathode materials may act as a type of catalyst for the fluorination (oxidation) of the carbon. The carbon fluorination leads to the formation of covalent bonds with sp^3 carbon and result in a strong decrease of the conductivity of the system with an increase of the band gap [126]. This can strongly influence the cycling performance of the cell.
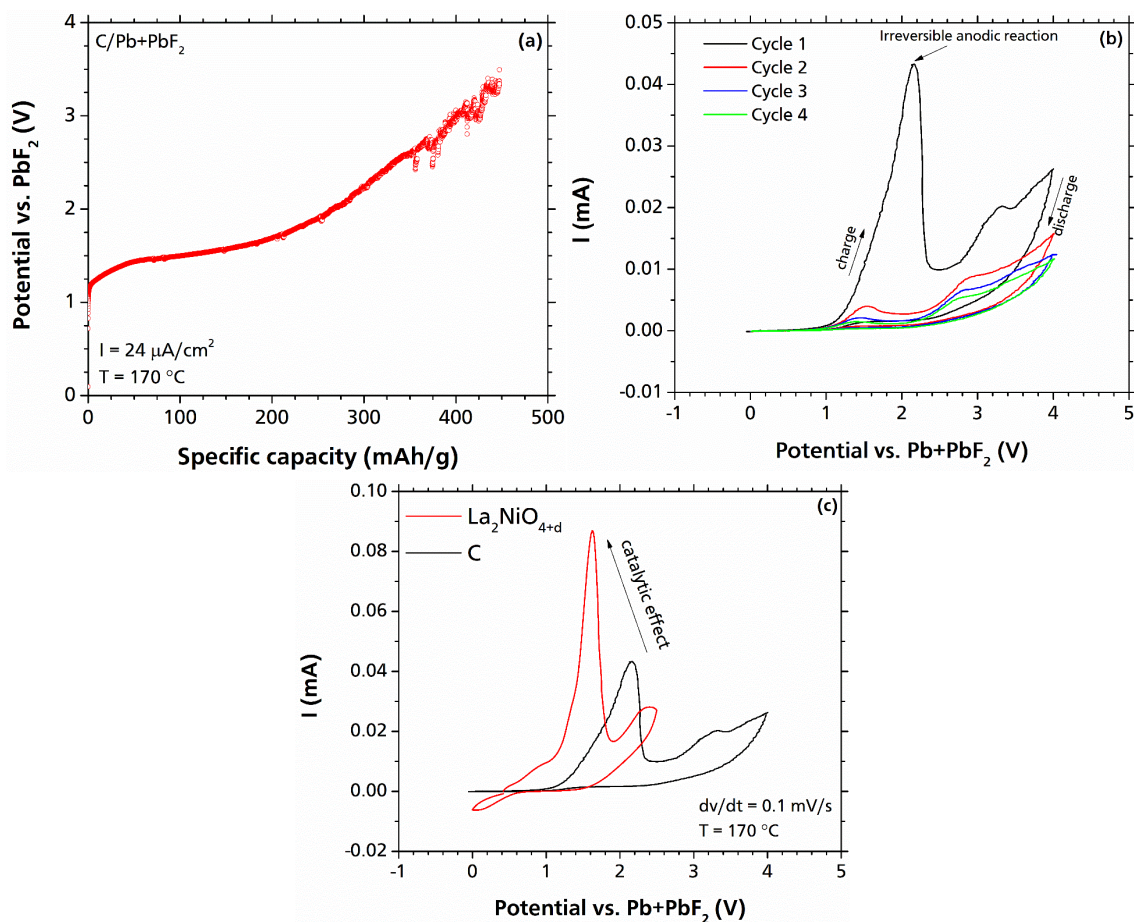
Figure 5-38. (a) Charge curve for a C/Pb+PbF$_2$ cell which was charged at 170 °C with a current density of 24 µA/cm^2 (10 µA) (the specific capacity is calculated based on the carbon active mass); **(b)** cyclic voltammograms of C/Pb+PbF$_2$; **(c)** cyclic voltammograms of La$_2$NiO$_{4+d}$ and C versus Pb+PbF$_2$. All of the cyclic voltammetry experiments were performed at T = 170 °C and scan rate = 0.1 mV/s.

5.4.1.1 Carbon Side Reaction in the La$_2$NiO$_{4+d}$ Cells

Figure 5-39 shows cyclic voltammograms of La$_2$NiO$_{4+d}$ against Zn+ZnF$_2$ and Pb+PbF$_2$ anode materials. Broad anodic peaks in the forward direction can be observed at ~ 2.4 V and ~ 1.7 V for La$_2$NiO$_{4+d}$ against Zn+ZnF$_2$ and Pb+PbF$_2$, respectively. As it is shown in the previous section, this peak can partly be assigned to oxidation of the carbon and can only be seen in the first cycle. Therefore, these broad peaks correspond to an irreversible anodic (side) reaction on the charge step, mostly carbon decomposition. It should be taken into consideration that no cathodic peak can be observed if potentials above ~ 2.4 V against Zn+ZnF$_2$ (~ 1.7 V against Pb+PbF$_2$) have been reached in the anodic reaction (as can be seen in **Figure 5-39**). However, reversible cathodic peaks can be observed in the backward direction upon limiting the cycling potential range to ~ 2 V for Zn+ZnF$_2$ (**Figure 5-39a**) and ~ 1.5 V for Pb+PbF$_2$ (**Figure 5-39b**). In this case the cathodic reversible peaks can be detected in the backward direction at ~ 1 V and ~ 0.6 V for Zn+ZnF$_2$ and Pb+PbF$_2$, respectively (see **Figure 5-39**). It is worth noting that the potential range for the irreversible anodic (side) reaction which is detected by cyclic voltammetry, corresponds to a rapid rise in the potential in the charge curves of La$_2$NiO$_{4+d}$/M+MF$_2$ (M = Zn, Pb) cells (**Figure 5-40a** and **Figure 5-41a**).
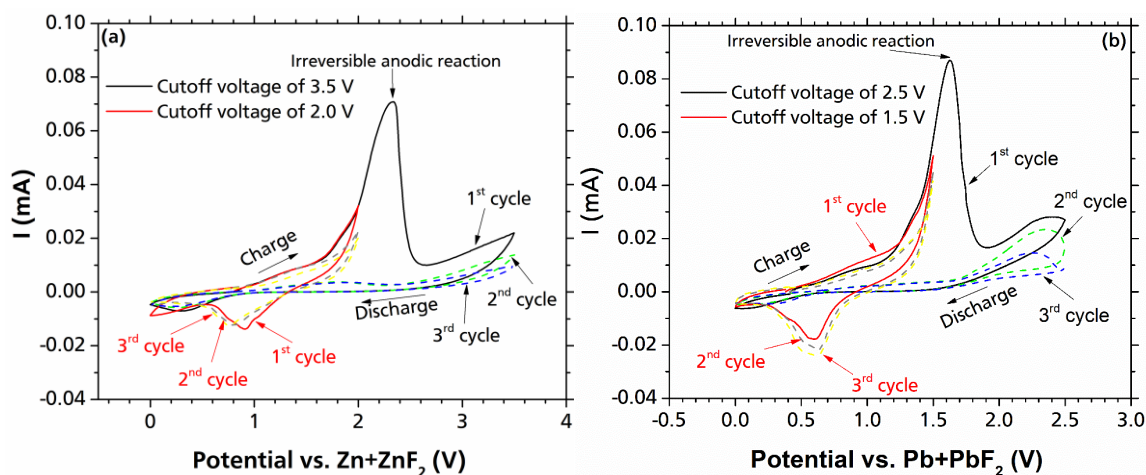
Figure 5-39. Cyclic voltammograms of La$_2$NiO$_{4+d}$ vs. (a) Zn+ZnF$_2$; (b) Pb+PbF$_2$. All the measurements have been performed at an operational temperature of 170 °C with a scan rate = 0.1 mV/s.

To investigate further on the nature of the irreversible anodic reactions which are observed via cyclic voltammetry, galvanostatic electrochemical impedance spectroscopy (EIS) has been performed for the La$_2$NiO$_{4+d}$ cell against M+MF$_2$ (M = Zn, Pb) during the first charging step. The Nyquist plots (for La$_2$NiO$_{4+d}$ against both anode composites of Zn+ZnF$_2$ and Pb+PbF$_2$) at low charge capacities consist of a semicircle at high frequencies (>10 kHz) corresponding to the impedance of the solid electrolyte and interface resistance between the electrolyte and the electrode material [85] followed by a straight line with a slope of ~ 45° at frequencies lower than 10 Hz arising from the diffusion processes within the active electrode materials [127], often referred to as Warburg impedance [64] (**Figure 5-40b**, **Figure 5-41b**). It is worth emphasizing that the semicircles corresponding to the solid electrolyte and interface resistances cannot be resolved, which also becomes evident from the Bode plots shown in **Figure 5-40c** (for La$_2$NiO$_{4+d}$/Zn+ZnF$_2$ cell) and **Figure 5-41c** (for La$_2$NiO$_{4+d}$/Pb+PbF$_2$ cell). It is found that a change in the impedance behavior can be observed when the cell is charged higher than ~ 130 mAh/g (against Zn+ZnF$_2$, **Figure 5-40a** and **b**). Therefore, two models have been used in order to fit the Nyquist curves (both models can be found in **Figure 5-40d**): For low capacities (lower than ~ 130 mAh/g, corresponds to ~ 2 V against Zn/ZnF$_2$) "Model 1" which consists of a RC circuit (C1 in parallel to R1) in series with a constant phase element (CPE2) (in order to describe the solid electrolyte plus interface resistance as well as the diffusion of fluoride ions into electrode materials) has been used. The second model (which is labeled as "Model 2" in **Figure 5-40d** and differs from the first model by the use of a second resistance R2 in parallel to the CPE2) is used for the charge potentials higher than 2.0 V which corresponds to charge capacities higher than ~ 130 mAh/g. The slope of the straight line in the low frequency region (corresponds to the Warburg element) rapidly increases once the potential of the cell increases sharply. Such an increase in the slope of the Warburg element is an indication for the development of a capacitive behavior which is accompanied by a sharp increase in the CPE α exponent values.

The changes of the CPE exponent α on charging has been plotted for La$_2$NiO$_{4+d}$/Zn+ZnF$_2$ and La$_2$NiO$_{4+d}$/Pb+PbF$_2$ which can be found in **Figure 5-40a** and **Figure 5-41a**, respectively. The change of alpha at the potential jump is in plausible agreement with the CV studies, which indicates that reactions arising above this potential are irreversible: The values of the exponent α are around 0.5 at lower potential region, before occurrence of the irreversible side reaction at the end of region (II)/region (III) which is accompanied by a rapid jump in the potential

(**Figure 5-40a** and **Figure 5-41a**). The exponent value of 0.5 is indicative for a Warburg-type behavior. Then the α exponent experiences a rapid increase up to ~ 0.8 for both $La_2NiO_{4+d}/Zn+ZnF_2$ and $La_2NiO_{4+d}/Pb+PbF_2$ cells at the onset of the region (III), where the potential in the charge curve rises sharply. This results in a blocking effect and significantly deteriorates the conductivity of the cell and consequently the discharge and cycling performance.

The resistivity R1 also increases for both $La_2NiO_{4+d}/Zn+ZnF_2$ and $La_2NiO_{4+d}/Pb+PbF_2$ cells in the capacity range which corresponds to occurrence of the irreversible side reaction (**Figure 5-41d**). The change in the impedance behavior of the $La_2NiO_{4+d}/Pb+PbF_2$ cell occurs at a higher charge capacity range compared to the $La_2NiO_{4+d}/Zn+ZnF_2$ cell. Therefore, the anode material seems to also have some impacts on the impedance behavior of the cell in correlation to the side reactions. This might be explained based on higher overpotentials that are introducing to the cell due to the internal resistances of the anode material. In chapter 5.5 it will be shown that higher overpotentials might be introduced to the system upon using $Zn+ZnF_2$ as the anode material.

Figure 5-40. (a) Results of the galvanostatic electrochemical impedance spectroscopy (EIS) and variations of α exponent by charging of the La_2NiO_{4+d} cell against $Zn+ZnF_2$ anode material at an operational temperature of 170 °C; (b) respective Nyquist curves at different charge capacities ($La_2NiO_{4+d}/Zn+ZnF_2$ cell); (c) respective Bode curves at different charge capacities ($La_2NiO_{4+d}/Zn+ZnF_2$ cell); (d) Equivalent circuits models that have been used in order to fit the impedance data.

To highlight the role of the carbon additive, XPS measurements of the C1s emission line were performed. On extended charging, additional broad high energy signals are appearing, in addition to a shift of the binding energy of the main sharp carbon signal by approximately 0.5 eV (see **Figure 5-42**) indicates an increasing oxidation (fluorination) of the carbon (or of a neighboring carbon atom) [128, 129]. To highlight this oxidation, the area-weighted average binding energy of each state-of-charge were calculated, which increases strongly with increased charging (see **Figure 5-42b**). It can be assumed that this would result in an increasing insulating behavior of the carbon additive on increased formation of oxidized C-O and/or C-F species. The partial fits for all the samples as well as details on the fitting procedure together with further partial spectra are shown in the Appendix (section 7.6). Further, XPS measurements did not serve to analyze the change of the Ni oxidation state due to the strong surface coverage of the $La_2NiO_{4.13}$ particles with electrolyte and carbon additive. This may be due to the fact that even partial coverage of the active cathode material by the solid electrolyte and the carbon additive prohibits a detailed analysis of the changes of the $La_2NiO_{4.13}$ particles on charging by means of surface sensitive techniques such as XPS, since the spectra become strongly dominated by the carbon and electrolyte species.
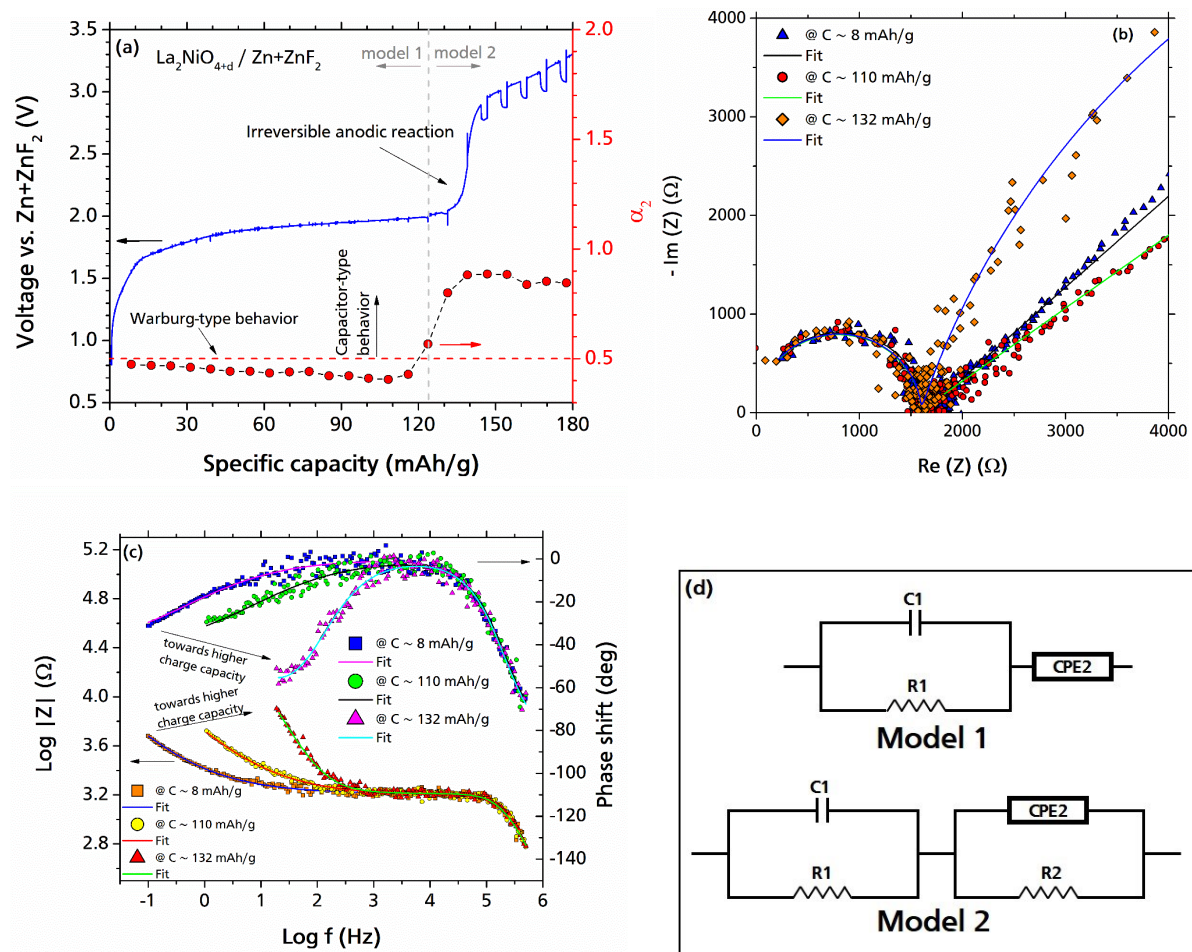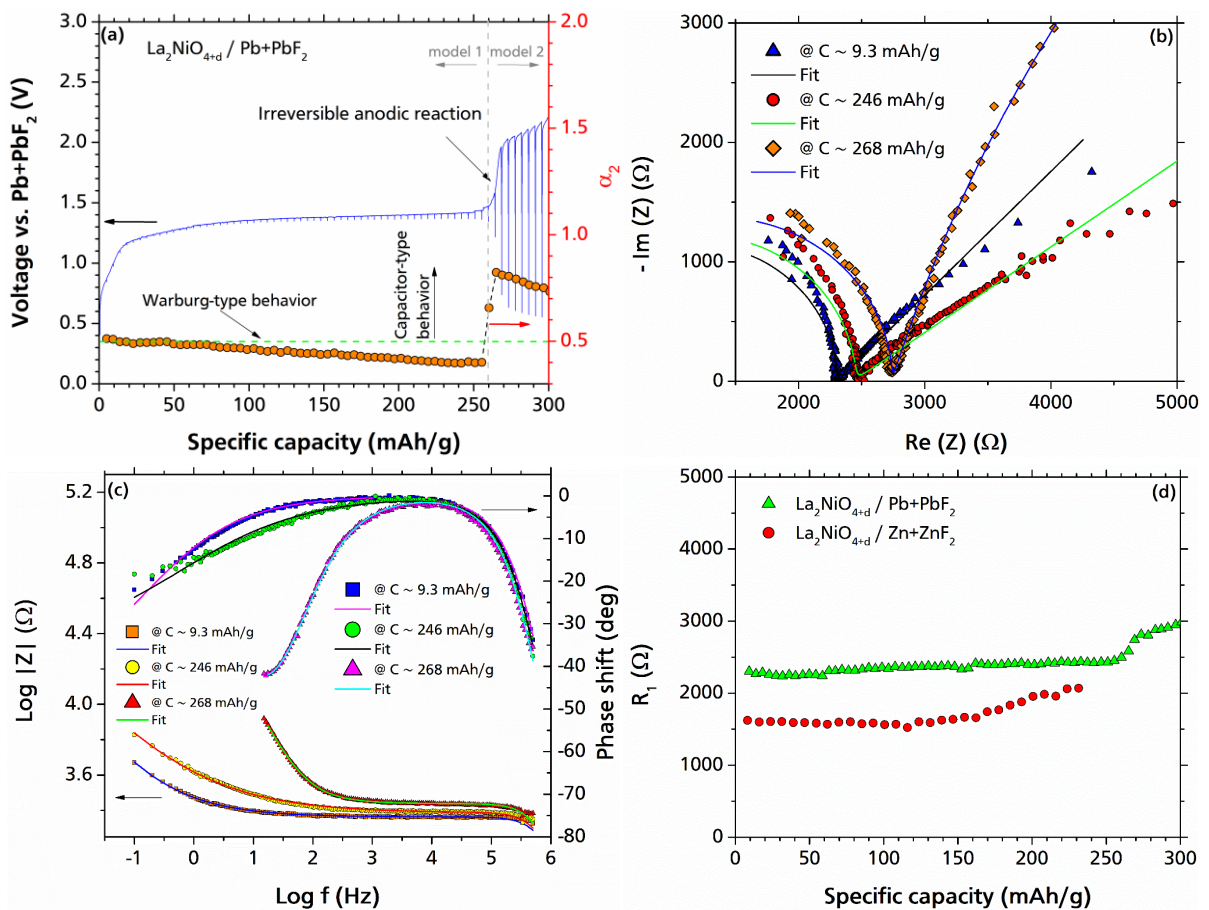

Figure 5-41. (a) Results of the galvanostatic electrochemical impedance spectroscopy (EIS) and variations of α exponent by charging of the electrochemical La_2NiO_{4+d} cell against Pb+PbF₂ anode material at an operational temperature of 170 °C; (b) respective Nyquist curves at different charge capacities (La_2NiO_{4+d} / Pb+PbF₂ cell); (c) respective BODE curves at different charge capacities (La_2NiO_{4+d} / Pb+PbF₂ cell); (d) variations of R₁ values by specific capacity for La_2NiO_{4+d} against Zn+ZnF₂ and Pb+PbF₂. The fittings have been performed according to the models that have been proposed in Figure 5-40d.
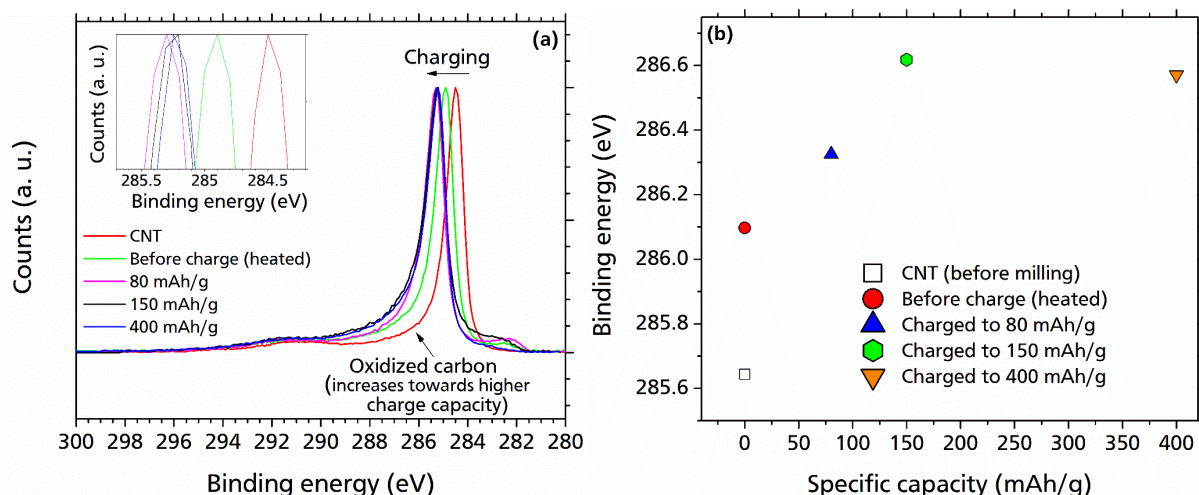
Figure 5-42. (a) XPS measurements (background corrected) of the C1s emission line on the carbon nanotube before mixing/milling (CNT) and samples before charge (heated at 170 °C inside an Ar-filled glovebox for 6 h) and after charge at different cutoff capacities of 80, 150 and 400 mAh/g; (b) changes of the area-weighted average binding energy of the C1 emission versus charge capacity for CNT and the samples before (heated) and after charge. For charged cells were: T = 170 °C and I = 24 μA/cm^2.

From the experiments performed, it is clear that the degree of oxidized (fluorinated) species increases within region (II) and (III); parts of the carbon (for preparation of the La_2NiO_{4+d} electrode material carbon nanotubes has been used) are already oxidized at potentials where the fluorination of $La_2NiO_{4.13}$ also takes place, i.e., within region (II), but within this range no strong increase in the impedance of the cell can be observed. At the transition to region (III) as well as within region (III), there seems to be a change in the principle impedance behavior of the cell (change from resistive to capacitive), which would imply that in this region the electrical conductivity of the carbon must be severely deteriorated. This can be correlated with previous studies: (1) Li et al. [130] have shown that fluorination starts at the defect sites of the carbon and then continues also to other sites. (2) Yue et al. have demonstrated that increasing degree of fluorination (increasing amount of defects) results in a strong decrease of the conductivity of carbon nanotubes [131]. This would be in principle agreement with the data recorded: Within region II, defect states of the carbon, which are induced to an even larger extent during the milling process, are likely to be fluorinated first; the electronegative fluoride ions at these former defect sites cause the change of the binding energy of the main sp^2 carbon signal due to their strong inductive effect. However, this would not result in a further decrease of conductivity, since those defects had broken the sp^2 networks of the carbon nanotubes already after milling. On increasing the degree of fluorination in region III (increase of oxidized carbon species), the sp^2 network of the carbon gets distorted even further by the fluorination of regular carbon sites, which would lead to an ongoing decrease of conductivity, hindering electron transfer to the active cathode material.

5.4.1.2 Carbon Side Reaction in La_2CoO_{4+d} Cells

Galvanostatic EIS measurements have also been performed for La_2CoO_{4+d}/M+MF$_2$ (M = Zn, Pb) cells in order to have a better understanding on the effect of the side reactions in relation to the electronic conductivity of the electrodes. The results of the EIS measurements can be found in **Figure 5-43**.

The Nyquist plots of La_2CoO_{4+d} vs. $Pb+PbF_2$ and $Zn+ZnF_2$ at different charge capacities can be found in **Figure 5-43b** and **d**, respectively. The general shape of the Nyquist plots for La_2CoO_{4+d} against both of the anode materials are quite similar and more or less like the Nyquist plots of $La_2NiO_{4+d}/M+MF_2$ cells (**Figure 5-40b** and **Figure 5-41b**): A semicircle at high potential range followed by a straight line with a slope of 45° at low frequency range. As it is discussed before, the straight line in low frequency region can be an indication for Warburg impedance which corresponds to diffusion processes within the electrode/the electrochemical reaction [132] which is very common in (solid-state) batteries [127]. For fitting the impedance data the models that have been proposed in **Figure 5-40d** were used: For the $La_2CoO_{4+d}/Pb+PbF_2$ cell "Model 1" has been used up to a charge capacity of ~ 255 mAh/g. At higher charge capacities the behavior of the cell at low frequency range deviates from a Warburg element (which has been fitted by a CPE element in "Model 1") and therefore a resistor has been added to "Model 2" for a better fitting (for the $La_2CoO_{4+d}/Zn+ZnF_2$ cell "Model 1" can be used only up to a charge capacity of almost 120 mAh/g).

Figure 5-43a and **c** show the variations of real resistivity (R_1) values by charge specific capacities for both $La_2CoO_{4+d}/Pb+PbF_2$ and $La_2CoO_{4+d}/Zn+ZnF_2$ cells, respectively. The R_1 values for both cells stay constant by charge capacity before roughly 60 mAh/g and more or less are equal to the resistivity of the electrolyte (see **Figure 5-43b**) suggesting that the conductivity of the cell is not influenced by the electrode materials. Then there is a sharp increase in the real resistivity after almost 60 mAh/g suggesting that the side reactions such as electronic matrix decomposition lead to a significant reduction in the conductivity. Above capacities of ~ 70 mAh/g the real resistivity increases linearly by capacity for both of the cells, nevertheless, the resistivity increases much sharper for the $La_2CoO_{4+d}/Zn+ZnF_2$ cell as compared to the $La_2CoO_{4+d}/Pb+PbF_2$ cell (**Figure 5-43a** and **c**). This may arise from a higher internal resistivity of the Zn/ZnF_2 anode material as compared to Pb/PbF_2 (chapter 5.5). It can be concluded that charging the cell beyond ~ 65 mAh/g leads to a significant increase in resistivity arising from proceeding the irreversible side reactions which highly influence the discharging profile.

It is worth noting that the impedance behavior of the $La_2NiO_{4+d}/M+MF_2$ cells are different from that in the $La_2CoO_{4+d}/M+MF_2$ cells. In fact, for the $La_2CoO_{4+d}/M+MF_2$ cells, the irreversible carbon side reaction results in a significant change in the real resistivity of the cell, though, the changes in the CPE α_2 exponent are less severe as compared to the $La_2NiO_{4+d}/M+MF_2$ cells (**Figure 5-43d**): For $La_2CoO_{4+d}/M+MF_2$ cells, the α_2 values fluctuate around 0.5 but for the $La_2NiO_{4+d}/M+MF_2$ cells the α_2 values increase rapidly up to 0.8 upon an intensive occurrence of the irreversible side reaction (**Figure 5-40a**, **Figure 5-41a**). However, the variations of the real resistivity (R_1) values are less severe for the $La_2NiO_{4+d}/M+MF_2$ (**Figure 5-41d**) in comparison to that within the $La_2CoO_{4+d}/M+MF_2$ cells.
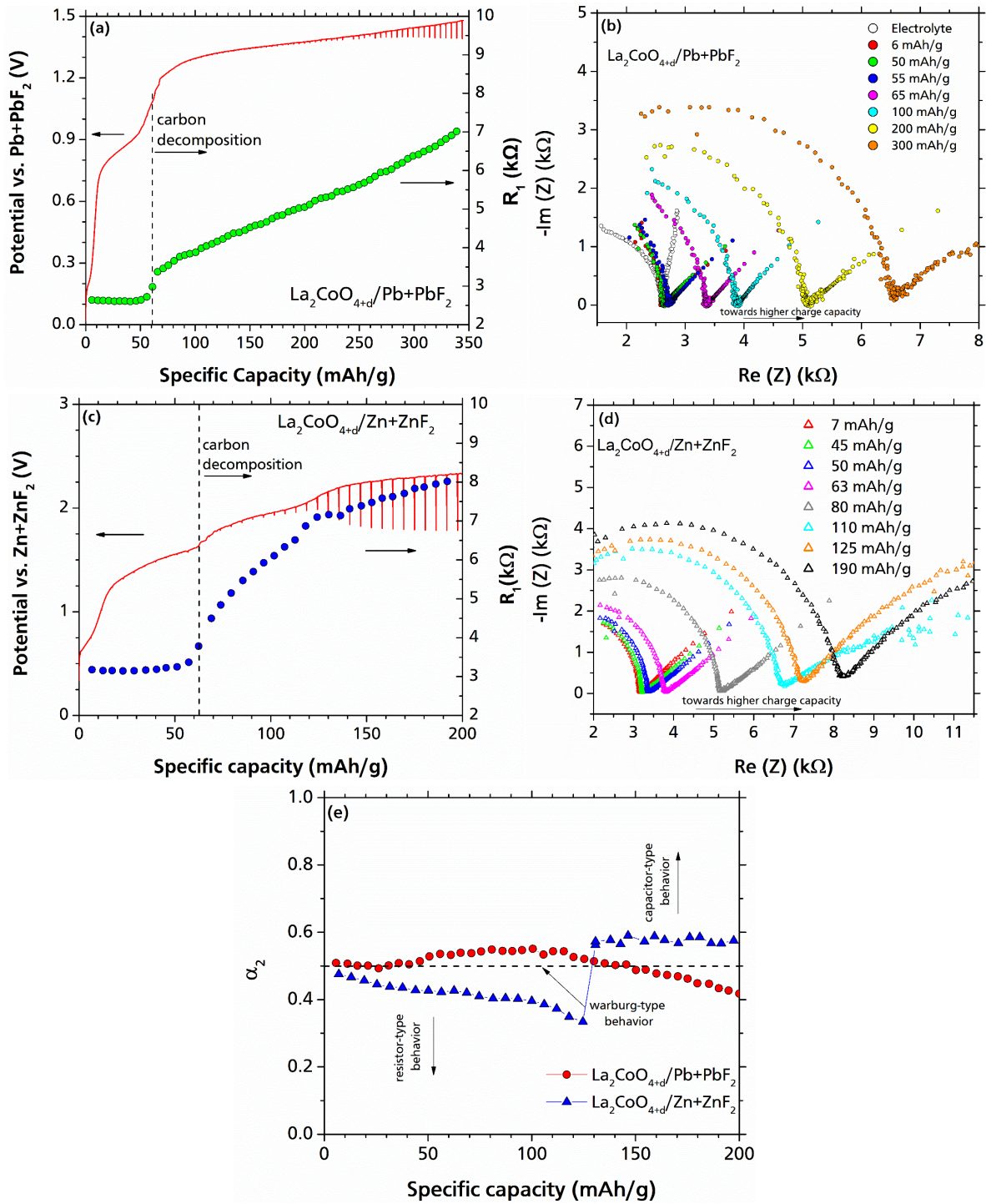
Figure 5-43. (a) Variations of R_1 values by charge capacity in a La_2CoO_{4+d}/Pb+PbF$_2$ cell; (b) respective Nyquist plots at different charge capacities for La_2CoO_{4+d} vs. Pb+PbF$_2$ cell; (c) variations of R_1 values by charge capacity in a La_2CoO_{4+d}/Zn+ZnF$_2$ cell; (d) respective Nyquist plots at different charge capacities for La_2CoO_{4+d} vs. Zn+ZnF$_2$ cell; (e) variations of α_2 exponent values for La_2CoO_{4+d}/M+MF$_2$ (M = Pb, Zn) cells. All the measurements have been performed at 170 °C with a charge current of 10 μ (24 μA/cm^2).

5.4.2 Cycling Performance

5.4.2.1 Cycling Performance of the La$_2$NiO$_{4+d}$ Cells

Taking into accont the findings of the previous section, the cycling conditions of the La$_2$NiO$_{4+d}$/Zn+ZnF$_2$ cells were optimized in order to obtain stable cycling behavior. Therefore, two cutoff criteria were set for the charging reaction: (1) a cutoff voltage of 2.3 V was chosen as a result from the impedance and cyclic voltammetry studies. Note that the evidences confirm the fact that within the La$_2$NiO$_{4+d}$ system the carbon side reaction happens even before $\sim$ 2.3 V as it is discussed previously, though, the conductivity of the cell is not significantly impaired below $\sim$ 2.3 V against Zn+ZnF$_2$. (2) different cutoff capacities of 30, 50, 80 and 120 mAh/g were then tested in order to find the optimized cycling conditions of the cell. **Figure 5-44** summarizes the electrochemical cycling behavior of the La$_2$NiO$_{4+d}$/Zn+ZnF$_2$ cells with respect to the different cutoff charge capacities. It should be taken into consideration that for all the measurements the absolute value of discharge current density of 12 μA/cm^2 was used in order to speed up the process which can take up to a few months (even with increased current). This shows that the La$_2$NiO$_{4+d}$ cathode material is less sensitive towards higher C-rates as compared to other K$_2$NiF$_4$-type compounds.

Clearly, the choice of the cutoff charging capacity can significantly influence the cycling stability. For the lower cutoff capacities of 30 and 50 mAh/g, the discharge capacity increased continuously to 30 and 50 mAh/g during the first 5 – 10 cycles (**Figure 5-44a, b,** and **e**). After those cycles, a Coulombic efficiency with an average of 98 – 99% (average Coulombic efficiency for the whole cycling range: 97.68% and 95.44% for charge cutoff capacities of 30 and 50 mAh/g, respectively) was obtained (**Figure 5-45**). The low Coulombic efficiency at the early cycle numbers most likely originates from the presence of the side reactions and shows that the cells can be activated to become cycling stable by the more careful subsequent charging/discharging within the first cycles.

For the cutoff capacity of 30 mAh/g the discharge capacity is highly stable at least over a range of 220 cycles with a Coulombic efficiency of almost 100 % (average Coulombic efficiency throughout the whole cycling range is 97.68%). However, after the cycle number 140, a small capacity loss can be observed followed by some discharge capacity fluctuations (**Figure 5-45a**); it should be taken into consideration that until then the battery was already running for almost 3 months, and it is hard to trace back the detailed origin of the capacity loss. Nevertheless, even then the overall capacity loss is still below 20%. For the cell with the cutoff capacity of 50 mAh/g the discharge capacity is very stable up to the cycle number 40 (**Figure 5-44b**), again with nearly 100% Coulombic efficiency (average Coulombic efficiency through the whole cycling range is 95.44%, see **Figure 5-45b**). After the 40th cycle (up to cycle number 60) the potential reaches to the critical cutoff capacity of 2.3 V, and the irreversible anodic reaction cannot be avoided any more. Therefore, the charge capacity reduces slightly, which consequently also results in a reduction of the discharge capacity. After the 60th cycle, a significant capacity drop below 30 mAh/g has been observed, which is followed by an increasing capacity loss due to continued destruction of the conductive matrix.

The charging plateau increases towards higher potentials while the potential of the discharging plateau lowers on increased cycling, resulting in a decrease of energy efficiency. Apparently, this is more severe the higher the cutoff capacity was chosen. This shows that some processes could happen at the interfaces (e.g., electrolyte to electrode material or carbon to electrode

material), which increase the internal impedance [133] of the cell and therefore lower the energy efficiency. However, this could also originate from overpotentials arising within the conversion-based anode material (which suffer from much larger volume changes which will be discussed in the next chapter) and must not necessarily be related to the intercalation based cathode material.
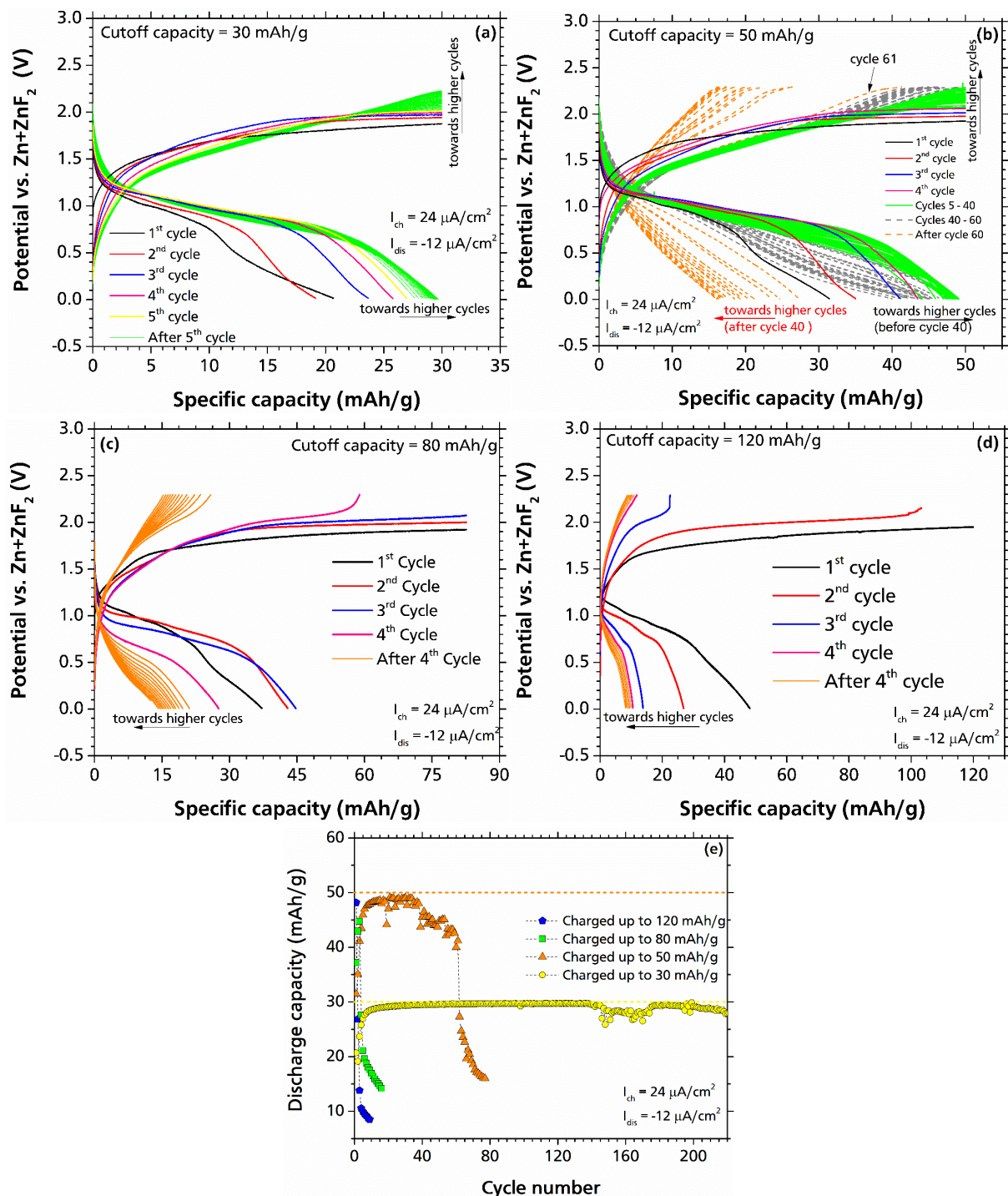
Figure 5-44. Cycling curves of the La₂NiO₄₊d/Zn+ZnF₂ cells cycled at T = 170 °C, I$_{ch}$ = +24 μ/cm², I$_{dis}$ = -12 μ/cm² and cutoff charge potential = 2.3 V at various cutoff capacities of (a) 30 mAh/g (for better depiction, only the first 80 cycles are shown); (b) 50 mAh/g; (c) 80 mAh/g; and (d) 120 mAh/g; (e) variations of the discharge specific capacity with cycle number for all of the mentioned cells.
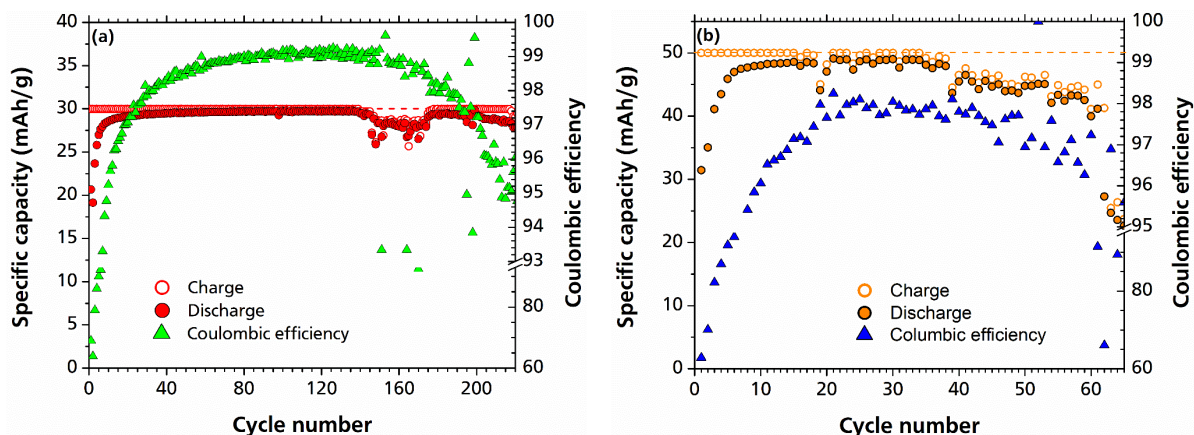
Figure 5-45. Charge/discharge capacities together with Coulombic efficiency against cycle number for the cells with the cutoff capacities of (a) 30 mAh/g; (b) 50 mAh/g at the experimental conditions that have been mentioned in Figure 5-44.

The obtained cycling performances of La_2NiO_{4+d} outperform the best cycling results for the other intercalation-based cathode materials such as La_2CoO_{4+d} (which will be discussed later in this chapter) with respect to cycling stability, effective capacity and cell potential. The reason for the stability can be understood as a result from the limiting of the charging capacity resulting in a limited oxidation of carbon within the first few cycles facilitating the maintenance of electrically conducting interfaces. Based on this, it is concluded that the careful oxidation of the carbon matrix results in a better separation of the $La_2NiO_{4.13}/La_2NiO_{4.13}F_{1.59}$ plateau from the side reaction, which enables the high cycling stability.

Interestingly, the phase behavior at extended cycling numbers is also different to what was observed for the first charge/discharge (with a cutoff capacity of 120 mAh/g). At cycle number 10 (for the cell with cutoff capacity of 30 mAh/g) the XRD measurements show that 2 high fluorine content phases with increased lattice parameter c (**Figure 5-46a**) coexist with a few other low fluorine content phases with different c parameters ranging from ~13.0 Å to 14.3 Å which the average phase (phase 2) has been shown in **Figure 5-46a**. For the cell with the cutoff capacity of 50 mAh/g also similar structural changes could be observed at higher cycle numbers (**Figure 5-46b**).

Quantitative calculations based on the Rietveld method show that the sum of the relative weight percent of the high fluorine content phases (after charge up to 30 mAh/g) are about 36%, however, almost 13% of those high fluorine content phases still can be found after the discharge (at 10th cycle) (**Table 5-19**). Therefore, ca. 23% of the active cathode material takes part in the redox reactions which corresponds to uptake of ~ 0.45 fluoride ions in total by the host compound. This is the amount of active fluoride charges corresponding to a specific capacity of 30 mAh/g for 100% Coulombic efficiency. The same argument is true for the cell with a cutoff capacity of 50 mAh/g after the 6th cycle: The summation of the relative fraction of the high fluorine content phases is around 45% of which almost 8% are retained after the discharge (see again **Table 5-19**). This shows participation of roughly 38% of the active cathode material in the redox reaction corresponding to uptake of ~ 0.76 F⁻. Since a Coulombic efficiency of close to 100 % is found, this would mean that $La_2NiO_{4.13}$ would have to take up approximately two fluoride ions ([0.45/23%] ≈ [0.76/38%] ≈ 2), which is in agreement with the structural changes found from the structural and compositional analysis of the charged state by ADT, XAS and EDX. In combination with the irreversibility of the side reaction of the carbon additives, it is concluded that the charging and discharging capacities at higher cycle numbers can be fully

assigned to the changes within the active cathode material $La_2NiO_{4.13}$. Therefore, it is important to note that the maximum capacity of $\sim 100 - 120$ mAh/g of the La_2NiO_{4+d} cathode material can be fully accessed within the contributing particles: A limiting of the charge capacity does not result in a limited homogenous overall degree of fluorination, i.e. the grains do not change from a homogenous composition of the un-fluorinated state $La_2NiO_{4.13}$ to a homogenous composition of a partly fluorinated state (e.g. $La_2NiO_{4.13}F_{0.4}$). Instead, the presence of highly fluorinated phases ($La_2NiO_{4.13}F_{1.59}$) in addition to nearly un-fluorinated particles is observed.
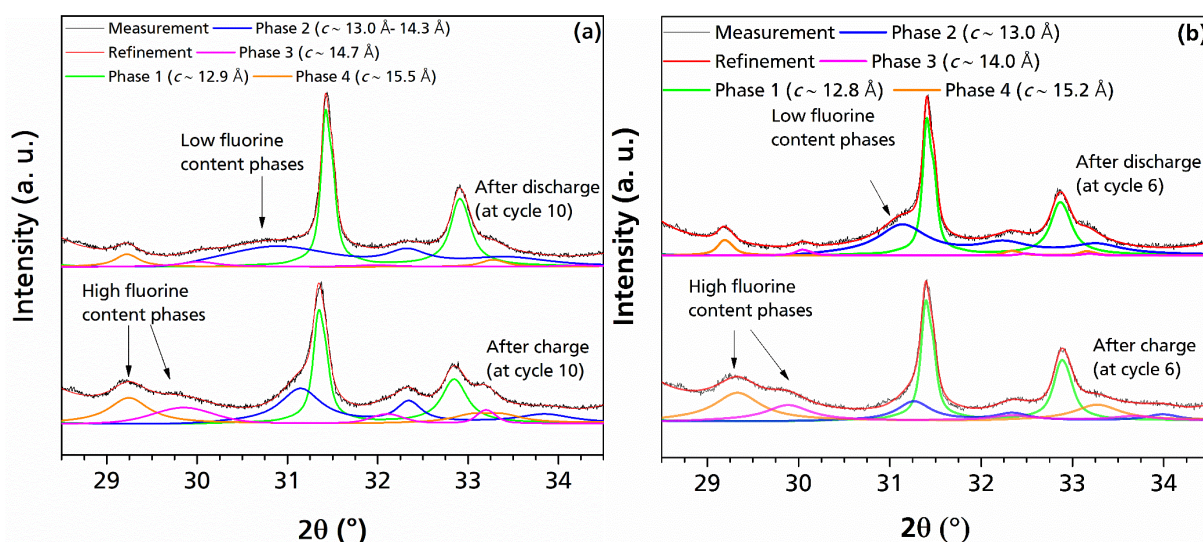
Figure 5-46. Excerpt of XRD measurements of the cathode materials for the La₂NiO₄₊d/Zn+ZnF₂ cells after charge and discharge (a) at 10th cycle for the charge cutoff capacity of 30 mAh/g; (b) at 6th cycle for the charge cutoff capacity of 50 mAh/g. The experimental conditions are mentioned in Figure 5-44.

Table 5-19. Relative fractions of the different phases of the La₂NiO₄₊d(Fy) active cathode material after charge and discharge against Zn+ZnF₂ (at T = 170 °C, Ich = +24 μA/cm², and Idis = −12 μA/cm²) at the 10th and 6th cycle for the cutoff capacities of 30 and 50 mAh/g, respectively.

	Phase 1 (low fluorine content phase) [%]	Phase 2 (low fluorine content phase) [%]	Phase 3 (high fluorine content phase) [%]	Phase 4 (high fluorine content phase) [%]	Summation of low fluorine content phases [%]	Summation of high fluorine content phases [%]
30 mAh/g (After charge)	32.7(±5)	31.1(±1)	26.8(±5)	9.5(±2)	63.5(±7)	36.3(±5)
30 mAh/g (After discharge)	47.1(±4)	40.5(±6)	4.8(±1)	7.6(±1)	87.6(±7)	12.4(±1)
50 mAh/g (After charge)	38.6 (±3)	15.7(±1)	19.4(±1)	26.2(±2)	54.4(±3)	45.7(±2)
50 mAh/g (After discharge)	45.8(±2)	46.3(±2)	1.5(±0.1)	6.3(±0.3)	92.1(±3)	7.9(±0.3)

By increasing the cutoff capacity to 80 and 120 mAh/g the capacity fading on increased cycling appeared to be higher. From **Figure 5-44c-e** it can be seen that for the cell with the charge cutoff capacity of 80 mAh/g the discharge capacity increases up to $\sim$ 46 mAh/g after three cycles; however, the cell experienced a severe capacity loss afterwards (**Figure 5-44c** and **e**). For the cell with the higher charge cutoff capacity of 120 mAh/g the first discharge capacity was measured to be $\sim$ 50 mAh/g. After 3 cycles, only 20 % of initial discharge capacity could be recovered (**Figure 5-44d** and **e**). This shows that lower cutoff capacities are preferable in order to improve their cycling behavior.

In order to investigate on C-rate dependency of the La_2NiO_{4+d} cells, a $La_2NiO_{4+d}/Zn+ZnF_2$ cell was cycled under different C-rates between C/8 – C for the cutoff capacity of 30 mAh/g which provides the highest cycle life of the cell. It should be taken into consideration that here the C-rate is calculated based on charge/discharge of the cell for 30 mAh/g within 1 h (which requires a current of 48.6 μA equal to 116.3 μA/cm^2). **Figure 5-47** shows the fact that by cycling the cell with a C-rate of C/8 ($I_{ch/dis}$ = 14.5 μA/cm^2) the obtained discharge capacities were $\sim$ 25 mAh/g with a potential plateau between $1 - 0.8$ V. Charge/discharge of the cell by a C-rate of C/6 (I = 19.37 μA/cm^2) resulted in an extra charge overpotential in the order of $\sim$ 0.2 V which is accompanied by a significant discharge potential drop (an average discharge potential drop of almost 0.5 V (**Figure 5-47a**)), though only a slight discharge capacity fading could be observed (**Figure 5-47b**). Increase in the C-rate up to C/4 (I = 29 μA/cm^2) led to a significant increase in the overpotential and the charge potential reached to the cutoff potential (2.3 V) at a much lower charging capacity (ca. 18 mAh/g) which resulted in a further discharge capacity loss (**Figure 5-47b**). Increase in the charge/discharge C-rate deteriorated further the charge/discharge capacity (less than 5 mAh/g) and was accompanied by a more drop in discharge potential.
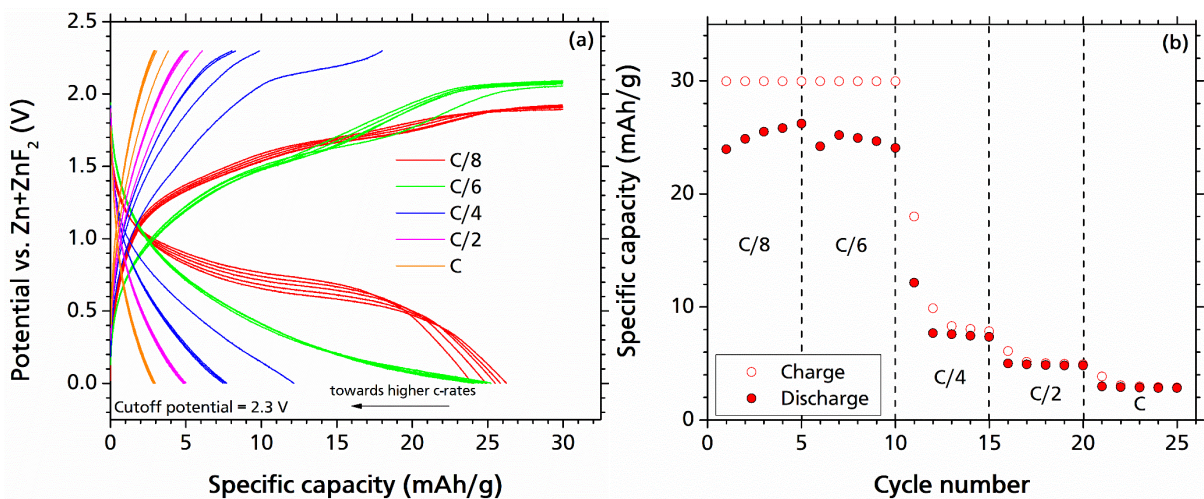
Figure 5-47. (a) Cycling curves of the **La₂NiO₄₊d/Zn+ZnF₂** cell at different C-rates; (b) respective specific charge/discharge capacity values against cycle number. The measurements were performed at T = 170 °C with equal charge and discharge current densities and a charge cutoff potential and capacity of 2.3 V and 30 mAh/g, respectively. Note that the C-rate here is defined as the charge/discharge current that is required to charge/discharge the cell for 30 mAh/g within 1 h (corresponds to I = 48.6 μA or 116.3 μA/cm²).

As discussed, charge overpotential increases (regardless of the cutoff conditions) by cycling of the cell (**Figure 5-44**). This increase in overpotential is more severe for higher cutoff capacities (e.g. 80 and 120 mAh/g). The introduced overpotentials may have different sources including the overpotentials arising from the conversion-based counter electrodes (anode materials). **Figure 5-48** shows an example on how one can improve the cycle life of a cell (using La_2NiO_{4+d} as the cathode material) by reducing the overpotentials arising from the conversion-based anode material: Using $Pb+PbF_2$ as the anode material results in less overpotentials on charging during the cycling (**Figure 5-48a**) and therefore a better cycle life can be observed as compared to a $La_2NiO_{4+d}/Zn+ZnF_2$ cell which was charged with the same cutoff capacity (70 mAh/g) at the same temperature and charge/discharge current density.

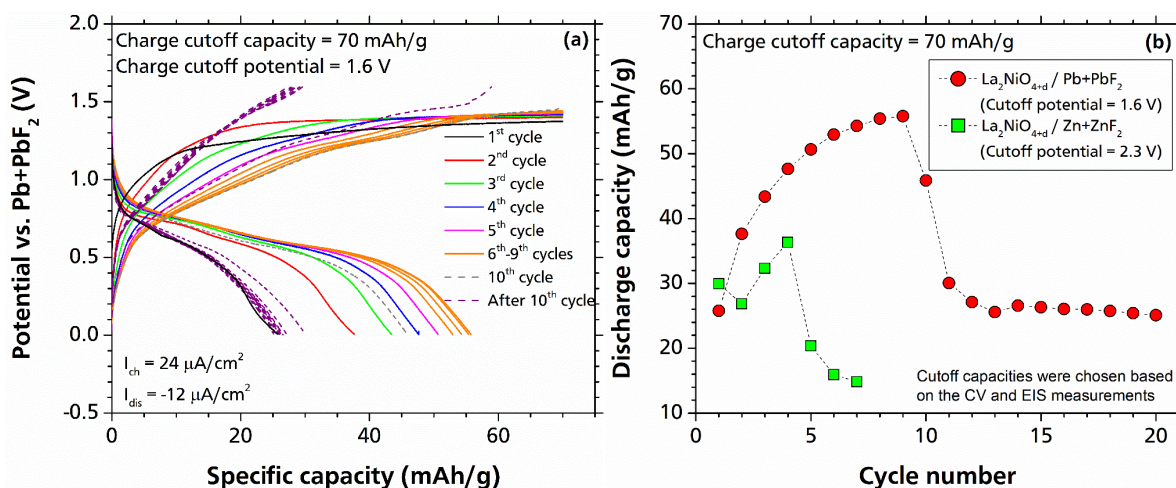**Figure 5-48. Cycling plots of $La_{2+d}NiO_4/Pb+PbF_2$ at T = 170 °C, I_{ch} = 24 µA/cm^2, I_{dis} = -12 µA/cm^2 and cutoff capacity and potential of 70 mAh/g and 1.6 V, respectively; (b) respective discharge capacity vs. cycle number in comparison to a $La_2NiO_{4+d}/Zn+ZnF_2$ cell with a charged cutoff capacity of 70 mAh/g at the same operational current and temperature. The charge cutoff potentials were chosen according to the CV and EIS studies in order to avoid destruction of the conductivity of the cell.**

5.4.2.2   Cycling Performance of the La_2CoO_{4+d} Cells

Figure 5-49a and **b** depicts the cycling curves of the $La_2CoO_{4+d}/Pb+PbF_2$ cells at cutoff capacities of 65 and 130 mAh/g, respectively. The cutoff capacities are selected in accordance with the impedance studies that have been discussed previously in this chapter. Overcharging the cell not only results in a reduction in the discharge capacity at the first cycle but also increases capacity fading at higher cycle numbers. In fact, the Coulombic efficiency at the first cycle for the cell that was charged up to 65 mAh/g is calculated to be almost 50% while it is only ∼ 18% for the cell charged up to 130 mAh/g (**Figure 5-49**). The discharge capacity reaches to less than 10 mAh/g from the second cycle for the charge cutoff capacity of 130 mAh/g, showing the severity of the capacity fading for this sample. On the other hand, the discharge capacity for the sample that was initially charged up to 65 mAh/g was still higher than 15 mAh/g after 20 cycles, which is roughly half of the discharge capacity of the first cycle (**Figure 5-49a** and **c**).

Figure 5-50 shows the cycling performance of the $La_2CoO_{4+d}/Zn+ZnF_2$ cell as compared to $La_2CoO_{4+d}/Pb+PbF_2$. The specific discharge capacity (at the first cycle) of the $La_2CoO_{4+d}/Zn+ZnF_2$ cell is 40 mAh/g which is ∼ 25% higher than the discharge capacity of the $La_2CoO_{4+d}/Pb+PbF_2$ cell. It is also found that during the first five cycles the reduction in the discharge capacity has almost the same pattern for both anode materials, $Pb+PbF_2$ and

Zn+ZnF$_2$ (**Figure 5-50b** and **c**). However, from the 5th cycle up to the 10th cycle the reduction in discharge capacity for the cell with Zn+ZnF$_2$ anode composite is more severe than for the Pb+PbF$_2$ cell (see **Figure 5-50c**). Nevertheless, using Zn+ZnF$_2$ as the anode material provides a higher discharge potential (between roughly 1 – 0.5 V) as compared to Pb+PbF$_2$ (almost twice larger (see **Figure 5-50a** and **b**)). Considering the higher discharge potential and capacity (especially in the first 5 cycles), Zn+ZnF$_2$ offers a higher energy density as compared to Pb+PbF$_2$ for La$_2$CoO$_{4+d}$ as an intercalation-based cathode material.
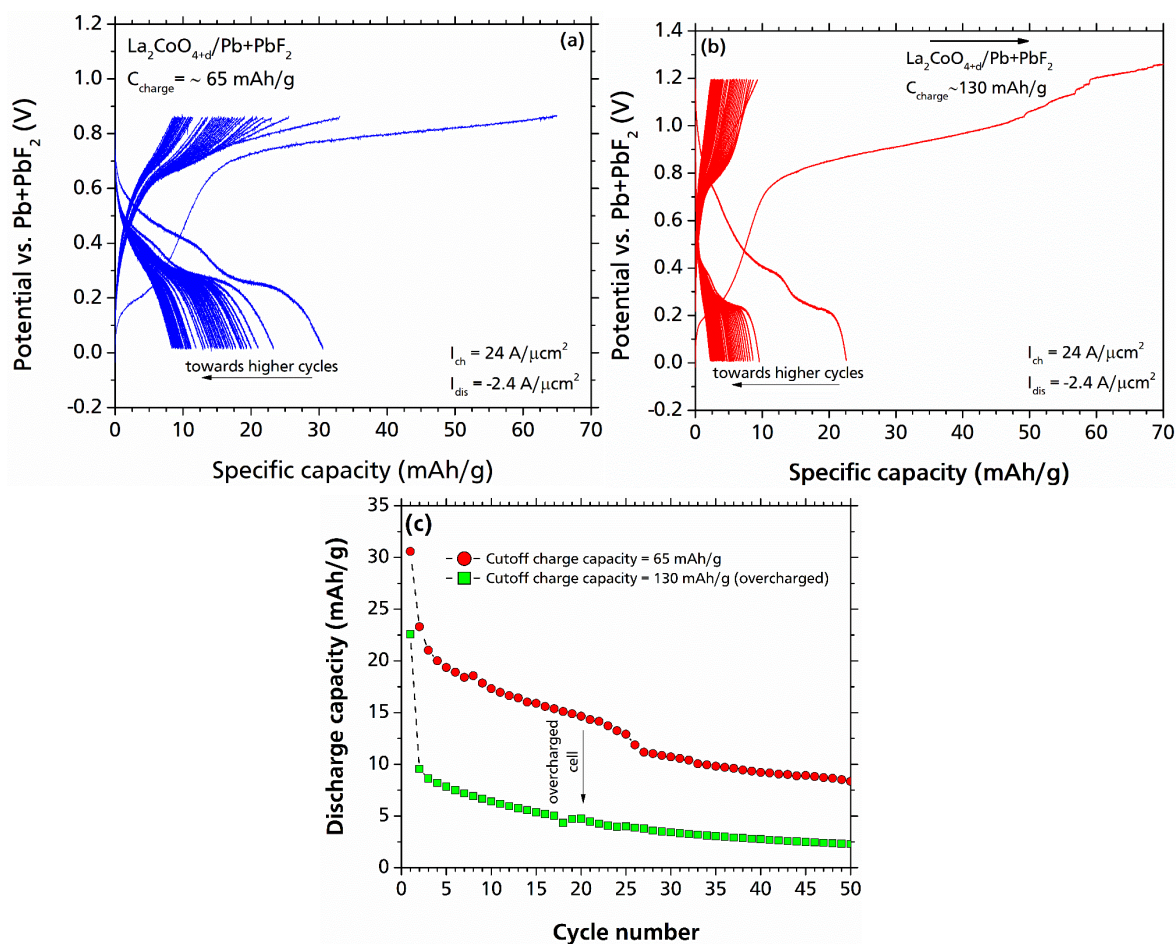

Figure 5-49. Cycling profiles of La₂CoO₄₊d/Pb+PbF₂ with charge cutoff capacity of (a) 65 mAh/g; (b) 130 mAh/g. (c) The effect of overcharging (one cell charged only up to ~ 65 mAh/g and the other charged up to ~ 130 mAh/g) on the discharge capacity fading. All the measurements have been performed at 170 °C, charge/discharge current density of 24/-2.4 µA/cm² and cutoff potential considered as the highest potential that has been reached within the first cycle at the respective cutoff capacity.

Coulombic and energy efficiencies have also been calculated for both La$_2$CoO$_{4+d}$/Pb+PbF$_2$ and La$_2$CoO$_{4+d}$/Zn+ZnF$_2$ systems (**Figure 5-51**). The Coulombic efficiency (depicted in **Figure 5-51a)** of the Zn+ZnF$_2$ cell is higher than the Pb+PbF$_2$ cell in the first cycle. However, from the 2nd cycle up to 7th cycle the Coulombic efficiency values significantly increase for both cells and from the 8th cycle it reaches to ~ 95% followed by small fluctuations around 100% afterwards. Note that the low Coulombic efficiencies at the first cycles confirms overlapping of the side reactions even below the critical cutoff conditions, though, the impedance of the cell is not significantly impaired within the cutoff capacity range of ~ 65 mAh/g. This is in agreement with what also has been observed for the La$_2$NiO$_{4+d}$ systems. The energy efficiency (**Figure 5-51b**) shows a similar trend for both cells for the early cycles (up to 6th cycle) with a relatively sharp increase within the first cycles. After the 6th cycle the energy efficiency of the Zn+ZnF$_2$

cell reduces continuously. This may come from an increase in the overpotentials arising from the high volume change of Zn/ZnF₂ conversion during the cycling.
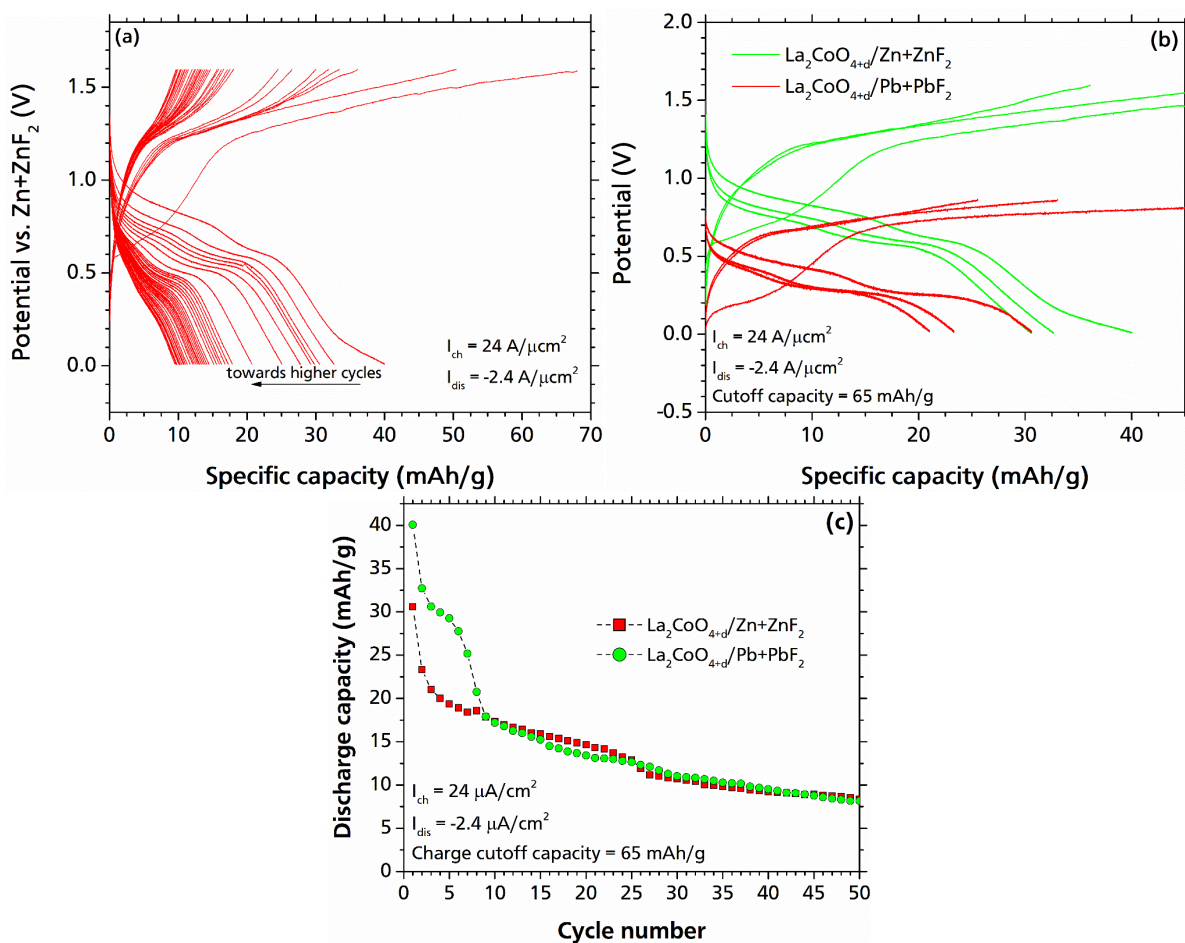
Figure 5-50. Cycling profile of La₂CoO₄₊d/Zn+ZnF₂ cell; (b) first 3 cycles of La₂CoO₄₊d against Zn+ZnF₂ and Pb+PbF₂ anode materials; (c) a comparison between the cycling performance of the La₂CoO₄₊d vs. Zn+ZnF₂ and Pb+PbF₂ counter electrode materials. All the measurements have been performed at T = 170 °C, I_{ch} = 24 μA/cm², I_{dis} = -2.4 μA/cm² and cutoff capacity of ~ 65 mAh/g while cutoff potential considered as the highest reached potential at the cutoff capacity within the first cycle.
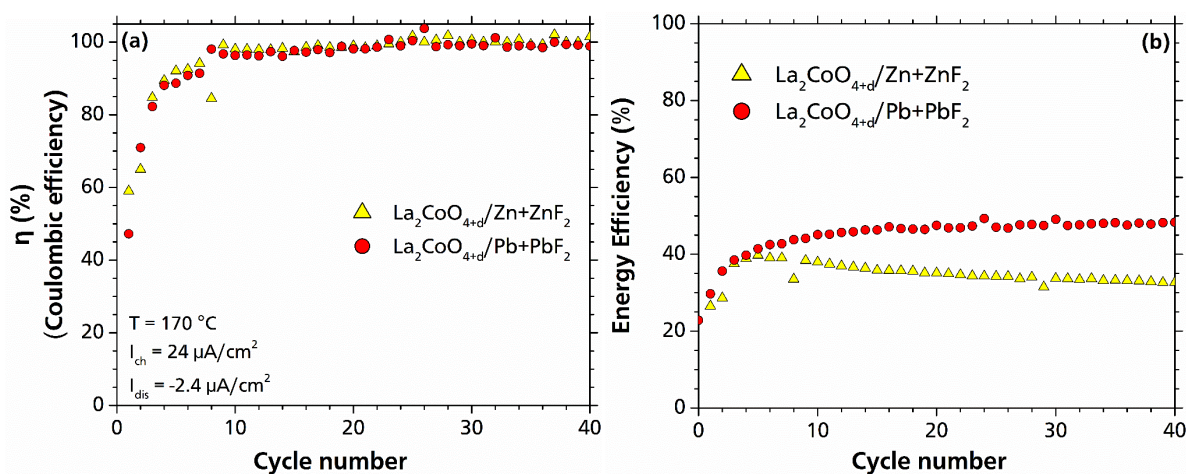
Figure 5-51. (a) Coulombic efficiency; and (b) energy efficiency of the La₂CoO₄₊d/Zn+ZnF₂ and La₂CoO₄₊d/Pb+PbF₂ cells at the charging conditions that is mentioned in the Figure 5-50.

5.4.3 Summary

In this chapter it was shown that carbon oxidation (fluorination) is a challenge for developing the fluoride ion batteries. The overlap of the carbon decomposition with the desired electrochemical reaction can result in an increase in the impedance of the cell. This would significantly influence the discharge capacity and also deteriorates the cycling performance of the cell. However, by regulating the charge cutoff criteria (capacity and potential) it is possible to preserve the conductivity of the cell and obtain improved cycling performance. **Figure 5-52** summarizes the cycling behavior (in terms of discharge capacity (**Figure 5-52a**) and average discharge potential (**Figure 5-52b**)) of $La_2(Co/Ni)O_{4+d}$ against $M+MF_2$ (M = Pb, Zn) cells at the optimized charge/discharge conditions. The results reveal that La_2NiO_{4+d} has a better cycling performance in terms of cycling stability, discharge capacity and potential as compared to La_2CoO_{4+d} cells. Stable discharge capacities within the first 50 cycles can be observed for the $La_2NiO_{4+d}/Zn+ZnF_2$ cell with the cutoff capacity of 50 mAh/g, however, the highest stability in potential was obtained for the same cell but with the cutoff capacity of 30 mAh/g (between $\sim 0.9 - 0.8$ V). It is also worth noting that the $La_2NiO_{4+d}/Zn+ZnF_2$ cell with the cutoff capacity of 30 mAh/g provides the highest cycle life (>220 cycles) that has ever been reported for FIBs. As a comparison, the discharge capacity of BiF_3 [14] (as a conversion type cathode material for FIB) drops to $\sim \frac{1}{4}$ of the first cycle at cycle number 20. However, it should be acknowledged that still the cells need to be further optimized in order to fulfill the requirements of the energy market. One of the major challenges concerns the conversion-based anode materials. In this respect, contributions to understanding the complexity of the conversion process within all-solid-state FIBs will be given in the next chapter.
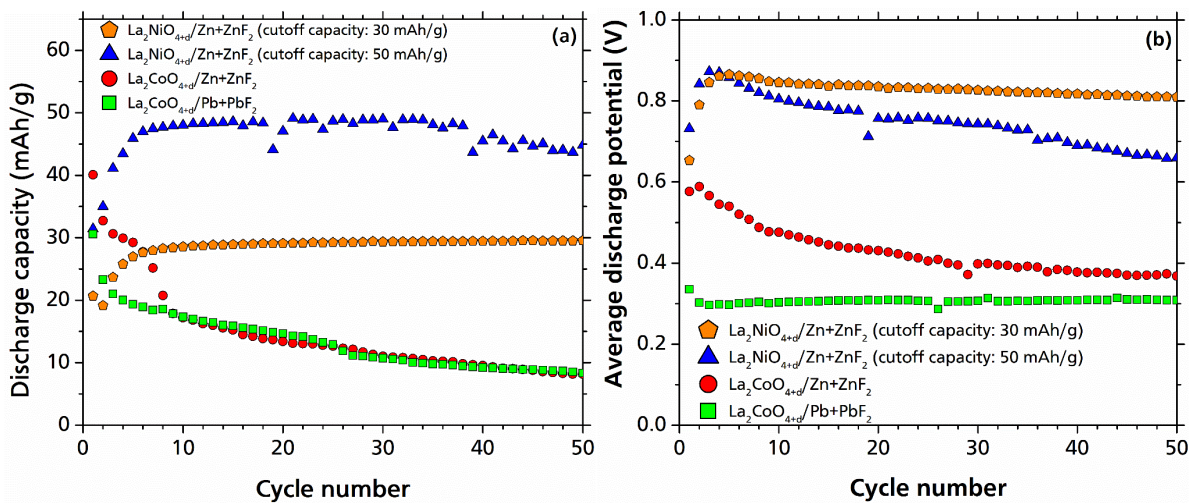
Figure 5-52. (a) Discharge capacity vs. cycle number; (b) average discharge potential vs. cycle number, for La_2MO_{4+d} (M = Co, Ni) cathode materials against $Pb+PbF_2$ or $Zn+ZnF_2$ anode materials. All the measurements have been performed at T = 170 °C and a charge current density of 24 µA/cm^2, however, discharge current density for La_2NiO_{4+d} and La_2CoO_{4+d} cells were -12 and -2.4 24 µA/cm^2, respectively. Charge cutoff capacity was 65 mAh/g for La_2CoO_{4+d} and 30 or 50 mAh/g for La_2NiO_{4+d} cells. Cutoff potential was setup to be 2.3 V for La_2NiO_{4+d} cells and for the La_2CoO_{4+d} cells the potential at the cutoff capacity at the first cycle was considered to be the charge cutoff potential. The average discharge potential was calculated based on $\int_0^{C_{max}} Edc \Big/ \int_0^{C_{max}} dC$.

5.5 Towards Understanding the Behavior of Conversion-Based Anode Materials

In the previous chapter it was shown that the Ruddlesden-Popper-type structures of $La_2(Co/Ni)O_{4+d}$ can be promising intercalation-based cathode materials with relatively good cycling stability for all-solid-state FIBs. However, the components within FIBs (including electrodes and electrolyte materials) are still at a very early stage of development [32, 33, 36, 38, 134, 135]. One key point for development of FIBs with intercalation-based electrode materials lies in the development of the anode materials. Apart from the development of combinations with improved cycling stability and increased energy density, such studies can also facilitate an improved understanding of the anode systems themselves. This can be emphasized by the following consideration: For lithium or sodium ion batteries, it is common practice to test new materials against lithium or sodium metal, which serve as well-defined standards in these cases; however, testing against the element is an impractical option for fluoride ion batteries. Since no state of the art standard electrode system is available for FIBs, intercalation systems might serve as reference systems since one can expect improved battery kinetics than for conversion materials from an analogy consideration to LIBs. For such a purpose, La_2CoO_{4+d} seems to be a suitable material due to two reason: First, the possibility to synthesize a pure fluorinated phase via chemical method. This is important when it comes to making symmetrical cells. Second, the separation of the charge plateaus of carbon decomposition and the desired electrochemical reaction (the region in which the impedance of the cell does not significantly change). For other systems, either it was not possible to make a pure fluorinated phase or the side reactions were highly overlapped with the desired electrochemical reaction. In this chapter the issue of volume change within the anode material during the redox reactions will be considered. Further, it is tried to point out the role of volume change in the impedance behavior. For such a purpose the impedance behavior of La_2CoO_{4+d} vs. conversion-based anode materials of $M+MF_2$ (M = Pb, Zn and Mn) will be investigated and it is tried to understand more about the nature of conversion-based reactions as well as the influences of the anode material on the behavior of the cell.

5.5.1 Overpotentials in Symmetrical Electrochemical Cells

The symmetrical cells made up of $M+MF_2||La_{0.9}Ba_{0.9}F_{2.9}||M+MF_2$ have been examined and compared with the symmetrical cell of the active cathode material, $La_2CoO_{4+d}||La_{0.9}Ba_{0.1}F_{2.9}||La_2CoO_{4+d}F_y$, in order to develop a better understanding on the overpotentials arising from the anode material. To make the symmetrical cell of the La_2CoO_{4+d}, the chemically fluorinated phase of $La_2CoO_{4+d}F_y$ (y ~ 0.5, see section 5.3.2.1a) has been mixed with the electrolyte ($La_{0.9}Ba_{0.1}F_{2.9}$) and black carbon in the very same ratios that have been used to make La_2CoO_{4+d} cathode material composite (section 4.2). The charge/discharge time has been selected based on a charge/discharge specific capacity of ~ 60 mAh/g in order to prevent any increase in the impedance of the cell in accordance to the EIS measurements.

The cycling behavior of the symmetrical cell of the cathode material, La_2CoO_{4+d}, can be found in **Figure 5-53a** and shows a very low overpotential (close to zero) at the early cycle numbers. However, the overpotential increases slightly up to ~ 20 mV after a few cycles without any further significant fluctuations. The symmetrical $Pb+PbF_2$ cell (**Figure 5-53b**) also shows a fairly low overpotential and good cycling stability over prolonged cycling. In contrast, the overpotentials increase constantly for $Zn+ZnF_2$ symmetrical cell (see **Figure 5-53b**), and the increase in overpotentials is significantly larger for $Mn+MnF_2$ symmetrical cell (see **Figure**

5-53c). The observations can be related to the volume changes engaged with $MF_2 \rightarrow M$ reaction which will be addressed later in this chapter.
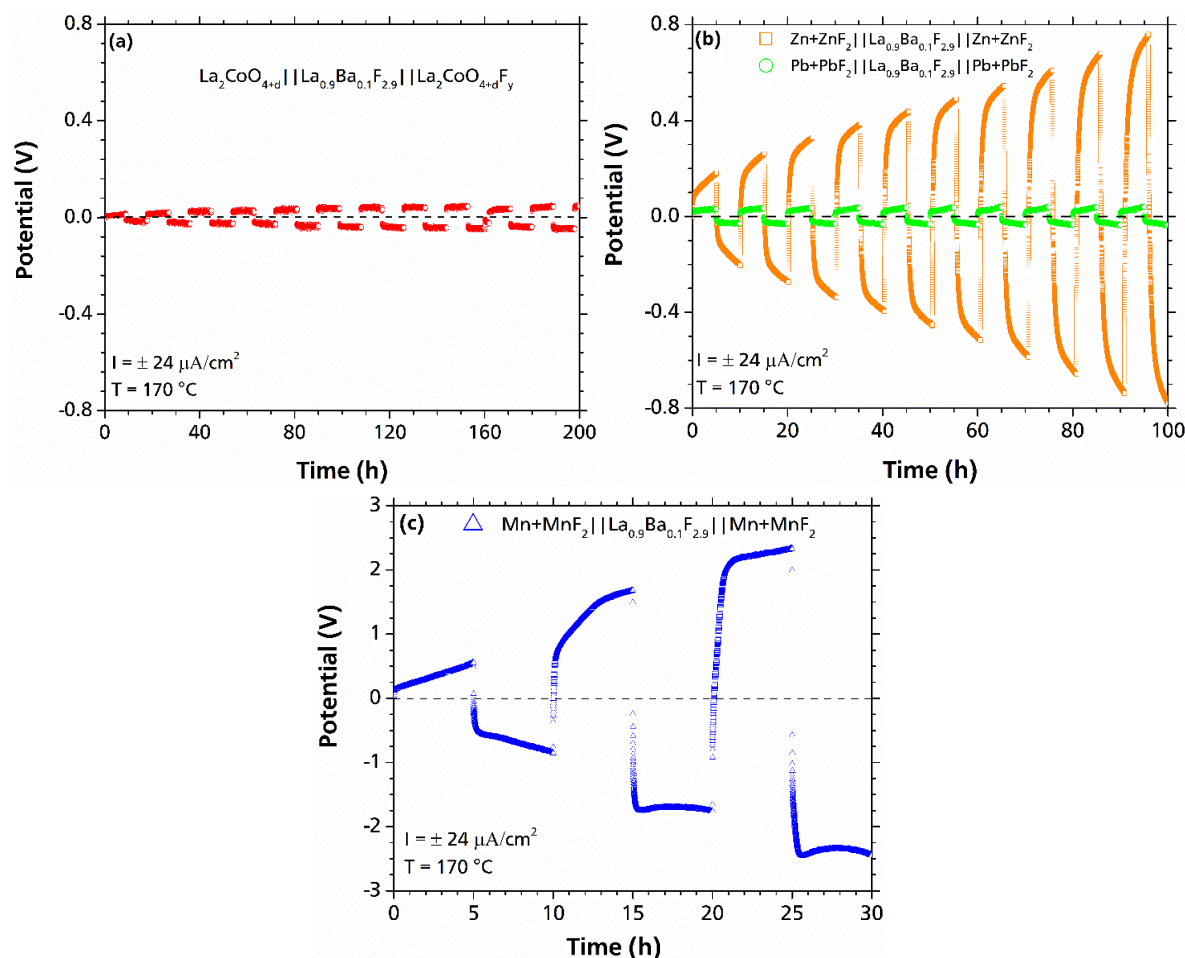
Figure 5-53. Cycling curves of symmetrical cells of (a) La$_2$CoO$_{4+d}$ (cathode material); (b) Pb+PbF$_2$, Zn+ZnF$_2$ anode materials; and (c) Mn+MnF$_2$ anode material. All the measurements have been performed at constant charge/discharge current densities of +/- 24 μA/cm^2 at T = 170 °C and the charge/discharge durations correspond to a specific capacity of ~ 60 mAh/g.

5.5.2 Impedance Behavior of the La$_2$CoO$_{4+d}$/M+MF$_2$ Cells

In this section the impedance behavior of the La$_2$CoO$_{4+d}$/M+MF$_2$ (M = Pb, Zn, and Mn) cells mainly within the low charge capacity region (<120 mAh/g) will be investigated. **Figure 5-54** depicts the Nyquist plots of the impedance spectra at different charge capacities. The models that have been proposed in **Figure 5-40d** have been used in order to fit the data.

In **Figure 5-54**, it can be seen that the impedance spectra of all the samples consist of two regions (examples of the fitting of selected spectra can be found in **Figure 5-55** and **Figure 5-56** for the fitting of the Nyquist and Bode plots, respectively): The first region describes a semicircle and is dominant at high frequencies above 10 kHz, which is typically arising from the solid electrolyte [127] and the interface resistance between the electrolyte and the electrode materials; however, separation of both effects was not possible from the impedance data recorded. This is also evident in the Bode impedance plots in **Figure 5-56**. The second part of the Nyquist curve looks like a straight line which relates to diffusion processes within the active materials of the electrodes at very low frequencies (lower than 10 Hz), i.e., a Warburg impedance.
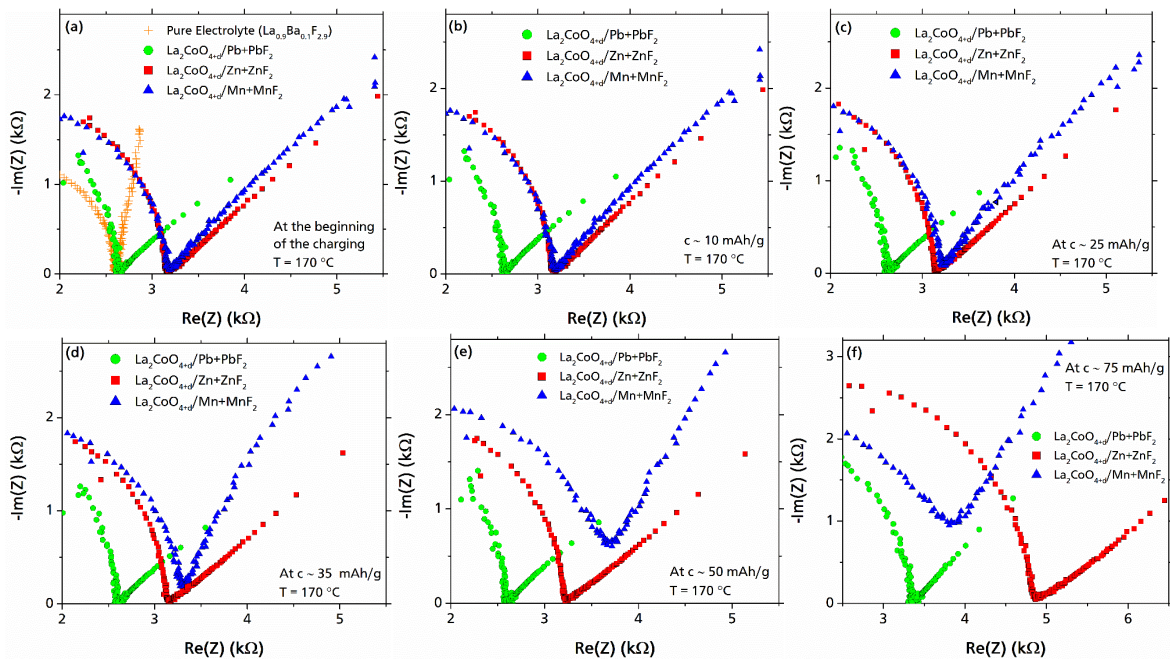
Figure 5-54. Nyquist Impedance for La₂CoO₄₊d cell against Pb+PbF₂, Zn+ZnF₂ and Mn+MnF₂ anode materials (a) before charge, (b) at c ~ 10 mAh/g, (c) at c ~ 25 mAh/g, (d) at c ~ 35 mAh/g, (e) at c ~ 50 mAh/g, (f) at c ~ 75 mAh/g. For all of the cells: T = 170 °C and I = +10.0 μA (+24 μA/cm²).
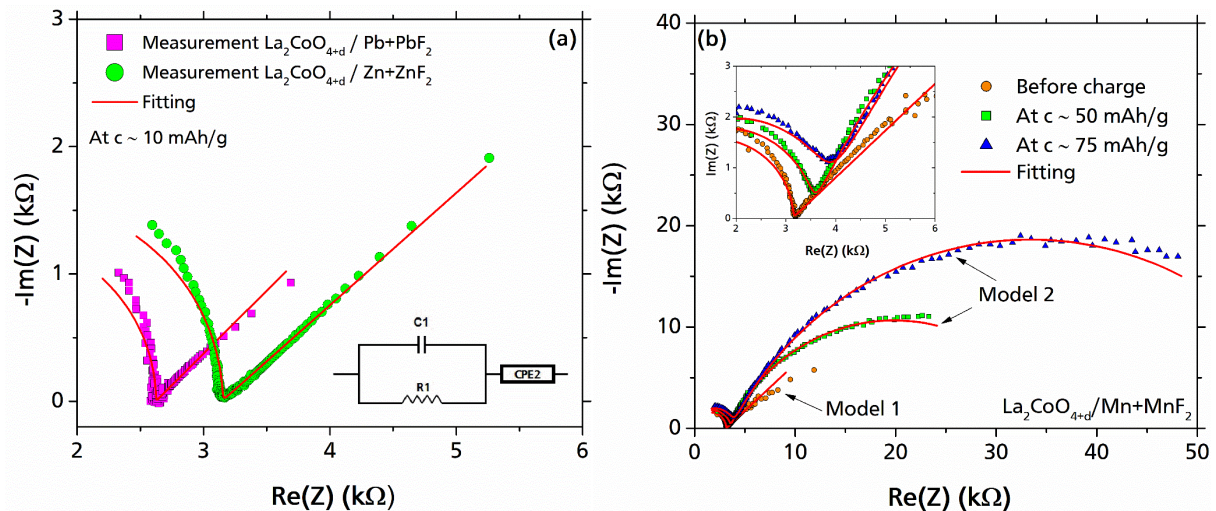
Figure 5-55. (a) Example of Nyquist plots with fitting for La₂CoO₄₊d against Pb+PbF₂ and Zn+ZnF₂ anode materials at c ~ 10 mAh/g; (b) example of Nyquist plots and fitting for La₂CoO₄₊d/Mn+MnF₂ at various cutoff capacities. The measurements have been performed at T = 170 °C and I = 10 μA (+24 μA/cm²) and the Nyquist curves have been fitted by the models that are provided in Figure 5-40d.
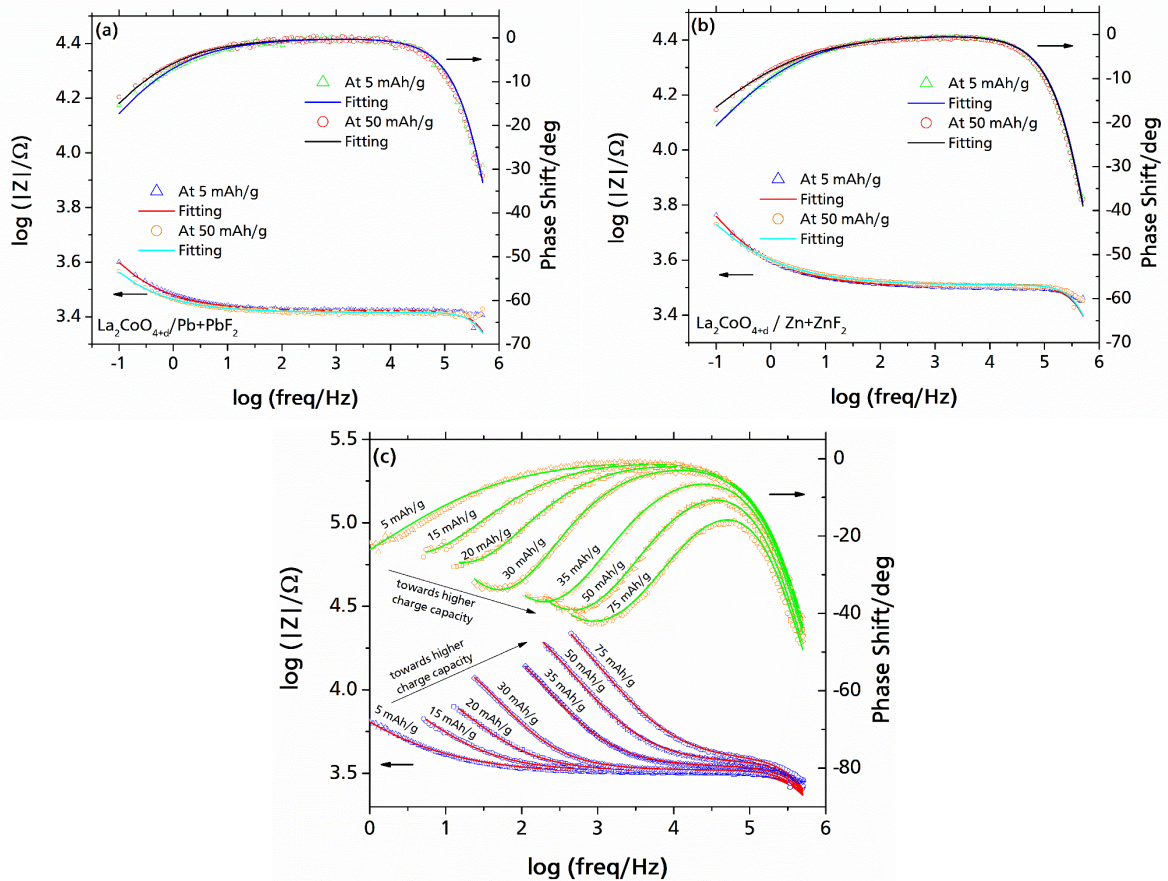
Figure 5-56. Example of fitting of bode plots for La₂CoO₄₊d against (a) Pb+PbF₂; (b) Zn+ZnF₂ cell; (c) Mn+MnF₂ at various cutoff capacities at the experimental conditions that is mentioned in Figure 5-55 with the models that are proposed in Figure 5-40d.

The behavior of the $La_2CoO_{4+d}/Mn+MnF_2$ cell strongly differs from the cells with $Zn+ZnF_2$ and $Pb+PbF_2$ as the active anode materials; the Nyquist curves recorded for this cell can only be sufficiently well fitted with the equivalent circuit of "model 1" (in **Figure 5-41d**) up to a capacity of ~ 20 mAh/g. For higher capacities, equivalent circuit of the "model 2" (again in **Figure 5-40d**) has to be used in order to obtain a suitable fit (see **Figure 5-55b**). This results from the appearance of a second semicircle at lower frequencies. Only below 20 mAh/g the impedance behavior is very similar to $Zn+ZnF_2$ anode material (**Figure 5-57a, b**). The impedance behavior can be described as follows: The first (part of a) semi-circle at the frequencies higher than ~ 10 kHz can be described as a resistor parallel to a capacitor which mainly shows the resistivity of the electrolyte. Therefore, the R_1 values for $Zn+ZnF_2$ and $Mn+MnF_2$ are very similar (**Figure 5-57a**) since both anode materials were mixed with the electrolyte. PbF_2 is a better fluoride ion conductor than $La_{0.9}Ba_{0.1}F_{2.9}$ and therefore, the resistance of the cell with $Pb+PbF_2$ is smaller. The second part which corresponds to the Warburg impedance with a slope of almost 45° can be described as a constant phase element with an α coefficient of around 0.5 (**Figure 5-57d**). The value of α does not significantly change for $Pb+PbF_2$ and $Zn+ZnF_2$, but strongly changes for $Mn+MnF_2$ at very low charge capacities where the conductive carbon decomposition is less probable. The change in the impedance behavior of the $Mn+MnF_2$ cell is well reflected in the Bode presentation of the impedance spectra (**Figure 5-56**): For all three anode systems, the phase shift in mid-range frequencies is almost zero for low charge capacities and the cell is dominated by resistive behavior. For $Pb+PbF_2$ and $Zn+ZnF_2$ this behavior does not significantly change for higher charge capacities (at least up to 50 mAh/g); in contrast for $Mn+MnF_2$ a

115

strong change of the phase angle around 20 mAh/g can be observed, justifying the use of the different equivalent circuit model.

The higher value of the α (CPE) exponent indicates an increased capacitive behavior, which can be understood in more detail on analyzing the fitted values of CPE2 of the equivalent circuit "model 2" (**Figure 5-40d**) for Mn+MnF$_2$. Here, one can see that the Warburg behavior of the second semicircle changes to a capacitive response from a calculation of the effective capacity:

$$C_{eff,2} = R_2^{(1/\alpha_2)-1} Q_2^{1/\alpha_2} \quad [136] \qquad (5.1)$$

The change of Q_2 and $C_{eff,2}$ on charging for Mn+MnF$_2$ is shown in **Figure 5-57c** and **d**, and indicates that, instead of dominating diffusion processes in the electrode, a capacitance in the order of $\sim 10^{-8}$ F is built up, which is in the order of magnitude expected for surface layer capacitances [66].

It is worth noting that the change in the impedance behavior of the Mn+MnF$_2$ cell appears at the potential range at which the intensive carbon side reaction (leading to a significant increase in the impedance) is less likely (also the R_1 values does not significantly change for the Mn+MnF$_2$ cell at this range). Therefore, it is suggested that this capacity-type behavior of the cell originates from the volume change which occurs during charge and can be explained as follows: On conversion of MnF$_2$ to Mn during charging step, a volume reduction by a factor of three takes place, and this is significantly higher as compared to Pb+PbF$_2$ and Zn+ZnF$_2$ (**Table 5-20**). Therefore, during the reduction of MnF$_2$ in the anode material there would be a significant shrinkage between the newly formed Mn and the MnF$_2$ particles (see the sketch in **Figure 5-58**). Thus, the newly formed Mn particles will lose physical contact with other particles, e.g., the conductive carbon matrix or the solid-electrolyte. Therefore, electrons cannot be easily transferred to (alternatively, fluoride ions be removed from) the MF$_2$ particles anymore, and will reside on the carbon matrix, effectively forming a surface layer capacitance. Clearly, this volume change effect should also impact the cycling behavior on extended cycling, which will be discussed later in this chapter.

Table 5-20. Volume comparison of metals and corresponding metal fluorides. Data values for M/MF$_2$ are taken from ref. [137].

M	V per M (Å³)	V per MF$_2$ (Å³)		conversion factor $f = V_{MF2}/V_M$
Mn	12.20		39.32	3.22
Zn	15.21		34.81	2.29
Pb	30.32	*Pnma*	52.56	1.73
Pb	30.32	*Fm-3m*	48.34	1.59
A$_2$BO$_4$	V per A$_2$BO$_4$ (Å³)	V per AB$_2$O$_4$F$_y$ [Å³]		conversion factor $f = V_{A2BO4Fy}/V_{A2BO4}$
La$_2$CoO$_{4+d}$	95.42	108.20		1.13
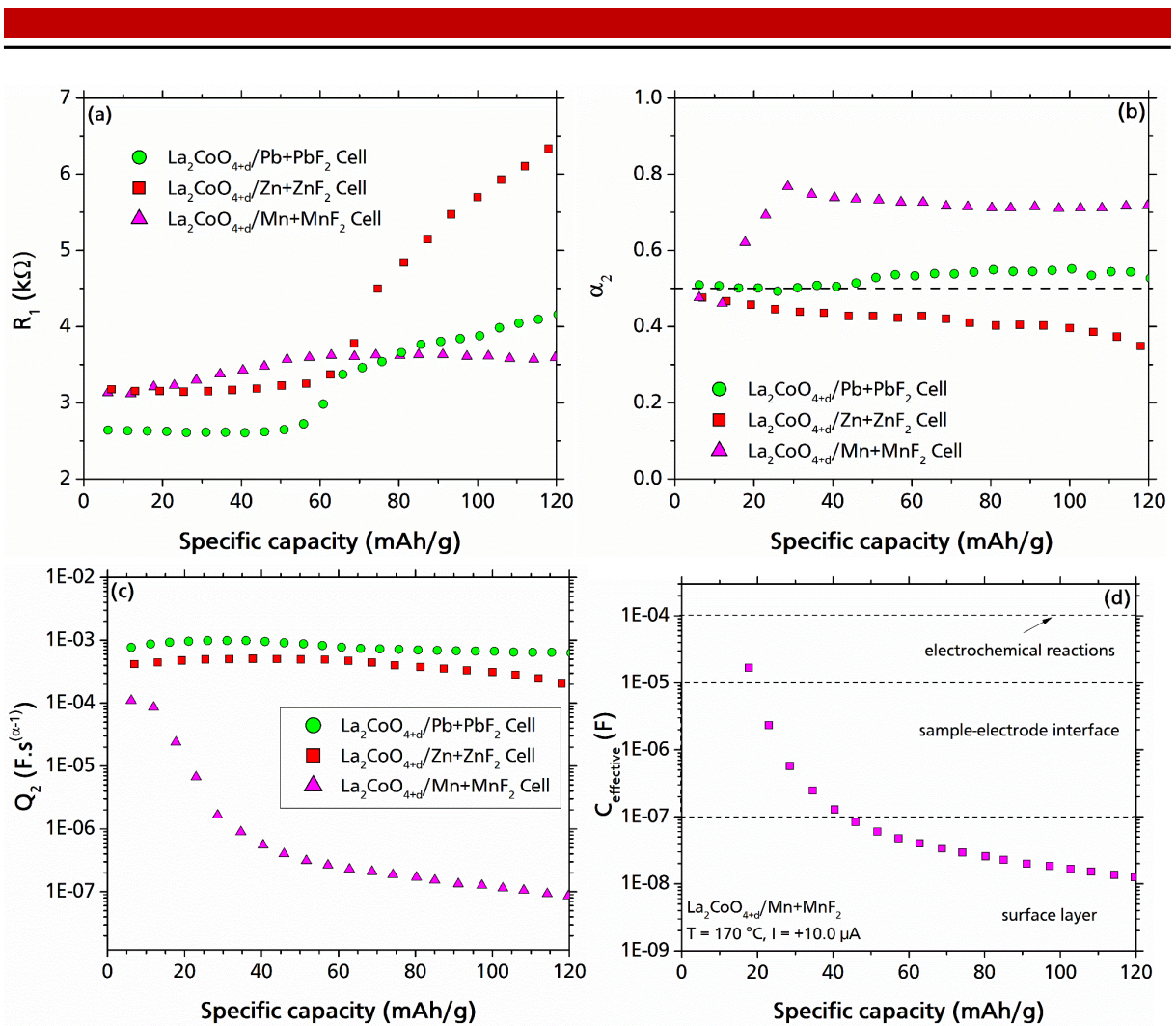
Figure 5-57. (a) R$_1$ values; (b) alpha (α); (c) Q values (based on the fitting) for the La$_2$CoO$_{4+d}$ against M+MF$_2$ anode materials during charging of the cell at T = 170 °C and I = +10.0 µA (+24 µA/cm^2); (d) C$_{effective}$ for La$_2$CoO$_{4+d}$/Mn+MnF$_2$ cell at different cutoff capacities higher than 20 mAh/g at the same charging condition.
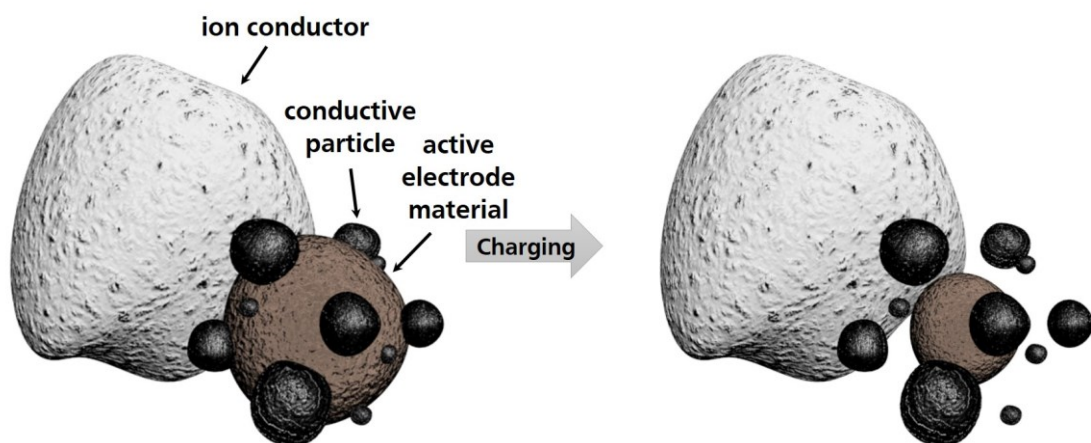
Figure 5-58. Schematic view of the volume changes during charge in the contact surface of the active anode material/electrolyte/carbon grains over the battery operation within the anode material.

5.5.3 Cycling Performance

Figure 5-59a and **b** show the charge and discharge curves of a $La_2CoO_{4+d}/Mn+MnF_2$ cell as compared to La_2CoO_{4+d} against $Pb+PbF_2$ and $Zn+ZnF_2$ anode materials. The charge plateau for the $La_2CoO_{4+d}/Mn+MnF_2$ cell is observed at a potential range of 1.5 – 2.5 V which is significantly higher than that for $Pb+PbF_2$ (0.6 – 0.8 V) and $Zn+ZnF_2$ (1.3 – 1.6 V) (**Figure 5-59a**). It is worth noting that the potential difference between Pb/PbF_2 and Zn/ZnF_2 is in a well agreement with what would be expected ($\Delta = 0.64$ V) according to the EMF series [57]. For Mn/MnF_2 a simple comparison to the EMF series is not possible; remarkably, the highest charging potential is observed for the Mn/MnF_2 anode material, although its discharge potential lies between the potentials of Pb/PbF_2 and Zn/ZnF_2 (**Figure 5-59b**). This is indicative for increased overpotentials of the Mn/MnF_2 cell, which can be estimated as follows: From voltage difference of the charging and the discharging profiles (**Figure 5-59a** and **b**) of the respective anode system, one can estimate an average overpotential η for the charge/discharge reaction (assuming $\Delta U_{ch-dis} = \eta_{ch} + \eta_{dis}$). By this, it is found that the overpotentials are significantly different for the different conversion-based anode systems (ΔU_{ch-dis} (Pb) = ~ 0.4 V < ΔU_{ch-dis} (Zn) = ~ 0.7 V < ΔU_{ch-dis} (Mn) = ~ 1.5 V).

Furthermore, the abovementioned trend for the overpotentials agrees well with the overpotentials determined from symmetrical cells shown in section 5.5.1. Moreover, the higher melting point of Mn (1519 K [92]) as compared to Pb (600 K [92]) and Zn (693 K [92]) may also have an influence on the overpotential of the anode material according to the empirical rule of Tamann [99], which states that the reactivity of a compound within a solid-state reaction is strongly enhanced the closer it is to the melting point of a compound.

It is also worth mentioning that the cells using $Zn+ZnF_2$ or $Mn+MnF_2$ as the anode material are more sensitive towards overcharging, regardless of the fact that the anode composite is used in high excess. This can be seen in **Figure 5-59b**: The cells which were charged up to 130 mAh/g in the first cycle show a significantly lower specific discharge capacity; for the cell with $Pb+PbF_2$ as the anode material, the reduction in the discharge capacity is only in the order of 25% (from 31 mAh/g to 23 mAh/g), whereas for the $Zn+ZnF_2$ cell the discharging capacity is reduced by almost 75% as compared to cells which have been only charged to 65 mAh/g and the capacity fading for the $Mn+MnF_2$ cell is higher since the capacity of the overcharged cell reduces by 90% (**Figure 5-59b**). This indicates that on low charge capacities, the intrinsic problems arise from the conversion-based anode side, whereas at higher charging capacities additional resistances formed on the (intercalation-based) cathode side from carbon decomposition result in a further increment of performance loss for such cells.

Figure 5-59c shows the cycling behavior of the $La_2CoO_{4+d}/Mn+MnF_2$ cell. Apart from a very large energy loss during the first cycle for the $L_2CoO_{4+d}/Mn+MnF_2$ cell (as compared to La_2CoO_{4+d} vs. $Pb+PbF_2$ or $Zn+ZnF_2$ cells (**Figure 5-50b**)) the capacity loss in the second cycle is severe and the specific charge/discharge capacities decrease below 7 mAh/g with a short discharge plateau at around 0.3 V. Such a large overpotential and consequently capacity fading can be related to the rapid change in the impedance behavior of the cell at the early stages of charging originating from the high overpotentials arising from the conversion of Mn to MnF_2.
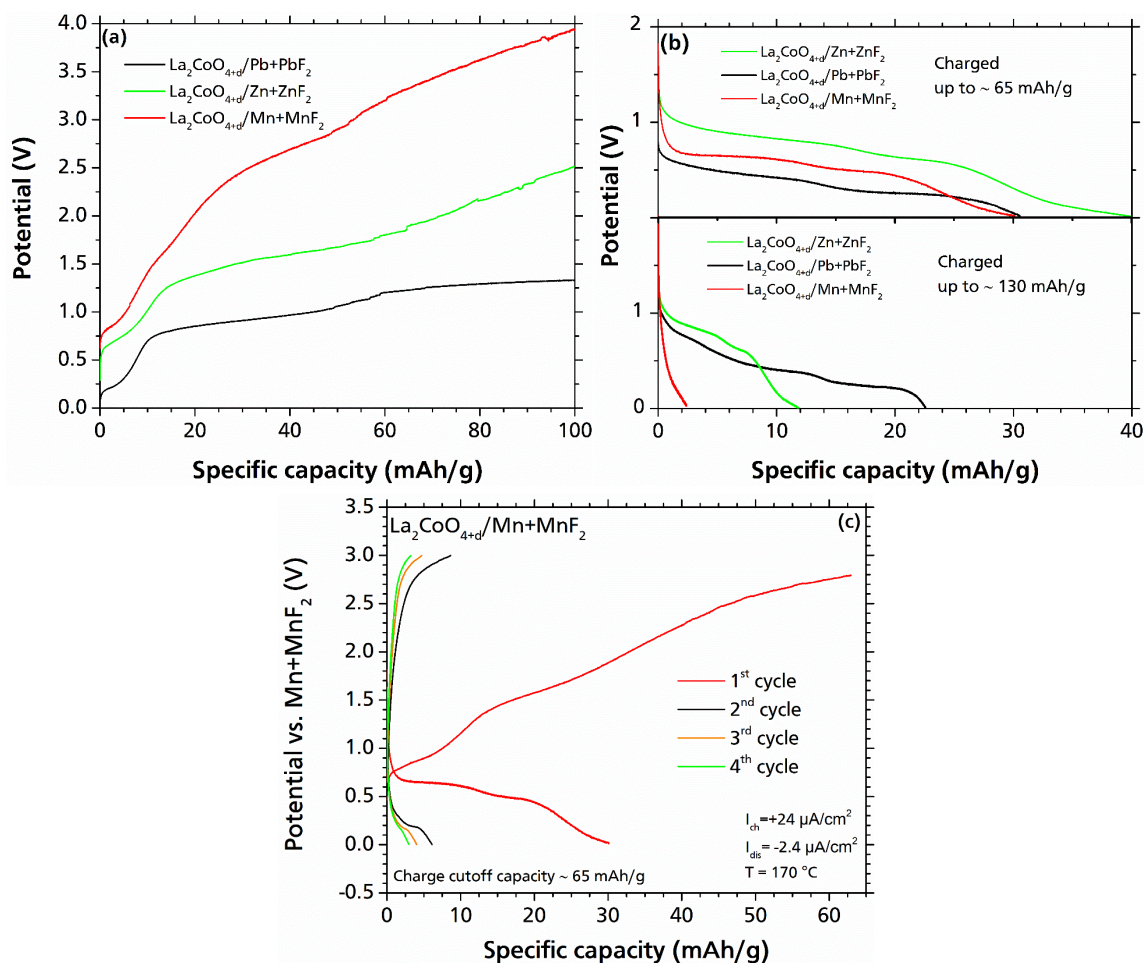
Figure 5-59. (a) Charge curves of La₂CoO₄₊d/M+MF₂ (M = Pb, Zn and Mn) cells; (b) discharge of the La₂CoO₄₊d/M+MF₂ (M = Pb, Zn, Mn) cells at two different charge cutoff capacity of 65 mAh/g and 130 mAh/g (overcharged cells); (c) cycling curves of La₂CoO₄₊d/Mn+MnF₂ cell with charge cutoff capacity (at the first cycle) of ~ 65 mAh/g (for further cycles the charge cutoff conditions were set according to the potential of the cell at the charge cutoff capacity within the first cycle). For all the cells: T = 170 °C, I_{ch} = 24 µA/cm² and I_{dis} = -2.4 µA/cm².

5.5.4 Summary

In this chapter La₂CoO₄₊d has been examined as an intercalation-based cathode reference material against three composite anode materials of M+MF₂ (M = Pb, Zn and Mn). The choice of La₂CoO₄₊d as the reference cathode material is mainly based on the separation of the charge plateaus of the carbon decomposition (destruction of the cell conductivity) and the desired electrochemical reaction, possibility to make a symmetrical cell of La₂CoO₄₊d and fairly good structural reversibility of this system.

It was found that at least a part of the overpotential during cycling of the cells can originate from the anode material due to the conversion nature of the reactions within the anode material. In this respect, the volume change during the cycling plays a vital role and higher volume changes (e.g. in Mn/MnF₂) result in higher overpotentials which also impairs the cycling of the symmetrical cells. Galvanostatic electrochemical impedance spectroscopy show that there is a change in the impedance behavior of the Mn/MnF₂ anode material as compared to Pb/PbF₂ or Zn/ZnF₂, in the early stage of charging: The CPE exponent α increase sharply in the early stages of charging which is an indication for a capacitive behavior. This behavior most likely arises from the huge volume change which is accompanied by the conversion based

reactions in the anode material and results in a poor cycling performance of La_2CoO_{4+d} against $Mn+MnF_2$ in comparison to $Pb+PbF_2$ and $Zn+ZnF_2$ anode materials.

Currently FIBs are at the early stages of development. However, in lack of a functional intercalation-based anode material, $Zn+ZnF_2$ can serve as a reasonable anode material with relatively good reversibility which provides good cycling stability. It is also worth noting that further efforts on making anode materials with higher potential such as $Mg+MgF_2$, $Ce+CeF_3$, $Al+AlF_3$ and CaF_2 have been done, however, the results were not promising as compared to $Zn+ZnF_2$ anode material in combination with the current conversion systems.

Last but not least, to overcome intrinsic problems with conversion-based electrode materials, several strategies have been proposed for lithium ion batteries that may appear as ideas to mitigate the effects of conversion-based electrodes for FIBs. For instance, using liquid electrolytes, preparing cells in thin electrode configurations [1], encapsulating the electrode material in a hollow structure [138, 139] and infiltrating into porous carbon hosts [140] may improve conversion-based systems. Nevertheless, Considering the limitations of the conversion-based electrode materials, even the state of the art of the LIBs still mainly use intercalation-based electrode materials. However, by further improvement of the conversion-based electrode materials, they may enter into the market of reversible batteries.

6 Conclusions and Outlook

6.1 Conclusions

Recently fluoride ion batteries have been proposed as an alternative energy storage system to lithium ion batteries. However, poor cycle life of the FIBs with conversion-based electrode materials is a major drawback of the FIB systems that have been introduced so far. In this dissertation, the concept of intercalation-based mechanism has been used in order to develop cathode electrode materials for FIBs to address the issue of poor cycling performance. Therefore, several compounds with different structures including Ruddlesden-Popper-type compounds ($LaSr(Mn/Fe/Co)O_4$ and $La_2(Co/Ni)O_{4+d}$) and Schafarzikite-type compounds ($(Co/Mg)_{0.5}Fe_{0.5}Sb_2O_4$) have been investigated within all-solid-state electrochemical systems. In a lack of well-developed intercalation-based anode materials for FIBs, several metal/metal fluorides have been examined as counter electrodes on the anode side.

As a primary approach, Ruddlesden-Popper-type (K_2NiF_4) compound of $LaSrMnO_4$ have been galvanostatically charged against a composite of $Pb+PbF_2$. The results showed a stepwise fluorination of the compound to form $LaSrMnO_4F$ and $LaSrMnO_4F_{2-\delta}$ in the first and second steps, respectively. The structural changes after an electrochemical fluorination (expansion of the cell along the *c*-axis together with contraction of the cell along the *a/b* axes) were in a good agreement with the structural changes over intercalation of fluoride ions into the vacant interlayers of $LaSrMnO_4$ by chemical methods which was previously reported by other research groups [48, 100]. This suggests a successful insertion of the fluoride ions into the vacant anion rocksalt interlayers of $LaSrMnO_4$ via the electrochemical method. This also shows that electrochemical fluorination can be a safer alternative method to fluorinate oxides. Even more important, the fluoride ions could be electrochemically removed (de-intercalated) from $LaSrMnO_4F_{2-\delta}$ host resulting in a good recovery of the initial oxide structure upon discharging to negative potentials. This is the first evidence that the intercalation of fluoride ions is fully reversible.

In other K_2NiF_4-type cathode composite compounds ($LaSr(Fe/Co)O_4$ and $La_2(Co/Ni)O_{4+d}$) fluoride ions could be electrochemically inserted (intercalated) resulting in structural changes in line with what has been observed for $LaSrMnO_4$, but without the intermediate stage which corresponds to occupation of only one interlayer. For the Schafarzikite-type structures of $(Co/Mg)_{0.5}Fe_{0.5}Sb_2O_4$ the intercalation of F^- ions resulted in structural changes in accordance with the results that have been obtained by insertion of ~ 0.5 fluoride ions by chemical methods. It can be concluded that Ruddlesden-Popper-type structures can accommodate more ions per formula unit as compared to Schafarzikite-type structures. Furthermore, a higher degree of reversibility in cathode materials with Ruddlesden-Popper-type structures as compared to Schafarzikite-type structures may arise from the dimensionality of the fluoride ion sublattices: 1D (channels) of fluoride ions in Schafarzikite-type structure (MSb_2O_4) vs. 2D (planes) of fluoride ions in Ruddlesden-Popper-type structure (A_2BO_4).

From the electrochemical performance point of view La_2NiO_{4+d} and La_2CoO_{4+d} appeared to be the most promising candidates among all other compounds in terms of structural reversibility, discharge capacity, energy density and cycling stability. According to the TEM based analysis (ADT and EDX) on a fluorinated $La_2NiO_{4+d}F_y$ single crystal, a total number of 1.59 – 1.72 fluoride ions could be inserted within the interstitial layers. For La_2CoO_{4+d}, however, the estimation for occupancy of the interlayers is ~ 1.2 fluoride ions based on the effective charge

capacity in relation with the structural changes during the galvanostatic charging of the cell. For both compounds, galvanostatic discharging results in a good recovery of the initial structure. However, potential of La_2NiO_{4+d} is higher than La_2CoO_{4+d}. This is due to the fact that, $Ni^{2+} \rightarrow Ni^{3+}$ has a higher potential as compared to $Co^{2+} \rightarrow Co^{3+}$ and when it comes to potential of the redox couple, the oxidizing power of the transition metal within the oxide is a determining factor. Therefore, La_2NiO_{4+d} would be more interesting as a high energy density cathode material.

The issue of overlapping of carbon oxidation with the desired electrochemical reaction within the cathode composite material could be observed in all examined systems. The cathode material seems to have a catalytic effect towards oxidation of carbon within the electrode composite. The carbon side reaction occurs at low potential region but does not significantly influence the conductivity of the cell. However, at higher potential/capacity region the side reaction results in a massive destruction of the conductivity of the cell leading to a poor cycling performance. It is not clear whether carbon oxidation occurs in two steps with intermediate conductive products or the morphology of the (carbon) oxidized particles is point-like and establishes a network only at high potentials. Regardless of the kinetic of carbon oxidation within the electrode material, cyclic voltammetry experiments and impedance spectroscopy show that the cutoff potential criteria play a vital role in the development of the carbon side reaction and consequently in cycle life of the cells. By selecting suitable cutoff criteria (capacity/potential), cycle lives as high as 220 cycles with a Coulombic efficiency close to 100% (97.68% in the whole cycling range) can be obtained within the La_2NiO_{4+d} system. This is the highest cycle life that has ever been reported for an FIB, suggesting that La_2NiO_{4+d} can be a suitable candidate to be considered as a high capacity and high potential cathode material for FIBs. It should be emphasized that the reported cycle life is obtained within an all-solid-state system and yet it is far more stable than other FIB systems including those that benefit from liquid electrolytes.

Slow formation of a stable interface within the first cycles may explain lower Coulombic efficiencies in the early cycles as compared to that at higher cycles which is also accompanied by a difference in the structural changes during the very first cycles and higher cycles.

Finally, the effect of volume change within the conversion-based electrode materials needs to be considered when it comes to the cycling stability of the whole cell; counter electrode materials with higher volume change were shown to build up higher internal resistances leading to a higher overpotential which results in a significant deterioration of the cycle life. On the contrary, cycling performance can be further improved by using anode materials with lower volume changes during redox reactions.

6.2 Outlook

Without any doubt, the best obtained cycling performance within this study is far away from being commercialized. The efforts in this dissertation were only a preliminary work in order to show that the intercalation mechanism in FIBs can pave the way to enhance the cycling performance. However, further efforts are required to get closer to application demands. In this respect, several measures are suggested in order to improve the FIB systems.

First of all, engineering of the active cathode materials is needed: The effect of doping on the cycling performance and energy density of the promising active cathode materials (such as La_2NiO_{4+d}) needs to be investigated. This is particularly important since doping can change the

site energy of the vacant interstitial sites and consequently may improve the energy density and cycle life. The other issue is to find out the optimized cathode material composite. This requires studies on finding replacements for carbon which seems to be problematic within the electrode composite or engineering the carbon particles in such a way to minimize the detrimental impact of carbon oxidation. Core-shell structures [40] may help for a better ionic and electronic conductivity. Also, the optimized ratio of active cathode material:conductive particles:electrolyte should be found. It is worth noting that some investigations have already been started within our research group in this respect. Using binder and applying pressure are also other engineering techniques that may have an influence on the cell performance, especially within all-solid-state batteries.

To obtain a better electrochemical behavior, counter electrodes need to be improved. In this study, conversion-based electrodes were mainly used since no state of the art for intercalation-based anode materials were available. Some efforts [44] within our research group have been done in order to develop intercalation-based anode materials for FIBs, though, they are still not operational at this state. However, some strategies such as using thin films [1], infiltrating the active electrode material into porous carbon hosts or dispersing or wrapping them in conductive matrices may mitigate the negative effect of volume change within conversion-based electrode materials [140].

Finally, enhancement of the electrolyte materials plays a vital role to develop FIBs further, especially when it comes to all-solid-state batteries. Particle engineering of the electrolyte may have some influences: For instance, sintering of $La_{0.9}Ba_{0.1}F_{2.9}$ may help to achieve a better electrochemical performance, as it is reported that sintering of this electrolyte material significantly improves the ionic conductivity [35].

7 Appendix

7.1 Cyclic Voltammetry (Complementary Information)

The initial potential sweep in cyclic voltammetry is expressed by:

$$E = E_i - vt \tag{7.1}$$

and the reverse sweep of the cycle is also represented by:

$$E = E_i + v't \tag{7.2}$$

where E_i is the initial potential, t is time and v and v' (often $v = v'$) are the sweep rates (rate of potential change) with a unit of (V/s).

During cyclic voltammetry, a small current starts flowing as soon as the potential approaches the reversible potential for the electrode process (for example reversible reduction of an oxidized species). The magnitude of the current rapidly increases. Then the current decrease due to depletion of the reactants which results in a concentration profile (as can be schematically seen in **Figure 7-1**) into solution leading to a decrease in the diffusion rate at the electrode surface. Therefore, the change in the current is accompanied by a maximum value, as can be seen in **Figure 7-2a**.
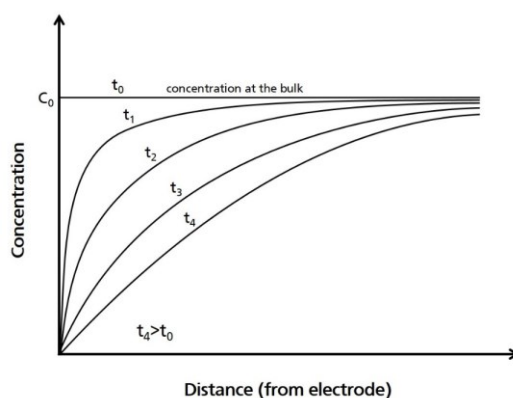

Figure 7-1. Schematic illustration of concentration profiles for reduction of an oxidized species in cyclic voltammetry.
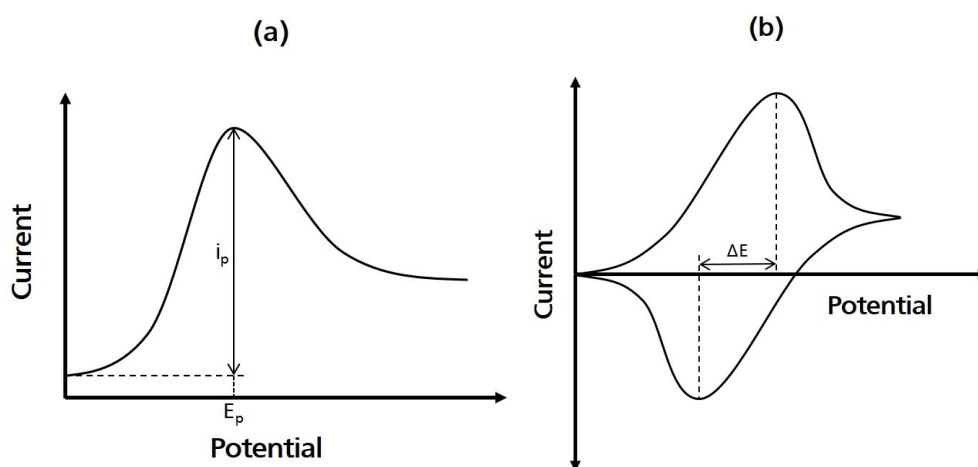

Figure 7-2. (a) Schematic depiction of the maximum peak current in cyclic voltammetry for reduction of an oxidized species; (b) schematic illustration of cyclic voltammetry plot for a reversible diffusion-controlled process [58].

The maximum current value can be determined by combining equation (7.1) with Fick's laws of diffusion (first law: $J = -D\frac{\partial C}{\partial X}$; second law: $\frac{\partial C}{\partial t} = D\left(\frac{\partial^2 C}{\partial x^2}\right)$) and the Nernst equation [58]:

$$i_p = \frac{0.447 F^{3/2} A n^{3/2} D^{1/2} C_0 v^{1/2}}{R^{1/2} T^{1/2}} \tag{7.3}$$

where i_p is the peak current, A is the electrode area and other parameters are the same identity as defined previously. Note that this equation has been obtained by numerical methods and therefore, the constant value of 0.447 may slightly be different in different textbooks. At 25 °C the abovementioned equation can also be rewritten as (Randles-Sevcik equation [63]):

$$j_{max} = 2.69 \times 10^5 n^{3/2} D^{1/2} C_0 v^{1/2} \tag{7.4}$$

where j_{max} is the maximum current density.

It is worth noting that equation 7.11(7.1) is only valid for small values of voltage sweep rate, typically below 1 mV/s. However, for higher sweep rates a correction due to the effect of electrical double layer on electrode kinetics, resulting in a capacitance effect at the electrode-electrolyte interface, must be implemented to the equation:

$$E = E_i - vt + r(i_f + i_c) \tag{7.5}$$

Where r is the cell resistance and i_f and i_c are faradic and capacity currents, respectively. For such a condition the position of the potential at which the maximum current is observed (E_p) depends on the scan rate v whereas the case that voltage sweep is very low in which E_p does not depend on the scan rate [63].

Figure 7-2b schematically shows a cyclic voltammogram of a reversible, diffusion-controlled reaction which exhibits an approximately symmetrical pair of current peaks. The voltage separation (ΔE) of the peaks is determined by:

$$\Delta E = \frac{2.3 RT}{nF} \tag{7.6}$$

and this value is independent of the voltage sweep rate. However, for quasi-reversible processes, the voltage at the current peak depends on the scan rate with a larger voltage separation ΔE, as can be seen in **Figure 7-3a**. In this case, the current peaks are separated and the shape of the peaks are more rounded.

Cyclic voltammograms of a fully irreversible electrode process consist of only a single peak, as is depicted in **Figure 7-3b**. For an irreversible process the potential of the current peak depends also to the voltage sweep rate. Assuming that the back reaction is really negligible the peak current as a function of peak potential can be determined by [141]:

$$i_p = 0.22 nFC_0 k_{app} exp\left[-\alpha\frac{nF}{RT}(E_m - E^0)\right] \tag{7.7}$$

where E_m is the voltage of the current peak, k_{app} is the apparent rate constant, and the other symbols are defined as described in this chapter.
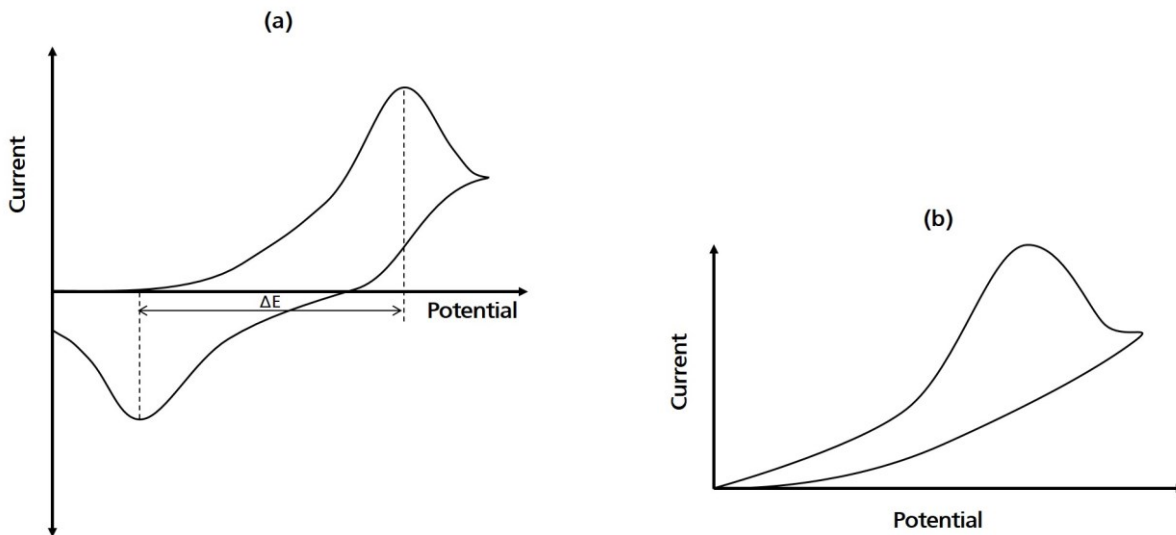
Figure 7-3. Schematic cyclic voltammograms of (a) a quasi-reversible process; (b) an irreversible process [58].

Often cyclic voltammograms of electrochemical systems are more complicated than the specific examples that have been provided. Especially for battery systems that several side reactions can overlap with the desired electrochemical reaction, it is not that simple to determine which peak belongs to which species or process. Nevertheless, cyclic voltammetry is a very important and widely used method to identify reversible couples which is specifically of great interest when it comes to secondary (rechargeable) batteries. Moreover, this method can provide information about the rate constant and transfer coefficient of an electrode process.

7.2   Complementary Information about Electrochemical Impedance Spectroscopy

7.2.1   Response to Small-Signal Excitation

Consider applying a time dependent sinusoidal signal. The voltage signal $V(t)$ can be expressed as a function of time (t) as follows:

$$V(t) = V_A Sin(\omega t) \tag{7.8}$$

where ω is the angular frequency and is equal to:

$$\omega = 2\pi f \tag{7.9}$$

and f is the applied AC frequency. In a linear system, the response of current to such a voltage signal is a sinusoid at the same frequency but shifted in phase, as can be seen in **Figure 7-4**, based on the ratio of capacitive and resistive components of the output current. Then the current response in a linear system is determined by:

$$I(t) = I_A sin(\omega t + \phi) \tag{7.10}$$

The complex impedance of the system can be written, in a similar form to Ohm's law, as a ratio of input voltage and response current as follows:

$$Z = \frac{V(t)}{I(t)} = \frac{V_A sin(\omega t)}{I_A sin(\omega t + \phi)} = Z_A \frac{sin(\omega t)}{sin(\omega t + \phi)} \tag{7.11}$$

The impedance can be described in terms of its magnitude ($Z_A = |Z|$) and the phase shift (ϕ) between current and voltage. It is also possible to express the impedance as a complex function. Then the potential and current response can be described as follows:

$$V(t) = V_A exp(j\omega t) \tag{7.12}$$

and

$$I(t) = I_A exp(j\omega t - j\phi) \tag{7.13}$$

Combining equation $(7.11) - (7.13)$ and knowing from basic mathematics that $exp(j\phi) = cos\phi + jsin\phi$, the following expression can be written for impedance:

$$Z = \frac{V}{I} = Z_A exp(j\phi) = Z_A(cos\phi + jsin\phi) = Z_{re} + jZ_{im} \tag{7.14}$$

Equation (7.14) shows that impedance can be expressed as a combination of a real or in-phase (Z_{re} or Z') and an imaginary or out-of-phase (Z_{im} or Z'') terms.

Then the phase shift at a chosen angular frequency is the ratio of imaginary and real impedance:

$$tan\phi = \frac{Z_{im}}{Z_{re}} \tag{7.15}$$
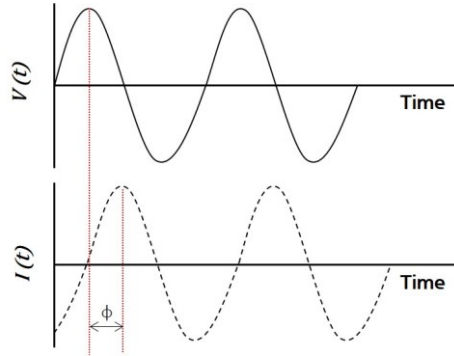
Figure 7-4. Schematic depiction of phase shift in current response due to applying an AC voltage [65].

7.2.2 Equivalent Circuits

For simple R|C circuits, the voltage across the both circuit elements are equal but the total current of the circuit is the summation of the currents that are flowing through the resistor and capacitor:

$$I(t) = \frac{V(t)}{Z} = \frac{V(t)}{R} - \frac{\omega C V(t)}{j} = V(t)\left[\frac{1}{R} - \frac{\omega C}{j}\right] = V(t)\frac{1 + (\omega RC)^2}{R - j\omega R^2 C} \tag{7.16}$$

Then the impedance can be expressed as:

$$Z = \frac{R}{1 + (\omega RC)^2} - j\frac{\omega R^2 C}{1 + (\omega RC)^2} \tag{7.17}$$

Equation (7.17) consists of a real part of $Z_{re} = \frac{R}{1+(\omega RC)^2}$ and an imaginary part of $Z_{im} = j\frac{\omega R^2 C}{1+(\omega RC)^2}$

The electrochemical systems often show more complicated behaviors that require additional impedance components. As an example, consider a highly conductive solution, where the impedance of the solution is low and can be represented by a pure resistance $R_{sol} = R_1$. The ions must first pass through the solution (R_1) to reach the electrode surface. Then the ions need to cross the electrode – electrolyte interface. This process is accompanied by charge transfer between the solution ions and electrons in the electrodes which results in a charge transfer resistance of $R_{ct} = R$. At the interface the opposite charges that do not take part in the charge transfer build up a double layer capacitance, $C_{dl} = C$. To describe such an ion transport process, a model that is described in **Figure 7-5a** may be used. For such a model the phase angle at the critical frequency is determined by $tan\phi = \frac{R/2}{R/2+R_1}$ (**Figure 7-5a**). Since the behavior of the electrolyte is considered to be a purely resistive, the phase angle at high frequencies equals 0° (**Figure 7-5c**). At lower frequencies, however, the interfacial kinetics process (expressed as $C_{dl}|R_{ct}$) dominates. Then an increase in the phase angle is detected due to the capacitance (C_{dl}) effect of the double layer (**Figure 7-5c**). Towards the lowest frequency range the charge transfer resistance becomes the predominant contributor to the total impedance and therefore, the phase angle reduces to 0°.
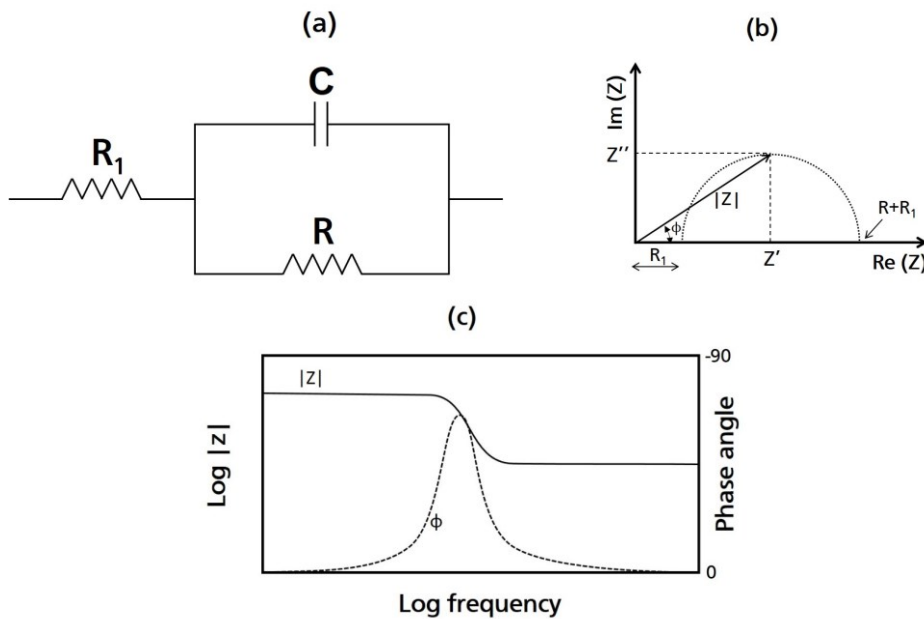

Figure 7-5. (a) Equivalent circuit for ion transport inside a highly conductive solution; (b) schematic Nyquist and (c) schematic Bode plots for such an ion transport in accordance with the proposed model [65].

7.2.3 Constant Phase Element

Effective equivalent capacitance (C_eff) of a CPE is a very important term that can be used for interpretation of the possible contributing phenomena in the impedance behavior. C_eff should be calculated according to the architecture of the equivalent circuit and the respective boundary conditions. Here the relationship for calculation of C_eff for three different equivalent circuits will briefly described. The first case is an equivalent circuit consist of a resistor R in parallel with a CPE (0.8 < α < 1). Then the circuit impedance is expressed as:

$$Z = \frac{R}{1 + j(2\pi f)^{\alpha}RQ} \tag{7.18}$$

Then the C_{eff} can be estimated from the value of Z_{im}^{max} which corresponds to the ω_{max}. The C_{eff} can be calculated according to the following [142]:

$$Q = sin(\alpha\pi/2)\frac{-1}{Z_{im}(\omega_{max})^{\alpha}} \tag{7.19}$$

$$C_{eff} = Q\frac{1}{(\omega_{max})^{1-\alpha}sin(\alpha\pi/2)} \sim Q(\omega_{max})^{\alpha-1} \tag{7.20}$$

Q (CPE coefficient) becomes a pure capacitance when $\alpha=1$, then:

$$\omega_{max} = \frac{1}{C_{eff}R} \;and\; Q = C_{eff} = \frac{1}{\omega_{max}R} = \frac{-1}{Z_{im}^{max}(\omega_{max})} \tag{7.21}$$

In the second case a CPE is in series, with a resistor R. The C_{eff} can be calculated by [68]:

$$C_{eff} = \frac{(RQ)^{1/\alpha}}{R} \tag{7.22}$$

For an equivalent circuit with a design of $R_1 - CPE|R$ (R_1 in series with another circuit consist of a CPE in parallel with R), C_{eff} is determined according to the following equation [143]:

$$C_{eff} = \left[\frac{QR_1R}{R_1+R}\right]^{1/\alpha}\frac{R_1+R}{R_1R} \tag{7.23}$$

7.2.4 Warburg Impedance

By assuming that the diffusion layer δ_L has an unlimited thickness within the applied AC frequency range, the rate-determining step in kinetic process may be the "semi-infinite" diffusion. Note that it is assumed that the diffusion layer is much smaller than the thickness of the sample. The equation for the "semi-infinite" Warburg impedance $Z_W(\omega)$ can be written as follows [65]:

$$Z_W(\omega) = \frac{R_W}{\sqrt{j\omega}} \tag{7.24}$$

where R_W is the diffusion resistance and for a Nernstian reversible case R_W can be determined by [144]:

$$R_W = \frac{RT\delta_L}{n^2F^2ADC_0} \tag{7.25}$$

7.3 Complementary Information About X-ray Powder Diffraction

7.3.1 Geometry of the Diffractometer

Two commonly used geometries in diffractometers are schematically depicted in **Figure 7-6**. The Bragg-Brentano geometry, which is based on reflection geometry, takes the advantage of the focusing of the diffracted beam resulting in both high resolution and high diffracted intensity. All the XRD measurements in the context of this dissertation have been performed using the Bragg-Brentano geometry. The advantage of the transmission geometry is that a small

amount of powder sample is required in this geometry, though, they have a lower resolution as compared to the reflection geometry (Bragg-Brentano).
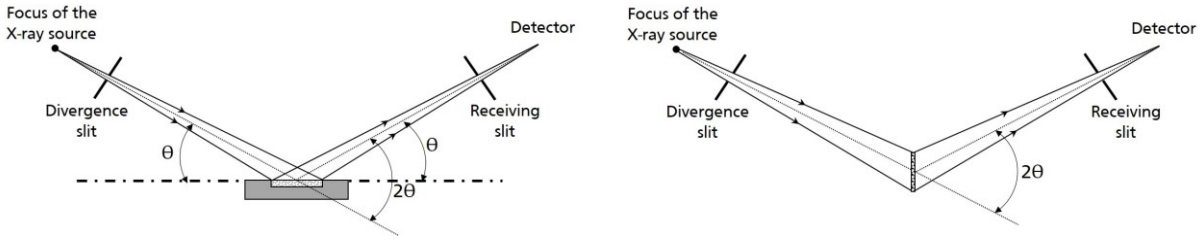

Figure 7-6. Schematic illustrations of the Bragg-Brentano (left) and transmission geometries (right) [70].

7.3.2 Peak Positions

Peak position is primarily determined by the unit cell dimensions: The diffraction angle (Θ_{hkl}) of a reflection from a series of lattice planes (hkl) is determined form the interplanar distance (d_{hkl}) and the wavelength (λ), according to the Bragg's law:

$$sin\theta_{hkl} = \frac{\lambda}{2d_{hkl}} \tag{7.26}$$

Note that the interplanar distance is a function of the unit cell parameters (and Miller indices, h, k, l). For each crystal system an equation for the inverse square of the interplanar distance ($1/d^2$) based on the Miller indices can be expressed. For instance, for cubic, tetragonal and orthorhombic systems the following relationships can be written:

$$\text{Cubic:} \qquad \frac{1}{d^2} = \frac{h^2 + k^2 + l^2}{a^2} \tag{7.27}$$

$$\text{Tetragonal:} \qquad \frac{1}{d^2} = \frac{h^2 + k^2}{a^2} + \frac{l^2}{c^2} \tag{7.28}$$

$$\text{Orthorhombic:} \qquad \frac{1}{d^2} = \frac{h^2}{a^2} + \frac{k^2}{b^2} + \frac{l^2}{c^2} \tag{7.29}$$

There are other factors that may affect the peak positions. In fact, various instrumental and specimen features may affect the peak position which is often known as systematic aberrations (distortions) and usually are merged into a single correction parameter, $\Delta 2\theta$:

$$2\theta_{obs} = 2\theta_{calc} + \Delta 2\theta \tag{7.30}$$

This correction parameter can be expressed in six factors for a the most commonly used Bragg-Brentano focusing geometry:

$$\Delta 2\theta = \frac{p_1}{tan2\theta} + \frac{p_2}{sin2\theta} + \frac{p_3}{tan\theta} + p_4 sin2\theta + p_5 cos\theta + p_6 \tag{7.31}$$

The first two parameters (p_1 and p_2) account for the axial divergence of the incident beam. It is worth mentioning that usually the soller slits minimize the axial divergence and therefore, these two parameters are often neglected for practical purposes [70]. The third parameter, p_3, accounts for the zero curvature of flat samples which are typically used in Bragg-Brentano goniometers. In fact, the geometry of the sample may distort the ideal focusing in which the curvature of the sample surface should vary with Bragg angle. The fourth parameter (p_4), which

is known as transparency shift (due to penetration of the beam into the sample), becomes more important when it comes to thick (more than 50 to 100 μm) and low absorption samples. The fifth parameter, p_5, is due to sample displacement and can be substantial when there is no easy way to control the exact position of the sample surface. The last parameter is called the zero shift error and is constant over the whole range of angles and usually arises due to improper settings of zero angles for one or more diffractometer axes. This aberration can be minimized by proper alignment of the goniometer.

7.3.3 Peak Shapes

The peak shapes can be described by the so-called peak shape function (PSF) which is a convolution of three functions of instrumental broadening (Ω), wavelength dispersion (Λ) and specimen function (Ψ):

$$PSF(\theta) = \Omega(\theta) \otimes \Lambda(\theta) \otimes \Psi(\theta) + b(\theta) \tag{7.32}$$

and b is the background function. The instrumental function, $\Omega(\theta)$, depends on multiple geometrical parameters including the specimen, slits, monochromatros, and the geometry of the source. The wavelength dispersion function reflects the distribution of the wavelength in the source which depends on the nature of the source and the monochromatization technique. The specimen function originates from dynamic scattering or deviate (yield a small width of the Bragg peaks) and physical properties of the specimen, e.g. crystallite (grain) size and microstrains. When the crystallite size is small (often ≤ 1μm) the peak widths may substantially increase (peak broadening). The same also holds true when the crystallites are strained. Therefore, the broadening effects introduced by the physical properties of the sample, often provide useful information in characterizing the material. This broadening (the excess width arising only from the physical properties in addition to all instrumental contributions) can be expressed as follows:

$$\beta = \frac{\lambda}{\tau \, cos\theta} \tag{7.33}$$

$$\beta = k \, \varepsilon \, tan\theta \tag{7.34}$$

where β is the broadening (in radians) and k is a constant which depends on how the microstrain is defined.

The intensity of the ith point ($1 \leq I \leq n$, where n is the total number of measured points) can generally expressed as follows:

$$Y(i) = b(i) + \sum_{k=1}^{m} I_k[y_k(x_k) + 0.5y_k(x_k + \Delta x_k)] \tag{7.35}$$

where $Y(i)$ is the intensity (of the ith point), $b(i)$ accounts for the background effect, $y(x)$ stands for the peak shape function, I_k is the intensity of the kth Bragg reflection, $x_k = 2\theta_i$ - $2\theta_k$ and Δx_k is the difference between the Bragg angles of $K\alpha_2$ and $K\alpha_1$ components in the doublet.

Gauss, Lorentz, Voigt, Pseudo-Voigt and Pearson-VII functions are the most commonly used peak shape function (y) that are used. Among them, Gaussian and Lorentzian distributions are the simplest peak shape functions which are compared in **Figure 7-7**. It can be seen that the Gauss function has no tails at the base but has a rounded maximum while the Lorenz function

is sharp near the maximum with a long tail on the sides near the base. Real peak shapes often are located somewhere between the Gauss and Lorentz distributions. Therefore, the peak shapes can be better represented as the mixture of the two functions.

Pseudo-Voigt function is a much simpler linear combination of Gauss and Lorentz functions. Then the Gauss and Lorentz functions are mixed in η/1-η ratio. The value of the mixing parameter (η) varies from 0 for a pure Lorentz to 1 for a pure Gauss function.

In all of the abovementioned peak shape functions the peak is centrosymmetric with respect to *x*-axis. In reality, however, the Bragg peaks are often asymmetric, especially at low Bragg angles, due to various instrumental factors such as axial divergence, non-ideal specimen geometry and non-zero curvature of the Debye rings. In order to reduce the peak asymmetry, a proper configuration of the instrument and its alignment is necessary. Nevertheless, the peak asymmetry cannot be completely eliminated, however, can be addressed in the profile fitting procedure. This can be done generally in three ways: 1- Introducing a multiplier that breaks the symmetry of the function resulting in an increase of the intensity on one side of the peak maximum (usually the low Bragg angle side) and a decrease on the opposite side. 2- Introducing split functions (split Pseudo-Voigt or split Pearson-VII) which employ two separate sets of peak shape parameters to represent the opposite sides of each peak. 3- Construction of the peak as a convolution of a symmetric peak shape and an asymmetrization function (can be empirical or base on the real instrumental parameters).
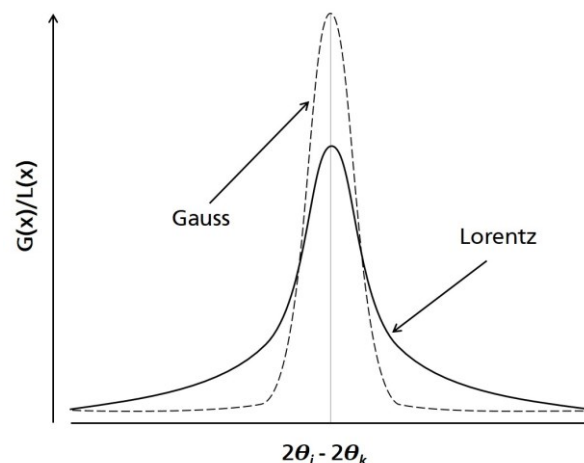
Figure 7-7. Schematic depiction of the Gauss and Lorentz peak shape functions with identical full widths at half maximum (FWHM).

7.3.4   Intensity of the Peaks

The factors that determine the peak intensity can generally be categorized in three groups: 1- Structural factors which are determined by the crystal structure; 2- Specimen factors such as shape and size, grain size and distribution, and microstructure; 3- Instrumental factors such as type of focusing geometry, slit and/or monochromator geometry, properties of radiation and detector. However, it should be taken into consideration that the peak intensity is primarily determined by the structural part and other factors have only secondary effects. Structural factors are mainly determined by the internal structure of the crystal (relative positions of atoms in the unit cell) and other characteristics such as thermal motion and population parameters.

Integrated intensity is a term that is often used to describe the intensity of a Bragg peak and it differs with the maximum of the peak. In fact, the integrated intensity is defined as the area under the peak which remains unchanged in case of broadening of the peak and therefore, reflects the true intensity of Bragg peaks in powder diffraction. For the sake of simplicity, the integrated intensity is often referred to as "intensity" [70]. Note that the integrated intensity is a function of atomic structure and also depends on specimen and instrumental parameters as well.

7.3.5 Mathematical Equations for Figures of Merit

$$R_p = \frac{\sum_{i=1}^{n}\left|Y_i^{obs} - Y_i^{calc}\right|}{\sum_{i=1}^{n}Y_i^{obs}} \times 100\% \tag{7.36}$$

$$R_{wp} = \left[\frac{\sum_{i=1}^{n}w_i\left(Y_i^{obs} - Y_i^{calc}\right)^2}{\sum_{i=1}^{n}w_i\left(Y_i^{obs}\right)^2}\right]^{1/2} \times 100\% \tag{7.37}$$

$$R_B = \frac{\sum_{j=1}^{m}\left|I_i^{obs} - I_i^{calc}\right|}{\sum_{j=1}^{m}I_i^{obs}} \times 100\% \tag{7.38}$$

$$R_{exp} = \left[\frac{n - p}{\sum_{i=1}^{n}w_i\left(Y_i^{obs}\right)^2}\right]^{1/2} \times 100\% \tag{7.39}$$

$$\chi^2 = \frac{\sum_{i=1}^{n}w_i\left(Y_i^{obs} - Y_i^{calc}\right)^2}{n - p} = \left[\frac{R_{wp}}{R_{exp}}\right]^2 \tag{7.40}$$

In the abovementioned equations n is the total number of points that have been measured in the experimental powder diffraction pattern, Y_i^{obs} and Y_i^{calc} are the observed and calculated intensity of ith point, respectively, w_i is the weight of the ith data point, I_i^{obs} and I_i^{calc} are the observed and calculated integrated intensity of the jth Bragg peak and p is the number of free least squares parameters [70].

7.4 Changes of Lattice Parameters of the Electrolyte During Charging

Table 7-1. Changes in lattice parameter of the La$_{0.9}$Ba$_{0.1}$F$_{2.9}$ electrolyte within the LaSrMnO$_4$/PbF$_2$ cell at the conditions that area stated at Figure 5-3.

Cutoff potential (V)	La$_{0.9}$Ba$_{0.1}$F$_{2.9}$ (P-3$_c$1)	
	a (Å)	c (Å)
Before charge	7.219(1)	7.388(2)
0.45	7.214(1)	7.380(1)
1.2	7.215(1)	7.373(1)
1.43	7.213(1)	7.377(1)
1.55	7.207(1)	7.372(1)
2	7.206(1)	7.372(1)
3	7.204(1)	7.368(1)

Table 7-2. Changes in lattice parameter of the La$_{0.9}$Ba$_{0.1}$F$_{2.9}$ electrolyte within the La$_2$CoO$_{4+d}$/Pb+PbF$_2$ cell at the conditions that are stated at Figure 5-19.

Charge cutoff capacity (mAh/g)	La$_{0.9}$Ba$_{0.1}$F$_{2.9}$ (P-3$_c$1)	
	a (Å)	c (Å)
Before charge	7.223(2)	7.392(3)
8	7.222(1)	7.384(2)
13	7.220(1)	7.388(3)
30	7.215(1)	7.376(2)
40	7.220(2)	7.380(2)
50	7.218(2)	7.380(2)
63	7.223(2)	7.385(2)
80	7.221(1)	7.388(2)
90	7.222(1)	7.389(2)
100	7.220(2)	7.385(2)
133	7.221(2)	7.388(2)

Table 7-3. Changes in lattice parameter of the La$_{0.9}$Ba$_{0.1}$F$_{2.9}$ electrolyte within the La$_2$NiO$_{4+d}$/Zn+ZnF$_2$ cell at the conditions that are stated at Figure 5-27.

Charge cutoff capacity (mAh/g)	La$_{0.9}$Ba$_{0.1}$F$_{2.9}$ (P-3$_c$1)	
	a (Å)	c (Å)
Before charge	7.223(1)	7.391(2)
10	7.223(1)	7.396(1)
30	7.217(1)	7.389(1)
40	7.222(1)	7.393(1)
50	7.221(1)	7.396(1)
65	7.225(1)	7.398(1)
90	7.224(1)	7.397(1)
110	7.220(1)	7.389(1)
120	7.225(1)	7.396(2)
135	7.221(1)	7.393(1)
155	7.220(1)	7.389(1)

7.5 TEM-Related Analysis of Charged / Un-charged La$_2$NiO$_{4+d}$F$_y$

The quality of the Fast-ADT data was good enough for crystal structure determination through direct methods and further refinement within the space group *Fmmm*. Structure refinement using the dynamical scattering theory [145] was possible for the un-fluorinated phase but the reflection quality of the fluorinated phase only allowed to perform a kinematical refinement. Nevertheless, both crystal refinements converged with good and acceptable R1 values for electron diffraction (see **Table 7-4** for further details; structural parameters extracted from the refinement can be found in **Figure 7-8**).
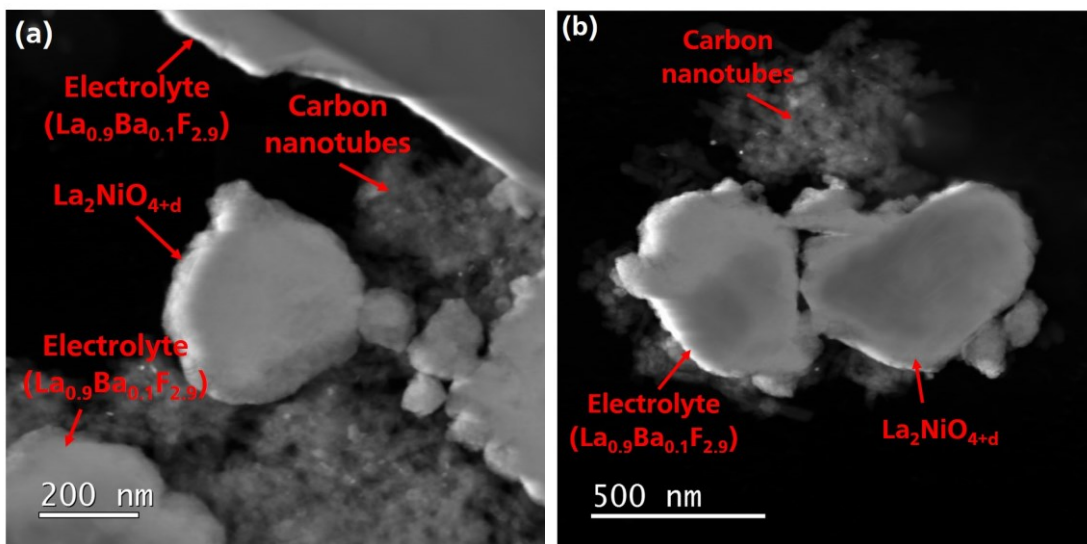
Figure 7-8. STEM-HAADF images for the un-charged sample showing the different phases present in the powder.
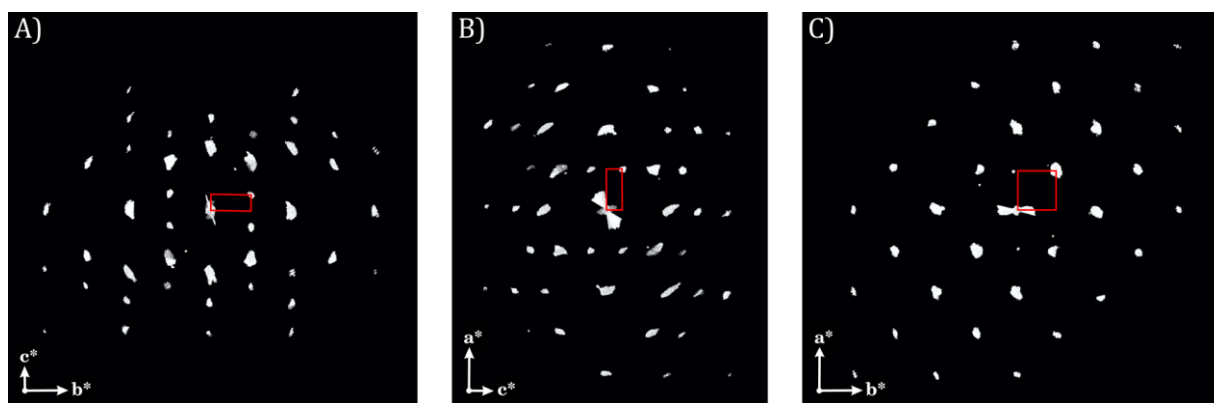

Figure 7-9. Projections of the reconstruction of the observed diffraction space along the main axes of the orthorhombic setting for the fluorinated phase (a*, b* and c*, respectively). The unit-cell is shown in red rectangles.

Table 7-4. Parameters of the crystal structure determination and refinement from both phases found in the after charged powder using electron diffraction.

	La_2NiO_4	$La_2NiO_4F_{1.72}$
Structure Solution		
Tilt range (°)	-45/35	-45/45
Acquired diffraction patterns	81	91
Num. of sampled reflections	3600	4466
Num. of ind. reflections	142	167
Used resolution (Å)	0.7	0.7
Ind. reflection coverage (%)	78.0	80.3
Overall B ($Å^2$)	2.213	2.510
R_{sym}	0.091	0.094
Residual R(F) (Sir2014 [82])	0.110	0.143
Refinement*		
Num. of used reflections (obs/all)	649/356	180/149
R1 (obs/all)	0.090/0.147	0.210/0.220

*The La_2NiO_4 structure refinement was performed using the dynamical scattering theory while the kinematical theory was used for the $La_2NiO_4F_{1.72}$ refinement.

Table 7-5. Structural parameters extracted from refinement of the Fast-ADT measurements from both phases found in the after charged powder using electron diffraction.

State of charge	Atom	Wyckoff site	x	y	z	Occupancy	Phase
Charged	La1	8i	1/2	0	0.1345	1	La_2NiO_{4+d} (*Fmmm*, $a = 5.77$ Å, $b = 5.74$ Å, $c = 13.24$ Å)
	Ni1	4a	0	0	0	1	
	O1	8e	1/4	1/4	0	1	
	O2	8i	0	0	0.1240		
	F1	8f	1/4	1/4	1/4	0.86	
Uncharged	La1	8i	1	0	0.1381	1	$La_2NiO_{4+d}F_y$ (*Fmmm*, $a = 5.63$ Å, $b = 5.56$ Å, $c = 15.14$ Å)
	Ni1	4b	1/2	0	0	1	
	O1	8e	1/2	0	0.1700	1	
	O2	8i	1/4	1/4	1/4	1	

7.6 XPS Analysis for Charged/Un-charged La$_2$NiO$_{4+d}$

Explanation of the C1s fit model:

- The Position of the sp^2 peak was limited to a value between 284.5 eV and 285 eV according to [146].
- The sp2-signal consists out of two peaks one with a 0.5 eV higher BE according to [146].
- BE distances between the main sp^2 peak and the other peaks were fixed to the following positions:
  - C-OH +1.50 eV [146]
  - C=O +2.29 eV [146]
  - COOH +3.99 eV [146]
  - C-F + 2.9 eV [129]
  - C-C-F +0.9 eV [129]
    (C-C-F is the characteristic BE of a neighboring carbon next to a fluorinated carbon).
- FWHM, were limited to twice the value of the main sp^2 peak.
- The area of the C-F and the C-C-F fit were set to be equal, in order to prevent overestimation of the C-C-F fit.

Note that XPS cannot be used to track the changes of the Ni oxidation state or other changes in the Ruddlesden-Popper-type phase. This originates from the fact that the particles of the active material show a strong coverage with the electrolyte and/or carbon species. Therefore, no Nickel signal could be observed, showing that the XPS spectra provide only information on the nano-crystalline carbon and electrolyte additives (**Figure 7-11**).
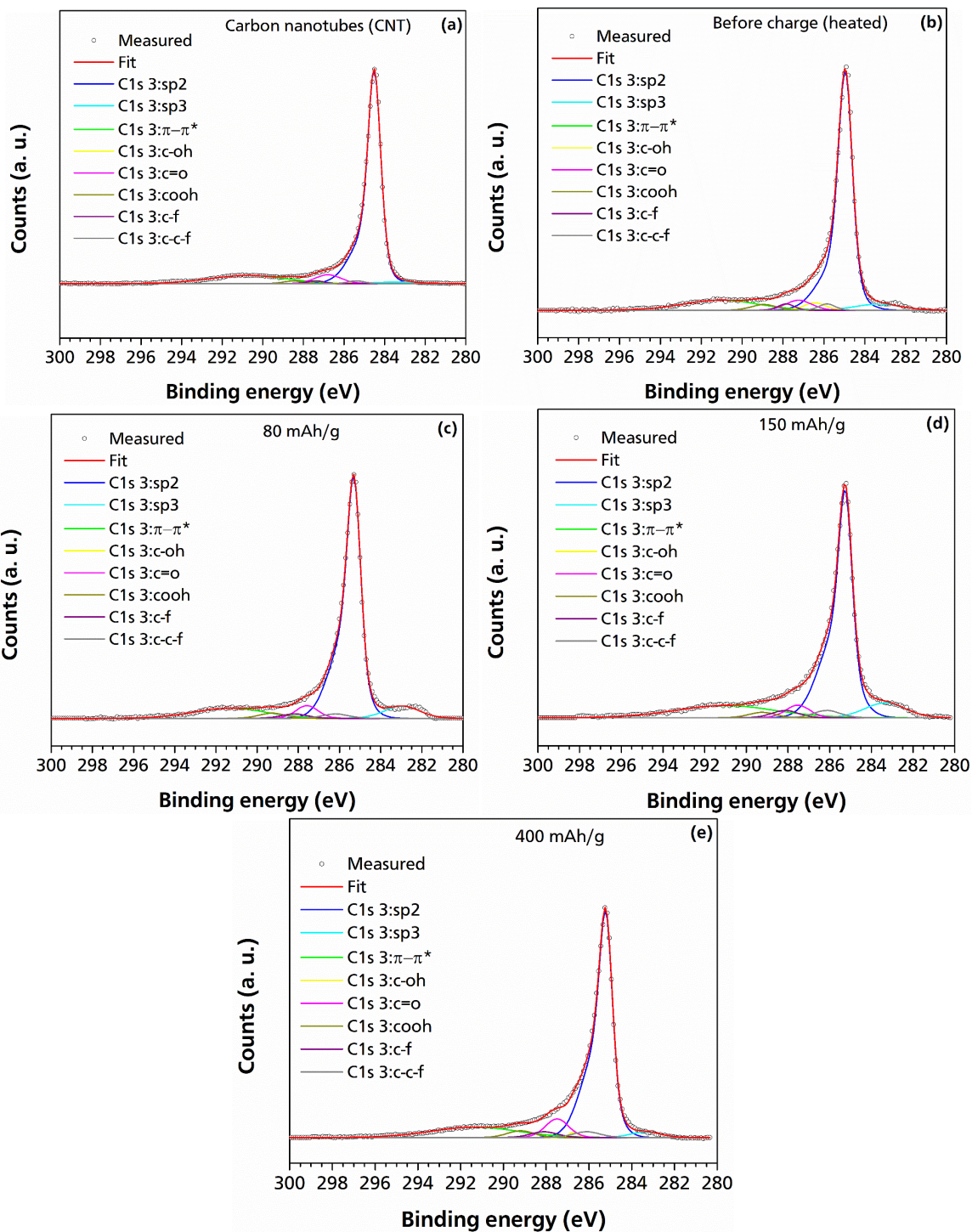
Figure 7-10. XPS spectra, fit, and partial fits of the carbon signal for carbon nanotubes (CNT) and before/after charging up to different cutoff capacities at T = 170 °C and I = 24 µA/cm². The uncharged sample has been heated to 170 °C for 6 h inside an Ar-filled glovebox.
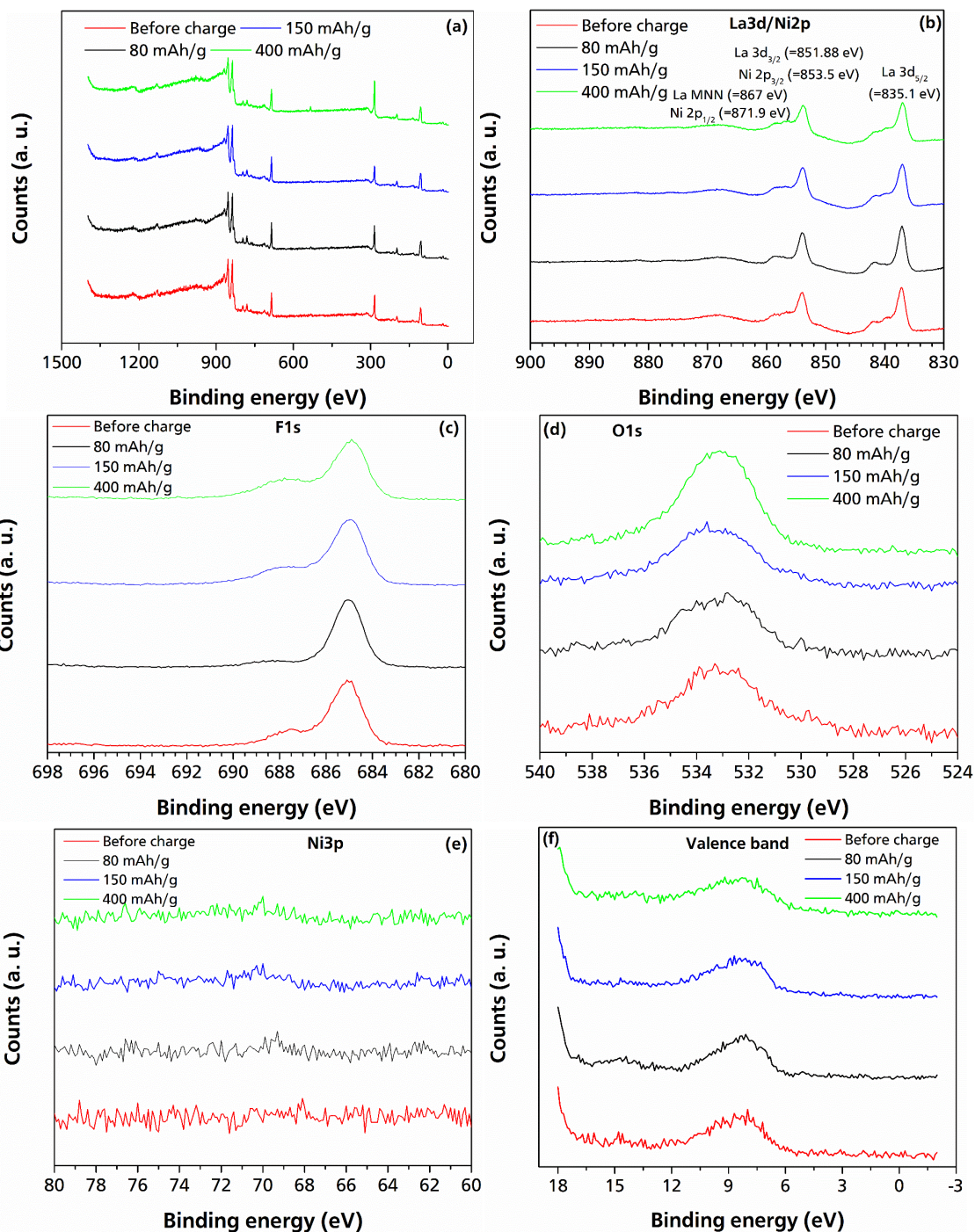
Figure 7-11. XPS survey (a) and detail spectra of La3d/Nip2 (b), F1s (c), O1s (d), Ni3p (e), and valence band (f) of the un-charged (heated at 170 °C for 6 h inside an Ar filled glovebox) and charged electrode composites containing 60 wt% of $La_{0.9}Ba_{0.1}F_{2.9}$, 30 wt% of $La_2NiO_{4+d}F_y$ and 10 wt% carbon nanotubes. The Ni3p (g) and the La3d (h) signals for pure $La_2NiO_{4.13}$ (without mixing with electrolyte and carbon nanotubes). For pure $La_2NiO_{4.13}$, the Ni3p signal can be easily resolved. The binding energies for La3d/Ni2p are taken from NIST database [147].

References

1. Nitta, N., et al., *Li-ion battery materials: present and future.* Materials Today, 2015. **18**(5): p. 252-264.
2. Tarascon, J.M., *Is lithium the new gold?* Nature Chemistry, 2010. **2**(6): p. 510.
3. Tahil, W., *The Trouble With Lithium*. 2006, Meridian International Research.
4. Vikström, H., S. Davidsson, and M. Höök, *Lithium availability and future production outlooks.* Applied Energy, 2013. **110**: p. 252-266.
5. IEA, *Technology roadmap, electric and plug-in hybrid electric vehicles*. 2011, International Energy Agency. p. 52.
6. Jaskula, B.W., *Mineral Commodity Summaries: Lithium*. 2019, United States Geological Survey (USGS). p. 98-99.
7. Mauger, A., et al., *Challenges and issues facing lithium metal for solid-state rechargeable batteries.* Journal of Power Sources, 2017. **353**: p. 333-342.
8. Sun, C., et al., *Recent advances in all-solid-state rechargeable lithium batteries.* Nano Energy, 2017. **33**: p. 363-386.
9. Sawicki, M. and L.L. Shaw, *Advances and challenges of sodium ion batteries as post lithium ion batteries.* RSC Advances, 2015. **5**(65): p. 53129-53154.
10. Choi, J.W. and D. Aurbach, *Promise and reality of post-lithium-ion batteries with high energy densities.* Nature Reviews Materials, 2016. **1**(4).
11. Shao, Y., et al., *Highly reversible Mg insertion in nanostructured Bi for Mg ion batteries.* Nano Letters, 2014. **14**(1): p. 255-60.
12. Jiao, H., et al., *A rechargeable Al-ion battery: Al/molten $AlCl_3$-urea/graphite.* Chemical Communications, 2017. **53**(15): p. 2331-2334.
13. Zhao, X., et al., *Chloride ion battery: A new member in the rechargeable battery family.* Journal of Power Sources, 2014. **245**: p. 706-711.
14. Anji Reddy, M. and M. Fichtner, *Batteries based on fluoride shuttle.* Journal of Materials Chemistry, 2011. **21**(43): p. 17059-17062.
15. *List of Occurrences*. [cited 2019 09.07.2019]; Available from: http://www.mindat.org/min-1576.html.
16. Baukal, W., *Electrochemical secondary cells which contains only solid materials*. 1974, Patent CA 953780 A1.
17. Kennedy, J.H. and R.C. Miles, *Ionic Conductivity of Doped Beta-Lead Fluoride.* Journal of Electrochemical Society, 1976. **123**(1): p. 10-14.
18. Kennedy, J.H. and J.C. Hunter, *Thin-Film Galvanic Cell $Pb/PbF_2/PbF_2,CuF_2/Cu$.* Journal of Electrochemical Society, 1976. **123**(12).
19. Schoonman, J., *A Solid-State Galvanic Cell with Fluoride-Conducting Electrolytes.* Journal of Electrochemical Society, 1976. **123**: p. 1772-1775.
20. Danto, Y., et al., *A $Pb|PbF_2|BiF_3|Bi$ thin solid film reversible galvanic cell.* Thin Solid Films, 1978. **55**(3): p. 347-354.
21. Schoonman, J., et al., *FluorideConducting Solid Electrolytes in Galvanic Cells.* Journal of Electrochemical Society, 1979. **126**: p. 709-713.
22. Schoonman, J. and A. Wolfert, *Alloy-Anodes in Fluoride Solid-State Batteries.* Journal of Electrochemical Society, 1981. **128**(7): p. 1522–1523.
23. Schoonman, J. and A. Wolfert, *Solid-state galvanic cells with fast fluoride conducting electrolytes.* Solid State Ionics, 1981. **3-4**(373-379).
24. Rongeat, C., et al., *Solid Electrolytes for Fluoride Ion Batteries: Ionic Conductivity in Polycrystalline Tysonite-Type Fluorides.* ACS Applied Materials & Interfaces, 2014. **6**(3): p. 2103-2110.
25. Bhatia, H., et al., *Conductivity Optimization of Tysonite-type $La_{1-x}Ba_xF_{3-x}$ Solid Electrolytes for Advanced Fluoride Ion Battery.* ACS Applied Materials & Interfaces, 2017. **9**(28): p. 23707-23715.

26. Rongeat, C., et al., *Nanostructured Fluorite-Type Fluorides As Electrolytes for Fluoride Ion Batteries.* The Journal of Physical Chemistry C, 2013. **117**(10): p. 4943-4950.

27. Rongeat, C., et al., *Development of new anode composite materials for fluoride ion batteries.* Journal of Materials Chemistry A, 2014. **2**: p. 20861-20872.

28. MacManus, J.L., D.J. Fray, and J.E. Evetts, *Fluorination of $Y_1Ba_2Cu_3O_{7-x}$ by a solid state electrochemical method.* Physica C, 1991. **184**: p. 172-184.

29. Delville, M.H., et al., *Electrochemical fluorination of La_2CuO_4: a mild "chimie douce" route to superconducting oxyfluoride materials.* Inorgic Chemistry, 2009. **48**(16): p. 7962-9.

30. Clemens, O., et al., *Electrochemical fluorination of perovskite type $BaFeO_{2.5}$.* Dalton Transactions, 2014. **43**(42): p. 15771-15778.

31. Gschwind, F., Z. Zao-Karger, and M. Fichtner, *A fluoride-doped PEG matrix as an electrolyte for anion transportation in a room-temperature fluoride ion battery.* Journal of Materials Chemistry A, 2014. **2**(5): p. 1214-1218.

32. Dieudonné, B., et al., *Exploring the $Sm_{1-x}Ca_xF_{3-x}$ Tysonite Solid Solution as a Solid-State Electrolyte: Relationships between Structural Features and F^- Ionic Conductivity.* The Journal of Physical Chemistry C, 2015. **119**(45): p. 25170-25179.

33. Dieudonné, B., et al., *The key role of the composition and structural features in fluoride ion conductivity in tysonite $Ce_{1-x}Sr_xF_{3-x}$ solid solutions.* Dalton Transactions, 2017. **46**(11): p. 3761-3769.

34. Zhang, L., et al., *Development of dense solid state thin-film electrolyte for fluoride ion batteries.* Journal of Alloys and Compounds, 2016. **684**: p. 733-738.

35. Chable, J., et al., *Fluoride solid electrolytes: From microcrystalline to nanostructured tysonite-type $La_{0.95}Ba_{0.05}F_{2.95}$.* Journal of Alloys and Compounds, 2017. **692**: p. 980-988.

36. Grenier, A., et al., *Solid Fluoride Electrolytes and Their Composite with Carbon: Issues and Challenges for Rechargeable Solid State Fluoride-Ion Batteries.* The Journal of Physical Chemistry C, 2017. **121**(45): p. 24962-24970.

37. Zhang, L., M.A. Reddy, and M. Fichtner, *Electrochemical performance of all solid-state fluoride-ion batteries based on thin-film electrolyte using alternative conductive additives and anodes.* Journal of Solid State Electrochemistry, 2018. **22**: p. 997–1006.

38. Grenier, A., et al., *Electrochemical reactions in fluoride-ion batteries: mechanistic insights from pair distribution function analysis.* Journal of Materials Chemistry A, 2017. **5**(30): p. 15700-15705.

39. Mohammad, I., et al., *Synthesis of Fast Fluoride-Ion-Conductive Fluorite-Type $Ba_{1-x}Sb_xF_{2+x}$ ($0.1 \leq x \leq 0.4$): A Potential Solid Electrolyte for Fluoride-Ion Batteries.* ACS Applied Materials & Interfaces, 2018. **10**(20): p. 17249-17256.

40. Davis, V.K., et al., *Room-temperature cycling of metal fluoride electrodes: Liquid electrolytes for high-energy fluoride ion cells.* Science, 2018. **362**(6419): p. 1144-1148.

41. Mohammad, I., et al., *Room-Temperature, Rechargeable Solid-State Fluoride-Ion Batteries.* ACS Applied Energy Materials, 2018. **1**(9): p. 4766-4775.

42. Mohammad, I., et al., *Introducing Interlayer Electrolytes: Toward Room-Temperature High-Potential Solid-State Rechargeable Fluoride Ion Batteries.* ACS Applied Energy Materials, 2019. **2**(2): p. 1553-1562.

43. Ebner, M., et al., *Visualization and Quantification of Electrochemical and Mechanical Degradation in Li Ion Batteries.* 2013. **342**(6159): p. 716-720.

44. Wissel, K., et al., *Developing intercalation based anode materials for fluoride-ion batteries: topochemical reduction of $Sr_2TiO_3F_2$ via a hydride based defluorination process.* Journal of Materials Chemistry A, 2018. **6**(44): p. 22013-22026.

45. Wissel, K., et al., *Topochemical Fluorination of La_2NiO_{4+d}: Unprecedented Ordering of Oxide and Fluoride Ions in $La_2NiO_3F_2$.* Inorganic Chemistry, 2018. **57**(11): p. 6549-6560.

46. Ishihara, T., *Perovskite Oxide for Solid Oxide Fuel Cells.* 2009: Springer.

47. Muller, O. and R. Roy, *The Major Ternary Structural Families.* 1974, Springer-Verlag,: New York.

48. Aikens, L.D., R.K. Li, and C. Greaves, *The synthesis and structure of a new oxide fluoride, LaSrMnO₄F, with staged fluorine insertion.* Chemical Communications, 2000. **21**(21): p. 2129-2130.

49. Liu, C.N., Z. G., and G. Cao, *Understanding electrochemical potentials of cathode materials in rechargeable batteries.* Materials Today, 2016. **19**(2): p. 109-123.

50. Wu, H. and Y. Cui, *Designing nanostructured Si anodes for high energy lithium ion batteries.* Nano Today, 2012. **7**(5): p. 414-429.

51. Koerver, R., et al., *Chemo-mechanical expansion of lithium electrode materials – on the route to mechanically optimized all-solid-state batteries.* Energy & Environmental Science, 2018. **11**(8): p. 2142-2158.

52. Luo, S., et al., *Binder-free LiCoO₂/carbon nanotube cathodes for high-performance lithium ion batteries.* Advanced Materials, 2012. **24**(17): p. 2294-8.

53. Huggins, R.A., *Energy Storage.* 2010, New York: Springer.

54. Zhi, M., et al., *Nanostructured carbon-metal oxide composite electrodes for supercapacitors: a review.* Nanoscale, 2013. **5**(1): p. 72-88.

55. Nic, M., J. Jirat, and B. Kosata, *IUPAC Compendium of Chemical Terminology (Gold Book)* 2017, International Union of Pure and Applied Chemistry.

56. Goodenough, J.B. and K.S. Park, *The Li-ion rechargeable battery: a perspective.* Journal of the American Chemical Society, 2013. **135**(4): p. 1167-76.

57. Lide, D.R., *CRC Handbook of Chemistry and Physics* Internet Version 2005 ed, ed. D.R. Lide. Vol. Internet Version 2005. 2005, Boca Raton, FL: CRC Press.

58. Linden, D.R., Thomas B., *Handbook of Batteries.* 3rd ed. 2001, New York: McGraw-Hill. 1453.

59. Bruce, P.G., B. Scrosati, and J.M. Tarascon, *Nanomaterials for rechargeable lithium batteries.* Angewandte Chemie International Edition, 2008. **47**(16): p. 2930-46.

60. Aricò, A.S., et al., *Nanostructured materials for advanced energy conversion and storage devices.* Nature Materials, 2005. **4**: p. 366-377.

61. Okubo, M., et al., *Nanosize Effect on High-Rate Li-Ion Intercalation in LiCoO₂ Electrode.* Journal of American Chemical Society, 2007. **129**(23): p. 7444-7452.

62. Berg, H., *Batteries for Electric Vehicles: Materials and Electrochemistry*. 2015, United Kingdom: Cambridge University Press.

63. Hamann, C.H., A. Hamnett, and W. Vielstich, *Electrochemistry*. 2007, Weinheim: WILEY-VCH.

64. Barsoukov, E. and J.R. Macdonald, *Impedance Spectroscopy, Theory Experiment and Applications*. 2nd ed, ed. E. Barsoukov and J.R. Macdonald. 2005, Hoboken, New Jersey: John Wiley & Sons, Inc.

65. Lvovich, V.F., *Impedance Spectroscopy: Applications to Electrochemical and Dielectric Phenomena*. 2012, Hoboken, New Jersey: John Wiley & Sons, Inc. .

66. Irvine, J.T.S., C.S. Derek, and A.R. West, *Electroceramics: Characterization by Impedance Spectroscopy* Advanced Materials, 1990. **2**: p. 132-138.

67. Jorcin, J.-B., et al., *CPE analysis by local electrochemical impedance spectroscopy.* Electrochimica Acta, 2006. **51**(8-9): p. 1473-1479.

68. Brug, G.J., et al., *The Analysis of Electrode Impedances Complicated by the Presence of a Constant Phase Element* Journal of Electroanalytical Chemistry, 1984. **176**(1-2): p. 275-295.

69. Zoltowski, P., *On the electrical capacitance of interfaces exhibiting constant phase element behaviour.* Journal of Electroanalytical Chemistry, 1998. **443**: p. 149-154.

70. Pecharsky, V.K. and P.Y. Zavalij, *Fundamentals of Powder Diffraction and Structural Characterization of Materials*. 2005, New York: Springer.

71. West, A.R., *Solid state chemistry and its applications* 2nd ed. 2014, Chichester, United Kingdom: John Wiley & Sons.

72. Kolb, U., E. Mugnaioli, and T.E. Gorelik, *Automated electron diffraction tomography - a new tool for nano crystal structure analysis.* Crystal Research and Technology, 2011. **46**(6): p. 542-554.

73. Mugnaioli, E. and U. Kolb, *Structure solution of zeolites by automated electron diffraction tomography – Impact and treatment of preferential orientation.* Microporous and Mesoporous Materials, 2014. **189**: p. 107-114.

74. Sáez Puche, R., J.L. Rodriguez, and F. Fernández, *Non-stoichiometric aspects and physical properties of La_2NiO_4 oxide.* Inorganica Chimica Acta, 1987. **140**: p. 151-153.

75. Matsuda, M., et al., *Electrophoretic fabrication of a-b plane oriented La_2NiO_4 cathode onto electrolyte in strong magnetic field for low-temperature operating solid oxide fuel cell.* Journal of the European Ceramic Society, 2016. **36**(16): p. 4077-4082.

76. Rice, D.E. and D.J. Buttrey, *An X-Ray Diffraction Study of the Oxygen Content Phase Diagram of $La_2NiO_{4+\delta}$.* Journal of Solid State Chemistry, 1993. **105**(1): p. 197-210.

77. Tabuchi, A., et al., *Small polaron transport in $LaSrCoO_4$.* Journal of Alloys and Compounds, 2006. **408**: p. 1214-1216.

78. de Laune, B.P., et al., *Topotactic Fluorine Insertion into the Channels of $FeSb_2O_4$-Related Materials.* Inorganic Chemistry Communications, 2017. **56**(16): p. 10078-10089.

79. Kolb, U., et al., *Towards automated diffraction tomography: part I-data acquisition.* Ultramicroscopy, 2007. **107**(6-7): p. 507-513.

80. Vincent, R. and P.A. Midgley, *Double conical beam-rocking system for measurement of integrated electron diffraction intensities.* Ultramicroscopy, 1994. **53**(3): p. 271-282.

81. Mugnaioli, E., T. Gorelik, and U. Kolb, *"Ab initio" structure solution from electron diffraction data obtained by a combination of automated diffraction tomography and precession technique.* Ultramicroscopy, 2009. **109**(6): p. 758-65.

82. Burla, M.C., et al., *Crystal structure determination and refinement via SIR2014.* Journal of Applied Crystallography, 2015. **48**: p. 306-309.

83. Petříček, V., M. Dušek, and L. Palatinus, *Crystallographic Computing System JANA2006: General features.* Zeitschrift für Kristallographie - Crystalline Materials, 2014. **229**(5): p. 345–352.

84. Palatinus, L., *PETS. Program for Analysis of Electron Diffraction Data*. 2011, Institute of Physics: Prague.

85. Nowroozi, M.A. and O. Clemens, *Insights on the Behavior of Conversion Based Anode Materials for Fluoride Ion Batteries by Testing Against an Intercalation-Based Reference Cathode.* ACS Applied Energy Materials, 2018. **1**: p. 6626−6637.

86. Nowroozi, M.A., et al., *La_2CoO_4: A New Intercalation Based Cathode Material for Fluoride Ion Batteries with Improved Cycling Stability.* Journal of Materials Chemistry A, 2018. **6**: p. 4658-4669.

87. Nowroozi, M.A., et al., *$LaSrMnO_4$: Reversible Electrochemical Intercalation of Fluoride Ions in the Context of Fluoride Ion Batteries.* Chemistry of Materials, 2017. **29**(8): p. 3441-3453.

88. Nowroozi, M.A., B. de Laune, and O. Clemens, *Reversible Electrochemical Intercalation and Deintercalation of Fluoride Ions into Host Lattices with Schafarzikite-Type Structure.* ChemistryOpen, 2018. **7**(8): p. 617-623.

89. Cho, J., et al., *A breakthrough in the safety of lithium secondary batteries by coating the cathode material with $AlPO_4$ nanoparticles.* Angewandte Chemie International Edition, 2003. **42**(14): p. 1618-21.

90. Lee, M.J., et al., *High performance $LiMn_2O_4$ cathode materials grown with epitaxial layered nanostructure for Li-ion batteries.* Nano Letters, 2014. **14**(2): p. 993-9.

91. A. Yamada, S.C.C., and K. Hinokuma, *Optimized $LiFePO_4$ for Lithium Battery Cathodes.* Journal of Electrochemical Society, 2001. **148**(3): p. A224-A229.

92. Vanýsek, P., *CRC Handbook of Chemistry and Physics* in *Section 8: Analytical Chemistry*, D.R. Lide, Editor. 2005, CRC Press: Boca Raton, FL. p. 8.20-29.

93. Koksbang, R., et al., *Cathode materials for lithium rocking chair batteries.* Solid State Ionics, 1996. **84**: p. 1-21.

94. Melot, B.C. and J.-M. Tarascon, *Design and Preparation of Materials for Advanced Electrochemical Storage.* Accounts of Chemical Research, 2013. **46**(5): p. 1226-1238.

95. Clemens, O., et al., *Reply to "Structural and magnetic behavior of the cubic oxyfluoride SrFeO$_2$F studied by neutron diffraction".* Journal of Solid State Chemistry, 2015. **226**: p. 326-331.

96. Blakely, C.K., et al., *Multistep synthesis of the SrFeO$_2$F perovskite oxyfluoride via the SrFeO$_2$ infinite-layer intermediate.* Journal of Fluorine Chemistry, 2014. **159**: p. 8-14.

97. Yamamoto, T. and H. Kageyama, *Hydride Reductions of Transition Metal Oxides.* Chemical Letters, 2013. **42**: p. 946-953.

98. Girgsdies, F. and R. Schöllhorn, *Spontaneous Topotactic Oxidation of La$_2$CoO$_4$ at Room Temperature.* Solid State Communications, 1994. **91**: p. 111-112.

99. Merkle, R. and J. Maier, *On the Tammann-Rule.* Zeitschrift für anorganische und allgemeine Chemie, 2005. **631**(6-7): p. 1163-1166.

100. Aikens, L.D., et al., *Staged fluorine insertion into manganese oxides with Ruddlesden–Popper structures: LaSrMnO$_4$F and La$_{1.2}$Sr$_{1.8}$Mn$_2$O$_7$F.* Journal of Materials Chemistry, 2002. **12**(2): p. 264-267.

101. Linden, D. and T.B. Reddy, *Handbook of Batteries.* 3rd ed. 2001, New York: McGraw-Hill. 1453.

102. Baukal, W., *Über reaktionsmöglichkeiten in elektroden von festkörperbatterien.* Electrochimica Acta, 1974. **19**(11): p. 687-694.

103. Longo, J.M. and P.M. Raccah, *The Structure of La$_2$CuO$_4$ and LaSrVO$_4$.* Journal of Solid State Chemistry, 1972. **6**: p. 526-531.

104. Mehta, A. and P.J. Heaney, *Structure of La$_2$NiO$_{4.18}$.* Physical Review B, 1994. **49**(1): p. 563-571.

105. Hahn, T., *International Tables for Crystallography.* 5 ed. Vol. A. 2005, Denmark: Springer.

106. Skinner, S.J. and G. Amow, *Structural observations on La$_2$(Ni,Co)O$_{4\pm\delta}$ phases determined from in situ neutron powder diffraction.* Journal of Solid State Chemistry, 2007. **180**(7): p. 1977-1983.

107. Rodríguez-Carvajal, J., M.T. Fernández-Díaz, and J.L. Martínez, *Neutron diffraction study on structural and magnetic properties of La$_2$NiO$_4$.* Journal of Physics: Condensed Matter, 1991. **3**: p. 3215-3234.

108. Slater, P.R., et al., *Fluorination of the Ruddlesden-Popper type cuprates, Ln$_{2-x}$A$_{1+x}$Cu$_2$O$_{6-y}$ (Ln=La, Nd; A=Ca, Sr).* Journal of Materials Chemistry, 1997. **7**(10): p. 2077-2083.

109. Zhang, R., et al., *La$_2$SrCr$_2$O$_7$F$_2$: A Ruddlesden-Popper Oxyfluoride Containing Octahedrally Coordinated Cr^{4+} Centers.* Inorganic Chemistry, 2016. **55**(6): p. 3169-74.

110. Moon, E.J., et al., *Fluorination of epitaxial oxides: synthesis of perovskite oxyfluoride thin films.* Journal of the American Chemical Society, 2014. **136**(6): p. 2224-2227.

111. Greaves, C. and M.G. Francesconi, *Fluorine insertion in inorganic materials.* Current Opinion in Solid State and Materials Science, 1998. **3**(2): p. 132-136.

112. Zhang, R., M.S. Senn, and M.A. Hayward, *Directed Lifting of Inversion Symmetry in Ruddlesden–Popper Oxide–Fluorides: Toward Ferroelectric and Multiferroic Behavior.* Chemistry of Materials, 2016. **28**(22): p. 8399-8406.

113. Samara, G.A., *Pressure and Temperature Dependences of the Ionic Conductivities of Cubic and Orthorhombic Lead Fluoride (PbF$_2$).* Journal of Physics and Chemistry of Solids, 1979. **40**(7): p. 509-522.

114. Jiang, H., et al., *First-principles study of the electronic structure of PbF$_2$ in the cubic, orthorhombic, and hexagonal phases.* Journal of Physics: Condensed Matter, 2004. **16**(18): p. 3081-3088.

115. Guo, G.W. and W.M. Temmerman, *Electronic structure and magnetism in La$_2$NiO$_4$.* Journal of Physics C: Solid State Physics, 1988. **21**: p. L803-L810.

116.   Huang, D.-p., et al., *Synthesis and electrical conductivity of La₂NiO₄₊δ derived from a polyaminocarboxylate complex precursor.* Materials Letters, 2006. **60**: p. 1892-1895.

117.   Buttrey, D.J., J.M. Honig, and C.N.R. Rao, *Magnetic properties of quasi-two-dimensional La₂NiO₄.* Journal of Solid State Chemistry, 1986. **64**(3): p. 287-295.

118.   Escudero, M.J., A. Fuerte, and L. Daza, *La₂NiO4₊δ potential cathode material on La₀.₉Sr₀.₁Ga₀.₈Mg₀.₂O₂.₈₅ electrolyte for intermediate temperature solid oxide fuel cell.* Journal of Power Sources, 2011. **196**: p. 7245– 7250.

119.   de Laune, B.P. and C. Greaves, *Structural and magnetic characterisation of CoSb₂O₄, and the substitution of Pb²⁺ for Sb³⁺.* Journal of Solid State Chemistry, 2012. **187**: p. 225-230.

120.   Gavarri, J.R. and A.W. Hewat, *Les antimonites antiferromagnetiques MnSb₂O₄ et NiSb₂O₄.* Journal of Solid State Chemistry, 1983. **49**(1): p. 14-19.

121.   Fjellvag, H. and A. Kjekshus, *Crystal and Magnetic Structure of MnSb₂O₄.* Acta Chemica Scandinavica A, 1985. **39**: p. 389-395.

122.   Whitaker, M.J., *Synthesis and Characterisation of Chemically Modified Schafarzikite and Pyrochlore Minerals* in *The School of Chemistry, College of Engineering and Physical Sciences* 2012, University of Birmingham.

123.   de Laune, B.P., et al., *Oxygen Insertion Reactions within the One-Dimensional Channels of Phases Related to FeSb₂O₄.* Inorganic Chemistry, 2017. **56**(1): p. 594-607.

124.   Padhi, A.K., K.S. Nanjundaswamy, and J.B. Goodenough, *Phospho-olivines as Positive-Electrode Materials for Rechargeable Lithium Batteries.* Journal of The Electrochemical Society, 1997. **144**(4): p. 1188-1197.

125.   Besenhard, J.O., *Handbook of Battery Materials*. 1999, New York: Wiley-VCH. 618.

126.   Robinson, J.T., et al., *Properties of fluorinated graphene films.* Nano Lett, 2010. **10**(8): p. 3001-5.

127.   Andre, D., et al., *Characterization of high-power lithium-ion batteries by electrochemical impedance spectroscopy. I. Experimental investigation.* Journal of Power Sources, 2011. **196**(12): p. 5334-5341.

128.   Moulder, J.F., et al., *Handbook of X Ray Photoelectron Spectroscopy: A Reference Book of Standard Spectra for Identification and Interpretation of XPS Data*, ed. Jill Chastain and J. Roger C. King. 1995, Minnesota: Physical Electronics.

129.   Nansé, G., et al., *Fluorination of carbon blacks: An X-ray photoelectron spectroscopy study: I. A literature review of XPS studies of fluorinated carbons. XPS investigation of some reference compounds.* Carbon, 1997. **35**(2): p. 175-194.

130.   Li, Y., et al., *Fluorinated multi-walled carbon nanotubes as cathode materials of lithium and sodium primary batteries: effect of graphitization of carbon nanotubes.* Journal of Materials Chemistry A, 2019. **7**(12): p. 7128-7137.

131.   Yue, H., et al., *Synthesis and characterization of fluorinated carbon nanotubes for lithium primary batteries with high power density.* Nanotechnology, 2013. **24**(42): p. 424003.

132.   Westerhoff, U., et al., *Analysis of Lithium-Ion Battery Models Based on Electrochemical Impedance Spectroscopy.* Energy Technology, 2016. **4**(12): p. 1620-1630.

133.   Zhang, Y.C., C.Y. Wang, and X.D. Tang, *Cycling degradation of an automotive LiFePO₄ lithium-ion battery.* Journal of Power Sources, 2011. **196**(3): p. 1513-1520.

134.   Grenier, A., *Development of solid-state Fluoride-ion Batteries: cell design, electrolyte characterization and electrochemical mechanisms.* 2016, Université Pierre et Marie Curie - Paris VI.

135.   Gschwind, F., et al., *Fluoride ion batteries: Theoretical performance, safety, toxicity, and a combinatorial screening of new electrodes.* Journal of Fluorine Chemistry, 2016. **182**: p. 76-90.

136.   Orazem, M.E. and B. Tribollet, *Electrochemical impedance spectroscopy* 2008, Hoboken, N.J.: Wiley.

137. *ICSD Database*. 1998 12.06.2017 20, November, 2017]; ICSD Database]. Available from: http://www2.fiz-karlsruhe.de/icsd_web.html.

138. Jayaprakash, N., et al., *Porous hollow carbon@sulfur composites for high-power lithium-sulfur batteries.* Angewandte Chemie International Edition, 2011. **50**(26): p. 5904-8.

139. Li, W., et al., *High-performance hollow sulfur nanostructured battery cathode through a scalable, room temperature, one-step, bottom-up approach.* Proceedings of the National Academy of Sciences of the United States of America, 2013. **110**(18): p. 7148-53.

140. Liu, Y., et al., *Lithium–tellurium batteries based on tellurium/porous carbon composite.* Journal of Materials Chemistry A, 2014. **2**(31): p. 12201-12207.

141. Nicholson, R.S., *Theory and Application of Cyclic Voltammetry for Measurement of Electrode Reaction Kinetics.* Analytical Chemistry, 1965. **37**(11): p. 1351-1355.

142. Hsu, C.H. and F. Mansfeld, *Technical Note: Concerning the Conversion of the Constant Phase Element Parameter Y_0 into a Capacitance.* Corrosion, 2001. **57**(9): p. 747-748

143. Hirschorn, B., et al., *Determination of effective capacitance and film thickness from constant-phase-element parameters.* Electrochimica Acta, 2010. **55**(21): p. 6218-6227.

144. Bisquert, J., *Theory of the Impedance of Electron Diffusion and Recombination in a Thin Layer.* 2002. **106**: p. 325-333.

145. Palatinus, L., V. Petricek, and C.A. Correa, *Structure refinement using precession electron diffraction tomography and dynamical diffraction: theory and implementation.* Acta Crystallographica Section A: Foundations and Advances, 2015. **71**(Pt 2): p. 235-44.

146. Yumitori, S., *Correlation of C_{1s} chemical state intensities with the O_{1s} intensity in the XPS analysis of anodically oxidized glass-like carbon samples.* Journal of Materials Science, 2000. **35**: p. 139– 146.

147. Alexander V. Naumkin, A.K.-V., Stephen W. Gaarenstroom, and Cedric J. Powell. *NIST X-ray Photoelectron Spectroscopy Database* 2000 September 15, 2012 [cited 2019 July 26, 2019]; 4.1:[Available from: https://srdata.nist.gov/xps/Default.aspx.

Curriculum Vitae

Personal Information

Name	Nowroozi, Mohammad Ali
Date of birth	30.06.1987

Working Experiences and Education

12.2015 – 02.2020   **Technische Universität Darmstadt**

Ph.D., Materialdesign durch Synthese, Department of Materials Science and Engineering
Research Assistant

01.2013 – 09.2015   **Shiraz Pasargad Institute**

University lecturer, Shiraz Pasargad Higher Education Institute, Shiraz, Iran

09.2009 – 09.2012   **Shiraz University**

Master, Department of Materials Science and Engineering, Shiraz University, Shiraz, Iran
Field of study: Materials science and engineering

06.2009 – 08.2009   **Shiraz Petrochemical Company**

Internship, Department of technical inspection and nondestructive testing (NDT), Shiraz Petrochemical Company, Shiraz, Iran

09.2005 – 09.2009   **Shiraz University**

Bachelor, Department of Materials Science and Engineering, Shiraz University, Shiraz, Iran
Field of study: Materials science and engineering

Publications

A. Publications in the context of the Ph.D. thesis

1. **Nowroozi, Mohammad Ali**; Wissel, Kerstin; Donzelli, Manuel; Hosseinpour, Niloofar; Plana-Ruiz, Sergi; Kolb, Ute; Schoch, Roland; Bauer Matthias; Muhammad Malik, Ali; Rohrer Jochen; Ivlev; Sergei, Kraus, Florain; Clemens, Oliver, *An all-solid-state fluoride ion battery using La_2NiO_{4+d} as a high voltage cathode material with ultra-high cycle life*, Submitted.

2. **Nowroozi, Mohammad Ali**; Ivlev, Sergei; Rohrer, Jochen; Clemens, Oliver, *La_2CoO_4: A New Intercalation Based Cathode Material for Fluoride Ion Batteries with Improved Cycling Stability*, **Journal of Materials Chemistry A**, 2018, (6), 4658-4669.
(This paper has been selected to be the back cover art of the journal: March 21, 2018, volume 6, issue 11).

3. **Nowroozi, Mohammad Ali**; Clemens, Oliver, *Insights on the Behavior of Conversion Based Anode Materials for Fluoride Ion Batteries by Testing Against an Intercalation-Based Reference Cathode*, **ACS Applied Energy Materials**, 2018, (1), 6626-6637.

4. **Nowroozi, Mohammad Ali**; De Laune, Benjamin; Clemens, Oliver, *Reversible Electrochemical Intercalation and Deintercalation of Fluoride Ions into Host Lattices with Schafarzikite Type Structure*, **ChemistryOpen**, 2018, (7), 617-623.

5. **Nowroozi, Mohammad Ali**; Wissel, Kerstin; Rohrer, Jochen; Munnangi, Annji Reddy; Clemens, Oliver, *$LaSrMnO_4$: Reversible Electrochemical Intercalation of Fluoride Ions in the Context of Fluoride Ion Batteries*, **Chemistry of Materials**, 2017, (29), 3441-3453.
(This paper has been selected to be the cover page of the journal: April 25, 2017, volume 29, number 8).

B. Publications in the context of the master thesis

1. **Nowroozi, M. A.**; Shokrollahi, H., *Magnetic and Structural Properties of Amorphous/ Nanocrystalline $Fe_{42}Ni_{28}Zr_8Ta_2B_{10}C_{10}$ Soft Magnetic Alloy Produced by Mechanical Alloying*, **Advanced Powder Technology**, 2013, (24), 1100-1108.

2. **Nowroozi, M. A**.; Shokrollahi, H., *The Effects of Milling Time and Heat Treatment on the Micro-Structural and Magnetic Behavior of $Fe_{42}Ni_{28}Zr_8Ta_2B_{10}C_{10}$ Synthesized by Mechanical Alloying*, **Journal of Magnetism and Magnetic Materials**, 2013, (335), 53-58.

3. **Nowroozi, M. A**.; Janghorban, K; Hashemi, B; Taghvaei, A. H.; Maleksaeedi, S., *Microstructural Evolution and Amorphous Phase Formation of $Fe_{42}Ni_{28}Zr_8Ta_2B_{10}C_{10}$ Alloy Produced by Mechanical Alloying*, **Powder Technology**, 2013, (233), 255-260.

C. Collaborations

1. Shahraei, Ali; Kuebler, Markus; Martinaiou, Ioanna; Kim, A. Creutz; **Nowroozi, Mohammad Ali**; Paul, Stephen; Weidler, Natascha; Stark, Rober W.; Clemens, Oliver; Kramm, Ulrike I., **Journal of Materials Chemistry A**, 2018, (6), 22310-22319.

2. Shahraei, Ali; Martinaiou, Ioanna; Kim, Alexander Creutz; Kuebler, Markus; Weidler, Natascha; Ranecky, Ranecky, Simon Theophil; Wallace, William David; **Nowroozi, Mohammad Ali**; Clemens, Oliver; Stark, Robert W., Kramm, Ulrike, **Chemistry: A European Journal**, 2018, (24), 12480-12484.

Conferences

1. **Oral presentation**; EUROMAT 2019, *September 2019*, Stockholm, Sweden
2. **Poster presentation**; 680th WE-Heraeus-Seminar on Materials Development for Automotive Propulsion, *October 2018*, Bad Honnef, Germany
3. **Oral presentation**; 18. Deutscher Fluortag, *September 2018*, Schmitten, Germany
4. **Oral presentation (in German)**; 47th Hischegg-Seminar Festkörperchemie, *June 2018*, Hirschegg, Austria
5. **Poster presentation**; 1st International Symposium on Solid-State Batteries, *May 2018*, EMPA, Dübendorf, Switzerland
6. **Poster presentation (Received "Science Award for Electrochemistry" for the poster)**; Volkswagen and BASF Science Award Electrochemistry, *November 2017*, Karlsruhe Institute of Technology, Karlsruhe, Germany
7. **Oral presentation**; 16th European Conference on Solid State Chemistry, *July 2017*, University of Strathclyde, Glasgow, UK
8. **Poster presentation**; Colloquium: Solid-State Batteries II, *November 2016*, House of Logistics and Mobility, Frankfurt, Germany
9. **Poster presentation**; 5th Joint Congress of Iranian Metallurgical Engineering Society and Iranian Foundrymen's Society, *October 2011*, Isfahan University of Technology, Isfahan, Iran

Acknowledgements